Influence of Pore Size Distribution on Drying Behaviour of Porous Media by a Continuous Model

(Einfluss der Porengrößenverteilung auf das Trocknungsverhalten poröser Medien mittels eines Kontinuumsmodells)

Dissertation

zur Erlangung des akademischen Grades

Doktoringenieur
(Dr.-Ing.)

von Master of Engineering **Thai Hong Vu**

geboren am 16. Juli 1974 in Yenbai, Vietnam

genehmigt durch die Fakultät für Verfahrens- und Systemtechnik
der Otto-von-Guericke-Universität Magdeburg

Promotionskommission:

Jun.-Prof. Dr.-Ing. Stefan Heinrich	(Gutachter)
Prof. Dr.-Ing. habil. Dr. h. c. Lothar Mörl	(Vorsitz)
Dr. Thomas Metzger	(Betreuer, Gutachter)
Prof. Dr.-Ing. habil. Evangelos Tsotsas	(Betreuer)
Prof. Dr. rer. nat. habil. Gerald Warnecke	(Mitglied)

eingereicht am 1. Juni 2006

Promotionskolloquium am 10. Juli 2006

To my parents

Acknowledgements

ABSTRACT

Die Trocknung poröser Materialien spielt eine wichtige Rolle in vielen verschiedenen Bereichen der Industrie, und sie ist zugleich einer der kompliziertesten technischen Prozesse. Im Prinzip kann man die Trocknung poröser Stoffe auf zwei Weisen beschreiben, mit Kontinuums- oder diskreten Modellen. Der erste Ansatz basiert auf der Beschreibung des Systems als fiktives Kontinuum und bedient sich effektiver Transportkoeffizienten. Im diskreten Modellansatz wird das poröse Medium als Netzwerk aus Poren repräsentiert und die Transportvorgänge werden direkt auf der Porenebene beschrieben.

Zur Entwicklung eines kontinuierlichen Trocknungsmodells kann die Volumenmittelungsmethode herangezogen werden, um makroskopische Transportgleichungen von grundlegenden mikroskopischen Gleichungen für die Gas-, Flüssig- und Feststoffphase abzuleiten. Es resultiert ein System aus Erhaltungsgleichungen für Masse, Impuls und Enthalpie, in welchen die gemittelten Zustandsvariablen (Feuchtegehalt, Temperatur und Gasdruck) sowie ein Satz von effektiven Parametern auftreten. Diese effektiven Parameter haben großen Einfluss auf das Trocknungsverhalten und müssen experimentell bestimmt werden oder aber mit großer Sorgfalt bezüglich der mikroskopischen Materialstruktur berechnet werden. Im Allgemeinen handelt es sich bei der Bestimmung dieser Parameter um ein offenes Problem, welches weiterer Forschung bedarf. Die Parameter sind im Einzelnen die Kapillardruckkurve, die Permeabilitäten, der effektive Diffusionskoeffizient und die effektive Wärmeleitfähigkeit.

Als ersten Schritt, um Grundlagenwissen über den Zusammenhang zwischen Porenstruktur und Trocknungskinetik zu sammeln, wird das poröse Medium in dieser Arbeit durch ein Kapillarenbündel mit einer Radienverteilung repräsentiert, für welches die genannten effektiven Größen berechnet werden. In diesem Modell spielt die Porengrößenverteilung die Schlüsselrolle, um eine Verbindung zwischen Mikrostruktur und makroskopischem Trockungsverhalten herzustellen. Durch Variation des mittleren Porenradius und der Verteilungsbreite sowie der Anzahl der Moden (monomodale und bimodale Verteilungen) wird der Einfluss der Porengrößenverteilung auf die effektiven Parameter und das Trocknungsverhalten analysiert. Die Ergebnisse werden mit der Kontrollvolumenmethode berechnet und als zeitliche Entwicklung von lokaler Feuchte, Temperatur und Gasdruck sowie als gemittelte Trocknungskurven gezeigt.

Das Kontinuumsmodell für die Geometrie des Kapillarbündels wird mit zwei diskreten Modellen verglichen, einem eindimensionalen Kapillarmodell und einem Porennetzwerkmodell für äquivalente Geometrien. Eine gute Übereinstimmung zwischen kontinuierlichem und diskretem Ansatz kann gezeigt werden.

Zusätzlich wird das kontinuierliche Trocknungsmodell für ein Referenzmaterial (Gasbeton) dazu benutzt, den Einfluss der Partikelgröße auf die Trocknungszeit zu untersuchen. Die Ergebnisse werden mit einem einfachen Diffusionsmodell und dem Modell des wandernden Trocknungsspiegels verglichen.

Neben der Trocknungsmodellierung werden auch verschiedene experimentelle Methoden eingesetzt, um die Porenstruktur und Porengrößenverteilung sowie das Sorptions- und Trocknungsverhalten von γ-Al_2O_3 Partikeln von 4.8 mm Durchmesser zu charakterisieren.

ABSTRACT

Being one of the most complex processes encountered in engineering, the drying of porous media has a vital role in many different industrial fields. In principle, the transport phenomena in the drying of porous media can be modeled using a continuous or discrete approach. The continuous approach is based on a description of the system as a fictitious continuum by using effective coefficients of heat and mass transfer. In the discrete approach the drying of porous media is represented by a network of pores and transport phenomena are directly described at the pore level.

In developing a continuous drying model, the volume averaging technique can be used to derive a system of macroscopic transport equations from a set of basic transport laws at microscopic level for gas, liquid and solid phases. The derived system represents the conservation equations of mass, energy and momentum, in which the average state variables (moisture content, temperature and gas pressure) and a set of effective parameters are employed. These effective parameters have strong effects on the material drying characteristics and must be determined experimentally or must be modeled with a great care about the material microscopic structure. In general, the problem of determining the model effective parameters is yet to be solved and deserves careful attention. These parameters are capillary pressure curve, liquid and gas permeabilities, effective diffusivity, and effective thermal conductivity.

As a first step in gaining a basic knowledge about how the material microstructure affects its drying kinetics, in this work, the porous medium are represented by a bundle of capillaries with a radius distribution to compute the mentioned effective parameters. In this model, the material pore size distribution is considered as the key to build a link between the material microstructure and its macro drying behaviour. By varying the mean pore radius and the broadness of the distribution as well as the number of modes (mono-modal and bi-modal distributions), the influence of pore size distribution on effective parameters and on drying behaviour is analysed. This analysis is realized with the help of the control volume method and the numerical results are presented as temporal evolution of local moisture content, temperature and gas pressure as well as overall drying curves. The continuous model for the bundle of capillaries geometry is compared with two discrete models, a one-dimensional capillary model and a pore network model using an equivalent geometry. A good agreement between the continuous and the discrete approaches is found.

In addition to the study of the influence of pore size distribution on drying behaviour, the continuous model is also used to investigate the influence of sample size on drying time, where a reference material (light concrete) is considered. The results are compared with a simple diffusion model and a receding front model.

Besides the numerical modelling of drying, several experimental techniques were used to characterize the pore structure, the pore size distribution, the sorption equilibrium and the drying kinetics of γ-Al_2O_3 particles of diameter 4.8 mm.

TABLE OF CONTENTS

Chapter 5 **EXPERIMENTS WITH γ-Al₂O₃ PARTICLE**

NOMENCLATURE

A	area	m^2
a	constant factor used in Eqs. (1-28), (1-29)	
b	constant factor used in Eqs. (1-28), (1-29)	
C_p	mass fraction weighted average heat capacity	$J.kg^{-1}.K^{-1}$
c	constant used in BET and Langmuir models	
c_p	specific heat capacity	$J.kg^{-1}.K^{-1}$
$\mathbf{D}$	diffusivity tensor	$m^2.s^{-1}$
D	diffusivity	$m^2.s^{-1}$
d	particle diameter	m
$\mathbf{F}$	vector presenting discretized governing equations	
F	component of $\mathbf{F}$	
F_1	function used in modified capillary pressure curve	
F_k	function used in modified relative permeability curves	
f	weighting factor	
f_a, f_b, f_c, f_d	coefficients in function F_k	
f_1, f_2	coefficients used in modified capillary pressure curve and transition region	
$f(\psi)$	function in Philip and De Vries model used in Eqs. (1-44), (1-45)	
$\mathbf{g}$	gravitational acceleration vector	$m.s^{-2}$
g	gravitational acceleration	$m.s^{-2}$
h_1, h_2	coefficients used in modified transition region of bi-modal pore size distributions	
h_i	enthalpy per unit mass for species i in the α-phase ($\alpha = s, w, g$)	$J.kg^{-1}$
h_α	mass average enthalpy of the α-phase ($\alpha = s, w, g$)	$J.kg^{-1}$
Δh_v	evaporation enthalpy	$J.kg^{-1}$
Δh_s	sorption enthalpy	$J.kg^{-1}$
$\mathbf{J}$	general flux vector	
J	component of $\mathbf{J}$	
$\mathbf{K}$	absolute permeability tensor	m^2
K	absolute permeability	m^2

K_{ij}	kinetic coefficients in Luikov's model used in Eqs. (1-53) to (1-55)	
k	relative permeability tensor	
k	relative permeability	
L	macroscopic characterisric length or thickness	m
M	mass	kg
$\tilde{M}$	molar mass	kg.mol^{-1}
ΔM_w	amount of water removed during drying	kg
ΔM_a	amount of air taken during drying	kg
$\dot{M}_{ev}$	mass evaporation rate per unit volume in Luikov's model used in Eqs.(1-50) to (1-52)	kg.m^{-3}.s^{-1}
m_{ratio}	mesh ratio	
$\dot{\mathbf{m}}$	mass flux vector	kg.m^{-2}.s^{-1}
$\dot{m}$	single scalar mass flux	kg.m^{-2}.s^{-1}
$\dot{\mathbf{m}}_v$	evaporation rate vector	kg.m^{-2}.s^{-1}
$\dot{m}_v$	single scalar evaporation rate	kg.m^{-2}.s^{-1}
N	number of species, number of grid nodes	
$\dot{N}$	molar flow rate	mol.s^{-1}
Nu	Nusselt number	
$\hat{\mathbf{n}}$	unit normal vector	
n_e	constant factor used in Eq. (1-28)	
n_g	molar gas density	mol.m^{-3}
P	pressure	Pa
Pr	Prandtl number	
q	heat flux vector	W.m^{2}
q	solution vector of state variables	
$\hat{\mathbf{q}}$	guessed value of solution vector **q**	
$\dot{q}$	heat flux	W.m^{2}
R	particle radius	m
$\tilde{R}$	universal gas constant	J.mol^{-1}.K^{-1}
Re	Reynolds number	
r	capillary radius	m
r_0	mean capillary radius	m
S	saturation	
Sc	Schmidt number	
Sh	Sherwood number	

T	stress tensor	$N.m^{-2}$
T	temperature	K
t	time	s
tol	tolerance for convergence	
$\mathbf{u}_i$	diffusion velocity of species i	$m.s^{-1}$
V	volume	m^3
$\dot{V}$	volumetric flow rate	$m^3.s^{-1}$
$\mathbf{v}$	mass average velocity	$m.s^{-1}$
$\mathbf{w}$	velocity of liquid-gas interface	$m.s^{-1}$
X	moisture content	$kg.kg^{-1}$
x	space coordinate	m
y	mass fraction	$kg.kg^{-1}$
$\tilde{y}$	molar fraction	$mol.mol^{-1}$
z	depth	m

Greek symbols

α	heat transfer coefficient	$W.m^{-2}.K^{-1}$
β	mass transfer coefficient	$m.s^{-1}$
Δ	difference	
δ	diffusion coefficient	$m^2.s^{-1}$
$\delta\mathbf{q}$	Newton-Raphson correction vector	
ε	volume fraction	
ε_{eq}	small positive number used in defining drying time	
ε_w^{err}	accuracy of water flow	
ε_a^{err}	accuracy of water flow	
$\in$	dimensionless factor in Luikov's used in Eqs. (1-50), (1-52)	
η	dynamic viscosity	Pa.s
θ	contact angle	rad
$\boldsymbol{\lambda}$	thermal conductivity tensor	$W.m^{-1}.K^{-1}$
λ	thermal conductivity	$W.m^{-1}.K^{-1}$
λ_{step}	linesearch factor	
$\dot{\nu}$	normalized evaporation rate	
ξ	normalized moisture content	
ρ	density	$kg.m^{-3}$
σ	surface tension	$N.m^{-1}$

σ_0	standard deviation of capillary radius	m
τ	viscous stress tensor	$N.m^{-2}$
τ	characteristic time	s
Φ	rate of volumetric heat generation	$J.s^{-1}.m^{-3}$
φ	relative humidity	
Ψ	conserved quantity	
Ψ_w	gravity potential of water	$m^2.s^{-2}$
Ψ_g	gravity potential of gas	$m^2.s^{-2}$
ψ	porosity	

Subscripts

A_E , A_W	east and west faces of a control volume
a	air
av	average
b	bound water
big	large pore
c	capillary
cr	critical
$diff$	diffusion
dry	dry
E	east node, node E
eff	effective
eq	equilibrium
F	moving evaporation front
$fill$	maximum capillary radius filled by liquid
fw	free water
g	gas
i	species i
irr	irreducible
l	liquid
max	maximum
min	minimum
N	node N
P	node P
p	particle
R	reference

s	solid
sat	saturation
sorb	adsorbed water
total	total
v	vapour
void	void
W	west node, node W
w	water
∞	bulk property
0	initial value
I	first drying period
II	second drying period

Superscripts

conv	convection
diff	diffusion
err	accuracy
T	transpose
t	at time *t*
*	saturation
-1	inverse

Mathematical symbols

$\dfrac{D}{Dt}$	material derivative
$\dfrac{d}{dt}$	time derivative
$\dfrac{\partial}{\partial x}$	partial derivative
∇	gradient operator
$\nabla\cdot$	divergence operator
$\dfrac{\partial \mathbf{F}}{\partial \mathbf{q}}$	Jacobian matrix
$\|\mathbf{F}\|$	norm of vector $\mathbf{F}$
$\langle \chi \rangle$	spatial average of function χ
$\langle \chi_s \rangle$	phase average of a function χ_s, which represents a property of the *s* phase

$\langle \chi_s \rangle^s$ intrinsic phase average of a function χ_s, which represents a property of the s phase

$\overline{\Psi}$ average of quantity Ψ

INTRODUCTION

Drying is a separation process in solid-liquid systems. Playing an important role in different industries (chemicals, pharmaceuticals, agriculture, etc.), drying is one of the most complex phenomena encountered in engineering because of the simultaneous heat and mass transfer taking place in the course of the process. In the past decades, drying of porous media has attracted the attention of many researchers all around the world. Although the investigation of drying processes both experimentally and theoretically has been realized for centuries, the coupling of heat and mass transfer and other phenomena in drying is still a challenging problem. Beside theoretical developments, numerical methods have been applied successfully to simulate the drying process of porous media at macroscopic scale as well as at microscopic scale.

In principle, the transport phenomena in porous media can be modelled using continuous or discrete approach. The continuous approach is based on a description of the system as a fictitious continuum by using effective coefficients for heat and mass transfer. In many cases, the drying characteristics of porous media can be simulated with very good accuracy by the continuous approach. However, this approach fails to describe the drying properties of different drying systems at microscopic level if, for example, the length scale separation is not fulfilled or if we have fractal fronts or disconnected liquid clusters. The discrete approach is developed in order to overcome these problems. In the discrete approach the drying of porous media is modelled by using a network of pores and the motion of the liquid-gas interface is modelled at the pore level (Laurindo and Prat, 1996 [44], 1998 [45]; Prat, 1998 [80], 2002 [81]; Segura and Toledo, 2005 [91]).

In developing a drying model based on the continuous approach, Whitaker (1977 [115]; 1980 [116]) used the volume averaging technique to derive a system of macroscopic transport equations from a set of basic transport laws at microscopic level (pore scale) for the three phases (gas, liquid and solid). In Whitaker's work, a porous medium was assumed to be equivalent to a continuum. A set of conservation equations for mass, energy and momentum was introduced using average state variables. The continuous model developed by Whitaker is considered as rigorous and the most advanced continuous model today. Therefore this model will be employed here in this research work.

The theory of Whitaker was later applied to several porous media, e.g. by Perré (1987 [66]), Turner (1991 [103]), Ouelhazi *et al.* (1991 [61]), Boukadida and Nasrallah (1995

[8]), Perré and Turner (1999 [71]). Numerical techniques were developed to simulate the drying process using the derived average conservation equations. Among others, Perré and Turner (1996 [69], [107], 1999 [71]) employed the control volume method to solve the problem. The advantage of this numerical method is that it ensures the conservation of mass and enthalpy through the boundaries of elements. The continuous model developed by Whitaker and later by Perré and Turner is well suited to describe the drying of porous media because the coupled heat and mass transfer is modelled using effective parameters, which have physical meaning and are not lumped parameters to compare with previous models. However, difficulties exist in applying Whitaker's model due to the mathematical complexity of the governing equations and the difficult determination of the effective model parameters (Tsotsas, 1992 [102]). These parameters have decisive effects on the simulated drying characteristics and must be determined experimentally or must be modelled with great care concerning the microscopic material structure. In general, the problem of determining the effective model parameters is yet to be solved and deserves careful attention. As a first step towards solving this problem, in this work, the influence of pore size distribution on the macroscopic material drying behaviour is investigated by employing the continuous approach and with the help of the control volume method.

In the continuous model of Whitaker, the capillary pressure, the liquid and gas permeabilities, the effective diffusivity and the effective thermal conductivity play important roles. These parameters are normally functions of one or all state variables (moisture content, temperature and pressure) and depend of course on material type. Under some simple conditions (isothermal drying, regular network, for instance), the relative permeability of liquid and the effective diffusivity of vapour can be computed from a simple pore network model (Nowicki *et al.,* 1992 [59]). In order to form a basic knowledge about how the pore size distribution of a material affects its drying kinetics, we employ in this work a one-dimensional capillary model, in which liquid flows by capillary pumping and friction and vapour is transported by diffusion, to compute the mentioned effective parameters. In this model, the material pore size distribution is considered as the key to build a link between the material's microstructure and its drying behaviour. The model will offer the possibility to directly compare the modern way of discrete and the traditional way of continuous modelling. This can help in the future to investigate to what extent they are equivalent and where the limits of continuous modelling are (Metzger *et al.*, 2006 [54]).

Objectives of the thesis

Aiming at studying the influence of pore size distribution on drying, the objectives of the thesis include:

❖ Presenting a solution technique for one-dimensional drying simulation based on a comprehensive mathematical model, which describes all relevant transport phenomena (heat, mass and momentum) by means of effective parameters, by using the volume averaging method and the control volume element method. Adapting this solution technique to three-dimensional problems with spherical symmetry in order to model the drying of spherical particles with symmetric drying conditions.

❖ Investigating the influence of effective transport parameters of the model on the drying processes at macroscopic scale by varying numerically their values.

❖ Investigating the influence of sample size on drying time by using the continuous model presented here and comparing the results with diffusion and receding front models.

❖ Developing a micro-macro link between the microstructure of porous materials and their macroscopic drying behaviour by using the material's pore size distribution. Investigating the influence of pore size distribution on drying kinetics via effective transport parameters, which are computed as functions of pore size distribution for a bundle of capillaries.

❖ Comparing drying simulations obtained by the continuous and the discrete approach for a simple reference pore geometry (bundle of capillaries) with different pore size distributions.

❖ Performing drying experiments to estimate some drying parameters and investigate the structure of a given material (γ-Al$_2$O$_3$ particles).

Structure of the thesis

The thesis is organized in five chapters. In the first part of Chapter 1, a short introduction into the basic concepts concerning drying analysis is given. The main part of this chapter is a review of drying models in which their historical development, their application and the estimation of effective parameters are considered.

Chapter 2 discusses and investigates the mathematical model of drying based on the continuous approach. In this chapter, a short introduction of the averaging method and the upscaling process used to obtain the macroscopic governing equations of drying from the basic laws of transport at pore scale level is given. A set of macroscopic equations for heat and mass transfer in porous media is presented. The set consists of three coupled partial differential equations in which the main variables are moisture content, temperature and pressure. In order to create a micro-macro link between the microstructure of porous materials and their macroscopic drying behaviour, the effective parameters of the continuous model are computed by using a capillary model, which takes into account the information of the microscopic structure of porous media via their pore size distribution and the state variables of the drying process.

The set of the partial differential equations presented in Chapter 2 is discretized in Chapter 3 by the control volume method. The discretization process transforms the partial differential equations into a set of nonlinear equations where the unknowns are state variables at a discrete set of points in space. The discretization process is modified to account for the drying problems with spherical symmetry. Newton-Raphson method is applied to solve the obtained nonlinear system of equations.

The results of the numerical simulation are presented in Chapter 4. In the first part of this chapter, a reference material (light concrete) is used to validate the solution method

presented in Chapter 2 and Chapter 3. The influence of different parameters, such as the shape (plate or sphere) and size of the sample, the drying conditions, material properties and effective transport parameters, on the drying kinetics is investigated. The influence of sample size is also examined by employing two other models: the diffusion and the receding front model. The numerical results are then compared with the results obtained by the model used in this work. In the second part of the chapter, the influence of pore size distribution on drying is considered by employing the micro-macro link presented in Chapter 2. In order to estimate the adequateness of this micro-macro link, the simulation results are compared with other discrete models.

Chapter 5 presents the experimental results for a representative material (γ-Al_2O_3). The first experiment uses scanning electron microscopy to investigate the material structure at macroscopic and pore level. The second experiment employs mercury porosimetry to determine the material pore size distribution. The information about pore size distribution from this experiment can be used for calculating effective transport parameters. In the third experiment, the sorption isotherm is determined using a dynamic vapour sorption device. The minimum moisture content determined in this experiment can be used to define the end point of the drying process at given conditions. Finally, the drying experiment with a magnetic suspension balance is introduced. By this experiment, the mass of a drying γ-Al_2O_3 particle is measured and drying kinetics are obtained. The information obtained in this experiment can be used to validate the numerical simulation and can be used in determining effective transport parameters. However, due to the lack of material data for the γ-Al_2O_3 particles, these tasks will have to be done in future work.

Chapter 1

BASIC CONCEPTS AND LITERATURE REVIEW

1.1. Introduction

In the study of the drying of porous media, the definition of parameters, such as material porosity, moisture content, saturation, gas pressure, capillary pressure, temperature and drying rate, are necessary to analyze and characterize the behaviour of the process. During the course of drying, different phenomena, such as mass and heat transfer, happen simultaneously. In drying, mass transfer can be of diffusive or convective nature, or the two phenomena can happen at the same time. These concepts appeared together with the development of different drying models, all in the effort to have a deeper knowledge of what happens inside a drying body with the ultimate objective of having better designs in various engineering problems related to drying. In this chapter, after the most basic concepts in drying modelling of porous media are introduced, the development of some drying models found in literature will be briefly reviewed. For more complete details about other terms and definitions we refer to, for example, Schluender and Tsotsas (1988 [89]), Dullien (1992 [18]), Krischer and Kast (1992 [40])

1.2. Basic concepts concerning drying

1.2.1. *Main parameters of drying models*

In drying models, the three independent variables of moisture content X (or saturation S), temperature T and total gas pressure P_g are commonly used. All other dynamic state variables can be expressed as functions of these three variables.

Porosity

The porosity of a porous material is the ratio of the total void or pore volume to the total volume of the material

$$\psi = \frac{V_{void}}{V_{total}}$$

(1-1)

The porosity of a given material is measured experimentally. Details of experimental methods can be found, for example, in the work of Dullien (1992 [18]). Among the methods used to determine the porosity of a given material, Hg-porosimetry is an effective one. However, its use is limited to pore radii $r > 3$ nm. This method will be discussed more extensively in Chapter 5.

Saturation and moisture content

Saturation is the volume fraction of void space filled by liquid

$$S = \frac{V_w}{V_{void}}$$

(1-2)

Saturation is dimensionless and takes values from 0 (when the medium is completely dry) to 1 (when the medium is completely saturated). Note that we use water as liquid throughout this work.

Besides the concept of saturation another quantity, which is commonly used, is moisture content. The moisture content is the ratio between the total mass of water and the mass of dry solid

$$X = \frac{M_w}{M_s} \frac{\text{(kg of water)}}{\text{(kg of dry solid)}}$$

(1-3)

The relationship between moisture content and saturation is

$$X = \frac{\psi \rho_w}{(1-\psi)\rho_s} \cdot S$$

(1-4)

where ρ_w and ρ_s are the density of water and the density of solid, respectively. Both moisture content X and saturation S are used extensively throughout this work.

Gas pressure

The gas phase, which is denoted by variables with the subscript g in this work, is a mixture of air and water vapour. The air and vapour phases are denoted by the subscript a and v, respectively. The total gas pressure is the sum of partial air and vapour pressures

$$P_g = P_v + P_a$$

(1-5)

It is assumed that the gas phase obeys ideal gas laws

$$P_i = \frac{\rho_i \widetilde{R} T}{\widetilde{M}_i}$$

(1-6)

where i stands for a, v, g; ρ_i for the mass density; $\widetilde{R}$ for the ideal gas constant and $\widetilde{M}_i$ for the molar mass. An average molar mass can be obtained to

$$\widetilde{M}_g = \widetilde{M}_a + (\widetilde{M}_v - \widetilde{M}_a)\frac{P_v}{P_g}$$

(1-7)

Relative humidity

The relative humidity φ is the ratio between the actual vapour pressure in the air-vapour mixture P_v and the saturation vapour pressure P_v^* at a given temperature

$$\varphi = \frac{P_v}{P_v^*(T)} \tag{1-8}$$

The relative humidity is dimensionless and can take values from 0 to 1.

1.2.2. *Capillary pressure and sorption isotherm*

Capillary pressure

The capillary pressure is the difference between the gas pressure P_g and the liquid water pressure P_w due to the surface tension σ at the gas-liquid interface in the pores. The capillary pressure is given by the Washburn equation

$$P_c = \frac{2\sigma \cos \theta}{r} \tag{1-9}$$

and

$$P_c = P_g - P_w \tag{1-10}$$

where r is the radius of the capillary tube and θ is the contact angle between water and solid.

Irreducible moisture content

The irreducible moisture content X_{irr} is a concept used as a simplified classification. Below this value water is adsorbed and above this value water is free. We have

$$X = X_{irr} + X_{fw} \tag{1-11}$$

where X_{fw} is the moisture content of free water.

Note that the definition of adsorbed water differs from that of bound water, which is fixed by chemical bonding. In this work, bound water is neglected.

Sorption isotherm

The two curves depicted in Figure 1.1 are sorption isotherms, which describe the relationship between equilibrium moisture content and relative humidity of air. These values can be obtained experimentally by allowing sufficiently long contact of a material with air under isothermal conditions (Strumillo and Kudra, 1986 [96]). The curve in which the moisture is adsorbed is the adsorption isotherm. Contrarily, if the moisture is desorbed the curve is called desorption isotherm.
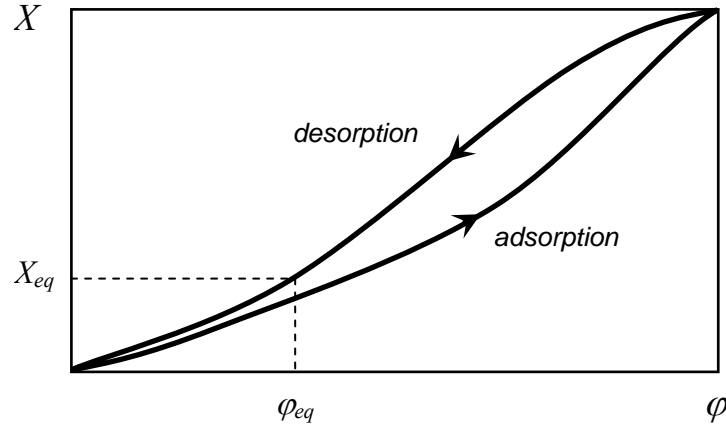
Figure 1.1 Sorption isotherms.

Studies about sorption isotherms can be found in many published works, see for example Kast (1988 [34]), Krischer and Kast (1992 [40]). The function of sorption isotherm can be obtained by fitting curves from experimental data. For example, for light concrete the sorption isotherm may be given as follows (Perré and Turner, 1999 [71])

$$\varphi(X) = \begin{cases} 1 & \text{if } X > X_{irr} \\ \dfrac{X}{X_{irr}}\left(2 - \dfrac{X}{X_{irr}}\right) & \text{if } X \le X_{irr} \end{cases} \tag{1-12}$$

The sorption equilibrium is characterized by equilibrium moisture content X_{eq} for a given relative humidity φ and temperature T. The equilibrium moisture content is the value of moisture content at which a material neither gains nor loses moisture, or in other words, it is the minimum moisture content to which a material can theoretically be dried in given drying conditions.

Relationship between moisture content and saturation

Figure 1.2 depicts an example of the relationship between moisture content (X and X_{fw}), saturation (S and S_{fw}) and relative humidity. The relationship between two first quantities is

$$S = \frac{X}{X_{sat}} \tag{1-13}$$

and

$$S_{fw} = \frac{X - X_{irr}}{X_{sat} - X_{irr}} \tag{1-14}$$

where X and S denote the moisture content and saturation in general, X_{sat} is the saturated moisture content and S_{fw} is the saturation of free water, which takes the value 0 in the region of adsorbed water (where $X \le X_{irr}$) and varies from 0 to 1 in the region of free

water (where $X_{irr} < X \leq X_{sat}$). From this figure, one can see that above X_{irr} the curves are closely tangential to the vertical axis of S and the relative humidity is nearly equal to unity. In fact, the relative humidity can take the value unity when moisture content is above X_{irr} (see Eq. (1-12), for instance).
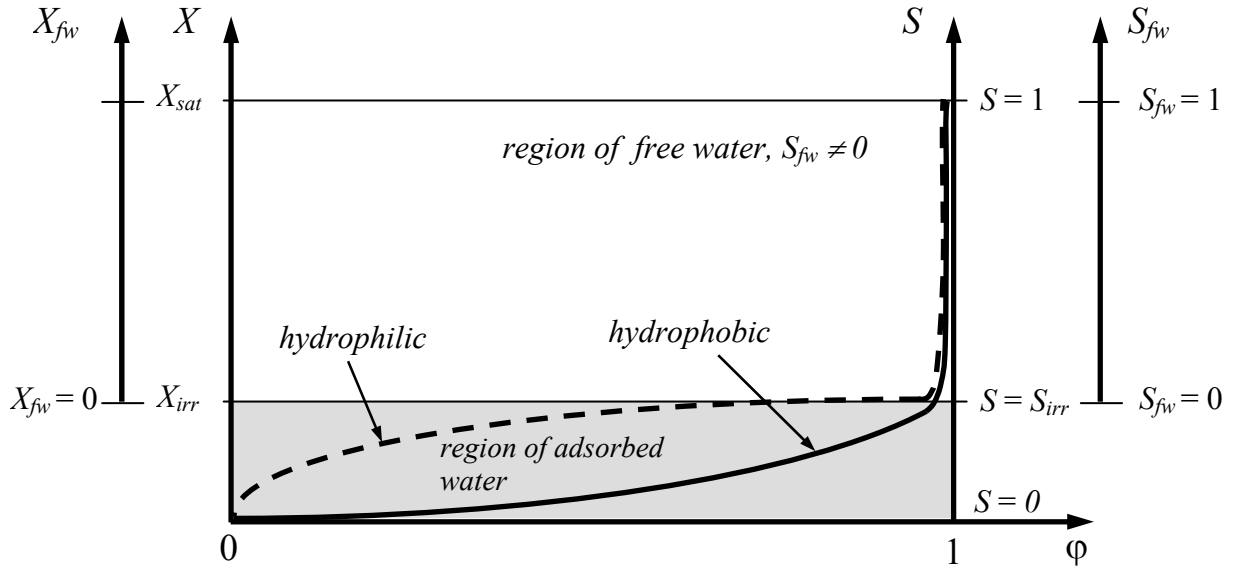
Figure 1.2 Relationship between moisture content, saturation and relative humidity.

1.2.3. Transport phenomena

During the course of a drying process, mass and heat transfer can take place in form of diffusion, convection and for heat transfer also in form of conduction. These phenomena can happen separately or simultaneously.

Diffusion of gas and liquid due to concentration gradient

In many cases of drying, the components of the mixture of air and vapour can be treated as obeying ideal gas laws. The molar flow rates of vapour and air are given by Fick's law

$$\dot{N}_v = -n_g A \delta_{va} \nabla \tilde{y}_v \quad \text{and} \quad \dot{N}_a = -n_g A \delta_{va} \nabla \tilde{y}_a \tag{1-15}$$

In the above equation, A is the relevant cross-section perpendicularly to the direction of motion; δ_{va} is the binary diffusion coefficient of vapour and air; $\tilde{y}_v$ and $\tilde{y}_a$ denote the molar fraction of vapour and air, respectively; n_g is the molar density of the gas mixture. The molar density is calculated from the ideal gas law

$$n_g = \frac{P_g}{\tilde{R}T} = \frac{\rho_g}{\tilde{M}_g} \tag{1-16}$$

In diffusion of binary mixtures, due to conservation reasons, the flow of vapour molecules is equal to the flow of air molecules but in the opposite direction: $\dot{N}_a = -\dot{N}_v$ ("*equimolar diffusion*"). Besides the concept of molar fraction $\tilde{y}$, the mass fraction y is

also used in drying analysis. The relationship between these two quantities can be written in the form

$$y_v = \tilde{y}_v \frac{\tilde{M}_v}{\tilde{M}_g} \quad \text{and} \quad y_a = \tilde{y}_a \frac{\tilde{M}_a}{\tilde{M}_g} \tag{1-17}$$

In term of mass flux, Eq. (1-15) can be written as follows

$$\dot{m}_v = -\frac{\tilde{M}_v P_g}{\tilde{R}T} \delta_{va} \nabla \tilde{y}_v \quad \text{and} \quad \dot{m}_a = -\frac{\tilde{M}_a P_g}{\tilde{R}T} \delta_{va} \nabla \tilde{y}_a \tag{1-18}$$

An alternative way to express diffusive fluxes is (Bird *et al.*, 2002 [5])

$$\dot{m}_v = -\rho_g \delta_{va} \nabla y_v \quad \text{and} \quad \dot{m}_a = -\rho_g \delta_{va} \nabla y_a \tag{1-19}$$

By applying for a porous medium (replace the binary diffusion coefficient δ_{va} by effective diffusivity D_{eff}), the diffusion of vapour and air can be expressed in the term of mass fraction as follows

$$\dot{m}_v = -\rho_g D_{eff} \nabla y_v \quad \text{and} \quad \dot{m}_a = -\rho_g D_{eff} \nabla y_a \tag{1-20}$$

where the effective diffusivity D_{eff} is a function of binary diffusion coefficient δ_{va}, saturation and the structure of the specific material.

Convection of gas and liquid due to total pressure gradient

The convective transport of liquid water and gas is described in terms of velocities of liquid water and gas. These velocities are given by the generalized Darcy law

$$\mathbf{v}_w = -\frac{\mathbf{K} \cdot \mathbf{k}_w}{\eta_w} (\nabla P_w - \nabla \Psi_w) \quad \text{and} \quad \mathbf{v}_g = -\frac{\mathbf{K} \cdot \mathbf{k}_g}{\eta_g} (\nabla P_g - \nabla \Psi_g) \tag{1-21}$$

where $\mathbf{v}_w$ and $\mathbf{v}_g$ are the mass average velocities, Ψ_w and Ψ_g are the gravity potentials. In many cases, the gravity effect is small and can be ignored. $\mathbf{K}$ is the absolute permeability tensor. This is a measure for the permeability, or the ability of a fluid to flow through a medium, when a single fluid is present in the medium. The absolute permeability is fluid independent and depends only on the structure of the drying material. The symbols $\mathbf{k}_w$ and $\mathbf{k}_g$ denote the relative permeability tensors of liquid water and gas. These tensors describe how permeability is reduced due to the presence of a second phase. The relative permeability depends on the saturation of the fluids.

Energy transport

Heat transfer in the drying of porous media takes place by different mechanisms: diffusion, convection, conduction and radiation. The first can be described in terms of molar gradient and the second in terms of pressure gradient. For convective drying, radiation is ignored. Heat transfer by conduction (due to temperature gradient) is computed by Fourier's law (Bird *et al.*, 2002 [5])

$$\mathbf{q}_{conduction} = -\lambda_{eff}\nabla T \tag{1-22}$$

In this equation, ∇T denotes the temperature gradient and λ_{eff} is the effective thermal conductivity tensor. This tensor depends on the structure of the material and its saturation. More details of energy transport will be given in the next chapter.

1.2.4. Drying curve and drying rate curve

In drying analysis, the characteristics of the process can be depicted by the drying curve or drying rate curve. Figure 1.3 shows a typical drying curve for the case of convective drying in which the average moisture content X (or saturation S) is plotted against time. These average values are calculated by integrating the values of X (or S) over the computational domain V at a given time

$$X_{av} = \frac{1}{V}\int_V XdV \quad \text{and} \quad S_{av} = \frac{1}{V}\int_V SdV \tag{1-23}$$
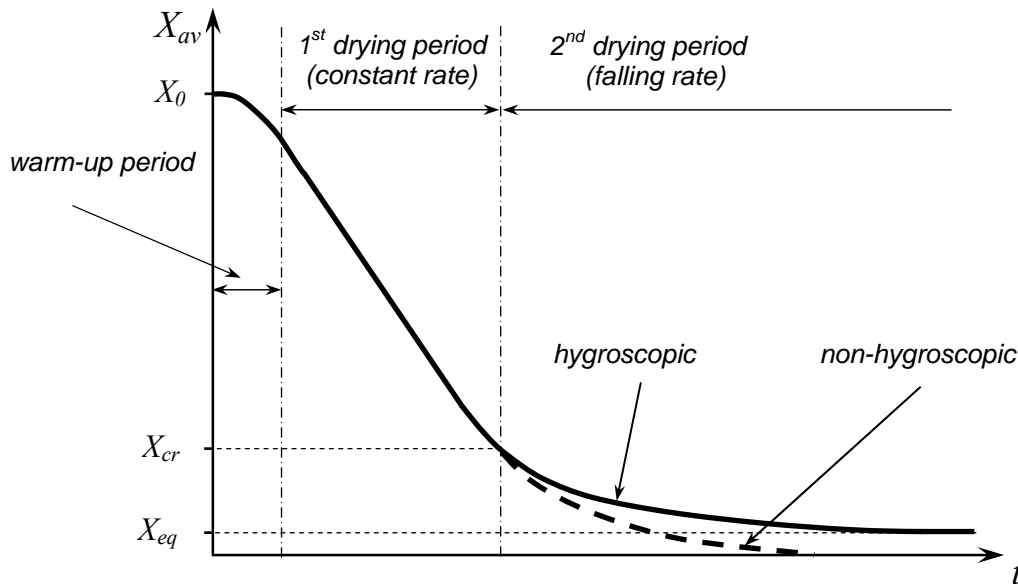
Figure 1.3 Drying curve: average moisture content versus time.

In Figure 1.3, the first drying period or the constant rate period commences after a short warm-up period. During the first drying period, free water is moved continuously to the external surface by capillary forces and moisture content is reduced at a constant rate. This is due to the fact that during this period the external surface is sufficiently wet, it behaves like a liquid surface and the drying rate is equal to the evaporation rate from this liquid surface, which depends only on the state of the drying gas and the transfer coefficients of the boundary layer. In this period, the temperature of solid remains at wet bulb temperature T_{wb} (see Figure 1.4). As drying proceeds and the moisture content reaches the critical moisture content X_{cr}, the first drying period ends and the second drying period or falling rate period commences. The critical or transition point, where moisture content is X_{cr}, depends on the drying rate of the first drying period and the properties of the sample. In the second drying period (falling rate period), the diffusion

11

forces dominate the capillary forces and the removal of liquid is mainly controlled by diffusion. During this period, the moisture content decreases slowly until it reaches the equilibrium value X_{eq} (below which the material can not be dried) for hygroscopic materials or goes down to zero for non-hygroscopic materials (in this case $X_{eq} \approx 0$). The temperature of the solid asymptotically rises to the temperature of drying air (Figure 1.4).
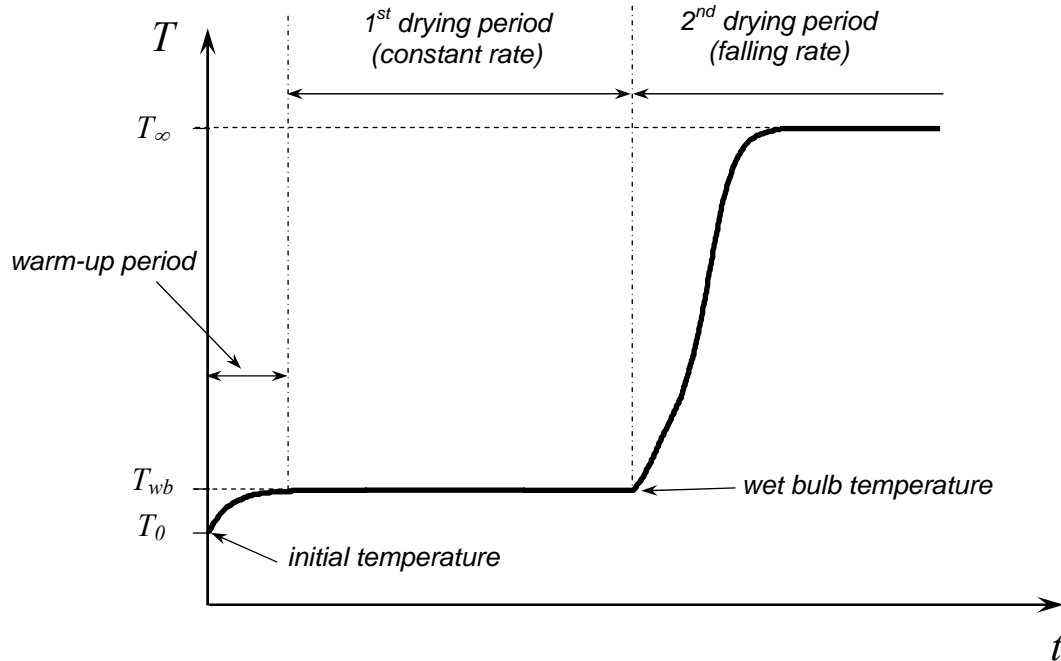
Figure 1.4 Temperature evolution during drying.
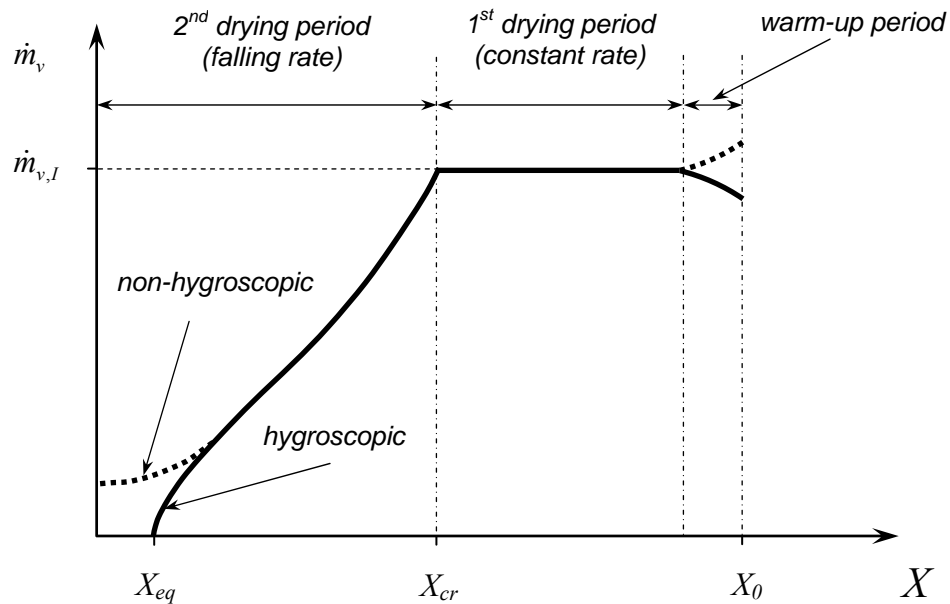
Figure 1.5 Drying rate curve: drying rate versus average moisture content.

The drying rate curve is an alternative way to depict the drying process (Figure 1.5). This curve is obtained by plotting the drying rate versus the (average) moisture content.

In constructing the drying rate curve, the drying rate or rather the vapour mass flux is calculated as follows (Krischer and Kast, 1992 [40])

$$\dot{m}_v = -\frac{M_s}{A}\frac{dX}{dt}$$

(1-24)

where A is the surface of the porous medium being dried.

As mentioned above, in the first drying period, the drying rate is constant and depends only on the state of drying gas (temperature T_∞ and relative humidity φ) and the transfer coefficients (mass and heat transfer coefficients β and α). In the second drying period, the drying rate is reduced and depends on intraparticle transport phenomena. At the end of the drying process, the drying rate goes to zero for hygroscopic materials (as the corresponding moisture content reaches the equilibrium value) or a finite value for non-hygroscopic materials.

The drying time is calculated by rearranging and integrating Eq. (1-24)

$$\tau_{dry} = \frac{M_s}{A}\int_{X_0}^{X_t}\frac{dX}{\dot{m}_v(X)}$$

(1-25)

where X_0 and X_t are the initial moisture content and the moisture content at time t, respectively.

1.3. Literature review of drying models

In this section, the historical development of different models of moisture migration during the drying of porous media as well as their restrictions and applications will be reviewed and discussed. Drying models were developed since the beginning of the twentieth century. Different methods and numerical solutions were presented and applied successfully for several porous media. A review of these methods until the 1980s was given by Fortes and Okos (1980 [21]), Keey (1980 [36]), Bories (1989 [7]). Reviews of empirical, analytical and numerical methods of drying until the 1990s can be found in the work of Tsotsas (1992 [102]).

1.3.1. Diffusion theory

Lewis and Sherwood are known as pioneers in developing mathematical drying models by applying the Fourier equation of heat conduction to the drying of solids. In this equation, temperature and thermal diffusivity were replaced by moisture and moisture diffusivity, respectively. Starting from the idea of Lewis, Sherwood (1929 [92]) provided solutions of the diffusion equation. Sherwood showed that the moisture transport involves two independent processes: the evaporation of moisture at the solid surface and the internal diffusion of liquid to the surface. The following simple diffusion model, in which the diffusivity of liquid is constant, was used to calculate the moisture distribution in a solid during drying and compared with experimental data of some materials (e.g. slabs of wood, clay and soap):

$$\frac{\partial X}{\partial t} = \delta_{eff} \nabla^2 X \tag{1-26}$$

where X is vaguely defined as moisture content, t represents time and δ_{eff} can be considered as an effective diffusion coefficient and is determined experimentally.

At the end of the 1930s, Ceaglske and Hougen (1937 [10]) and Hougen *et al.* (1939 [29]) pointed out that the moisture distribution cannot be calculated correctly only from Eq. (1-26). It was noted that the moisture movement in a solid during drying is due to not only diffusion but also due to other mechanisms such as gravity, external pressure, capillarity, convection and vaporization-condensation where a temperature gradient is applied. Experimental data was collected for some different kinds of porous media (clay, paper pulp, sand, lead shot, porous brick and wood) and compared with the numerical results obtained by Sherwood's model to show the limitation of this model and prove their criticism.

By using the capillary theory to describe the drying of granular materials (such as coarse, medium and fine sand) and based on the collected experiment data, Ceaglske and Hougen (1937 [10]) suggested that the effective diffusion coefficient δ_{eff} should be considered as varying during drying and proposed the following diffusion model

$$\frac{\partial X}{\partial t} = \nabla.\left(\delta_{eff} \nabla X\right) \tag{1-27}$$

The effective diffusion coefficient is now known as a function of moisture content, temperature, material type and drying history. In solving the diffusion equation, this parameter is usually taken as constant or in form of linear, exponential or polynomial functions of moisture content. One example of these functions was given by Suzuki and Maeda (1978 [97])

$$\delta_{eff}(X) = (aX + b)^{n_e} \tag{1-28}$$

where a, b and n_e are constant factors. Suzuki and Maeda also presented an approximation method to describe the moisture distribution within drying porous materials in which the effective diffusion coefficient is expressed as an exponential function of moisture content

$$\delta_{eff}(X) = a.e^{b.X} \tag{1-29}$$

where a and b are constant factors as in the Eq. (1-28). This is a common function used to describe the effective diffusion coefficient. Suzuki and Maeda then solved the nonlinear diffusion problem by using dimensionless variables for diffusion coefficient, moisture content, time and space. It was shown that the steady-flux model (pseudo-steady state) is fairly accurate when it is employed in low moisture content drying. However, it was also found that the diffusion model leads to noticeable error when it is applied to high moisture content drying. The reason is that in this case capillary pumping has strong effect and this mechanism must be taken into account.

To determine the effective diffusion coefficient, in the past decades, a large number of works were carried out. For example, the works of Saravacos and Raouzeos (1986 [88]), Jaros *et al.* (1992 [32]), Mourad *et al.*, (1996 [57]), Ribeiro *et al.* (2002 [86]), Li

and Kobayashi (2005 [47]), Srikiatden and Roberts (2005 [95]) concentrated on materials in food industry and agriculture, Koponen (1987 [38]) dealt with wood, Ketelaars *et al.* (1995 [37]) studied clay, Pel *et al.* (1996 [63]) considered fired-clay brick, sand-lime brick and gypsum.

In developing the diffusion model, heat transfer was included in examining the problem, for example, in the work of Thijssen and Coumans (1985 [98]). A short-cut method was proposed to calculate drying rates in non-isothermal drying of particles and hollow spheres. In their work, heat transfer was taken into account in the calculation of the evaporation rate and the sample temperature. Shrinking and non-shrinking materials were considered. The method proposed by Thijssen and Coumans is based on the numerical solution of the diffusion equation with variable diffusion coefficient (as a function of moisture content) and based on the result (isothermal drying rate versus average moisture content) of drying experiments with a slab at different temperatures. By using this method, the information obtained from the isothermal drying experiments is applied to other geometries and non-isothermal conditions. Dimensionless variables (moisture content, time, space coordinate, and diffusion coefficient) were used in the study. Instead of solving numerically the non-linear diffusion equation, a calculation procedure was applied in a step-by-step manner where the conditions for each new step were obtained from the experimental drying curves.

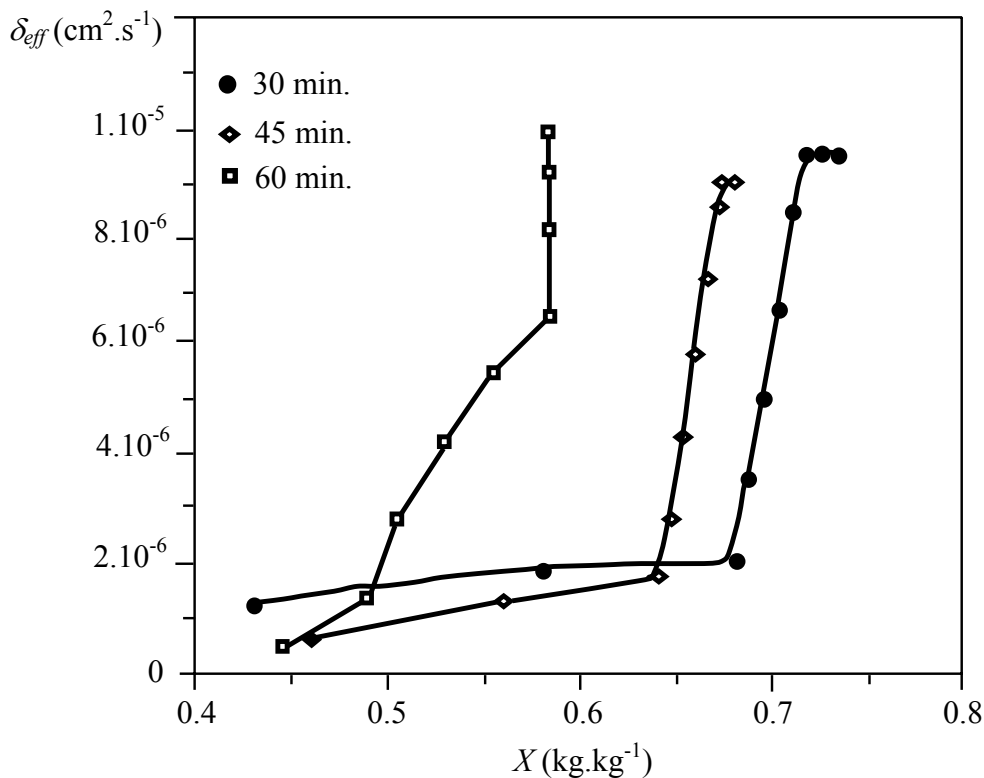**Figure 1.6** Determination of effective diffusion coefficient for food gel based on comparison of MRI data with diffusion model: effective diffusion coefficient as function of drying time and moisture content (Schrader and Litchfield, 1992 [90]).

To measure moisture profiles during drying, some advanced methods such as scanning neutron radiography or nuclear magnetic resonance imaging (MRI) were used recently

in a number of studies. Among others are the works of Blackband and Mansfield (1986 [6]) on solid blocks of nylon, Schrader and Litchfield (1992 [90]) on food gel, Pel *et al.* (1993 [64]) on brick and kaolin clay, McDonald *et al.* (1996 [53]) on sandstone and rock, Koptyug *et al.* (2000 [39]) on alumina pellets. By using these advanced methods, the measured moisture profiles can be used directly to determine the effective diffusion coefficient. In the work of Schrader and Litchfield, MRI was used to measure moisture profiles in a cylinder of food gel during drying at room temperature (1992 [90]). The measured profiles were then compared with the numerical results calculated by the diffusion model and in this way the effective diffusion coefficient was computed. As an example, Figure 1.6 shows the variation of the obtained effective diffusion coefficient at $t = 30$, 45 and 60 minutes of drying. It was pointed out that the diffusion model seems not to be a good method to predict the interior moisture profile of food gel. Koptyug *et al.* (2000 [39]) used MRI to study the diffusion of water in alumina pellets and showed that MRI can provide good information on the real-time variation of liquid content in the course of drying of porous solids. MRI is a good experimental method because it is able to measure moisture content at any point within a complex material. Additionally, it provides a quick, accurate, non-destructive method and therefore allows the evaluation of various drying models.

More recently, Guillard *et al.* (2002 [25]) used the diffusion model to predict the moisture distribution in multi-component heterogeneous food where components of high/low water activity are placed adjacent to one another. The calculation of moisture distributions compared well to experimental results and it was proposed that in this special application the model could be useful. Efremov (2002 [19]) used another approach for the description of the drying kinetics of porous materials. The approach is based on the analytical solution of the diffusion equation (for one-dimensional isotropic diffusion) with a flux-type boundary condition in form of mass flux. In this work, the drying kinetics (dimensionless moisture content versus time and drying rate) are determined by applying the Laplace transformation to express the mass flux. Porto and Lisbôa (2004 [79]) developed a three-dimensional model based on the diffusion model with constant diffusion coefficient in order to describe the drying process of a parallelepipedic oil shale particle. Lim *et al.* (2004 [48]) introduced an equation derived from diffusion equation in which the diffusion coefficient is a function of space. Akpinar and Dincer used the diffusion model to investigate moisture transfer in a slab of potato (2005 [1]) and in eggplant slices (2005 [2]). The works dealt with drying processes at different air temperatures and flow velocities. The influence of boundary conditions on drying process was investigated. The model is limited to the one-dimensional problem of an infinite slab. In their works, the thermo-physical properties of the drying material are taken as constant and the effect of heat transfer on the moisture loss is neglected.

The diffusion model can lead to wrong prediction and misinterpretation of the moisture distribution or of the drying behaviour due to the fact that only moisture transport is considered and that the physical meaning of the diffusion coefficient is either lost (in the case of a constant) or it becomes a lumped parameter of all simultaneous effects (in the case of a variable). However, this model is still used as simple way to describe drying for a certain situation.

1.3.2. *Receding front theory*

Different versions of the so-called receding front model were developed in order to get a better understanding and describe the influence of other mechanisms (capillarity, gravity or external forces in gradients of pressure and temperature) on the motion of water during drying. According to this model, at the critical point (when the falling rate period starts) an evaporation front arises and gradually moves into the interior of the body (Tsotsas, 1992 [102]). The moving evaporation front divides the system into two zones: the wet and the dry zone as shown in Figure 1.7. For a hygroscopic material, the dry zone is called the sorption zone due to the adsorptive nature of moisture retention. In the dry zone, the free water content is zero and the main mechanism of moisture transfer is vapour flow. However, in this region the movement of adsorbed water may also play an important role (Chen and Schmidt, 1990 [12]). During drying, the position of the receding evaporation front varies with time.
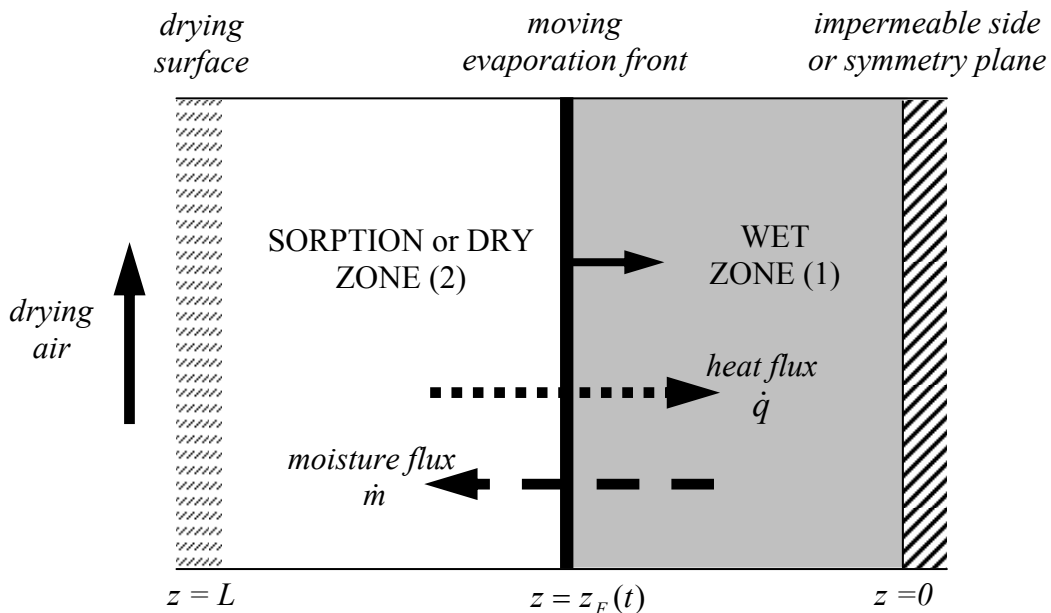
Figure 1.7 Receding front model.

The receding front model was first developed in the 1960s. A review of the development of the receding front model can be found in the work of Tsotsas (1992 [102]). The simplest version of the receding front model is a model where saturation *S* is 1 in the wet region and 0 in the dry region. In the following paragraph, the model presented by Chen and Schmidt (1990 [12]) is shown as one example. According to Chen and Schmidt, the set of one-dimensional equations describing the coupled heat and mass transfer can be written as follows (with subscripts 1 and 2 denoting the wet and dry zones):

In the wet zone (0 < z < z_F (t)

$$\frac{\partial X_{fw}}{\partial t} = \frac{\partial}{\partial z}\left(\delta_l \frac{\partial X_{fw}}{\partial z}\right) \tag{1-30}$$

$$\rho c_{p,w} \frac{\partial T_1}{\partial t} = \frac{\partial}{\partial z}\left(\lambda_{eff} \frac{\partial T_1}{\partial z}\right) \tag{1-31}$$

where δ_l is the liquid transfer coefficient and $c_{p,w}$ is the specific heat capacity of water. The term X_{fw} is the moisture content of free water and λ_{eff} is the effective thermal conductivity, which is calculated by

$$\lambda_{eff} = \lambda_l + \frac{\delta_v' \widetilde{M}_v}{\widetilde{R}T} \frac{\partial P_v^*(T)}{\partial T} \Delta h_v \tag{1-32}$$

where λ_l is the thermal conductivity of liquid, Δh_v the evaporation enthalpy, $P_v^*(T)$ the saturation vapour pressure and δ_v' the vapour transfer coefficient, which covers the contribution of both convective and diffusive flows

$$\delta_v' = \delta_v \left(1 + \frac{\dfrac{k_g K P_v}{\eta}}{\delta_v + \dfrac{k_g K}{m\eta}\left(P_g - P_v\right)}\right) \tag{1-33}$$

where m is the ratio of air and vapour diffusion coefficient, k_g the relative permeability of gas phase, η the dynamic viscosity and δ_v the vapour diffusion coefficient.

In the dry or sorption zone (z < z_F (t) < L):

$$\rho \frac{\partial X_{sorb}}{\partial t} = \rho \frac{\partial}{\partial z}\left(\delta_{sorb} \frac{\partial X_{sorb}}{\partial z}\right) + \frac{\partial}{\partial z}\left(\frac{\delta_v' \widetilde{M}_v}{\widetilde{R}T} \frac{\partial P_v}{\partial z}\right) \tag{1-34}$$

$$\rho c_{p,v} \frac{\partial T_2}{\partial t} = \frac{\partial}{\partial z}\left(\lambda_v \frac{\partial T_2}{\partial z}\right) \tag{1-35}$$

where $c_{p,v}$ is the specific heat capacity of vapour, λ_v the thermal conductivity of vapour, X_{sorb} the adsorbed water content and δ_{sorb} the adsorbed water transfer coefficient. For a non-hygroscopic material, X_{sorb} is zero and δ_{sorb} is negligible. $\widetilde{M}_v$ denotes the molar mass of vapour and P_v is the partial vapour pressure.

In addition to the above equations, the mass and heat transfer at the moving boundary must fulfill the following conditions

$$\rho \delta_l \frac{\partial X_{fw}}{\partial z} = \rho \delta_{sorb} \frac{\partial X_{sorb}}{\partial z} + \frac{\delta_v' \widetilde{M}_v}{\widetilde{R}T} \frac{\partial P_v}{\partial z} \tag{1-36}$$

$$\lambda_{eff}\frac{\partial T_1}{\partial z} = \lambda_v \frac{\partial T_2}{\partial z} + \Delta h_v \frac{\delta_v^{'} \widetilde{M}_v}{\widetilde{R} T}\frac{\partial P_v}{\partial z} \tag{1-37}$$

$$T_1 = T_2 ; \qquad X_{fw} = 0 \tag{1-38}$$

Sorption isotherm is applied in the model and the surface boundary conditions are needed. For more details, we refer to Chen and Schmidt (1990 [12]).

A drawback of the receding front approach is that the diffusion equation is used instead of more fundamental concepts like capillary pressure, liquid pressure gradients, permeability, etc. to describe the capillary activity in the wet zone. In addition, heat transfer is only described by an effective thermal conductivity. Difficulties appear in determining the boundary of the moving evaporation front and the coefficients for heat and mass transfer, which are functions of dry and wet zones.

1.3.3. Drying model of Philip and de Vries

Philip and De Vries (1957 [78]) and De Vries (1958 [16]) extended the previous treatment of diffusion equations by including effects of capillary flow and vapour transport. In their work, the thermal energy equation was also incorporated into the set of the governing equations to describe the drying process. This set of equations was treated under the combination of moisture and temperature gradients. The obtained system consists of diffusion-like equations whose coefficients must be determined by experiment. The model is briefly presented below.

Liquid water transfer:

Free liquid water movement is macroscopically described by Darcy's law

$$\dot{\mathbf{m}}_w = -\rho_w \frac{K \cdot k_w}{\eta_w}\left(\nabla P_w - \nabla \Psi_w\right) \tag{1-39}$$

where Ψ_w is the gravity potential. By expressing the term ∇P_w as a function of X and T and by substituting this function into Eq. (1-39) the liquid water flux can be written as a combination of three components due to moisture gradient, temperature gradient and gravity (Van der Kooi, 1971 [109])

$$\dot{\mathbf{m}}_w = -\delta_{wX}\nabla X - \delta_{wT}\nabla T + \rho_w \frac{K \cdot k_w}{\eta_w}\nabla \Psi_w \tag{1-40}$$

where δ_{wX} and δ_{wT} are the isothermal and thermal diffusivities of water given by

$$\delta_{wX} = \rho_w \frac{K \cdot k_w}{\eta_w}\left(\frac{\partial P_w}{\partial X}\right) \tag{1-41}$$

$$\delta_{wT} = \rho_w \frac{K \cdot k_w}{\eta_w}\left(\frac{\partial P_w}{\partial T}\right) \tag{1-42}$$

Water vapour transfer:

The transport of water vapour by molecular diffusion is described macroscopically by Fick's first law and by using the assumption of a steady diffusion in a closed system between an evaporation source and a condensation sink, a commonly used expression for the vapour flux in terms of moisture and temperature gradients

$$\dot{\mathbf{m}}_v = -\delta_{vX}\nabla X - \delta_{vT}\nabla T \tag{1-43}$$

where δ_{vX} and δ_{vT} are the isothermal and thermal diffusivities of vapour, respectively. These terms are expressed as (De Vries (1987 [17])

$$\delta_{vX} = f(\psi)\delta_{va}\frac{P_g}{P_g - P_v}\frac{\widetilde{M}_v g}{\widetilde{R}T}\frac{\rho_v}{\rho_l}\frac{\partial P_w}{\partial X} \tag{1-44}$$

$$\delta_{vT} = f(\psi)\delta_{va}\frac{P_g}{P_g - P_v}\frac{\rho_v}{\rho_w}\frac{\zeta}{P_v^*}\frac{dP_v^*(T)}{dT} \qquad \zeta = \frac{(\nabla T)_{av}}{(\nabla T)} \tag{1-45}$$

In these equations, $f(\psi)$ is a function of porosity and moisture content (see De Vries (1987 [17]) for more details), δ_{va} the diffusion coefficient of vapour in air, g the gravitational acceleration, $P_v^*(T)$ the saturation vapour pressure, $(\nabla T)_{av}$ the average air temperature gradient, ρ_v and ρ_w are the densities of vapour and liquid.

In addition to liquid and vapour transfer, Philip and De Vries assumed that the gas pressure can be treated as constant and the gas phase momentum equation can be ignored.

Mass and heat conservation equations:

The partial differential equations of mass and energy are formulated as follows (Philip and De Vries, 1957 [78], Fortes and Okos, 1980 [21])

$$\frac{\partial X}{\partial t} = \nabla \cdot (\delta_T \nabla T) + \nabla \cdot (\delta_X \nabla X) + \nabla \cdot \left(\frac{K \cdot k_w}{\eta_w}\nabla \Psi_w\right) \tag{1-46}$$

$$(\rho C_p)\frac{\partial T}{\partial t} = \nabla \cdot (\lambda \nabla T) + \Delta h_v \nabla \cdot (\delta_{vX}\nabla X) \tag{1-47}$$

where $\delta_T = \delta_{wT} + \delta_{vT}$ is the overall thermal mass diffusivity, $\delta_X = \delta_{wX} + \delta_{vX}$ is the overall isothermal mass diffusivity, λ denotes the thermal conductivity and ρC_p is the volumetric heat capacity of the moist porous medium. Note that convective energy terms are assumed negligible.

The theory of Philip and De Vries has become generally known and has been applied to porous media other than soil, which was chosen to investigate the heat and mass transfers by the authors. The major restrictions of the theory are that it does not include the gradient of gas pressure; there is no convection contribution in heat equation, and the coefficients of the model are complicated.

1.3.4. *Luikov's theory*

Independently of Philip and De Vries's work, Luikov (1966 [50], [51]; 1975 [52]) investigated the heat and mass transfer during drying of capillary-porous bodies by employing the principles of irreversible thermodynamics. In this theory, the total moisture flux is assumed to be made up of three components: the first one is due to a gradient in moisture content, the second due to a gradient in temperature and the last due to a gradient in the total pressure (Turner, 1991 [103])

$$\dot{\mathbf{m}}_m = -\rho_s \delta_m \left(\nabla X + \delta_T \nabla T + \delta_P \nabla P_g \right) \tag{1-48}$$

where $\dot{\mathbf{m}}_m$ is the total moisture flux, δ_m the moisture diffusion coefficient, δ_T the thermal gradient coefficient and δ_P the pressure gradient coefficient.

The conservation equations of Luikov's model are written in the form (Turner, 1991 [103])

$$\rho_s \frac{\partial X}{\partial t} + \nabla \cdot \dot{\mathbf{m}}_m = 0 \tag{1-49}$$

$$\in \rho_s \frac{\partial P_g}{\partial t} + \nabla \cdot \dot{\mathbf{m}}_g = \dot{M}_{ev} \tag{1-50}$$

$$\left(\rho C_p \right) \frac{\partial T}{\partial t} + \left(c_{p,w} \dot{\mathbf{m}}_w + c_{p,g} \dot{\mathbf{m}}_g \right) \cdot \nabla T = -\nabla \cdot \dot{\mathbf{q}} - \Delta h_v \dot{M}_{ev} \tag{1-51}$$

in which $\dot{\mathbf{q}} = -\lambda \nabla T$, with λ the thermal conductivity of the moist body; $\dot{\mathbf{m}}_w$ is calculated from Darcy's law (see Eq. (1-39), for instance); $\dot{\mathbf{m}}_g = -k_p \nabla P_g$ with k_p as the filtration coefficient; $\dot{M}_{ev}$ is the mass rate of evaporation per unit volume

$$\dot{M}_{ev} = \in \rho_s \frac{\partial X}{\partial t} \tag{1-52}$$

where $\in$ is a dimensionless factor characterizing resistance to vapour diffusion in a body (Fortes and Okos, 1980 [21]).

By using the above conservation equations, three interdependent partial differential equations involving variables *X, T* and *P* can be obtained as

$$\frac{\partial X}{\partial t} = K_{11} \nabla^2 X + K_{12} \nabla^2 T + K_{13} \nabla^2 P_g \tag{1-53}$$

$$\frac{\partial T}{\partial t} = K_{21} \nabla^2 X + K_{22} \nabla^2 T + K_{23} \nabla^2 P_g \tag{1-54}$$

$$\frac{\partial P_g}{\partial t} = K_{31} \nabla^2 X + K_{32} \nabla^2 T + K_{33} \nabla^2 P_g \tag{1-55}$$

where the kinetic coefficients K_{ij} depend not only on temperature and moisture content but also on material properties and drying conditions. For example

$$K_{11} = \frac{k_m}{c_m \rho_s}; \qquad K_{12} = k_x \cdot K_{11}; \qquad K_{13} = k_p \cdot K_{11}$$

where k_m is the coefficient of moisture conductivity, c_m the moisture capacity, ρ_s the density of the dry solid and k_x the thermogradient coefficient related to the moisture content difference. For more details on the computation of these kinetic coefficients, we refer to Luikov (1975 [52]), Irudayaraj and Wu (1996 [31]), Lewis and Ferguson (1990 [46]).

It is noted that under the assumption of constant gas pressure, Luikov's equations are similar to those proposed by Philip and De Vries. The biggest problem encountered in using Luikov's equations is the definition of the coefficients K_{ij}. In practice, it is often not possible to obtain these parameters to solve the full system of equations. However, Luikov's theory provides a well-established model in the treatment of simultaneous heat and mass transfer of the drying problem. The solution of Luikov's partial differential equations was studied numerically by Lewis and Ferguson (1990 [46]) and by Irudayaraj and Wu (1996 [31]). These equations are still commonly employed today and quite often solved by the finite element method.

1.3.5. Krischer's theory

Krischer is also among the first researchers who have investigated the role of heat and mass transfer during drying of porous media. The research work of Krischer was and is still used today as a basis for much of the development in drying theory. In his work (1992 [40]), which was first published in 1956, Krischer proposed a set of equations to describe the moisture transport for several geometries (plate, cylinder and sphere). Krischer assumed that moisture transfer is controlled by the combined influence of capillary flow of liquid and diffusion of vapour.

In Krischer's model, the liquid flux is calculated from Darcy law (see Eq. (1-39), for example) and the vapour flux is written as (Van der Kooi, 1971 [109])

$$\dot{m}_v = -\frac{\delta_{va}}{\mu} \frac{P_g}{P_g - P_v} \frac{\widetilde{M}_v}{\widetilde{R}T} \nabla P_v \qquad (1\text{-}56)$$

where μ (> 1) is called the diffusion resistance factor and describes the decrease of the vapour flow in the considered material in comparison with that in stagnant gas.

In using the theory of Krischer, Berger and Pei (1973 [4]) included the sorption isotherm (empirically obtained) into the model as a coupling equation among liquid, vapour and heat transfer. Based on Krischer's theory, Berger and Pei introduced two balance equations for heat and mass (the gas pressure was taken as constant). In this model all phenomenological coefficients (e.g. liquid conductivity, vapour diffusivity, thermal conductivity) are taken as constant. Heat transfer is assumed to take place only by conduction through the solid skeleton.

The overall mass and heat balance equations proposed by Berger and Pei (1973 [4]) are expressed in terms of moisture content and vapour pressure as follows

$$\rho_s K^* \nabla^2 X + \delta_v \frac{\tilde{M}_v}{\tilde{R}T} \left[\frac{1}{\varepsilon_s}(\varepsilon_g - \varepsilon_w)\nabla^2 P_v - \frac{\rho_s}{\rho_w}\nabla X \nabla P_v \right]$$
$$= \rho_s \left(1 - \frac{1}{\rho_w}\frac{\tilde{M}_v P_v}{\tilde{R}T}\right)\frac{\partial X}{\partial t} + \frac{1}{\varepsilon_s}\frac{\tilde{M}_v}{\tilde{R}T}(\varepsilon_g - \varepsilon_w)\frac{\partial P_v}{\partial t} \tag{1-57}$$

$$\frac{\lambda_s}{\rho_s c_{p,s}}\nabla^2 T + \frac{\Delta h_v}{\rho_s c_{p,s}}\frac{\tilde{M}_v}{\tilde{R}T}\left\{ \delta_v\left[\frac{1}{\varepsilon_s}(\varepsilon_g - \varepsilon_w)\nabla^2 P_v - \frac{\rho_s}{\rho_w}\nabla X \nabla P_v \right] \right.$$
$$\left. - \frac{1}{\varepsilon_s}(\varepsilon_g - \varepsilon_w)\frac{\partial P_v}{\partial t} + \frac{\rho_s}{\rho_w}P_v\frac{\partial X}{\partial t} \right\} = \frac{\partial T}{\partial t} \tag{1-58}$$

where δ_v is the vapour diffusivity; K^* is the liquid conductivity; ε_s, ε_w and ε_g are the volume fraction of solid, water and gas, respectively.

The main difficulties encountered in using Krischer's model to predict the drying rate are the assumption of surface boundary conditions (Krischer postulated that "at the surface of the drying material the corresponding equilibrium values of the dependent variables were reached instantaneously at the beginning of the drying process") and the application of the sorption isotherm for the whole range of moisture content (Berger and Pei, 1973 [4]). Even though sorption isotherm is taken into account, the approach of Berger and Pei does not offer much innovation over Luikov's and Philip and De Vries' models (Turner, 1991 [103]). In addition, as for the previous models, experimental tests are needed to ensure its validity.

1.3.6. *Whitaker's model*

In the late 1970s and early 1980s, Whitaker (1977 [115]; 1980 [116]) presented a set of equations to describe the simultaneous heat, mass and momentum transfer in porous media. Based on the traditional conservation laws, the model proposed by Whitaker, an important milestone in the development of drying theory, incorporated all mechanisms for heat and mass transfer: liquid flow due to capillary forces, vapour and gas flow due to convection and diffusion, internal evaporation of moisture and heat transfer by convection, diffusion and conduction. By using the volume averaging method, the macroscopic differential equations were defined in terms of average field quantities. Whitaker's model is one of the basics of this research work and will be discussed in detail in Chapter 2.

The advantage of Whitaker's model is that it offers a very good representation of the physical phenomena occurring in porous media during drying. However, the problem encountered in using Whitaker's model is the difficulty in determining its complicated transport coefficients, such as the effective diffusivity and permeabilities, which depend strongly on the material properties and structure (problem encountered also in all above models). These parameters are either function of moisture content or temperature or both moisture content and temperature. In addition, the coupled equations of heat and mass transfer, which are strongly nonlinear, require very complicated numerical methods to be solved.

The theory of Whitaker was further developed and applied in drying analysis of various porous media, for example in the drying analysis of *sand* (Whitaker and Chou, 1983 [119]; Hadley, 1985 [26]; Oliveira and Fernandes, 1986 [60]; Puiggali *et al.*, 1988 [83]), *glass beads* (Quintard and Puiggali 1986 [84]; Kaviany and Mittal, 1987 [35]), *sandstone* (Wei *et al.*, 1985 [113]; [114]), *porous insulators* (Tien and Vafai, 1990 [99]); *brick* (Nasrallah and Perré, 1988 [58]), *cellular materials* (Crapiste *et al.*, 1988 [14], [15]), *wood* (Spolek and Plumb, 1980 [94]; Michel *et al.*, 1987 [56]; Perré, 1987 [66]; Lartigue *et al.*, 1990 [42]). In these works, the model is usually quite successfully matched against experimental data. The above works highlight the acceptance of the complete theory. Some of the important advances made in developing Whitaker's theory are selected for discussion below.

Whitaker and Chou (1983 [119]) simplified the theory to obtain two nonlinear equations for the distribution of saturation and temperature. In this work, the gas pressure is assumed as constant, the gas momentum equation is ignored and a quasi-steady state is applied. It is interesting to note that there is a resemblance of these two equations to the equations proposed by Luikov and Philip and DeVries (Turner, 1991 [103]). In this simplified case, the comparison between theory and experiment was made by Hougen *et al.* (1939 [29]). The important conclusion is that the gas phase momentum equation must be included in solving the comprehensive set of equations. Crapiste *et al.* (1988 [14]; [15]) applied Whitaker's model to investigate the drying of cellular materials. To validate the model, a comparison of one-dimensional drying to the experimental drying of apple and potato was presented and a good agreement was found. Wei *et al.* (1985 [113]) applied Whitaker's model to the drying of a cylinder of sandstone subjected to convective heating. The obtained partial differential equations in one dimension were solved by a three-point, two-level implicit finite difference method. The calculated results were compared with experimental results and showed a quite good agreement.

Ferguson (1995 [20]) focused on a two-dimensional problem of the high temperature drying of spruce. The numerical results highlighted the advantage of the discretization technique (control volume finite element method) in solving the problem with structured and unstructured meshes. A numerical investigation was conducted by Boukadida *et al.* (2000 [9]) to study the convective drying of a slab of clay-brick. The work analyzed the influence of the properties of the surrounding drying agent (temperature, gas pressure and vapour concentration) as well as the initial medium conditions (temperature and moisture content) on the drying process by considering several configurations. However, the full investigation of the effect of the boundary layer on the coupled heat and mass transfer still requires further work, as concluded by the authors. Silva (2000 [93]), based on Whitaker's theory, presented a general model to describe the momentum, heat and mass transfer in drying problems with moving boundary. By using the volume averaging method, a set of equations for multi-phase systems was applied to porous media. Numerical results showed a good agreement with the experimental data of kaolin drying.

One of the most significant advances in developing Whitaker's theory as well as in modelling the drying of porous media comes from the work of Perré *et al.* (1986 [65]; 1987 [66]), Nasrallah and Perré (1988 [58]). In their work, the drying of two quite different porous media − clay-brick and softwood − was investigated. The most important advance in the work of Perré is the consideration of bound water (Perré *et al.*

1989 [76], Perré and Degiovanni, 1990 [68], Perré *et al.* 1993 [77]). By considering bound water, the driving potential for bound water migration was assumed to be proportional to the gradient in the bound moisture content. For the case of wood, Perré and his colleagues introduced two equations to calculate the transport of this kind of bound water (Perré *et al.* 1993 [77]):

$$\frac{\partial \overline{\rho_b}}{\partial t} + \nabla .\left(\overline{\rho_b . \mathbf{v}_b}\right) = -\dot{m}_b \tag{1-59}$$

$$\overline{\rho_b . \mathbf{v}_b} = -\overline{\rho}_c .\delta_b .\nabla\left(\frac{\overline{\rho_b}}{\overline{\rho_c}}\right) \tag{1-60}$$

where $\dot{m}_b$ is the rate of bound water evaporation, the subscripts b and c denote bound water and cellulose matter, respectively. For wood, the diffusion coefficient of bound water δ_b is calculated in m^2/s from the following equation (Perré and Degiovanni, 1990 [68])

$$\delta_b = \exp\left(-9.9 + 9.8 \cdot X_b - \frac{4300}{T}\right) \tag{1-61}$$

where X_b is moisture content of bound water and T is temperature (in Kelvin).

In his work, Perré solved the one-dimensional problem of drying with three state variables (temperature, pressure and moisture content). The control volume method was applied to solve the nonlinear partial differential equations. The mathematical schemes for equidistant and non-equidistant meshes were discussed (Nasrallah and Perré, 1988 [58]). The authors also investigated the sensitivity upon model parameters by numerically varying the effective diffusivity, effective thermal conductivity, intrinsic and relative permeabilities as well as external drying conditions (heat and mass transfer coefficients).

With the rapid development of computer technology, modern computers allow the simulation of drying not only in one dimension but also in two and three dimensions. Besides, numerical methods are also more efficient in obtaining accurate results and reducing the computational time. Among the advancements during the 1990s in the study of drying of porous media is the simulation of drying processes in two dimensions with unstructured meshes proposed by Perré (1997 [67]), Perré and Turner (1998 [70]). The first comprehensive three-dimensional drying model using structured meshes was introduced by Perré and Turner (1999 [71]). In this work, a homogeneous model, which employed the full set of conservation equations, was considered. A cube of light concrete (isotropic medium) and a board of wood (anisotropic medium) were chosen to investigate the influence of the number of exchange faces. Several simulation results for low and high temperature drying of softwood were presented and discussed. By comparing the different simulation results, the study showed that a three dimensional model is required to describe correctly the drying behaviour of porous media.

Concerning the heterogeneity of material properties, Perré (1997 [67]) developed a heterogeneous drying model for wood. The variation of the material property information such as capillary pressure and absolute permeability was taken into account with the help of experiments (Perré and Turner 2001 [73]; [74]). The material

information of wood obtained from this work was later applied to a two-dimensional heterogeneous drying model (Perré and Turner 2002 [75]). In this work, the effects of material heterogeneity and local material direction on the heat and mass transport during drying were investigated. Two cases of low and high temperature drying were considered. Following this direction, more recently, Truscott (Truscott, 2004 [100]; Truscott and Turner, 2005 [101]) developed a three-dimensional heterogeneous drying model for wood. The work considered the heterogeneity of the material properties, which vary within the transverse plane with respect to the position that defines the radial and tangential directions. Two nonlinear partial equations for moisture content and temperature (pressure was assumed as constant) were solved.

To summarize, in this chapter, some basic concepts in drying modelling of porous media are introduced. A brief review of the development of some drying models, their application and their restrictions is presented. Among the others, the model developed by Whitaker is the most complete one. Details of Whitaker's model as well as the upscaling of the basic laws of transport from microscopic to macroscopic level to get a set of macroscopic equations for drying of porous media will be discussed in the next chapter.

Chapter 2

MATHEMATICAL FORMULATION

2.1. Introduction

In the first part of this chapter, the mathematical formulation of the drying processes of porous media, which is based on the model developed by Whitaker (1977 [115]; 1980 [116]) and later by Perré and Turner (1999 [71]), is presented. First, the basic equations of mass and energy transport at pore (microscopic) level in the drying of a rigid, homogeneous and isotropic medium are briefly recalled. The thermodynamic relations, assumptions and boundary conditions are reported. Second, the volume averaging method is introduced. This method is then applied to derive a continuous drying model for porous media at macroscopic level.

In the second part of this chapter, based on the work of Metzger and Tsotsas (2005 [55]), Metzger *et al.* (2006 [54]), a capillary model is used to compute the transport parameters, namely capillary pressure, absolute and relative permeabilites for liquid and gas, which are used in the continuous model derived in the first part. By representing the porous medium by a bundle of capillaries with a radius distribution, these parameters are computed as functions of liquid saturation. These functions create a micro-macro link between the microstructure of a material and its macroscopic drying behaviour and allow us to investigate the influence of pore size distribution on the material drying kinetics.

2.2. Pore scale equations

2.2.1. *Conservation equations*

We consider the motion of liquid and vapour phase through a rigid porous medium as shown in Fig. 2.1, which shall illustrate how the macroscopic behaviour of the drying process is related to the pore scale phenomena. In this figure, the left-hand side depicts the pore scale (microscopic scale), and the right-hand side describes the macroscopic scale (a particle). At the pore level, we consider part of the porous structure with three phases: solid, liquid and gas. The solid phase is denoted by s, the liquid phase (water) is denoted by w and the gas phase, which contains both air (denoted by a) and vapour (denoted by v), is denoted by g. In drying analysis, one of the primary objectives is to compute the distribution of moisture content, temperature and internal gaseous pressure

within the porous medium during the drying process. At pore level, the (local) moisture content, the temperature and the gaseous pressure at each point can be determined using suitable laws of physics such as conservation of mass, linear momentum and energy of each phase: solid, liquid and gas. These conservation laws are discussed in the following (Whitaker, 1977 [115]; 1998 [117]).

Pore level   *Macroscopic level*
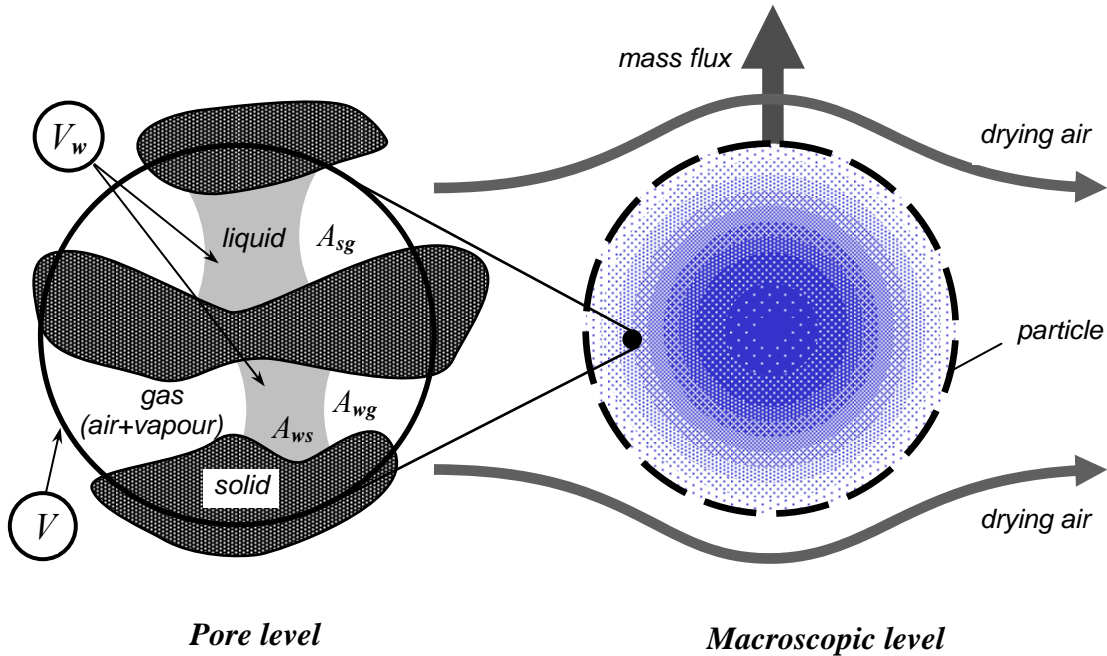
Figure 2.1 Drying process in porous media: from pore scale to macroscopic scale.

Mass conservation:

By assuming that no chemical reaction happens during drying, the total mass conservation equation of each phase can be written as

$$\frac{\partial \rho}{\partial t} + \nabla \cdot (\rho \mathbf{v}) = 0 \tag{2-1}$$

and the mass conservation equation of each species in the phase is

$$\frac{\partial \rho_i}{\partial t} + \nabla \cdot (\rho_i \mathbf{v}_i) = 0 \quad \text{for } i = 1, 2, ..., N \tag{2-2}$$

In the above equations, the first terms on the left-hand side are the change of mass due to accumulation, the second terms express the change of mass due to convection, $\mathbf{v}$ is the mass average velocity and ρ is the total mass density of the phase under consideration

$$\mathbf{v} = \sum_{i=1}^{N} \frac{\rho_i}{\rho} \mathbf{v}_i \tag{2-3}$$

$$\rho = \sum_{i=1}^{N} \rho_i \tag{2-4}$$

where N denotes the total number of species, ρ_i the density and $\mathbf{v}_i$ the velocity of the species i.

Principle of linear momentum:

For each phase, the principle of linear momentum can be written as

$$\rho \frac{D\mathbf{v}}{Dt} = \nabla \cdot \mathbf{T} \tag{2-5}$$

In this work, the contribution of body force such as gravitation force is neglected. In the above equation, $\mathbf{T}$ is the stress tensor. The angular momentum principle requires this tensor to be symmetric

$$\mathbf{T} = \mathbf{T}^{T} \tag{2-6}$$

Energy conservation:

The thermal energy equation of each phase is

$$\frac{\partial}{\partial t}(\rho h) + \nabla \cdot (\rho h \mathbf{v}) = -\nabla \cdot \mathbf{q} + \frac{DP}{Dt} + \boldsymbol{\tau} : \nabla \mathbf{v} + \Phi \tag{2-7}$$

where h is the enthalpy per unit mass, $\mathbf{q}$ the conductive heat flux vector, $\boldsymbol{\tau}$ the viscous stress tensor. The term $\boldsymbol{\tau} : \nabla \mathbf{v}$ is the viscous dissipation, P the pressure, $\frac{DP}{Dt}$ the compression work and Φ presents the source or sink of electromagnetic radiation. The conductive heat flux vector $\mathbf{q}$ is computed by Fourier' law

$$\mathbf{q} = -\lambda \nabla T \tag{2-8}$$

in which λ represents the thermal conductivity.

In our analysis, the contribution of Φ is neglected. Furthermore, we assume that for liquid and gas phase the viscous dissipation and the compression work can be neglected

$$\boldsymbol{\tau} : \nabla \mathbf{v} = 0; \qquad \frac{DP}{Dt} = 0 \tag{2-9}$$

In this case the energy equation is reduced to

$$\frac{\partial}{\partial t}(\rho h) + \nabla \cdot (\rho h \mathbf{v}) = -\nabla \cdot \mathbf{q} \tag{2-10}$$

We will also assume that the enthalpy is independent of pressure and that all heat capacities are constant so that

$$h = c_p (T - T_R) \tag{2-11}$$

holds, where c_p is specific heat capacity and T_R is the reference temperature.

The conservation laws discussed above are now applied to each phase of the three-phase system under consideration.

2.2.1.1. Solid phase

The solid phase is considered to be rigid and fixed in space with zero velocity

$$\mathbf{v}_s = 0 \tag{2-12}$$

This means that for this phase we need to study only the conservation of energy (2-7), which now becomes

$$\rho_s \frac{\partial h_s}{\partial t} = -\nabla \cdot \mathbf{q}_s \tag{2-13}$$

If we make use of Eq. (2-8) and take into account the assumption (2-11), we have

$$\rho_s c_{p,s} \frac{\partial T_s}{\partial t} = \lambda_s \nabla^2 T_s \tag{2-14}$$

2.2.1.2. Liquid phase

For the liquid phase, which contains water as the only component, the mass conservation equation is

$$\frac{\partial \rho_w}{\partial t} + \nabla \cdot (\rho_w \mathbf{v}_w) = 0 \tag{2-15}$$

The use of Eqs. (2-8) and (2-11) allows us to write the energy conservation of liquid phase as

$$\rho_w c_{p,w} \left(\frac{\partial T_w}{\partial t} + \mathbf{v}_w \cdot \nabla T_w \right) = \lambda_w \nabla^2 T_w \tag{2-16}$$

2.2.1.3. Gas phase

The gas phase is more complicated than the solid and the liquid phase since it contains two components: air and vapour. The total mass conservation of the gas phase is

$$\frac{\partial \rho_g}{\partial t} + \nabla \cdot (\rho_g \mathbf{v}_g) = 0 \tag{2-17}$$

Writing the species velocity $\mathbf{v}_i$ in terms of the mass average velocity $\mathbf{v}_g$ and the diffusion velocity $\mathbf{u}_i$

$$\mathbf{v}_i = \mathbf{v}_g + \mathbf{u}_i \qquad i = a, v \tag{2-18}$$

allows us to write the mass conservation of air and vapour in the form

$$\frac{\partial \rho_i}{\partial t} + \nabla \cdot (\rho_i \mathbf{v}_g) = -\nabla \cdot (\rho_i \mathbf{u}_i) \qquad i = a, v \tag{2-19}$$

Furthermore, by expressing the diffusive flux $\rho_i \mathbf{u}_i$ as

$$\rho_i \mathbf{u}_i = -\rho_g \delta_{v,a} \nabla \left(\frac{\rho_i}{\rho_g} \right) \tag{2-20}$$

where $\delta_{v,a}$ is the binary molecular diffusion coefficient for vapour and air, we have

$$\frac{\partial \rho_i}{\partial t} + \nabla \cdot (\rho_i \mathbf{v}_g) = \nabla \cdot \left[\rho_g \delta_{v,a} \nabla \left(\frac{\rho_i}{\rho_g} \right) \right] \qquad i = a, v \tag{2-21}$$

For a multi-component phase, the appropriate form of the energy equation (2-10) is

$$\frac{\partial}{\partial t} \left(\sum_{i=1}^{N} \rho_i h_i \right) + \nabla \cdot \left(\sum_{i=1}^{N} \rho_i h_i \mathbf{v}_i \right) = -\nabla \cdot \mathbf{q} \tag{2-22}$$

where h_i is the enthalpy per unit mass of the component i, and the mass average enthalpy h is defined in a similar way to the mass average of velocity as

$$h = \sum_{i=1}^{N} \frac{\rho_i}{\rho} h_i \tag{2-23}$$

By using Eq. (2-22) for the gas phase we have

$$\rho_g c_{p,g} \left(\frac{\partial T_g}{\partial t} + \mathbf{v}_g \cdot \nabla T_g \right) = \lambda_g \nabla^2 T_g - \nabla \cdot (\rho_a h_a \mathbf{u}_a + \rho_v h_v \mathbf{u}_v) \tag{2-24}$$

where

$$c_{p,g} = (\rho_a c_{p,a} + \rho_v c_{p,v})/\rho_g \tag{2-25}$$

In addition to the above conservation equations, ideal gas laws are assumed for partial and total gas pressures

$$P_i = \frac{\rho_i \tilde{R} T}{\tilde{M}_i} \tag{2-26}$$

where i stands for a, v or g, $\tilde{R}$ is the ideal gas constant and $\tilde{M}_i$ stands for molar mass of air, vapour or gas. The constraint for partial and total gas pressures is

$$P_a + P_v = P_g \tag{2-27}$$

2.2.2. *Boundary conditions*

In order to complete the set of equations listed above, the boundary conditions that connect the transport equations for the three separate phases need to be specified. In Figure 2.1, A_{wg} represents the interface area between liquid and gas phases, A_{sw} the interface area between solid and liquid and A_{sg} the interface area between solid and gas. It should also be noted that

$$A_{wg} = A_{gw}; \quad A_{sw} = A_{ws}; \quad A_{sg} = A_{gs} \tag{2-28}$$

The boundary conditions for the solid-liquid interface A_{ws} are quite simple and can be written as

$$\begin{cases} \mathbf{v}_w = 0 & (a) \\ \mathbf{q}_s \cdot \hat{\mathbf{n}}_{ws} = \mathbf{q}_w \cdot \hat{\mathbf{n}}_{ws} & (b) \\ T_s = T_w & (c) \end{cases} \qquad (2\text{-}29)$$

where $\hat{\mathbf{n}}_{ws}$ represents the unit normal vector directed from the liquid phase toward the solid phase and $\hat{\mathbf{n}}_{sw} = -\hat{\mathbf{n}}_{ws}$.

Similarly, the boundary conditions for the solid-gas interface A_{sg} are written in the form

$$\begin{cases} \mathbf{v}_g = 0 & (a) \\ \mathbf{q}_s \cdot \hat{\mathbf{n}}_{sg} = \mathbf{q}_g \cdot \hat{\mathbf{n}}_{sg} & (b) \\ T_s = T_g & (c) \end{cases} \qquad (2\text{-}30)$$

The boundary conditions for liquid-gas interface A_{wg} are more complex than those listed above. This surface is treated as a moving surface and the boundary conditions are defined as

$$\begin{cases} \rho_v(\mathbf{v}_v - \mathbf{w}) \cdot \hat{\mathbf{n}}_{gw} = \rho_w(\mathbf{v}_w - \mathbf{w}) \cdot \hat{\mathbf{n}}_{gw} & (a) \\ \rho_a(\mathbf{v}_a - \mathbf{w}) \cdot \hat{\mathbf{n}}_{gw} = 0 & (b) \\ \rho_g(\mathbf{v}_g - \mathbf{w}) \cdot \hat{\mathbf{n}}_{gw} = \rho_w(\mathbf{v}_w - \mathbf{w}) \cdot \hat{\mathbf{n}}_{gw} & (c) \\ \rho_w(h_v - h_w)(\mathbf{v}_w - \mathbf{w}) \cdot \hat{\mathbf{n}}_{gw} = (\mathbf{q}_w - \mathbf{q}_g) \cdot \hat{\mathbf{n}}_{gw} & (d) \\ T_w = T_g & (e) \end{cases} \qquad (2\text{-}31)$$

In the above equations $\mathbf{w}$ denotes the velocity of the *w-g* interface.

The pore scale equations for the three phases are now complete. In the next section, our attention will focus on the problem of deriving the macroscopic equations by using the volume averaging method.

2.3. Volume averaging method

The volume averaging method (Whitaker, 1977 [115]; 1980 [116]; 1999 [118]) is a technique that can be used to rigorously derive continuum equations for multiphase systems. In the study of drying, we would like to know how water is transported through the pores to the external surface where it is removed by drying air. The direct analysis of this process using transport equations at pore level is impossible due to the complex structure of porous media. By using the volume averaging method, the governing equations of drying, which are valid within a particular phase, can be spatially smoothed to produce equations that are valid everywhere. The smoothed equations obtained in this way can be solved by classical methods. Although the volume averaging method has been widely used, the method has its own drawbacks, especially

the difficulties encountered in determining the effective parameters (as numerical values) that appear in the macroscopic governing equations.

In the volume averaging method we associate an averaging volume V to every point $\mathbf{x}$ in the porous sample. The chosen volume can be of any shape. In Figure 2.1 the averaging volume V is represented by a circle. This representative element volume (REV) will serve as a bridge in the upscaling process of the transport equations from pore scale to macroscopic scale. It should be noted that the size of the averaging volume, namely its diameter d, must be large compared with the pore scale characteristic length l (as reference to variations at pore level) but small compared with the macroscopic characteristic length L (as reference to variations of macroscopic variables): $l<<d<<L$. At each point $\mathbf{x}$, the total volume V is made up of the volumes of solid, liquid and gas phases

$$V = V_s + V_w + V_g \tag{2-32}$$

Evidently, the volumes of the liquid and gas phases are functions of time since during the drying process water in liquid phase is transformed into vapour. The representative element volume leads to the definition of average values. There are three types of average that are used in the study of drying in porous media: spatial average, phase average and intrinsic average. The spatial average of a function χ is represented by $\langle \chi \rangle$ and is defined by

$$\langle \chi \rangle = \frac{1}{V} \int_V \chi \, dV \tag{2-33}$$

When we are interested in the average of some quantity associated with a single phase, the phase average is employed. The definition of the phase average concerns only the volume of the phase that we are interested in. For example, the phase average of the temperature in the solid phase is defined by

$$\langle T_s \rangle = \frac{1}{V} \int_{V_s} T_s \, dV \tag{2-34}$$

It should be noted that the drawback of the phase average is that if T_s is constant, the phase average is not equal to this value. In this case, the intrinsic average is a more appropriate representation. The intrinsic average, for example, of temperature in the solid phase is

$$\langle T_s \rangle^s = \frac{1}{V_s} \int_{V_s} T_s \, dV \tag{2-35}$$

Related to the definition of different volume averages, the volume fractions of the three phases are defined by

$$\varepsilon_s = \frac{V_s}{V} \qquad \varepsilon_w = \frac{V_w}{V} \qquad \varepsilon_g = \frac{V_g}{V} \tag{2-36}$$

Evidently, the sum of these volume fractions is unity. The phase average and intrinsic average are related by

$$\langle T_s \rangle = \varepsilon_s \langle T_s \rangle^s \tag{2-37}$$

The principle tool of the volume averaging method is the so-called averaging theorem, which can be expressed as

$$\langle \nabla \chi_w \rangle = \nabla \langle \chi_w \rangle + \frac{1}{V} \int_{A_{ws}} \hat{\mathbf{n}}_{ws} \chi_w dA + \frac{1}{V} \int_{A_{wg}} \hat{\mathbf{n}}_{wg} \chi_w dA \tag{2-38}$$

When we encounter the average of a divergence, we use the averaging theorem in the following form

$$\langle \nabla \cdot \mathbf{v}_w \rangle = \nabla \cdot \langle \mathbf{v}_w \rangle + \frac{1}{V} \int_{A_{ws}} \mathbf{v}_w \cdot \hat{\mathbf{n}}_{ws} dA + \frac{1}{V} \int_{A_{wg}} \mathbf{v}_w \cdot \hat{\mathbf{n}}_{wg} dA \tag{2-39}$$

When we need to compute the volume average of a time derivative, for example

$$\left\langle \frac{\partial T_w}{\partial t} \right\rangle = \frac{1}{V} \int_{V_w} \frac{\partial T_w}{\partial t} dV \tag{2-40}$$

we use the general transport theorem

$$\left\langle \frac{\partial T_w}{\partial t} \right\rangle = \frac{\partial \langle T_w \rangle}{\partial t} - \frac{1}{V} \int_{A_{wg}} T_w \mathbf{w} \cdot \hat{\mathbf{n}}_{wg} dA - \frac{1}{V} \int_{A_{ws}} T_w \mathbf{w} \cdot \hat{\mathbf{n}}_{ws} dA \tag{2-41}$$

By using the averaging theorem and the general transport theorem, the process to derive the volume-averaged transport equations can be summarized as follows: First, the corresponding pore level equation is integrated over the averaging volume. Second, the averaging and the general transport theorems are applied together with the analysis of magnitude to eliminate negligible terms. Third, the macroscopic equations are obtained with definitions of effective parameters based on the results of the obtained volume-averaged equations.

To illustrate this process, the mass conservation equation of liquid is considered here. By integrating Eq. (2-15) over volume V_w and by dividing the result by V we have

$$\frac{1}{V} \int_{V_w} \frac{\partial \rho_w}{\partial t} dV + \frac{1}{V} \int_{V_w} \nabla \cdot (\rho_w \mathbf{v}_w) dV = 0 \tag{2-42}$$

or in another form

$$\left\langle \frac{\partial \rho_w}{\partial t} \right\rangle + \langle \nabla \cdot (\rho_w \mathbf{v}_w) \rangle = 0 \tag{2-43}$$

The application of general transport theorem allows us to write the first term of (2-43) as

$$\left\langle \frac{\partial \rho_w}{\partial t} \right\rangle = \frac{\partial \langle \rho_w \rangle}{\partial t} - \frac{1}{V} \int_{A_{wg}} \rho_w \mathbf{w} \cdot \hat{\mathbf{n}}_{wg} dA - \frac{1}{V} \int_{A_{ws}} \rho_w \mathbf{w} \cdot \hat{\mathbf{n}}_{ws} dA \tag{2-44}$$

Because the velocity of the *w-s* interface is zero, the last term of this equation is zero and equation (2-43) becomes

$$\frac{\partial \langle \rho_w \rangle}{\partial t} - \frac{1}{V} \int_{A_{wg}} \rho_w \mathbf{w} \cdot \hat{\mathbf{n}}_{wg} \, dA + \langle \nabla \cdot (\rho_w \mathbf{v}_w) \rangle = 0 \tag{2-45}$$

The integration and differential in the last term of this equation can be interchanged by the use of the averaging theorem (2-39) as

$$\langle \nabla \cdot (\rho_w \mathbf{v}_w) \rangle = \nabla \cdot \langle \rho_w \mathbf{v}_w \rangle + \frac{1}{V} \int_{A_{ws}} \rho_w \mathbf{v}_w \cdot \hat{\mathbf{n}}_{ws} \, dA + \frac{1}{V} \int_{A_{wg}} \rho_w \mathbf{v}_w \cdot \hat{\mathbf{n}}_{wg} \, dA \tag{2-46}$$

By noting that the *w-s* interface is impermeable, $\mathbf{v}_w \cdot \hat{\mathbf{n}}_{ws}$ is zero, the substitution of (2-46) into (2-45) leads to

$$\frac{\partial \langle \rho_w \rangle}{\partial t} + \nabla \cdot \langle \rho_w \mathbf{v}_w \rangle + \frac{1}{V} \int_{A_{wg}} \rho_w (\mathbf{v}_w - \mathbf{w}) \cdot \hat{\mathbf{n}}_{wg} \, dA = 0 \tag{2-47}$$

Since it is quite reasonable to neglect the variation of the density ρ_w, we have

$$\langle \rho_w \rangle = \varepsilon_w \langle \rho_w \rangle^w = \varepsilon_w \rho_w \tag{2-48}$$

and we get the final form for the average mass conservation equation of the liquid phase

$$\rho_w \frac{\partial \varepsilon_w}{\partial t} + \rho_w \nabla \cdot \langle \mathbf{v}_w \rangle + \langle \dot{m} \rangle = 0 \tag{2-49}$$

where

$$\langle \dot{m} \rangle = \frac{1}{V} \int_{A_{wg}} \rho_w (\mathbf{v}_w - \mathbf{w}) \cdot \hat{\mathbf{n}}_{wg} \, dA \tag{2-50}$$

is the evaporation rate.

For more details about the derivation of the other equations (mass conservation equation of gas, energy conservation equation) we refer to Whitaker (1977 [115]; 1998 [117]; 1999 [118]).

2.4. Macroscopic equations of drying processes in porous media

The macroscopic transport equations can be obtained by averaging the pore scale transport equations over the averaging volume as introduced in previous section. This set of macroscopic equations is summarized as follows (Whitaker, 1977 [115]):

1. The mass conservation equation for the liquid phase

$$\rho_w \frac{\partial \varepsilon_w}{\partial t} + \rho_w \nabla \cdot \langle \mathbf{v}_w \rangle + \langle \dot{m} \rangle = 0 \tag{2-51}$$

2. The mass conservation equation for vapour in the gas phase

$$\frac{\partial}{\partial t}\left(\varepsilon_g \langle \rho_v \rangle^g\right) + \nabla \cdot \left(\langle \rho_v \rangle^g \langle \mathbf{v}_g \rangle\right) - \langle \dot{m} \rangle = \nabla \cdot \left[\langle \rho_g \rangle^g \mathbf{D}_{eff} \cdot \nabla \left(\frac{\langle \rho_v \rangle^g}{\langle \rho_g \rangle^g}\right)\right] \tag{2-52}$$

3. The mass conservation equation for air in the gas phase

$$\frac{\partial}{\partial t}\left(\varepsilon_g \langle \rho_a \rangle^g\right) + \nabla \cdot \left(\langle \rho_a \rangle^g \langle \mathbf{v}_g \rangle\right) = \nabla \cdot \left[\langle \rho_g \rangle^g \mathbf{D}_{eff} \cdot \nabla \left(\frac{\langle \rho_a \rangle^g}{\langle \rho_g \rangle^g}\right)\right] \tag{2-53}$$

4. The conservation equation of energy

$$\langle \rho \rangle C_p \frac{\partial \langle T \rangle}{\partial t} + \left[\rho_w c_{p,w} \langle \mathbf{v}_w \rangle + \langle \rho_g \rangle^g \langle c_p \rangle^g \langle \mathbf{v}_g \rangle\right] \cdot \nabla \langle T \rangle + \Delta h_v \langle \dot{m} \rangle$$
$$= \nabla \cdot \left(\lambda_{eff} \nabla \langle T \rangle\right) \tag{2-54}$$

where

$$\langle \rho \rangle C_p = \varepsilon_s \rho_s c_{p,s} + \varepsilon_w \rho_w c_{p,w} + \varepsilon_g \langle \rho_v \rangle^g c_{p,v} + \varepsilon_g \langle \rho_a \rangle^g c_{p,a} \tag{2-55}$$

with

$$\langle \rho \rangle = \varepsilon_s \rho_s + \varepsilon_w \rho_w + \varepsilon_g \langle \rho_v \rangle^g + \varepsilon_g \langle \rho_a \rangle^g \tag{2-56}$$

and Δh_v is evaporation enthalpy.

It should be noted that in Eq. (2-54) local thermal equilibrium is assumed

$$\langle T \rangle := \langle T_s \rangle^s = \langle T_w \rangle^w = \langle T_g \rangle^g \tag{2-57}$$

The effective diffusivity $\mathbf{D}_{eff}$ and effective thermal conductivity λ_{eff}, which appear in Eqs. (2-52) to (2-54), are obtained from the process of upscaling from pore scale transport equations to macroscopic equations. These parameters are functions of moisture content and material properties (for more details, see Whitaker 1977 [115]).

The capillary pressure is defined as the difference between gas pressure and liquid pressure

$$\langle P_c \rangle = \langle P_g \rangle^g - \langle P_w \rangle^w \tag{2-58}$$

and the vapour pressure is calculated from sorption isotherm.

Concerning the liquid and gas phase equations of motion, the analysis of the conservation of linear momentum (2-5) leads to the following volume-averaged equations

$$\langle \mathbf{v}_w \rangle = -\frac{\mathbf{K} \cdot \mathbf{k}_w}{\eta_w} \cdot \nabla \langle P_w \rangle^w \tag{2-59}$$

$$\langle \mathbf{v}_g \rangle = -\frac{\mathbf{K} \cdot \mathbf{k}_g}{\eta_g} \cdot \nabla \langle P_g \rangle^g \tag{2-60}$$

where $\mathbf{K}$ is the absolute permeability tensor, $\mathbf{k}_w$ and $\mathbf{k}_g$ denote the relative permeability tensors of liquid and gas, respectively. Note that in deriving the above equations, the effect of gravity has been neglected.

In order to apply the control volume method, the equations (2-51)÷(2-54) must be reformulated and put in the following form

$$\frac{\partial}{\partial t}\Psi - \nabla \cdot \mathbf{J} = 0 \tag{2-61}$$

where Ψ is any scalar quantity and $\mathbf{J}$ is the flux of mass or energy. This requirement can be satisfied with the use of the set of equations proposed by Perré and Turner (1999 [71]). A simpler version of those equations will be derived here based on the system (2-51)÷(2-60). Differently to the model of Perré and Turner, bound water, which is neglected in the present work, will not appear in the reformulation based directly on the system (2-51)÷(2-60).

To reformulate the system (2-51)÷(2-60), we need to choose a set of main variables that will represent the whole drying process. It is evident that the variables appearing in the above system of equations are not independent of one another. A possible choice for a set of independent variables can be average temperature $\langle T \rangle$, volume fraction of liquid water ε_w and intrinsic phase average of air density in the gas phase $\langle \rho_a \rangle^g$. The consequence of this choice is that only three independent equations, in which those variables are involved, are required.

In order to simplify the further development, we will drop the average notation $\langle \ \rangle$ and understand that all variables are used in an average sense, for example, T will be understood as $\langle T \rangle$, P_a as $\langle P_a \rangle^g$ etc.

By adding equations (2-51) and (2-52) we have the conservation equation for water in both liquid and gas phase as

$$\frac{\partial}{\partial t}\left(\rho_w \varepsilon_w + \varepsilon_g \rho_v\right) + \nabla \cdot \left(\rho_w \mathbf{v}_w + \rho_v \mathbf{v}_g\right) = \nabla \cdot \left[\rho_g \mathbf{D}_{eff} \cdot \nabla\left(\frac{\rho_v}{\rho_g}\right)\right] \tag{2-62}$$

The important consequence in combining the two equations (2-51) and (2-52) is that in the resulting equation, the evaporation rate, which is complicated to compute, disappears. Eq. (2-62) will serve as the first of the three required independent equations.

The second equation is taken as the conservation equation for air in the gas phase (2-53) rewritten here by dropping the average symbol $\langle \ \rangle$

$$\frac{\partial}{\partial t}\left(\varepsilon_g \rho_a\right)+\nabla\cdot\left(\rho_a \mathbf{v}_g\right)=\nabla\cdot\left[\rho_g \mathbf{D}_{\text{eff}}\cdot\nabla\left(\frac{\rho_a}{\rho_g}\right)\right] \tag{2-63}$$

The third equation is more complicated and will be derived from the conservation equation of energy (2-54). Firstly, by using the formula for the mass fraction weighted average heat capacity C_p (Eq. (2-55)) we get

$$\left(\varepsilon_s \rho_s c_{p,s}+\varepsilon_w \rho_w c_{p,w}+\varepsilon_g \rho_v c_{p,v}+\varepsilon_g \rho_a c_{p,a}\right)\frac{\partial T}{\partial t}$$
$$+\left[\rho_w c_{p,w}\mathbf{v}_w+\left(\rho_v c_{p,v}+\rho_a c_{p,a}\right)\mathbf{v}_g\right]\cdot\nabla T+\Delta h_v \dot{m}=\nabla\cdot\left(\lambda_{\text{eff}}\nabla T\right) \tag{2-64}$$

Due to the assumption about the linearity of enthalpies (2-11), the first term of (2-64) can be rewritten in the form

$$\left(\varepsilon_s \rho_s c_{p,s}+\varepsilon_w \rho_w c_{p,w}+\varepsilon_g \rho_v c_{p,v}+\varepsilon_g \rho_a c_{p,a}\right)\frac{\partial T}{\partial t}$$
$$=\varepsilon_s \rho_s \frac{\partial}{\partial t}h_s+\varepsilon_w \rho_w \frac{\partial}{\partial t}h_w+\varepsilon_g \rho_v \frac{\partial}{\partial t}h_v+\varepsilon_g \rho_a \frac{\partial}{\partial t}h_a \tag{2-65}$$

By using the relationship

$$\frac{\partial}{\partial t}\left(\varepsilon_i \rho_i h_i\right)=\varepsilon_i \rho_i \frac{\partial}{\partial t}h_i+h_i \frac{\partial}{\partial t}\left(\varepsilon_i \rho_i\right) \tag{2-66}$$

and respecting that

$$h_s \frac{\partial}{\partial t}\left(\varepsilon_s \rho_s\right)=0 \tag{2-67}$$

we obtain further

$$\left(\varepsilon_s \rho_s c_{p,s}+\varepsilon_w \rho_w c_{p,w}+\varepsilon_g \rho_v c_{p,v}+\varepsilon_g \rho_a c_{p,a}\right)\frac{\partial T}{\partial t}=$$
$$\frac{\partial}{\partial t}\left(\varepsilon_s \rho_s h_s+\varepsilon_w \rho_w h_w+\varepsilon_g \rho_v h_v+\varepsilon_g \rho_a h_a\right) \tag{2-68}$$
$$-\left[h_w \frac{\partial}{\partial t}\left(\varepsilon_w \rho_w\right)+h_v \frac{\partial}{\partial t}\left(\varepsilon_g \rho_v\right)+h_a \frac{\partial}{\partial t}\left(\varepsilon_g \rho_a\right)\right]$$

Secondly, by using the assumption about the linearity of enthalpies (2-11) and the formula

$$\nabla\cdot\left(\rho h \mathbf{v}\right)=\left(\rho \mathbf{v}\right)\cdot\nabla h+h\nabla\cdot\left(\rho \mathbf{v}\right) \tag{2-69}$$

the second term on the left-hand side of Eq. (2-64) is rewritten in the form

$$\left[\rho_w c_{p,w}\mathbf{v}_w+\left(\rho_v c_{p,v}+\rho_a c_{p,a}\right)\mathbf{v}_g\right]\cdot\nabla T$$
$$=\nabla\cdot\left[\rho_w h_w \mathbf{v}_w+\left(\rho_v h_v+\rho_a h_a\right)\mathbf{v}_g\right]-\left[h_w \nabla\cdot\left(\rho_w \mathbf{v}_w\right)+h_v \nabla\cdot\left(\rho_v \mathbf{v}_g\right)+h_a \nabla\cdot\left(\rho_a \mathbf{v}_g\right)\right] \tag{2-70}$$

Thirdly, the latent heat of evaporation at temperature T can be expressed as

$$\Delta h_v = h_v - h_w \tag{2-71}$$

so that

$$\Delta h_v \dot{m} = h_v \dot{m} - h_w \dot{m} \qquad (2\text{-}72)$$

Furthermore, the evaporation rate $\dot{m}$ can be computed in two different ways using the conservation equation (2-51) for water in liquid phase and the conservation equation (2-52) for water in gas phase (vapour) as

$$\dot{m} = -\rho_w \frac{\partial}{\partial t}(\varepsilon_w) - \rho_w \nabla \cdot (\mathbf{v}_w) \qquad (2\text{-}73)$$

and

$$\dot{m} = \frac{\partial}{\partial t}(\varepsilon_g \rho_v) + \nabla \cdot (\rho_v \mathbf{v}_g) - \nabla \cdot \left[\rho_g \mathbf{D}_{eff} \cdot \nabla\left(\frac{\rho_v}{\rho_g}\right)\right] \qquad (2\text{-}74)$$

By substituting equations (2-68), (2-70), (2-72), (2-73) and (2-74) into the conservation equation of energy (2-64), after some manipulations we arrive at

$$\frac{\partial}{\partial t}\left(\varepsilon_s \rho_s h_s + \varepsilon_w \rho_w h_w + \varepsilon_g \rho_v h_v + \varepsilon_g \rho_a h_a\right) + \nabla \cdot \left[\rho_w h_w \mathbf{v}_w + (\rho_v h_v + \rho_a h_a)\mathbf{v}_g\right]$$
$$- h_a\left[\frac{\partial}{\partial t}(\varepsilon_g \rho_a) + \nabla \cdot (\rho_a \mathbf{v}_g)\right] - h_v \nabla \cdot \left[\rho_g \mathbf{D}_{eff} \cdot \nabla\left(\frac{\rho_v}{\rho_g}\right)\right] = \nabla \cdot (\lambda_{eff} \nabla T) \qquad (2\text{-}75)$$

Now, if the term $\left[\dfrac{\partial}{\partial t}(\varepsilon_g \rho_a) + \nabla \cdot (\rho_a \mathbf{v}_g)\right]$ is computed using the air conservation equation (2-63), we get

$$\frac{\partial}{\partial t}\left(\varepsilon_s \rho_s h_s + \varepsilon_w \rho_w h_w + \varepsilon_g \rho_v h_v + \varepsilon_g \rho_a h_a\right) + \nabla \cdot \left[\rho_w h_w \mathbf{v}_w + (\rho_v h_v + \rho_a h_a)\mathbf{v}_g\right]$$
$$= h_a \nabla \cdot \left[\rho_g \mathbf{D}_{eff} \cdot \nabla\left(\frac{\rho_a}{\rho_g}\right)\right] + h_v \nabla \cdot \left[\rho_g \mathbf{D}_{eff} \cdot \nabla\left(\frac{\rho_v}{\rho_g}\right)\right] + \nabla \cdot (\lambda_{eff} \nabla T) \qquad (2\text{-}76)$$

This conservation equation of energy can be further simplified by assuming that within an averaging volume the variation of enthalpy is small compared with its value. Then, we obtain the final form

$$\frac{\partial}{\partial t}\left(\varepsilon_s \rho_s h_s + \varepsilon_w \rho_w h_w + \varepsilon_g \rho_v h_v + \varepsilon_g \rho_a h_a\right) + \nabla \cdot \left[\rho_w h_w \mathbf{v}_w + (\rho_v h_v + \rho_a h_a)\mathbf{v}_g\right]$$
$$= \nabla \cdot \left[\rho_g h_a \mathbf{D}_{eff} \cdot \nabla\left(\frac{\rho_a}{\rho_g}\right)\right] + \nabla \cdot \left[\rho_g h_v \mathbf{D}_{eff} \cdot \nabla\left(\frac{\rho_v}{\rho_g}\right)\right] + \nabla \cdot (\lambda_{eff} \nabla T) \qquad (2\text{-}77)$$

This equation will serve as the third equation in the system of three required equations needed to find the three independent variables T, ε_w and ρ_a.

To summarize, we note that, in order to apply the control volume method, the macroscopic conservation equations of liquid water (2-62), air (2-63) and energy (2-77) are used together with the motion equations for liquid water and gas, Eqs. (2-59) and (2-60). This set of equations represents the macroscopic equations governing the drying process under consideration. To complete this set of equations, the constraints and constitutive relations such as thermodynamic relations (ideal gas behaviour, sorption

isotherm), capillary pressure, enthalpy-temperature relations, the physical properties of the material being dried as well as initial and boundary conditions are needed. All these issues will be discussed in the next chapter together with the volume control method.

2.5. Effective parameters by capillary model

The effective parameters, which are used in the continuous model proposed by Whitaker and further developed by Perré and Turner, must be either taken as empirical functions or measured experimentally for a given material because the volume averaging method does not provide values, it only proves that these parameters are the right ones. These parameters are sorption isotherm, capillary pressure, absolute and relative permeabilites, effective diffusivity and effective thermal conductivity. The determination of these effective parameters is actually a complicated problem and remains a challenge today. Among others research works that dealt with this problem, Lasseux *et al.* (1996 [43]), Quintard and Whitaker (1988 [85]) introduced a method to determine the permeability tensor for two-phase flow. However the method is difficult to apply in practical applications because of its mathematical complexity. Starting from experiments, Perré and Turner (2001 [73]; [74]) introduced a function for calculating capillary pressure and absolute permeability, but only for softwood.

In this section, based on the work of Metzger and Tsotsas (2005 [55]) for bundle of capillary, the capillary pressure, the absolute and relative permeabilites are computed as functions of material pore size distribution. The effective diffusivity and effective thermal conductivity are considered as dependent on porosity ψ and saturation *S*. These parameters will then be used in the continuous drying model presented in the last section, which is capable of modelling the spatial and temporal evolution of moisture content, temperature and gaseous pressure. The aim of this approach is to understand, on a fundamental basis, how a variation of pore size distribution changes the drying behaviour of porous media. However, it should be pointed out that the pore size distribution alone is not enough to characterize the drying behaviour of a porous medium; it is only the most accessible structural information.

In order to compute the capillary pressure and the permeabilites, we represent the porous medium by a bundle of capillaries (Metzger and Tsotsas, 2005 [55]). In this model, the capillary tubes are set perpendicular to the exchange surface of the porous body and the solid phase is arranged in parallel. The model is strictly one-dimensional since it is assumed that there is no lateral resistance to heat or mass transfer between the solid and capillaries, hence local thermal equilibrium is fulfilled (as it is one assumption of the continuous model). The model is illustrated in Figure 2.2 together with its behaviour during drying. We restrict ourselves to large enough pore sizes so that for every capillary the boundary between the gas and liquid phases can be described by a meniscus having a capillary pressure. Like gas and solid, liquid phase is automatically continuous (no clusters), which is required in the continuous model. In this model, Kelvin effect is neglected and molecular diffusion is considered without Knudsen effect since we assume the diameter of the pores are bigger than 50 nm (the mean free part of air molecular) (Krischer, 1992 [40]). During drying, larger capillaries will empty first, because they have the lower capillary pressure. However, the capillary pumping is subjected to friction leading to a non-trivial moisture profile. For convenience, instead

of moisture content *X*, saturation *S* will be used (Eq. (1-4)). In the following section, formulations will be presented to compute the capillary pressure, permeabilities, effective diffusivity and effective thermal conductivity.
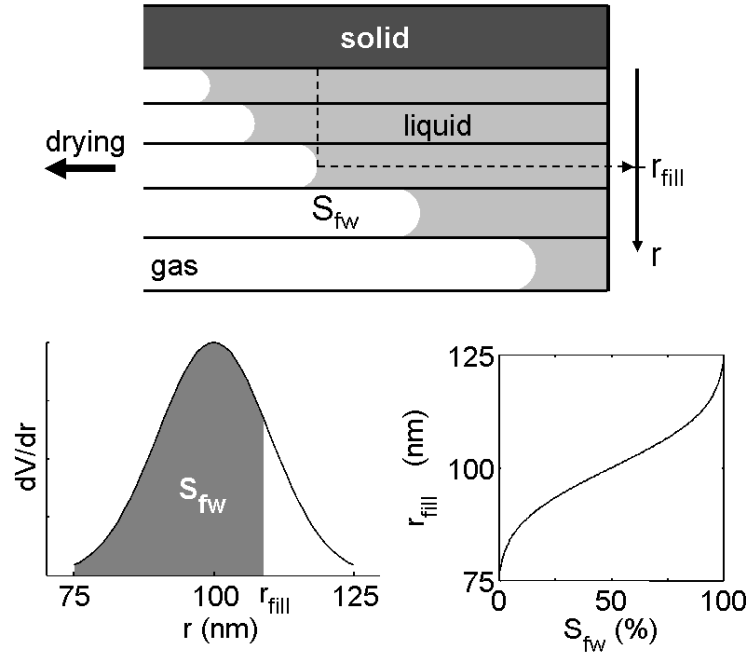

Figure 2.2 Partially saturated bundle of capillaries: relationship between free water saturation S_{fw} and maximum radius filled r_{fill} (for mono-modal pore size distribution $r_0 = 100$ nm $\sigma_0 = 10$ nm).

2.5.1. *Pores size distribution and saturation*

Two types of pore size distributions (capillary radius distributions) are used here. The first one is a mono-modal normally distributed pore volume:

$$\frac{dV}{dr} = \frac{C}{\sqrt{2\pi}\sigma_0} e^{-\frac{1}{2}\left(\frac{r-r_0}{\sigma_0}\right)^2} \qquad (2\text{-}78)$$

where r_0 is the mean pore radius, σ_0 the standard deviation and *C* a constant. This normal distribution is truncated at $r_0 \pm 2.5\sigma_0$. The integral of the pore size distribution computed in this truncated range must be equal to the void volume of the sample or, in other words, the total volume fraction of liquid for *S* = 1 must correspond to the porosity ψ of the sample. However, in this work, this integral is set to unity for the sake of simplicity (see Eq. (2-79) below).

The second type is a bimodal distribution, which consists of two mono-modal models (with different mean pore radii and deviations) named here as *small* pore and *large* pore distributions. In bimodal distributions, the volume fractions of *small* pores and *large* pores as well as the transition region between two kinds of pores are taken into account. The computational treatment of the transition region will be discussed below. Like mono-modal distribution, the integral of the pore size distribution in this case is set to unity. Evidently, different choices are possible for capillary radius distributions.

However the mono- and bimodal distributions are considered to be enough for a systematic investigation.

If the porous medium is partially saturated with water, the assumption of ideal lateral transfer between the capillaries implies that for a given local free water saturation S_{fw} small capillaries are filled up to a maximum radius r_{fill} (see Figure 2.2) such that

$$S_{fw} = \int_{r_{min}}^{r_{fill}} \frac{dV}{dr} dr \qquad (2\text{-}79)$$

where r_{min} is the smallest capillary radius of the bundle.

The localization of free water S_{fw} is the key for computing effective parameters as function of saturation. Based on Eq. (2-79), the maximum radius r_{fill} can be computed for a given S_{fw}. For any saturation under the irreducible value, the saturation of free water S_{fw} is zero and the maximum radius filled by liquid r_{fill} is set to r_{min}.

2.5.2. *Sorption isotherm*

Adsorbed water, which may play an important role in the drying of hygroscopic materials, needs to be modelled separately since it depends mainly on material properties (the influence of pore size distribution is neglected because the condensation due to Kelvin effect only plays an important role at very high level of relative humidity). In our simulations, we chose the same type of temperature independent sorption isotherm as Perré and Turner (1999 [71]) used for concrete (see Figure 2.3)

$$\varphi = \frac{S}{S_{irr}} \cdot \left(2 - \frac{S}{S_{irr}} \right) \quad \text{for } S \leq S_{irr} \qquad (2\text{-}80)$$

where φ is the relative humidity, S_{irr} is the maximum amount of adsorbed water and $S = S_{irr} + S_{fw}$; in the presence of free water, $\varphi = 1$.
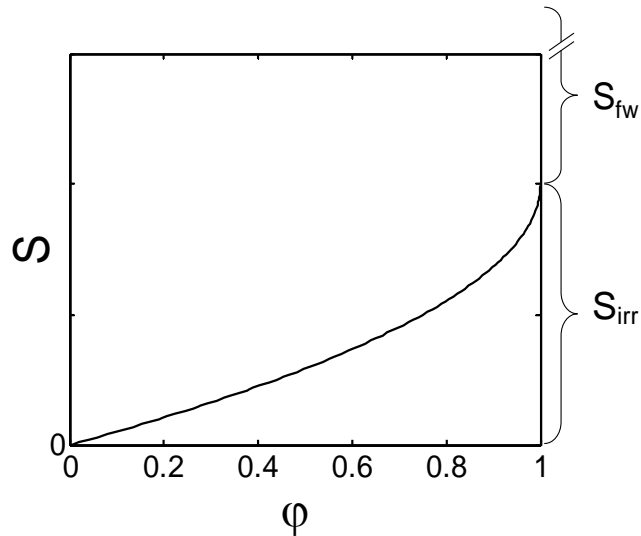

Figure 2.3 Sorption isotherm used for bundle of capillaries.

2.5.3. *Capillary pressure*

Besides vapour pressure, the capillary pressure is also linked to saturation by a state equation given by the meniscus in the largest filled capillary

$$P_c\left(S_{fw}, T\right) = \frac{2 \cdot \sigma(T)}{r_{fill}\left(S_{fw}\right)}$$

(2-81)

In the above equation, zero contact angle is assumed. The temperature dependency of surface tension is given by Eq. (A1-4) (Appendix 1).

In order to illustrate the influence of pore size distribution on the effective parameters, four different cases of pore size distribution are considered. The parameters of the distributions and the corresponding absolute permeabilities are presented in Table 2.1. For the bimodal distributions, the volume is equally distributed to the two modes (48% each). The adsorbed water region is for $S < 15\%$, and transition region for bimodal distributions is for $S \approx 57.5\%$.

The capillary pressure curves for these four pore size distributions are illustrated in Figure 2.4. Naturally, with decreasing saturation, the capillary pressure increases. The overall level of capillary pressure is determined by the mean pore size r_0 of the mode and its range of variation is determined by the standard deviation σ_0. For bimodal distributions, a sudden change of capillary pressure is observed when the larger mode is emptied, which – for numerical reasons – is extended into a transition region (see Appendix 3). In the sorption region, capillary pressure is set constant at the value corresponding to only the smallest pores being filled.

Table 2.1. Pore size distributions and absolute permeabilities.

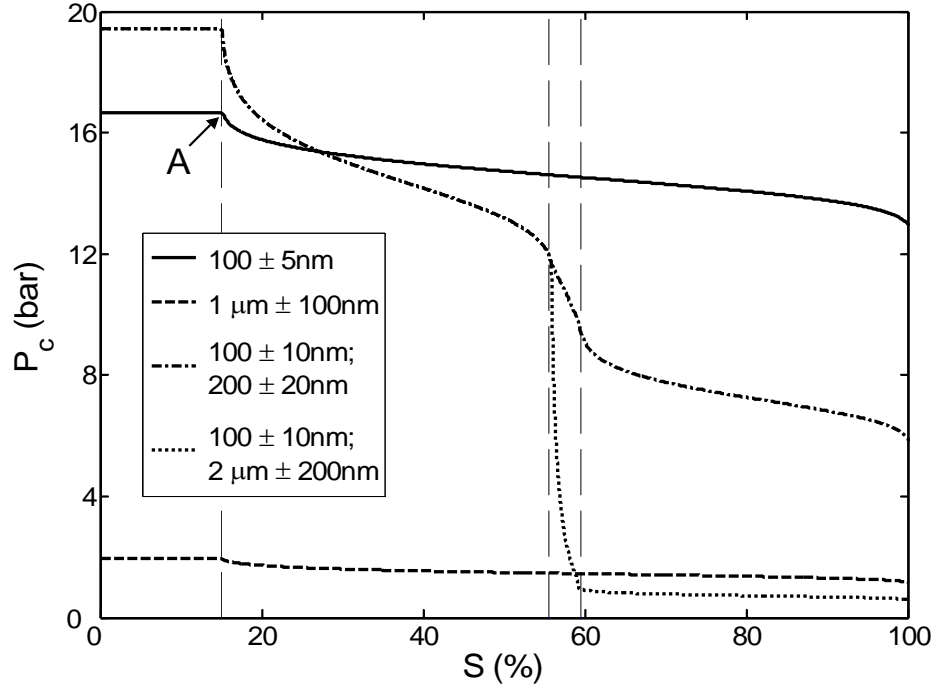|	$r_0 \pm \sigma_0$ (nm)	K ($\cdot 10^{-15}$ m^2)	
Case 1	100 ± 5	1.238	mono-modal
Case 2	1000 ± 100	124.6	
Case 3	$100 \pm 10; 200 \pm 20$	3.119	bimodal
Case 4	$100 \pm 10; 2000 \pm 200$	245.1	

Figure 2.4 Capillary pressure for four cases of capillary radius distribution.

2.5.4. *Absolute permeability*

Considering one capillary which is fully saturated by water, on the one hand, the volumetric flow rate is calculated from the Poiseille's equation

$$\dot{V} = \frac{1}{8\eta} \cdot \frac{\Delta P_w}{L} \cdot \pi \cdot r^4 \tag{2-82}$$

where L is the capillary length, r the capillary radius, η the dynamic viscosity (temperature dependent) and P_w the water pressure.

One the other hand, the mean velocity $\bar{v}$ (volumetric flow rate per total cross section of porous medium) of the liquid can be described by the generalized Darcy law (Eq. (2-59). In this calculation, we assume that gravitational effects are negligible and that velocity is small enough to neglect inertial effects. If we apply Darcy law to a fully saturated capillary ($k_w = 1$), we obtain

$$\bar{v} = \frac{K}{\eta} \cdot \frac{\Delta P_w}{L} \tag{2-83}$$

By comparing Eqs. (2-82) and (2-83), the absolute permeability can be found to be

$$K = \frac{1}{8} r^2 \tag{2-84}$$

An extension to the bundle of capillaries yields

$$K = \frac{1}{8} \int\limits_{r_{\min}}^{r_{\max}} r^2 \frac{dV}{dr} dr \tag{2-85}$$

where the interval $[r_{min}, r_{max}]$ is the total range of the pore size distribution.

The absolute permeabilities of the four different pore size distributions given in Table 2.1 are computed using Eq. (2-85). The absolute permeability K does not depend on temperature or pressure. It is mainly determined by the mean radius (of the large pores). The broadness of the distribution contributes little to K. For the bimodal cases, there is only a small contribution from small pores.

2.5.5. *Relative permeabilities*

The relative permeability of liquid and gas phases are computed in a similar way as the absolute permeability

$$k_w(S_{fw}) = \frac{1}{8K} \int\limits_{r_{\min}}^{r_{fill}} r^2 \frac{dV}{dr} dr \tag{2-86}$$

$$k_g(S_{fw}) = \frac{1}{8K} \int\limits_{r_{fill}}^{r_{\max}} r^2 \frac{dV}{dr} dr \tag{2-87}$$

Clearly, the total of these two quantities is unity.

Like the absolute permeability, the relative permeabilities do not depend on either temperature or pressure. The relative permeabilities for the four considered cases are depicted in Figure 2.5 (mono-modal) and Figure 2.6 (bimodal). The relative permeabilities are almost directly proportional to the corresponding phase saturation, but the curvature of the functions $k_{w,g}(S)$ increases with broader pore size distribution – in an unfavourable way for liquid transport and favourable for gas transport. Again, the contribution from small pores (in bimodal cases) is small. Below the irreducible saturation the relative permeability of liquid k_w is zero.

In order to avoid sudden changes of slope or even jumps of the capillary pressure and transport parameter functions, which would cause numerical problems when these functions are used in the continuous model, the pore size distribution has to be slightly modified. These modifications are discussed in Appendix 3.
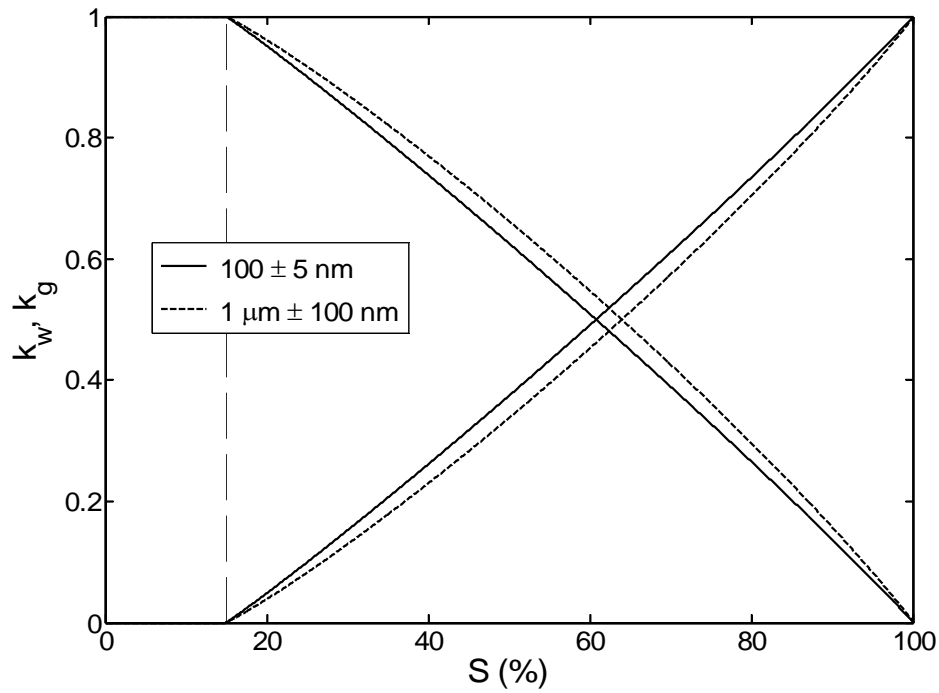
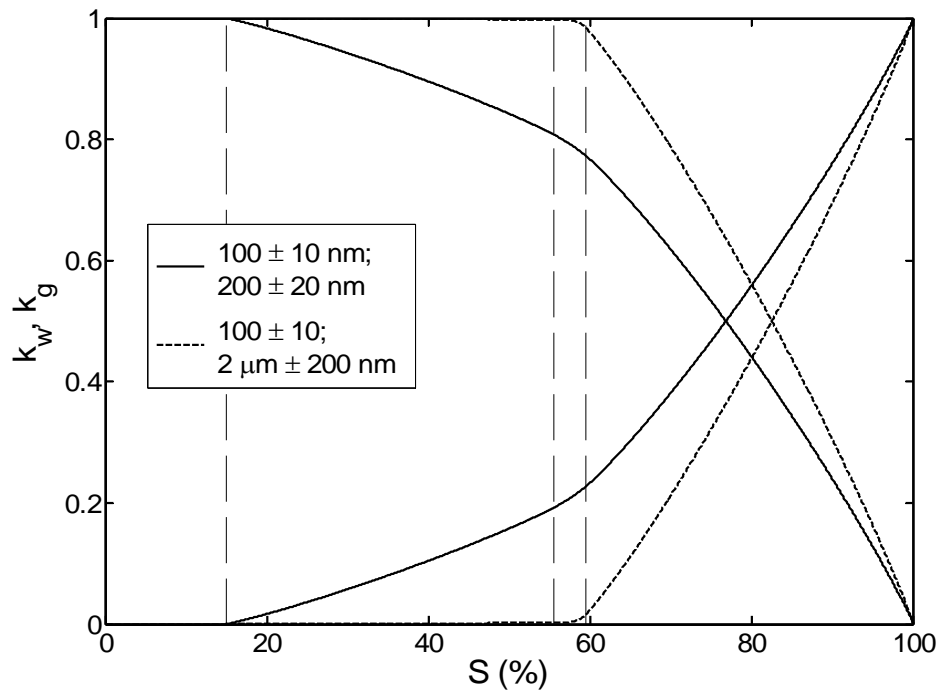**Figure 2.5** Relative permeabilities for two cases of mono-modal distributions.

Figure 2.6 Relative permeabilities for two cases of bi-modal distributions.

2.5.6. *Effective vapour diffusivity*

The effective vapour diffusivity does not depend on the distribution of the pores, but the evaporation area. Therefore this transport parameter is assumed as a function of saturation, porosity and the binary diffusion coefficient

$$D_{eff}(S,T,P) = (1-S)\cdot\psi\cdot\delta_{va}(T,P) \tag{2-88}$$

The binary diffusion coefficient δ_{va} is considered as temperature and pressure dependent (Eq. (A1-13) – Appendix 1). The Knudsen effect is neglected for the investigated pore sizes.

2.5.7. *Effective thermal conductivity*

Like effective vapour diffusivity, this transport parameter is also assumed to be independent of pore size distribution. As heat conduction occurs in all phases in parallel, the heat flux or thermal conductivity contributions must be weighted according to their respective volume fractions of the phases. If the contribution of gas is neglected, then the effective thermal conductivity can be computed as

$$\lambda_{eff}(S,T) = (1-\psi)\cdot\lambda_s(T) + S\cdot\psi\cdot\lambda_w(T) \tag{2-89}$$

In this work, the thermal conductivity of solid λ_s is taken as constant, while the thermal conductivity of liquid water λ_w is temperature dependent (Eq. (A1-5) – Appendix 1).

To summarize, in this chapter, the mathematical model of drying developed by Whitaker (1977 [115]; 1980 [116]) is presented. Starting from the basic transport laws of mass and heat at pore (microscopic) level, the macroscopic conservation equations that govern the drying processes in porous media are derived with the use of the volume averaging method. The governing equations obtained by Whitaker are then reformulated in a ready-to-use form suitable for the control volume method. The result of the reformulation is a system of equations, which is actually a simplified version of that proposed by Perré and Turner (1999 [71]). Based on the work of Metzger and Tsotsas (2005 [55]), the effective parameters used in the continuous drying model, namely the capillary pressure, the absolute and relative permeabilities, are computed as functions of pore size distribution. In the next chapter we will study the use of the control volume method in solving the drying model presented in this chapter.

Chapter 3

NUMERICAL METHOD

3.1. Introduction

In this chapter, the numerical method used to solve the above-described continuous drying model is presented. In principle, the finite element method, the finite difference method or the control volume method can be employed. Quite a few works were carried out trying to find the best technique for the simulation of drying. In the quest for a quicker, more accurate and less expensive solution even mixtures of different methods appeared, for example the so-called control volume finite element method (Ferguson, 1995 [20]); Perré and Turner, 1998 [70], 2000 [72]). In many textbooks on numerical methods for heat and mass transfer, the control volume method (Patankar, 1980 [62]) is praised for its accuracy in solving problems involving conservation of different quantities. The method has been applied in drying simulation by, for example, Hadley (1985 [26]), Perré (1987 [66]), Nasrallah and Perré (1988 [58]), Perré and Degiovanni (1990 [68]), Turner (1991 [103]), Turner and Ferguson (1995 [104], [105]), Turner and Perré (1995 [106]; 1996 [107]; 2001 [108]), Boukadida and Nasrallah (1995 [8]), Boukadida *et al.* (2000 [9]), Jayantha and Turner (2003 [33]), Truscott (2004 [100]), Truscott and Turner (2005 [101]). The basic idea of the control volume method is simple. In this method, the calculation domain is divided into a number on non-overlapping control volumes, which are each associated with a grid point (node) (Patankar, 1980 [62]). The system of differential equations is then integrated over each control volume. Piecewise profiles expressing the variation of variables and related quantities are used to evaluate the required integrals. For each control volume, the result is a discrete version of the differential equations involving the variables related to the central node of this control volume and to the nodes connected to it. The discretized equations obtained in this way describe the conservation principles for the control volume just as differential equations describe those principles for an infinitesimal volume. The most important feature of the control volume method that makes it different from others is that conservation requirement of the basic physical quantities such as mass and energy will be satisfied at any discrete level: across a control volume element, over a group of control volume elements or over the whole calculation domain. The control volume method will be employed in this work to solve the set of governing equations derived in the last chapter. In the next sections, the discretization of those equations by the control volume method is presented.

3.2. The governing equations and main variables

For convenience, in this section, the set of three governing equations derived in the last chapter is repeated together with the equations of motion (generalized Darcy's law) for liquid and gas phases:

The conservation equation for water in both liquid and gas phase

$$\frac{\partial}{\partial t}\left(\rho_w \varepsilon_w + \varepsilon_g \rho_v\right) + \nabla \cdot \left(\rho_w \mathbf{v}_w + \rho_v \mathbf{v}_g\right) = \nabla \cdot \left[\rho_g \mathbf{D}_{eff} \cdot \nabla\left(\frac{\rho_v}{\rho_g}\right)\right]; \tag{3-1}$$

The conservation equation for air in gas phase

$$\frac{\partial}{\partial t}\left(\varepsilon_g \rho_a\right) + \nabla \cdot \left(\rho_a \mathbf{v}_g\right) = \nabla \cdot \left[\rho_g \mathbf{D}_{eff} \cdot \nabla\left(\frac{\rho_a}{\rho_g}\right)\right]; \tag{3-2}$$

The conservation equation of energy

$$\frac{\partial}{\partial t}\left(\varepsilon_s \rho_s h_s + \varepsilon_w \rho_w h_w + \varepsilon_g \rho_v h_v + \varepsilon_g \rho_a h_a\right) + \nabla \cdot \left[\rho_w h_w \mathbf{v}_w + \left(\rho_v h_v + \rho_a h_a\right)\mathbf{v}_g\right]$$

$$= \nabla \cdot \left[\rho_g h_a \mathbf{D}_{eff} \nabla\left(\frac{\rho_a}{\rho_g}\right)\right] + \nabla \cdot \left[\rho_g h_v \mathbf{D}_{eff} \nabla\left(\frac{\rho_v}{\rho_g}\right)\right] + \nabla \cdot \left(\lambda_{eff} \nabla T\right); \tag{3-3}$$

The equation of motion for the liquid phase

$$\mathbf{v}_w = -\frac{\mathbf{K}k_w}{\eta_w}\nabla P_w; \tag{3-4}$$

And the equations of motion for the gas phase

$$\mathbf{v}_g = -\frac{\mathbf{K}k_g}{\eta_g}\nabla P_g, \tag{3-5}$$

where the dynamic viscosity of water η_w and of gas η_g are temperature dependent (see Appendix 1).

Besides the above governing equations, the conditions for mass and heat transfer at the external drying surfaces of the porous medium must be specified. It is assumed that at the external drying surfaces the fluxes of mass and heat are described for convective drying by the boundary layer theory with Stefan correction

$$\mathbf{J}_w \cdot \hat{\mathbf{n}} = \dot{\mathbf{m}}_v = \beta \frac{P_g \tilde{M}_v}{\tilde{R}T} \ln\left(\frac{P_g - P_{v,\infty}}{P_g - P_v}\right) \tag{3-6}$$

and

$$\mathbf{J}_e \cdot \hat{\mathbf{n}} = \dot{\mathbf{q}} + \Delta h_v \dot{\mathbf{m}}_v = \alpha\left(T - T_\infty\right) + \Delta h_v \beta \frac{P_g \tilde{M}_v}{\tilde{R}T} \ln\left(\frac{P_g - P_{v,\infty}}{P_g - P_v}\right) \tag{3-7}$$

in which $\mathbf{J}_w$ and $\mathbf{J}_e$ are the fluxes of water and heat respectively, $P_{v,\infty}$ and T_∞ are vapour pressure and temperature of bulk drying air, $\hat{\mathbf{n}}$ is the outward-pointing normal vector at the boundary surface, β and α are mass and heat transfer coefficients. Additionally, the gas pressure at the external drying surfaces is fixed at the pressure of the bulk drying air

$$P_g = P_\infty \tag{3-8}$$

Sorption isotherm, capillary pressure, ideal gas laws and enthalpy-temperature relations will complete the set of Eqs. (3-1)÷(3-8) by helping to express all variables as functions of three state variables. Besides, initial conditions are needed.

In this work, we restrict ourselves to one-dimensional problems and the discretization will be presented for this case. As mentioned in the last chapter, the three independent variables T, ε_w and ρ_a are sufficient to describe the characteristics of the drying process in porous media. However, it is more convenient to work with the moisture content $X = \left(\varepsilon_w \rho_w\right)/\left(\varepsilon_s \rho_s\right)$ and the phase average of the gas density $\overline{\rho}_a = \varepsilon_g \rho_a$ than with the volume fraction of water ε_w and the intrinsic gas density ρ_a. The use of X and $\overline{\rho}_a$ will simplify the conservation equations of water and air and, more importantly, X is a common quantity to describe drying. Due to this reason, we will pursue our work with the set of state variables $\left(X, T, \overline{\rho}_a\right)$ but in the presentation of numerical results the gas pressure P_g will replace $\overline{\rho}_a$.

3.3. Discretization of the conservation equation of water

In order to discretize the conservation equation of water, we first rewrite this equation in term of the main variables $\left(X, T, \overline{\rho}_a\right)$. By using the equations of motion of liquid water and air (3-4) and (3-5), Eq. (3-1) can be expressed as

$$\varepsilon_s \rho_s \frac{\partial X}{\partial t} + \frac{\partial}{\partial t}\left(\varepsilon_g \rho_v\right) - \nabla J_w = 0 \tag{3-9}$$

where J_w is the total flux of water

$$J_w = \rho_w \frac{K \cdot k_w}{\eta_w} \nabla P_w + \rho_v \frac{K \cdot k_g}{\eta_g} \nabla P_g + \rho_g D_{eff} \nabla y_v \tag{3-10}$$

in which y_v is the mass fraction of vapour: $y_v = \rho_v / \rho_g$.

Next, we need to express the water pressure P_w, the gas pressure P_g and the mass fraction y_v in terms of the main variables. The water pressure P_w can be obtained from the definition of the capillary pressure P_c, which is a function of temperature T and moisture content X

$$P_w = P_g - P_c\left(T, X\right) \tag{3-11}$$

By use of ideal gas laws and sorption isotherms $P_v(X,T)$, the gas pressure P_g can be expressed as

$$P_g = P_a + P_v = \rho_a \frac{\tilde{R}T}{\tilde{M}_a} + P_v(X,T) = \frac{\overline{\rho}_a}{\varepsilon_g} \frac{\tilde{R}T}{\tilde{M}_a} + P_v(X,T) \tag{3-12}$$

where the volume fraction of gas phase is expressed as

$$\varepsilon_g = 1 - \varepsilon_s - \varepsilon_w = (1 - \varepsilon_s) - \frac{\varepsilon_s \rho_s}{\rho_w} X \tag{3-13}$$

In order to compute the mass fraction y_v, the gas, air and vapour densities are obtained from the ideal gas law

$$\rho_v = \frac{P_v \tilde{M}_v}{\tilde{R}T} \qquad\qquad \rho_a = \frac{P_a \tilde{M}_a}{\tilde{R}T} \qquad\qquad \rho_g = \rho_a + \rho_v \tag{3-14}$$

leading to

$$y_v = \frac{\rho_v}{\rho_g} = \frac{P_v}{P_g} \frac{\tilde{M}_v}{\tilde{M}_a + (\tilde{M}_v - \tilde{M}_a)\dfrac{P_v}{P_g}} \tag{3-15}$$
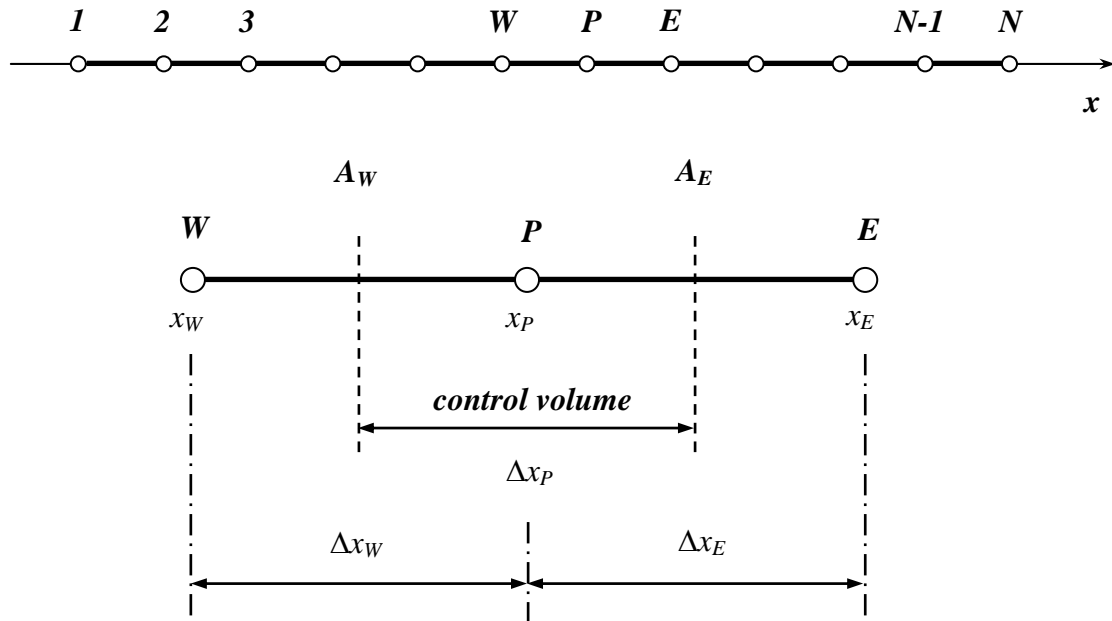

Figure 3.1 Control volume mesh (top) and normal control volume element (bottom) for one-dimensional drying problems.

The conservation equation of water (3-9) is now ready to be discretized. To do this, we will employ a control volume mesh with N grid nodes along the x-axis of a Cartesian coordinate system, as shown in Figure 3.1. The distances between the grid nodes need not to be equal. Each node P has its two neighbour nodes: W on the left-hand side and E on the right-hand side (W stands for west and E stands for east side). We denote the distance between node P and W by Δx_W and between node P and E by Δx_E. The dash lines define the two faces of the control volume A_W and A_E. The exact positions of the faces are one of the important characteristics of the control volume mesh, especially with non-equidistant grid points. However, for the sake of simplicity, we will assume

that the control volume face is positioned at the middle of the two adjacent nodes so that the length of the control volume element computed from its west face A_W to its east face A_E is

$$\Delta x_P = \frac{1}{2}\left(\Delta x_W + \Delta x_E\right) \tag{3-16}$$

For the one-dimensional problem under consideration we assume unit size of the control volume element in both y and z direction implying that both surface areas of A_W and A_E are equal to unity.

For known state variables of the drying process $\left(X, T, \overline{\rho}_a\right)$ at time t, the task now is to find their values at time $t + \Delta t$. By integrating Eq. (3-9) over the control volume element and over the time we have

$$\int\limits_{t}^{t+\Delta t}\int\limits_{x_W}^{x_E}\left[\varepsilon_s\rho_s\frac{\partial X}{\partial t} + \frac{\partial}{\partial t}\left(\varepsilon_g\rho_v\right)\right]dxdt - \int\limits_{t}^{t+\Delta t}\int\limits_{x_W}^{x_E}\nabla J_w dxdt = 0 \tag{3-17}$$

These integrals are difficult to evaluate. For simplicity, we separate the time and space integrations and assume that the grid-point values of X and $\varepsilon_g\rho_v$ at node P prevail throughout the control volume so that

$$\int\limits_{t}^{t+\Delta t}\int\limits_{x_W}^{x_E}\left[\varepsilon_s\rho_s\frac{\partial X}{\partial t} + \frac{\partial}{\partial t}\left(\varepsilon_g\rho_v\right)\right]dxdt = \Delta x_P\left[\left(\varepsilon_s\rho_s X + \varepsilon_g\rho_v\right)_P^{t+\Delta t} - \left(\varepsilon_s\rho_s X + \varepsilon_g\rho_v\right)_P^{t}\right] \tag{3-18}$$

where superscripts denote time and subscripts the grid node.

The discretization of the second term of (3-17) is not as easy as the first. We have

$$\int\limits_{t}^{t+\Delta t}\int\limits_{x_W}^{x_E}\nabla J_w dxdt = \int\limits_{t}^{t+\Delta t}\left[\left(J_w\right)_E - \left(J_w\right)_W\right]dt \tag{3-19}$$

In order to evaluate the time integration, an assumption about the variation of the flux should be made. Here we assume that the flux J_w varies between the time t and $t + \Delta t$ in such a way that its integration over time can be expressed as

$$\int\limits_{t}^{t+\Delta t}J_w dt = \left[fJ_w^{t+\Delta t} + \left(1 - f\right)J_w^{t}\right]\Delta t \tag{3-20}$$

where f is a weighting factor between 0 and 1.

By varying the weighting factor f, different integration schemes are available. For example, when f takes the values 0, 0.5 and 1, we have the fully explicit, Crank-Nicolson and fully implicit schemes, respectively. In this work, we will use the fully implicit scheme ($f=1$). For detailed discussion about advantages and disadvantages of each scheme we refer to the work of Patankar (1980 [62]). The use of the fully implicit integration scheme leads to

$$\int\limits_{t}^{t+\Delta t}\int\limits_{x_W}^{x_E}\nabla J_w dxdt = \left[\left(J_w\right)_E^{t+\Delta t} - \left(J_w\right)_W^{t+\Delta t}\right]\Delta t \tag{3-21}$$

and the conservation equation of water (3-1) is now discretized in time and space as

$$\frac{(\Delta x_W + \Delta x_E)}{2\Delta t}\left[\left(\varepsilon_s \rho_s X + \varepsilon_g \rho_v\right)_P^{t+\Delta t} - \left(\varepsilon_s \rho_s X + \varepsilon_g \rho_v\right)_P^t\right] + \left[(J_w)_E^{t+\Delta t} - (J_w)_W^{t+\Delta t}\right] = 0 \qquad (3\text{-}22)$$

In order to compute the flux J_w at two faces A_W and A_E at time $(t + \Delta t)$, we use the finite difference method so that the gradient terms in Eq. (3-10), e.g. at A_W, are evaluated as

$$\nabla P_w = \frac{(P_w)_P - (P_w)_W}{\Delta x_W}; \qquad \nabla P_g = \frac{(P_g)_P - (P_g)_W}{\Delta x_W}; \qquad \nabla y_v = \frac{(y_v)_P - (y_v)_W}{\Delta x_W} \qquad (3\text{-}23)$$

Special care must be taken for the (space dependent) coefficients in Eq. (3-10), since simple linear interpolation between two grid nodes may lead to unrealistic results. Two different schemes are used here for the coefficients of diffusion and convection terms. For the coefficients of the diffusion terms, the average of the two nodal points is used (since the face lies at the middle, this corresponds to linear interpolation); but for the coefficients of the convective terms, the upstream weighting is used, since this was shown to lead to the physically correct solutions in multiple phase situations (Patankar, 1980 [62]). The upstream weighting scheme is more complex as it requires knowledge about the direction of the gas or liquid flow. For example, $(k_w)_{A_W} = (k_w)_P$ if the flow is away from node *P*.

The discretization of the conservation of water is now complete and can be written explicitly as

$$\frac{(\Delta x_W + \Delta x_E)}{2\Delta t}\left[\left(\varepsilon_s \rho_s X + \varepsilon_g \rho_v\right)_P^{t+\Delta t} - \left(\varepsilon_s \rho_s X + \varepsilon_g \rho_v\right)_P^t\right]$$

$$+ \left[\left(\rho_w \frac{K \cdot k_w}{\eta_w}\right)_{A_E}^{t+\Delta t} \frac{(P_w)_E^{t+\Delta t} - (P_w)_P^{t+\Delta t}}{\Delta x_E} + \left(\rho_v \frac{K \cdot k_g}{\eta_g}\right)_{A_E}^{t+\Delta t} \frac{(P_g)_E^{t+\Delta t} - (P_g)_P^{t+\Delta t}}{\Delta x_E}\right.$$

$$+ \left(\rho_g D_{eff}\right)_{A_E}^{t+\Delta t} \frac{(y_v)_E^{t+\Delta t} - (y_v)_P^{t+\Delta t}}{\Delta x_E}\left] - \left[\left(\rho_w \frac{K \cdot k_w}{\eta_w}\right)_{A_W}^{t+\Delta t} \frac{(P_w)_P^{t+\Delta t} - (P_w)_W^{t+\Delta t}}{\Delta x_W}\right.\right. \qquad (3\text{-}24)$$

$$+ \left(\rho_v \frac{K \cdot k_g}{\eta_g}\right)_{A_W}^{t+\Delta t} \frac{(P_g)_P^{t+\Delta t} - (P_g)_W^{t+\Delta t}}{\Delta x_W} + \left(\rho_g D_{eff}\right)_{A_W}^{t+\Delta t} \frac{(y_v)_P^{t+\Delta t} - (y_v)_W^{t+\Delta t}}{\Delta x_W}\right] = 0$$

The discretization procedure outlined above is only valid for a normal control volume element with three grid nodes. For elements, which are situated on the boundary of the calculation domain, only two grid nodes are involved in the discretized formulation and to compensate the boundary conditions of heat and mass transfer must be applied.

Figure 3.2 shows how the two boundary elements can be identified and gives their corresponding boundary conditions. For the first element, the discrete version of water conservation writes

$$\frac{\Delta x_E}{2\Delta t}\left[\left(\varepsilon_s \rho_s X + \varepsilon_g \rho_v\right)_1^{t+\Delta t} - \left(\varepsilon_s \rho_s X + \varepsilon_g \rho_v\right)_1^t\right] + \left[(J_w)_{A_E}^{t+\Delta t} - (J_w)_1^{t+\Delta t}\right] = 0 \qquad (3\text{-}25)$$

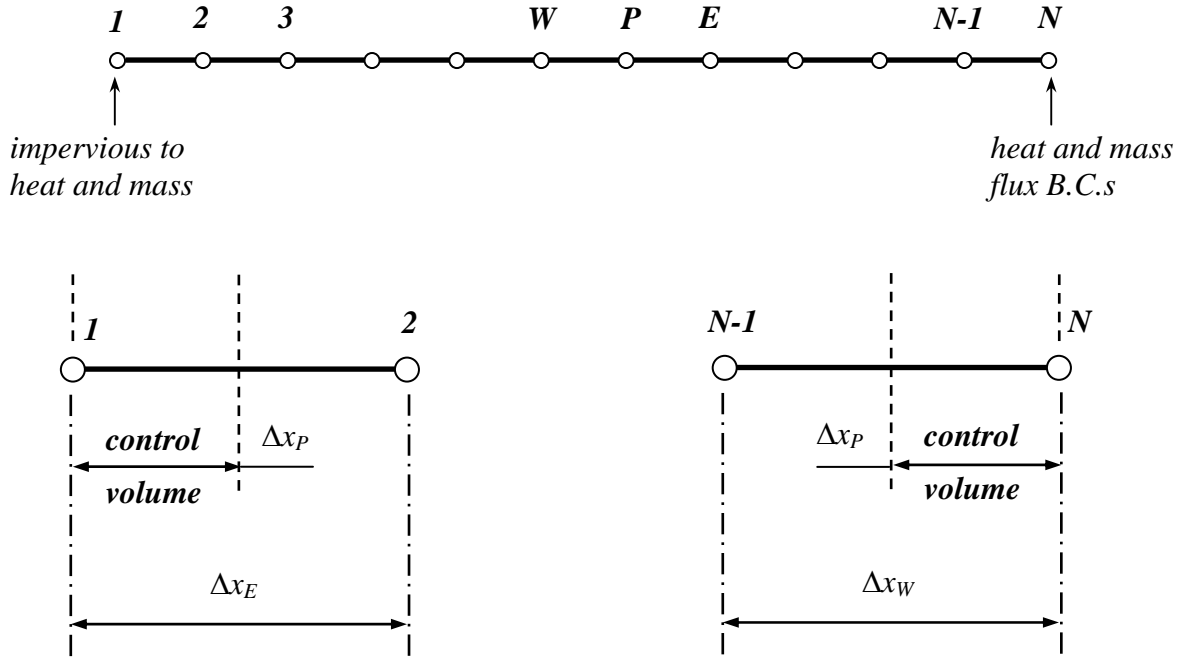where $(J_w)_{A_E}^{t+\Delta t}$ can be computed as above and $(J_w)_1^{t+\Delta t}$ is set to zero.

Figure 3.2 Boundary elements.

For the Nth element, we get

$$\frac{\Delta x_w}{2\Delta t}\left[\left(\varepsilon_s\rho_s X + \varepsilon_g\rho_v\right)_N^{t+\Delta t} - \left(\varepsilon_s\rho_s X + \varepsilon_g\rho_v\right)_N^t\right] + \left[\left(J_w\right)_N^{t+\Delta t} - \left(J_w\right)_{A_W}^{t+\Delta t}\right] = 0 \qquad (3\text{-}26)$$

with an internal surface A_W and an external boundary condition given by Eq. (3-6)

$$\left(J_w\right)_N^{t+\Delta t} = \beta\frac{\left(P_g\right)_N^{t+\Delta t}\tilde{M}_v}{\tilde{R}T_N^{t+\Delta t}}\ln\left[\frac{\left(P_g\right)_N^{t+\Delta t} - P_{v,\infty}}{\left(P_g\right)_N^{t+\Delta t} - \left(P_v\right)_N^{t+\Delta t}}\right] \qquad (3\text{-}27)$$

3.4. Discretization of the conservation equation of air

The conservation equation of air is somewhat simpler than that of water. By following the same discretization procedure as in the last section, we get for internal volume elements

$$\frac{(\Delta x_W + \Delta x_E)}{2\Delta t}\left[(\bar{\rho}_a)_P^{t+\Delta t} - (\bar{\rho}_a)_P^t\right] + \left[(J_a)_{A_E}^{t+\Delta t} - (J_a)_{A_W}^{t+\Delta t}\right] =$$

$$\frac{(\Delta x_W + \Delta x_E)}{2\Delta t}\left[(\bar{\rho}_a)_P^{t+\Delta t} - (\bar{\rho}_a)_P^t\right] +$$

$$+ \left[\left(\rho_a \frac{K \cdot k_g}{\eta_g}\right)_{A_E}^{t+\Delta t} \frac{(P_g)_E^{t+\Delta t} - (P_g)_P^{t+\Delta t}}{\Delta x_E} + (\rho_g D_{eff})_{A_E}^{t+\Delta t} \frac{(y_a)_E^{t+\Delta t} - (y_a)_P^{t+\Delta t}}{\Delta x_E}\right]$$

$$- \left[\left(\rho_a \frac{K \cdot k_g}{\eta_g}\right)_{A_W}^{t+\Delta t} \frac{(P_g)_E^{t+\Delta t} - (P_g)_P^{t+\Delta t}}{\Delta x_W} + (\rho_g D_{eff})_{A_W}^{t+\Delta t} \frac{(y_a)_E^{t+\Delta t} - (y_a)_P^{t+\Delta t}}{\Delta x_W}\right] = 0$$

(3-28)

where

$$y_a = \frac{\rho_a}{\rho_g} = \frac{\bar{\rho}_a}{\varepsilon_g \rho_g} = \frac{\bar{\rho}_a}{\varepsilon_g \left(\dfrac{\bar{\rho}_a}{\varepsilon_g} + \dfrac{P_v \tilde{M}_v}{\tilde{R}T}\right)}$$

(3-29)

For the first boundary element (1) we have

$$\frac{\Delta x_E}{2\Delta t}\left[(\bar{\rho}_a)_1^{t+\Delta t} - (\bar{\rho}_a)_1^t\right] + (J_a)_{A_E}^{t+\Delta t} = 0$$

(3-30)

However, for the boundary element (*N*), which is in contact with the drying air, the conservation of air is no more of use. The reason is that at the external drying surface the flux of air is controlled by the pressure of the drying air. Here instead of using the conservation equation (3-2), we have to consider the condition (3-8), which can be transformed into a more suitable form making use of the main variable $\bar{\rho}_a$ (Perré and Turner, 1999 [71])

$$\varepsilon_g(P_v - P_\infty) + \frac{\bar{\rho}_a \tilde{R}T}{\tilde{M}_a} = 0$$

(3-31)

and we get the discrete form

$$\left(\varepsilon_g\right)_N^{t+\Delta t}\left[(P_v)_N^{t+\Delta t} - P_\infty\right] + \frac{(\bar{\rho}_a)_N^{t+\Delta t} \tilde{R}T_N^{t+\Delta t}}{\tilde{M}_a} = 0$$

(3-32)

3.5. Discretization of the conservation equation of energy

The conservation equation of energy (3-3) is discretized in a similar way as that of water. By following the development in section 3.3, Eq. (3-3) is rewritten as

$$\frac{\partial}{\partial t}\Psi - \nabla J_e = 0$$

(3-33)

where Ψ is defined by

$$\Psi = \left(\varepsilon_s \rho_s h_s + \varepsilon_w \rho_w h_w + \varepsilon_g \rho_v h_v + \varepsilon_g \rho_a h_a\right)$$

(3-34)

and

$$J_e = \rho_g h_a D_{eff} \cdot \nabla y_a + \rho_g h_v D_{eff} \cdot \nabla y_v + \lambda_{eff} \nabla T$$
$$- \left[\rho_w h_w \frac{K \cdot k_w}{\eta_w} \cdot \nabla P_w + (\rho_v h_v + \rho_a h_a) \frac{K \cdot k_g}{\eta_g} \cdot \nabla P_g \right] \tag{3-35}$$

Consequently, the discretized conservation equation of energy for a normal control volume element becomes

$$\frac{\Delta x_W + \Delta x_E}{2\Delta t} \left(\Psi_P^{t+\Delta t} - \Psi_P^t \right) + \left[(J_e)_{A_E}^{t+\Delta t} - (J_e)_{A_W}^{t+\Delta t} \right] = 0 \tag{3-36}$$

For element 1, which is a boundary element impervious to heat transfer, we have

$$\frac{\Delta x_E}{2\Delta t} \left(\Psi_1^{t+\Delta t} - \Psi_1^t \right) + (J_e)_{A_E}^{t+\Delta t} = 0 \tag{3-37}$$

and for element N at the boundary open to drying air we get (using Eq. (3-7))

$$\frac{\Delta x_E}{2\Delta t} \left(\Psi_N^{t+\Delta t} - \Psi_N^t \right) + \left[(J_e)_N^{t+\Delta t} - (J_e)_{A_W}^{t+\Delta t} \right] = 0 \tag{3-38}$$

with

$$(J_e)_N^{t+\Delta t} = \alpha \left(T_N^{t+\Delta t} - T_\infty \right) + (\Delta h_v)_N^{t+\Delta t} \beta \frac{(P_g)_N^{t+\Delta t} \tilde{M}_v}{\tilde{R} T_N^{t+\Delta t}} \ln \left[\frac{(P_g)_N^{t+\Delta t} - P_{v,\infty}}{(P_g)_N^{t+\Delta t} - (P_v)_N^{t+\Delta t}} \right] \tag{3-39}$$

Note that when the heat capacity is given in the form (see Eq. (2-55))

$$\overline{\rho C_p} = \langle \rho \rangle C_p = \varepsilon_s \rho_s c_s + \varepsilon_w \rho_w c_w + \varepsilon_g \rho_v c_v + \varepsilon_g \rho_a c_a \tag{3-40}$$

the expression (3-34) should be rewritten as

$$\Psi = \left(\varepsilon_s \rho_s c_s + \varepsilon_w \rho_w c_w + \varepsilon_g \rho_v c_v + \varepsilon_g \rho_a c_a \right)(T - T_R) + \varepsilon_g \rho_v \Delta h_{v0}$$
$$= \overline{\rho C_p}(T - T_R) + \varepsilon_g \rho_v \Delta h_{v0} \tag{3-41}$$

where Δh_{v0} is the vaporization enthalpy at T_R (see Appendix 1).

3.6. Discretization for problems with spherical symmetry

In drying analysis, the porous medium to be dried may be a particle of spherical shape. If, additionally, the drying conditions can be considered as spherically symmetric, the above one-dimensional discretization can be adapted to avoid the use of costly three-dimensional simulations with complicated meshes and large number of unknowns.

Figure 3.3 illustrates the shell-shape volume elements (only part of the shells is shown with the spherical interface S_W and S_E). We only consider the general conservation equation

$$\frac{\partial}{\partial t} U - \nabla \cdot \mathbf{J} = 0 \tag{3-42}$$

to show how the discretization is done in this case.

By integrating Eq. (3-42) over a control volume element and over time and by using the divergence theorem

$$\int\limits_{\Delta V_P} \nabla \cdot \mathbf{J} dV = \int\limits_{S_W \cup S_E} \mathbf{J} \cdot \mathbf{n} dA \tag{3-43}$$

we get

$$\frac{\Delta V_P}{\Delta t}\left(U_P^{t+\Delta t} - U_P^t\right) - \left(S_E J_{S_E} - S_W J_{S_W}\right) = 0 \tag{3-44}$$

where ΔV_P is the volume of the element, S_E and S_W are the areas of the two faces indicated in Figure 3.3.

The gradients needed to evaluate the flux $\mathbf{J}$ are still computed in the same way as for the one-dimensional geometry presented in the last section. Only the weighting by (shell) volumes and (spherical) interfaces now plays an important role.
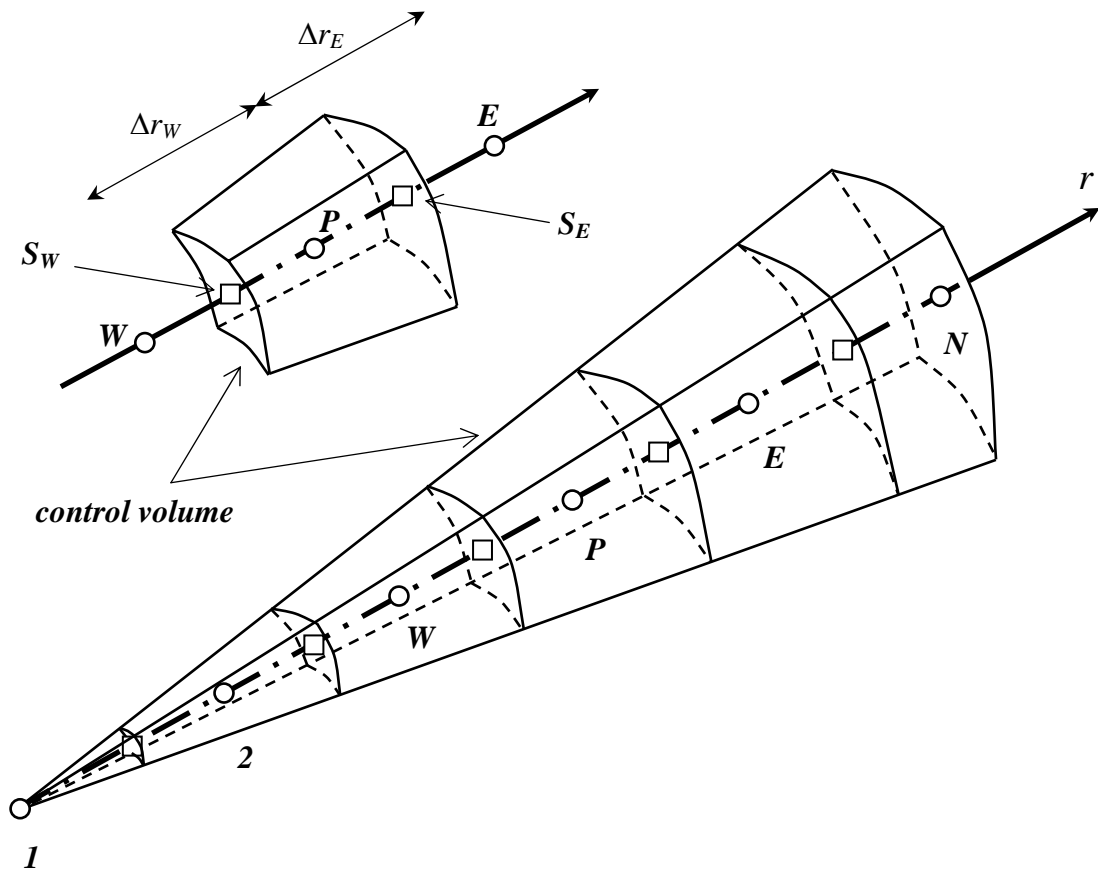
Figure 3.3 Control volume mesh (bottom) and control volume element (top) for drying problems with spherical symmetry.

3.7. Numerical procedure for solving the discretized equations

The above discretization of the conservation equations of water, air and energy leads to a nonlinear system of equations with unknown $\mathbf{q}^{t+\Delta t}$ as follows

$$F_i\left(\mathbf{q}^{t+\Delta t}, \mathbf{q}^t, \Delta t\right) = 0 \qquad i = 1, ..., N \tag{3-45}$$

or in matrix form

$$\mathbf{F}\left(\mathbf{q}^{t+\Delta t}, \mathbf{q}^t, \Delta t\right) = \mathbf{0} \tag{3-46}$$

where

$$\mathbf{q}^t = \left\{ \begin{array}{c} X_1 \\ T_1 \\ (\overline{\rho}_a)_1 \\ ... \\ X_N \\ T_N \\ (\overline{\rho}_a)_N \end{array} \right\}^t \qquad\qquad \mathbf{q}^{t+\Delta t} = \left\{ \begin{array}{c} X_1 \\ T_1 \\ (\overline{\rho}_a)_1 \\ ... \\ X_N \\ T_N \\ (\overline{\rho}_a)_N \end{array} \right\}^{t+\Delta t} \tag{3-47}$$

To solve this system of equations, we use the Newton-Raphson method. The basic idea of this method comes from the Taylor expansion of $\mathbf{F}$ around the current value of $\mathbf{q}^{t+\Delta t}$

$$\mathbf{F}\left(\mathbf{q}^{t+\Delta t} + \delta\mathbf{q}, \mathbf{q}^t, \Delta t\right) = \mathbf{F}\left(\mathbf{q}^{t+\Delta t}, \mathbf{q}^t, \Delta t\right) + \left(\frac{\partial\mathbf{F}}{\partial\mathbf{q}^{t+\Delta t}}\right) \cdot \delta\mathbf{q} + O\left(\delta\mathbf{q}^2\right) \tag{3-48}$$

where $\left(\dfrac{\partial\mathbf{F}}{\partial\mathbf{q}^{t+\Delta t}}\right)_{ij} = \dfrac{\partial F_i}{\partial q_j^{t+\Delta t}}$ is the Jacobian matrix of $\mathbf{F}$.

By neglecting the terms of order $\delta\mathbf{q}^2$ and higher and by setting $\mathbf{F}\left(\mathbf{q}^{t+\Delta t} + \delta\mathbf{q}, \mathbf{q}^t, \Delta t\right) = \mathbf{0}$ we get a set of linear equations for the correction $\delta\mathbf{q}$ that move each component of $\mathbf{F}$ closer to zero

$$\left(\frac{\partial\mathbf{F}}{\partial\mathbf{q}^{t+\Delta t}}\right) \cdot \delta\mathbf{q} = -\mathbf{F}\left(\mathbf{q}^{t+\Delta t}, \mathbf{q}^t, \Delta t\right) \tag{3-49}$$

The correction $\delta\mathbf{q}$ is then added to the solution vector

$$\mathbf{q}_{new}^{t+\Delta t} = \mathbf{q}_{old}^{t+\Delta t} + \delta\mathbf{q} \tag{3-50}$$

and the process is iterated until convergence is reached.

For more details about the Newton-Raphson method, we refer to Press (1992 [82]). The main steps in our computational procedure are outlined hereafter.

Initial step: Set the drying time $\tau_{drying} = 0$, set the total drying time τ_{total}, set an initial value for Δt, set the tolerance *tol* for convergence and set the main variables to their initial values: $\mathbf{q}^0 = \left[X_1^0, T_1^0, (\overline{\rho}_a)_1^0, X_2^0, T_2^0, (\overline{\rho}_a)_2^0, \ldots, X_N^0, T_N^0, (\overline{\rho}_a)_N^0 \right]^T$

Begin outer loop: while $\tau_{drying} < \tau_{total}$ do

Set: $\hat{\mathbf{q}}^{t+\Delta t} = \mathbf{q}^t$

Begin inner loop: while $\left\| \mathbf{F}\left(\hat{\mathbf{q}}^{t+\Delta t}, \mathbf{q}^t, \Delta t\right) \right\| > tol$ do

Step 1. Compute $\mathbf{F} = \mathbf{F}\left(\hat{\mathbf{q}}^{t+\Delta t}, \mathbf{q}^t, \Delta t\right)$ with the help of the discretization formulae presented in section 3.3÷3.6

Step 2. Compute the correction: $\delta\mathbf{q} = -\left(\dfrac{\partial \mathbf{F}}{\partial \hat{\mathbf{q}}^{t+\Delta t}}\right)^{-1} \cdot \mathbf{F}$

Step 3. Solve the line search problem:

Find λ_{step} such that : $\left\| \mathbf{F}\left(\hat{\mathbf{q}}^{t+\Delta t} + \lambda_{step}\delta\mathbf{q}, \mathbf{q}^t, \Delta t\right) \right\| < \left\| \mathbf{F}\left(\hat{\mathbf{q}}^{t+\Delta t}, \mathbf{q}^t, \Delta t\right) \right\|$

where the symbol $\|\cdot\|$ denotes the norm of vector: $\|\mathbf{F}\| = \sqrt{\mathbf{F}^T \cdot \mathbf{F}}$. If no solution is found, reduce Δt, set $\hat{\mathbf{q}}^{t+\Delta t} = \mathbf{q}^t$ and go to *Step 1*.

Step 4. Update variables: $\hat{\mathbf{q}}^{t+\Delta t} = \hat{\mathbf{q}}^{t+\Delta t} + \lambda_{step}\delta\mathbf{q}$

End inner loop

Set: $\tau_{drying} = \tau_{drying} + \Delta t$ and $\mathbf{q}^{t+\Delta t} = \hat{\mathbf{q}}^{t+\Delta t}$

End outer loop

Print out results

In the above procedure, at each iteration of the outer loop, the value of $\mathbf{q}^t$ is known and the task is to find $\mathbf{q}^{t+\Delta t}$ that satisfies (3-46). This task is fulfilled by the inner loop. The inner loop starts with the guessed value $\hat{\mathbf{q}}^{t+\Delta t} = \mathbf{q}^t$. During the course of the inner loop, the value of $\hat{\mathbf{q}}^{t+\Delta t}$ is updated according to the correction $\delta\mathbf{q}$ until $\hat{\mathbf{q}}^{t+\Delta t}$ satisfies (3-46). Note that the derivative $\dfrac{\partial F_i}{\partial q_j}$ is computed using the finite difference formula:

$$\frac{\partial F_i}{\partial q_j} = \frac{F_i(\mathbf{q} + \Delta\mathbf{q}) - F_i(\mathbf{q})}{\Delta q_j} \tag{3-51}$$

in which all the components of the vector $\Delta\mathbf{q}$ are set to zero except that the jth component is set to Δq_j. Theoretically, Δq_j needs to be small enough compared with

q_j. In our calculations, it is observed that $\Delta q_j = 10^{-7} \div 10^{-8}$ always leads to good convergence.

To summarize, in this chapter the control volume method is applied to discretize the governing equations of drying established in the last chapter. Besides the one-dimensional discretization, problems with spherical symmetry are also considered. As result, a nonlinear system of equations is obtained with unknowns as state variables at gird nodes. The Newton-Raphson method is used to solve the resulting equations. In the next chapter the numerical method described here will be applied in the analysis of different drying problems.

Chapter 4

NUMERICAL RESULTS

4.1. Introduction

In this chapter, numerical results of the drying simulation of porous media are presented. In the first part of the chapter, the drying of a material with well-known properties is considered. Evidently, it would be interesting to numerically investigate the drying behaviour of γ-Al$_2$O$_3$ particles since experimental works are realized with this material. Unfortunately, due to the fact that γ-Al$_2$O$_3$ particles have nano pores and due to the lack of material properties, the numerical investigation of γ-Al$_2$O$_3$ will only be reported in a future work. Instead, light concrete is chosen as a reference material because the material properties are available in literature (Perré and Turner, 1999 [71]). This reference material is used to understand the influence of parameters such as the geometry and material characteristics on drying kinetics. Firstly, the accuracy of the numerical simulations is checked by considering the accuracy of water and air flows. The influence of the space discretization on numerical results is also examined. Then, two geometrical configurations are studied: in the first, we consider the drying of a sphere of similar size as the γ-Al$_2$O$_3$ particles used in our experimental works; in the second, we examine the drying behaviour of a plate whose thickness is equal to the diameter of the sphere. The effect of geometric shape can then be investigated by comparing the drying kinetics of the two configurations.

By numerically varying the material properties, a parametric study is realized to see how the three transport parameters (effective diffusivity, absolute permeability and effective thermal conductivity) influence the drying processes. Similarly, the influence of drying conditions such as the state of the drying air (relative humidity, temperature) and transfer coefficients as well as the initial condition of the sample (initial moisture content) is investigated. In addition, the effect of sample size is considered by varying the thickness (of the plate) or the radius (of the sphere). The results are compared with a simple diffusion model and a receding front model for the case of isothermal drying.

In the second part of the chapter, the influence of the pore size distribution on the drying behaviour of porous materials is considered by applying the capillary model presented in Chapter 2 to calculate the material properties (capillary pressure, absolute and the relative permeabilities). The results are obtained for mono- and bimodal pore size distributions. A study is realized on the influence of the parameters of these distributions. When the capillary model is employed, the influence of other factors such as drying conditions and other material properties is also studied. Finally, the numerical

results obtained here are compared with the numerical simulations obtained by one-dimensional capillary model proposed by Metzger and Tsotsas (2005 [55]) and two-dimensional network model proposed by Irawan *et al.* (2006 [30]).

4.2. The geometric progression mesh

In drying simulations, both equidistant and non-equidistant meshes can be used. However with the same number of grid nodes (the same number of control volume elements), a non-equidistant mesh may be a better option. With a non-equidistant mesh, the mesh can be refined at places where large changes are expected to happen. In general, near the external exchange surface a fine mesh is needed to account for large gradients in the state variables.

In our calculations, the meshes are built so that the distance between two consecutive grid nodes is gradually decreased from the centre of the sample (first node) to its exchange surface (last node) in a geometric progression way. If we define the mesh ratio m_{ratio} (≤ 1) as the ratio of the distances between the last two nodes and the first two ones

$$m_{ratio} = \frac{x_N - x_{N-1}}{x_2 - x_1} \tag{4-1}$$

then the position of node *i* is given by

$$x_i = x_1 + \frac{m^{i-1} - 1}{m - 1} \Delta x \tag{4-2}$$

where

$$m = \left(m_{ratio}\right)^{\frac{1}{N-2}} \tag{4-3}$$

$$h = \frac{m^{N-1} - 1}{m - 1} \tag{4-4}$$

$$\Delta x = \frac{x_N - x_1}{h} \tag{4-5}$$

Note that in our analysis, the size of the sample is the distance from the impermeable side to the external exchange surface.

4.3. Definition of total drying time

For the determination of the total drying time τ_{dry}, the average moisture content X_{av} and the equilibrium moisture content X_{eq} are needed. The average moisture content X_{av} is computed as follows

$$X_{av} = \frac{1}{V_{total}} \sum_{i=1}^{N} X_i \cdot V_i \tag{4-6}$$

where V_{total} is the total volume of the sample, X_i and V_i are moisture content and volume of element i, respectively. The equilibrium moisture content X_{eq} is unique for a given drying condition and can be obtained from sorption isotherm.

The drying process is considered to be completely finished when the moisture content everywhere in the sample reaches the value X_{eq}. This condition can be considered as satisfied when the average moisture content X_{av} reaches the value of X_{eq}. However, if this condition is satisfied, the drying time may become infinite. Therefore, for convenience, in our analysis the drying is considered as complete when $X_{av}=X_{eq}+\varepsilon_{eq}$, where ε_{eq} is a small positive number. The total drying time of the process is defined by taking the corresponding drying time τ_{dry} at this average value X_{av}.

4.4. Drying simulation of a reference material: light concrete

4.4.1. *Material properties*

The material properties of light concrete used in this part are given by Perré and Turner (1999 [71]) with porosity $\psi = 0.8$, solid density $\rho_s = 2500\,\text{kg.m}^{-3}$ and heat capacity $\overline{\rho C_p} = \varepsilon_s \rho_s \left(840 + 4185X\right)\,\text{J.kg}^{-1}.\text{K}^{-1}$. The fully saturated material has its moisture content $X_{sat} = 1.6$.

The sorption isotherm is

$$\varphi(X,T) = \frac{P_v}{P_v^*(T)} = \begin{cases} 1 & , \ \text{if } X > X_{irr} \\ \dfrac{X}{X_{irr}}\left(2 - \dfrac{X}{X_{irr}}\right), & \text{if } X \le X_{irr} \end{cases} \tag{4-7}$$

where $X_{irr} = 0.07$ is the irreducible moisture content. The saturation vapour pressure $P_v^*(T)$ is given by Antonie's equation (see Eq.(A1-9) – Appendix 1).

The capillary pressure is computed from

$$P_c = 40 \cdot \sigma(T) \cdot e^{\left(8.4057 \times 10^{-0.3476 X_{fw}}\right)} \tag{4-8}$$

where the surface tension σ is a function of temperature (Eq. (A1-4) – Appendix 1) and X_{fw} is the moisture content of free water: $X_{fw} = X - X_{irr}$.

The absolute permeability is taken as constant: $K = 2 \times 10^{-13}\,\text{m}^2$.

The relative permeabilites for liquid k_w and for gas k_g phases are calculated from the following relationship

$$k_w = \begin{cases} 0 & X > X_{irr} \\ \left(S_{fw}\right)^3 & X \leq X_{irr} \end{cases} \tag{4-9}$$

$$k_g = \begin{cases} 1 & X > X_{irr} \\ 1 + \left(2S_{fw} - 3\right)\left(S_{fw}\right)^2 & X \leq X_{irr} \end{cases} \tag{4-10}$$

The effective diffusivity is calculated from

$$D_{eff} = 0.2 \cdot \delta_{va} \cdot k_g \tag{4-11}$$

where δ_{va} is the binary diffusivity of vapour in air (Eq. (A1-13) – Appendix 1) and k_g is the relative permeability of gas.

The effective thermal conductivity has contributions of both solid and liquid (the contribution of gas is neglected). It is computed as

$$\lambda_{eff} = \left(0.142 + 0.46X\right) \text{ W.m}^{-1}.\text{K}^{-1} \tag{4-12}$$

4.4.2. Verification of the numerical results (cross check)

The accuracy of the numerical simulations presented below can be checked by comparing the total change of moisture content with the integral of the evaporation flow rate. A similar check can be done for air.

4.4.2.1 Accuracy of water flow (ε_w^{err})

There are two ways to calculate the amount of water, which has been removed after the drying process is finished. On the one hand, this amount of water can be calculated by

$$\left(\Delta M_w\right)_1 = \left[\left(X_{av}\right)_{start} - \left(X_{av}\right)_{end}\right] \cdot \rho_0 \cdot V_{total} \tag{4-13}$$

where ρ_0 is the density of the solid matrix, V_{total} is the total volume of the sample, $\left(X_{av}\right)_{start}$ and $\left(X_{av}\right)_{end}$ are the average moisture contents at the beginning and at the end of the drying process. On the other hand, ΔM_w can be calculated by integrating the vapour flow of out of porous medium at the external boundary $\left(J_w\right)_N$

$$\left(\Delta M_w\right)_2 = \int_0^{\tau_n} \left(J_w\right)_N \tag{4-14}$$

where τ_n is the drying time at the end of the simulation process. The comparison of these two values $\left(\Delta M_w\right)_1$ and $\left(\Delta M_w\right)_2$ gives us the accuracy of the computed water flow: $\varepsilon_w^{err} = \left|\left(\Delta M_w\right)_1 - \left(\Delta M_w\right)_2\right| / \left(\Delta M_w\right)_1$, which can be found in Appendix 2 for various sample radii and drying conditions. It is observed that the maximum error is 3.8%, and the typical error is less than 0.3 %.

4.4.2.2 Accuracy of air flow (ε_a^{err})

The accuracy of air flow can be estimated by comparing the total mass of air that flows into the sample and the difference between the total mass of air inside the sample at the end and at the beginning of the drying process.

The total mass of air that flows into the porous medium during drying can be computed by considering the control volume element at the external exchange surface. The inward air flux into this element is the air flux into the porous medium. This inward air flux can be computed by the difference between the change of air content in this element and the outward flux from this element, its integral yields

$$\left(\Delta M_a\right)_1 = \int_0^{\tau_n} \left(\frac{V_N \cdot \Delta\left(\overline{\rho}_a\right)_N}{\Delta t} - \left(J_a\right)_{A_W} \cdot A_W \right) dt \tag{4-15}$$

where $\Delta\left(\overline{\rho}_a\right)_N$ is the change of the average air density of the boundary element during time step Δt, V_N the volume of the element at the exchange surface, A_W the surface area of the west face of this element and $\left(J_a\right)_{A_W}$ is the air flux from this element into the next one.

The difference between the total mass of air at the end and at the beginning of the drying process is

$$\left(\Delta M_a\right)_2 = \left[\sum_{i=1}^N \left(\overline{\rho}_a\right)_i \cdot V_i \right]^{end} - \left[\sum_{i=1}^N \left(\overline{\rho}_a\right)_i \cdot V_i \right]^{start} \tag{4-16}$$

where $\left(\overline{\rho}_a\right)_i$ and V_i are the average air density and the volume of element i, respectively.

By comparing the two values $\left(\Delta M_a\right)_1$ and $\left(\Delta M_a\right)_2$ given by the equations (4-15) and (4-16), the accuracy of air flow can be computed as: $\varepsilon_a^{err} = \left|\left(\Delta M_a\right)_1 - \left(\Delta M_a\right)_2\right| / \left(\Delta M_a\right)_1$. The accuracy of air flow is reported in Appendix 2 for various sample radii and drying conditions. Similar to the estimation of ε_w, the maximum error is 5.5 % and the typical error is less than 0.3 %.

4.4.3. Influence of space discretization

In this section we examine how the space discretization (the number of gird nodes of the mesh and the way these nodes are distributed) influences the simulation results.

4.4.3.1. Influence of number of nodes (elements)

Firstly, the influence of the space discretization is investigated by changing the number of grid nodes (or elements) used in the control volume mesh for the same sample size. The mesh ratio is set to $m_{ratio} = 0.2$. The results are introduced in Figure 4.1 for a sphere sample with radius $R = 2.5$ mm. All drying conditions are taken as in the reference case presented below (see Section 4.4.4).

Theoretically, the finer the mesh (larger number of grid nodes is used), the more accurate the numerical results. It is observed that the number of the grid nodes has strong effect on the second drying period. If the used mesh is coarse (for example 5 elements, the blue solid curve in Figure 4.1), large errors appear. It is evident that to account for sudden changes in the state variables (X, T and P), especially near the exchange surface where the gradients of these state variables are considerable, fine meshes are required. With a coarse mesh those strong gradients cannot be modelled correctly and the accumulated error will lead to incorrect drying rate curves. From Figure 4.1, it is observed that for our considered case, the mesh with $N = 51$ grid nodes seems to be suitable since larger N increases the computational time without significant gain in precision**.**
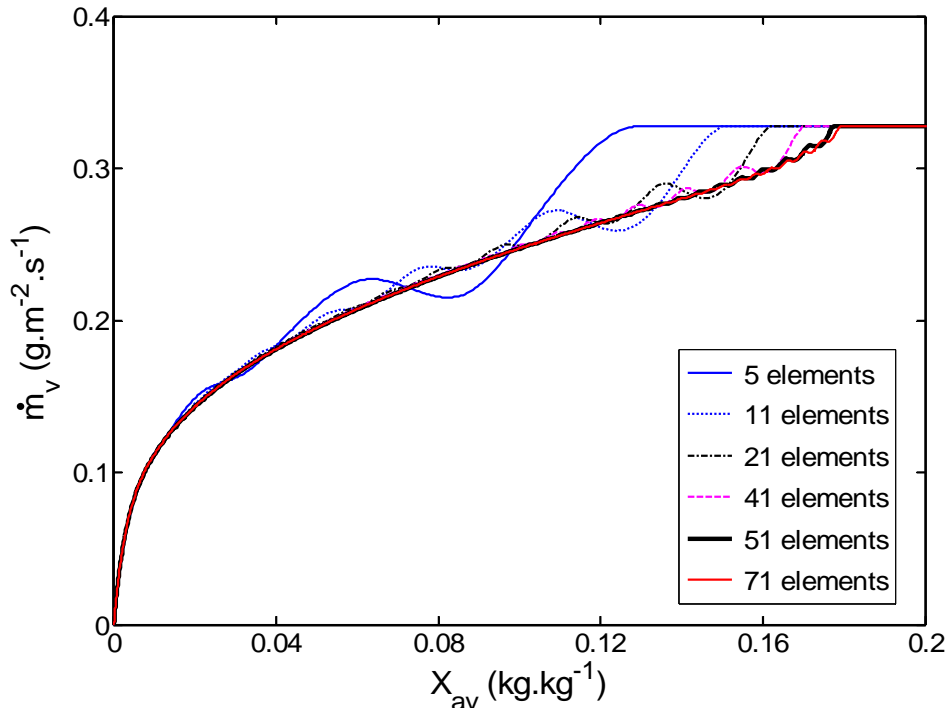
Figure 4.1 Influence of space discretization: drying rate curves for different number of elements ($T_\infty = 80^\circ$C and $\varphi = 0$).

4.4.3.2. *Influence of mesh ratio*

In this section, the influence of the mesh ratio m_{ratio} is considered. Numerical simulations are realized for a mesh of 51 grid nodes with different values of the mesh ratio m_{ratio}. All drying conditions are applied as in the reference case. The volume distributions of the elements are presented in Figure 4.2. The evaporation rates at the end of the simulations are plotted in Figure 4.3. In these figures, the dashed blue curve stands for the simulation results by using an equidistant mesh ($m_{ratio} = 1$). It can be seen that the drying rate curve is smoother with smaller mesh ratios (finer mesh at the exchange surface). If the mesh ratio is large, not only the large gradients are modelled with lower precision, but the duration of the first drying period is also overestimated. This is due to the fact the moisture content of the element at the exchange surface must reach the irreducible moisture content X_{irr} before the second drying period commences.

With a large mesh ratio, this element has large volume and it takes more time to reach X_{irr}.
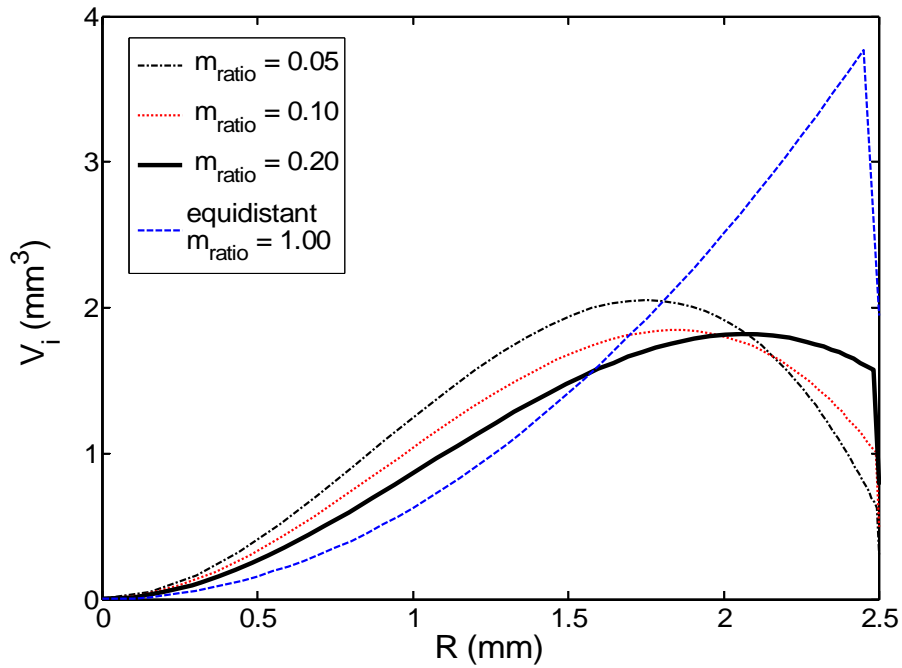
Figure 4.2 Distribution of volumes of elements for different mesh ratios.
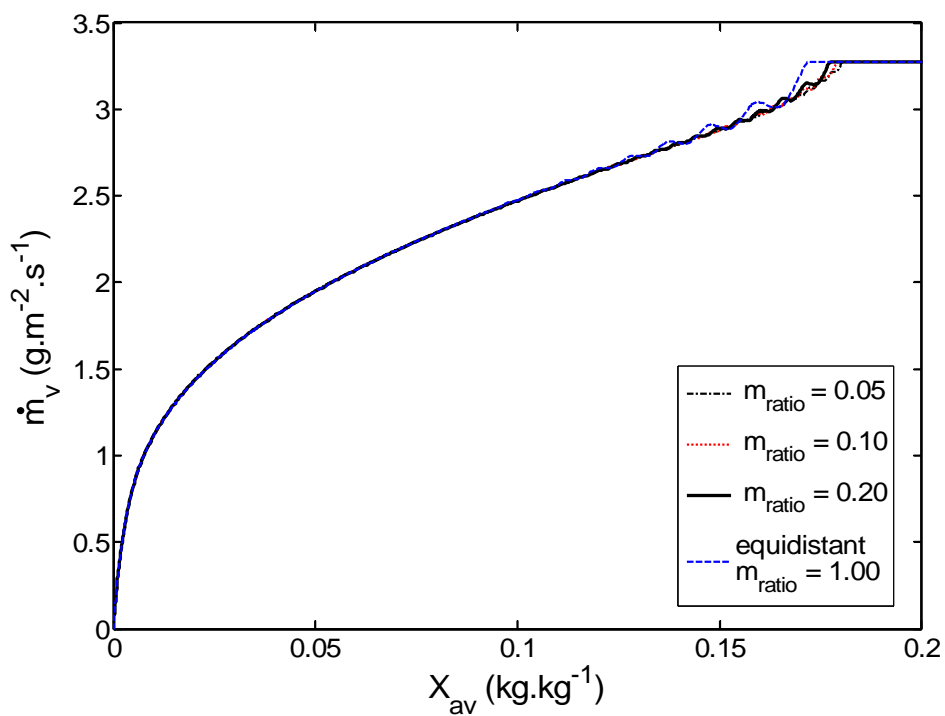
Figure 4.3 Influence of space disretization: drying rate curves for different mesh ratios
($T_\infty = 80^{\circ}$C and $\varphi = 0$).

4.4.4. *Drying simulation for a sphere*

We examine here the drying of a sphere of light concrete with radius $R = 2.5$ mm. For the comparison purpose, the drying simulation in this section is considered as the reference case. The mesh used in our simulation contains 51 nodes. The mesh ratio m_{ratio} is set to 0.2. We use $\varepsilon_{eq} = 10^{-17}$ in determining the total drying time (see Section 4.3). The initial temperature of the sample is $T_0 = 20^o$C, the initial moisture content is $X_0 = 1$ (investigation of the influence of the initial moisture content will be discussed in Section 4.4.9 below) and the initial pressure is $P_0 = 1$ bar for the whole sample. The boundary conditions applied to the sample are considered as symmetric. Therefore the drying problem of the sphere can be solved by the control volume method in one dimension. The heat transfer coefficient is $\alpha = 14.25$ W.m^{-2}.K^{-1} and mass transfer coefficient is $\beta = 0.015$ m.s^{-1}. The drying air has vapour pressure of $P_{v,\infty} = 0$ and temperature $T_\infty = 80^o$C.

The temporal evolution of moisture, temperature and pressure for approximately every 0.5 mm in distance (corresponding to nodes 1, 6, 13, 21, 33 and 51 from the centre to the surface) is shown in Figure 4.4 to Figure 4.6. In Figure 4.4, the dashed curve presents the average moisture content.

The profiles of moisture, temperature and pressure of the sample at different drying time are presented in Figure 4.7 to Figure 4.9. The moisture profiles are plotted at the times when the average moisture content X_{av} has the values 0.3, 0.2, 0.1, 0.07 and 0.04 which correspond to the drying time of 15.0, 17.1, 19.5, 20.4 and 21.4 min. Two more profiles are shown for each variable (moisture, temperature and pressure) at two characteristic times in the drying process. The first profile is at the end of the first drying period when the moisture content at the exchange surface drops below the irreducible moisture content (and no more free water is left at the surface), which corresponds to the critical moisture content $X_{cr} = 0.1774$ and the drying time $\tau = 17.6$ min. The second is at the time when all free water has been removed from the sample, which corresponds to $\tau = 23.1$ min.
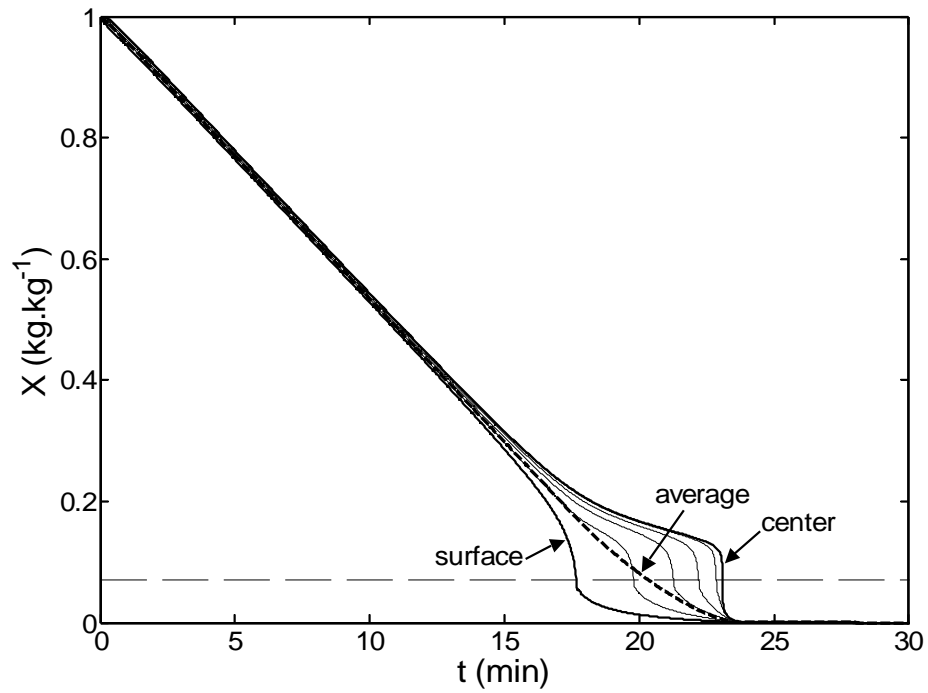
Figure 4.4 Drying of a sphere of light concrete: temporal evolution of moisture content for approximately every 0.5 mm in distance ($T_\infty = 80^\circ$C and $\varphi = 0$).
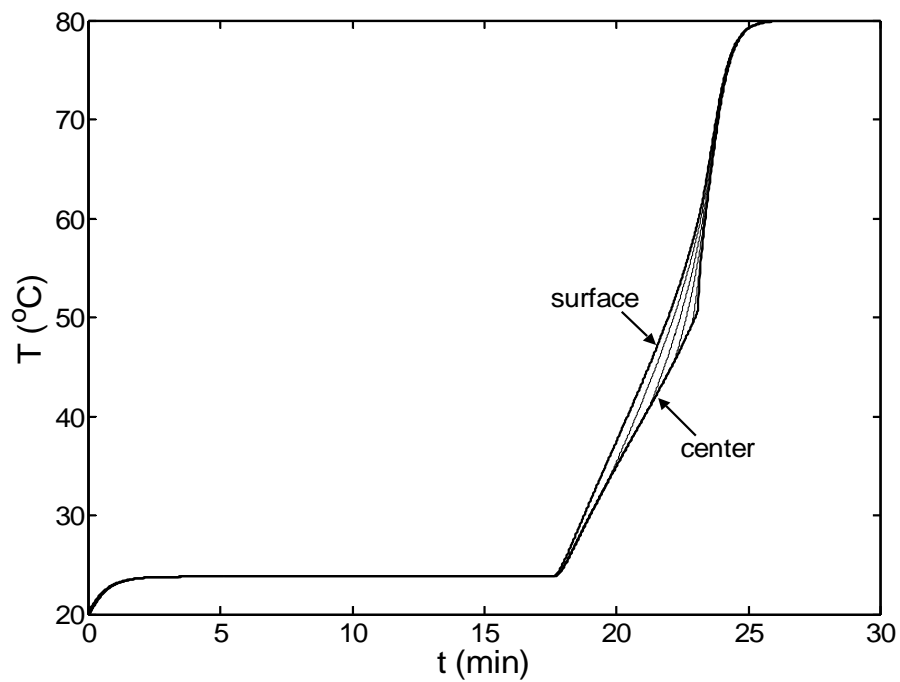
Figure 4.5 Drying of a sphere of light concrete: temporal evolution of temperature for approximately every 0.5 mm in distance ($T_\infty = 80^\circ$C and $\varphi = 0$).
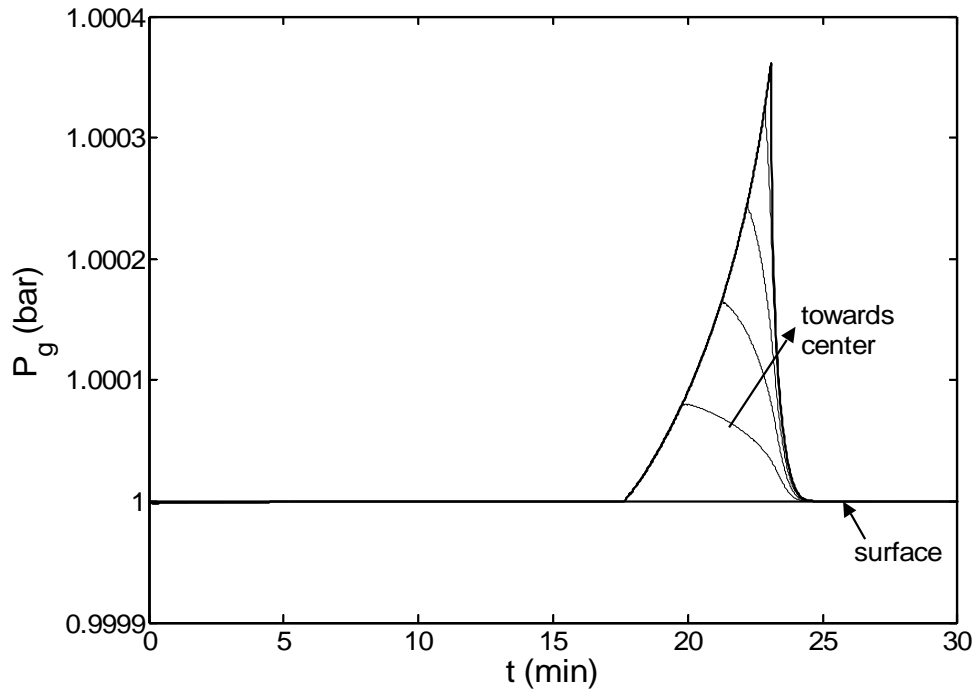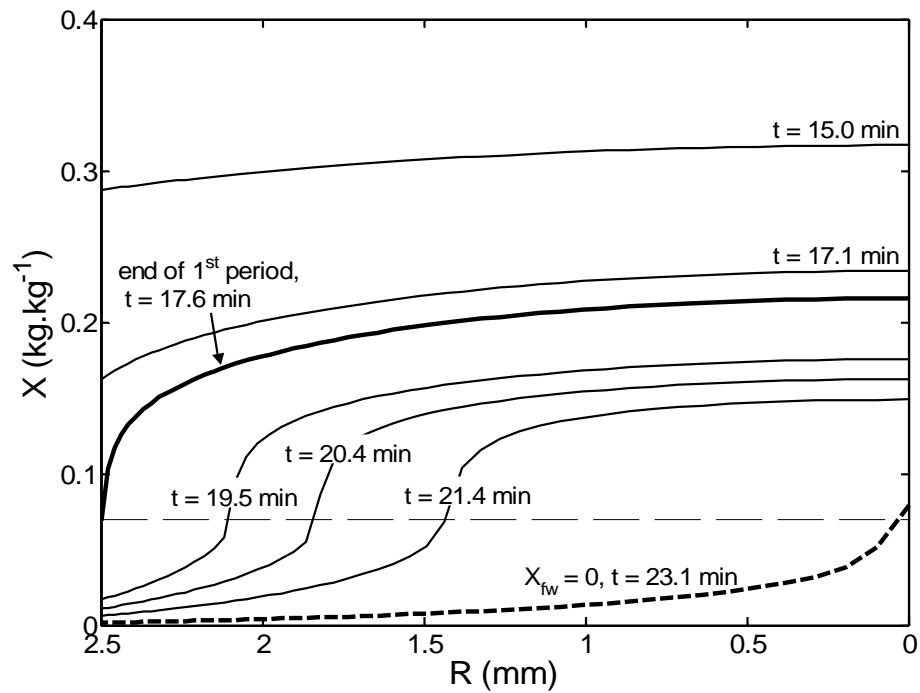
Figure 4.6 Drying of a sphere of light concrete: temporal evolution of pressure for approximately every 0.5 mm in distance ($T_\infty = 80^{\circ}$C and $\varphi = 0$).

Figure 4.7 Drying of a sphere of light concrete: moisture profiles ($T_\infty = 80^{\circ}$C and $\varphi = 0$).
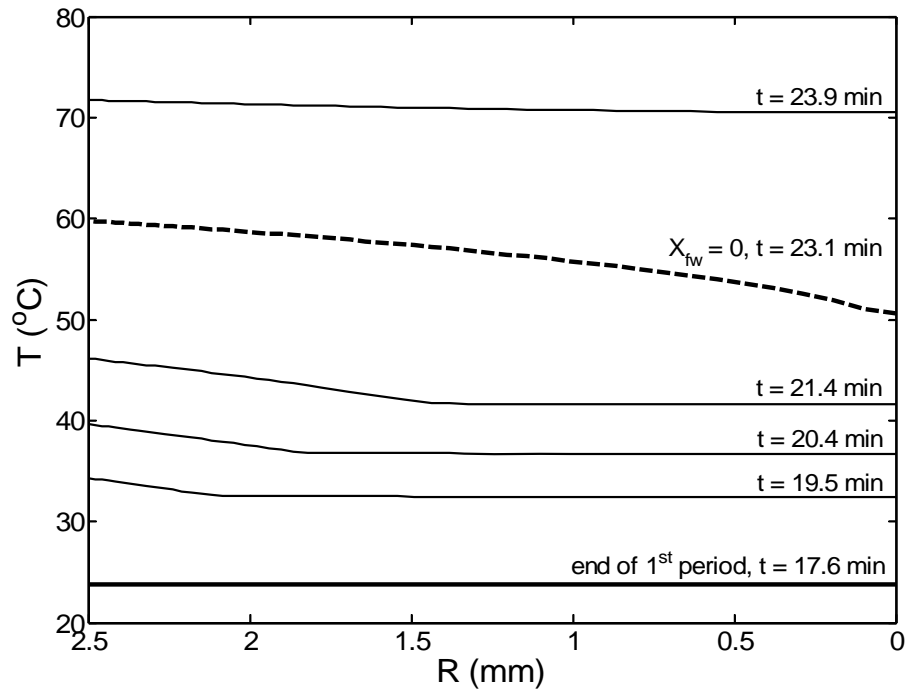
Figure 4.8 Drying of a sphere of light concrete: temperature profiles
($T_\infty = 80^{\circ}$C and $\varphi = 0$).
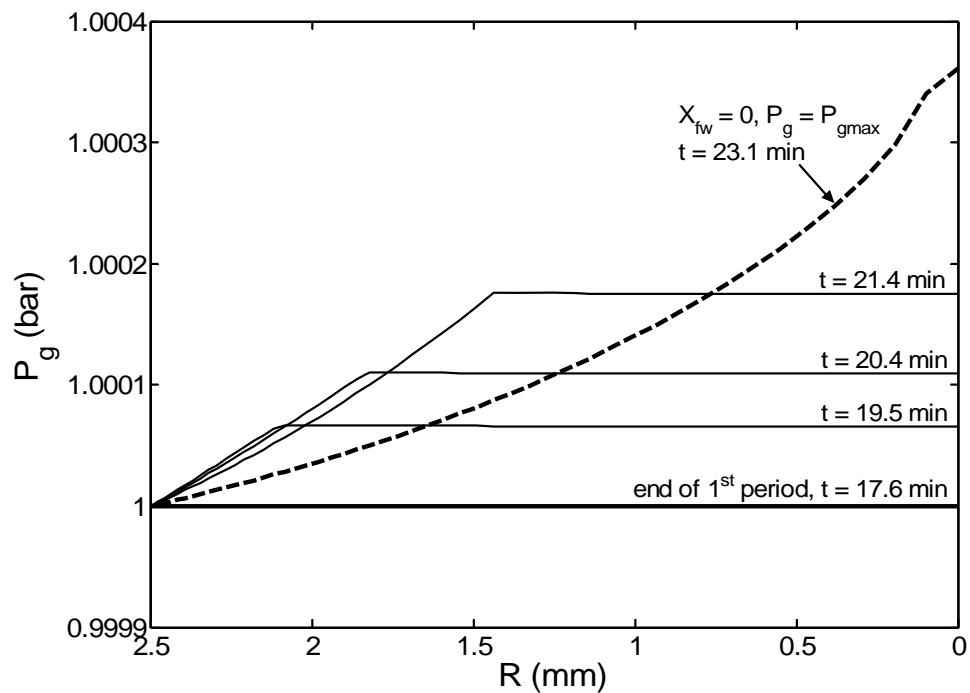
Figure 4.9 Drying a sphere of light concrete: pressure profiles
($T_\infty = 80^{\circ}$C and $\varphi = 0$).

From the above figures some important drying characteristics can be observed. Starting from a uniform initial moisture content $X_0 = 1$ (corresponding to saturation $S_0 = 62.5\%$)

over the whole sample, after a short warm-up period, the moisture content is reduced at a constant rate (constant slope of the curves in Figure 4.4). This is called the first drying period (or constant rate drying period). During the first drying period (approximately 17.6 minutes), free water is brought to the surface by capillary forces where heat supplied by the convectional air is used for the rapid vaporisation of water. Due to this reason, the sample remains at the wet bulb temperature of the drying air ($T_{wb} = 23.81^{\circ}$C Figure 4.5). The moisture gradient increases (relative permeability k_w decreases) and the moisture profiles as function of radius appear fairly flat (Figure 4.7 drying time 15.0 and 17.1 min). Within this period, the pressure stays constant at the atmospheric pressure (Figure 4.9). As the drying process continues, the moisture content at the surface reaches the irreducible value $X_{irr} = 0.07$ (the average moisture content of the whole sample reaches the critical moisture content $X_{cr} = 0.1774$) and the second drying period commences. In the second drying period, the dominating forces are viscous forces. The front separating the regions of adsorbed water and free water recedes from the surface into the sample (Figure 4.7, drying time from 17.6 to 23.1 min). This process is finished when the moisture content everywhere in the sample is below the irreducible value, i.e. when all free water of the sample has been removed (Figure 4.7, drying time 23.1 min). During this period, heat transfer is almost unchanged (resistance in the sample is slightly increased), but mass transfer experiences an important additional resistance. Heat is used not only to evaporate water but also to increase the temperature of the sample. Therefore, the temperature of the sample starts to rise from the wet bulb temperature. The centre of the sample stays cooler than the outside (Figure 4.8, drying time from 19.5 to 23.9 min). This is due to the fact that the evaporation of water takes place not at the surface but at a place inside the sample (front). The free water region heats up until a new equilibrium is attained (if we assume a stationary front). At the front, heat is consumed for evaporation. As we can see from Figure 4.6, in the second drying period, an over-pressure appears due to Stefan effect (see Section 4.4.6 below). The pressure inside the sample increases to its maximum value (Figure 4.9, drying time 23.1 min) whereas the pressure at the surface always stays at the atmospheric pressure (1 bar). When the receding front has passed through the whole sample, the sample becomes dry and the entire porous medium is in the hygroscopic zone. The moisture content goes down to the equilibrium value. The temperature of solid gradually approaches the dry bulb temperature of the drying air ($T_{\infty} = 80^{\circ}$C – Figure 4.5) and the pressure falls back to the atmospheric pressure (Figure 4.6). It is clear that it takes a longer time for the element at the centre to reach equilibrium than for the others. The total drying time of this drying process is $\tau_{dry} = 28.4$ min.

4.4.5. *Drying simulation for a plate and comparison with a sphere*

In order to study the effect of geometry on drying behaviour, the drying of a plate is considered and its drying behaviour is compared with that of the sphere presented in the previous section. The thickness of the plate is assumed to be equal to the diameter of the sphere. The same material properties and drying conditions (T_{∞}, α, β, φ, etc.) are applied. The plate is considered to have infinite width and length so that mass and heat transfers take place only on the two surfaces of the plate in a symmetric way. Because of the symmetry of the problem, only half of the plate (from the middle plane to one of the surfaces) needs to be modelled by the control volume method in one dimension. The mesh used in our calculation is the same as that used in the drying simulation of the

sphere above (51 grid nodes with mesh ratio m_{ratio} equal to 0.2). The average moisture content is plotted as function of time for the two geometries in Figure 4.10. The evaporation rate and the normalized drying rate curves are given in Figure 4.11. The moisture profiles are introduced in Figure 4.12. These profiles are plotted at the times when the average moisture content X_{av} has the values 0.3, 0.2, 0.1 and 0.07, at the end of the first drying period and at the time at which $X_{fw} = 0$.

The results show that the evaporation rate in the first drying period depends only on the state of drying air ($P_{v,\infty}$, T_∞) and the transfer coefficients (α and β). Therefore with the same drying conditions the evaporation rates of both samples (sphere and plate) are identical in the first drying period (Figure 4.11.a). However, because the surface over volume ratio is large for the sphere, the whole drying process of the sphere is shorter (28.5 minutes compared to 90.6 minutes of the plate – Figure 4.10). In the first drying period, the moisture of the sphere is reduced faster than that of the plate (Figure 4.10) and the sphere has lower critical moisture content X_{cr} (0.1774 compared to 0.2020 - Figure 4.11.a). This leads to a different of ξ at the beginning of the process (Figure 4.11.b). From Figure 4.12 we can see that in the first drying period, there is a little difference in moisture profiles for the two cases. But in the second drying period ($X_{av} = $ 0.1 and 0.07 – Figure 4.12, for example), due to different weighting of the control volume element, we have different profiles. For the plate, the evaporation front has reached much further and the drying rate is lower (Figure 4.11.a). Since light concrete is a hygroscopic material, the evaporation rate goes down to zero at the end of the process in both cases.
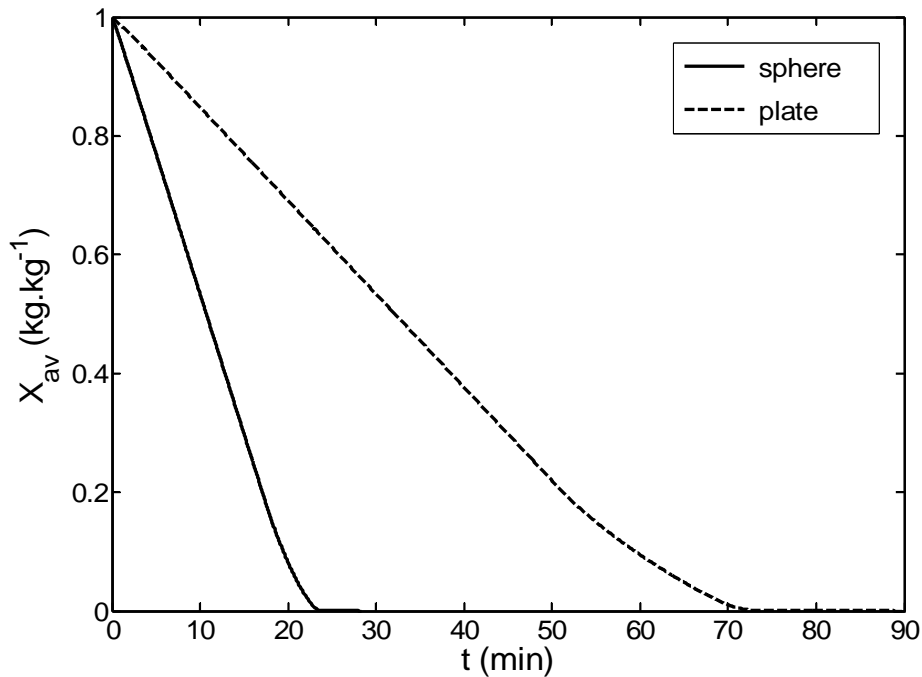
Figure 4.10 Comparison between sphere and plate: evolution of average moisture content ($T_\infty = 80^\circ C$, $\varphi = 0$).
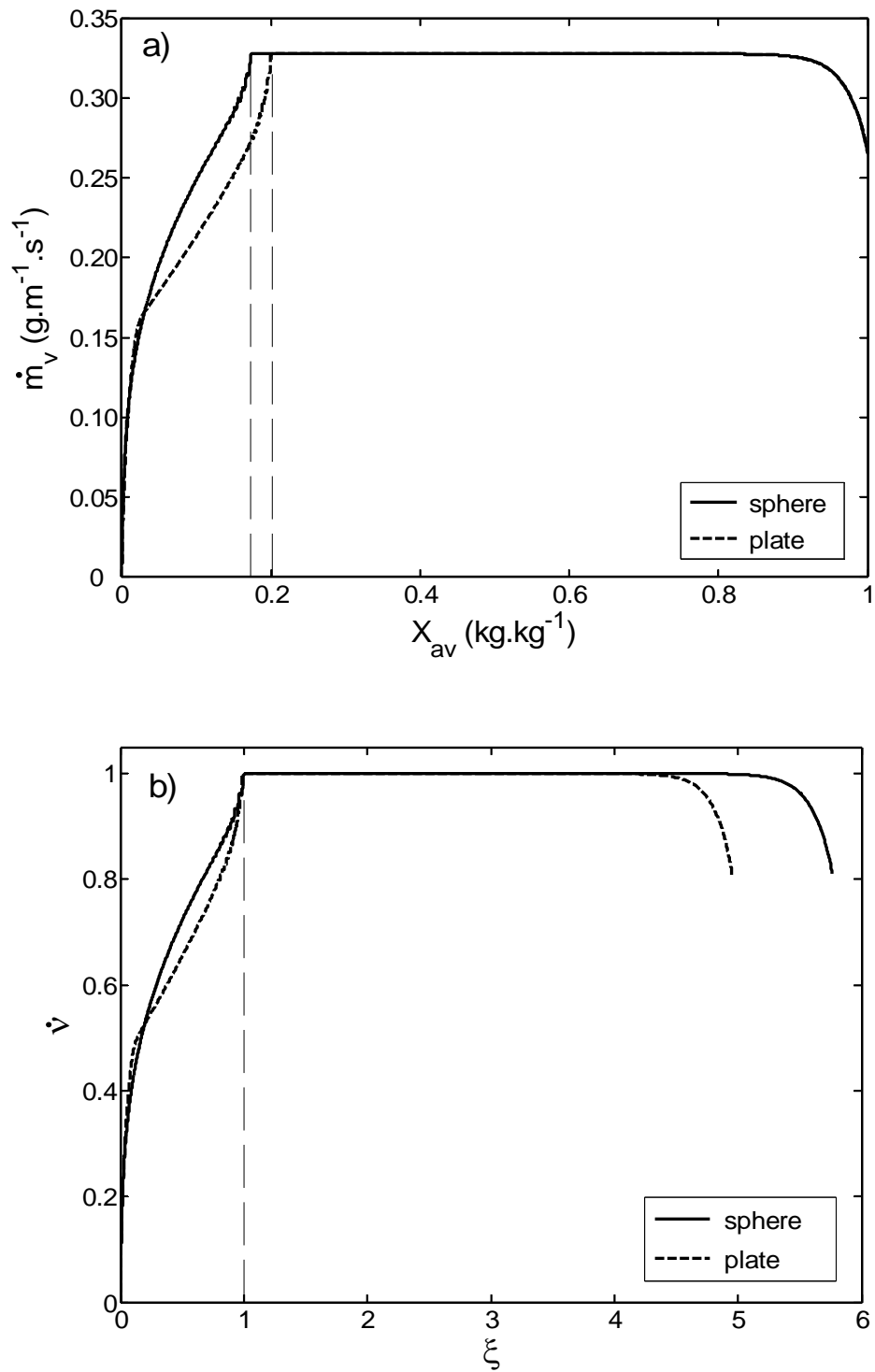
Figure 4.11 Comparison between the drying behaviour at $T_\infty = 80^{\circ}$C and $\varphi = 0$ of sphere and plate:
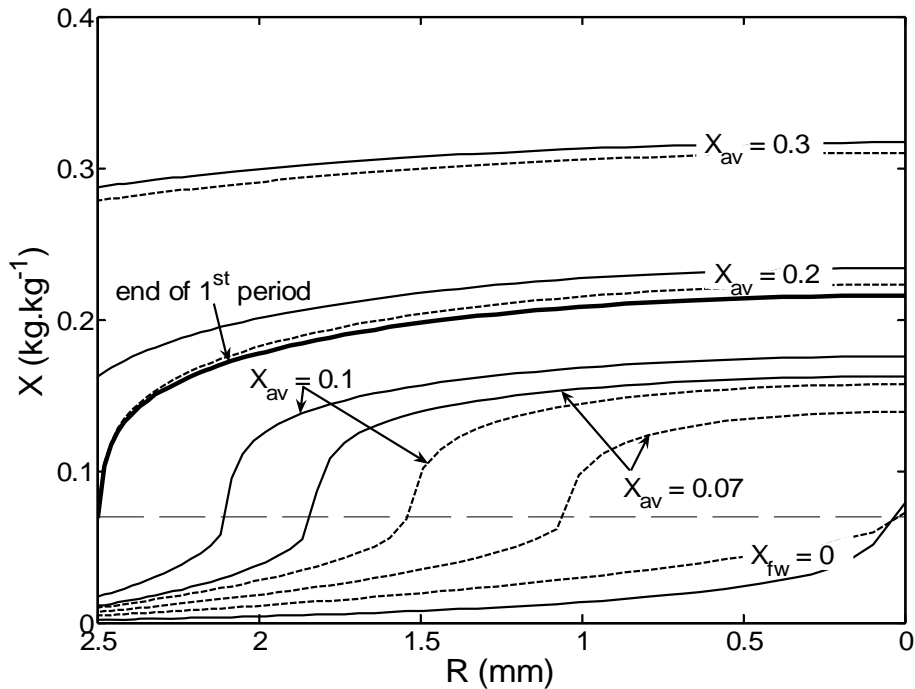a) drying rate curve and b) normalized drying rate curves

Figure 4.12 Moisture profiles for sphere (solid curves) and plate (dashed curves)
($T_\infty = 80^\circ$C and $\varphi = 0$).

4.4.6. *Analysis of fluxes of air, vapour and liquid water during drying*

In order to analyze liquid water, air and vapour fluxes, we consider the drying of a plate of light concrete with drying air at $T_\infty = 80^\circ$C and $\varphi = 0$. To have a better view of the fluxes during the drying process the sample size of the plate is chosen to be of 20 mm (from the impermeable plane to the external surface). A mesh with 51 elements and mesh ratio $m_{ratio} = 0.2$ is used. All other drying conditions and material properties are the same as in the reference case.

The simulation results are presented in Figure 4.13 to Figure 4.16. These figures present the outward fluxes computed at the east faces of elements 1, 4, 8, 12, 17, 22, 29, 38 and 51 (for approximately every 2.5 mm in distance). Note that element 1 is positioned at the centre and element 51 at the exchange surface of the plate. Figure 4.13 presents the total outward fluxes of water (containing convection term of water, vapour and diffusion term of vapour). The vapour flux (evaporation flux) out of the porous medium at the external boundary is also given in this figure. The outward liquid fluxes are presented in Figure 4.14. The outward diffusion fluxes of vapour are introduced in Figure 4.15. From these results we can see that after a short period of heating up (zone I, Figure 4.13 and Figure 4.14) the liquid flux curves are nearly flat during the constant rate period (zone II). During this period, air is saturated with vapour and water is removed by capillary forces from everywhere at almost the same rate. From centre to surface these rates add up. As the sample begins to dry out, the falling rate period begins (zone III). From this point the vapour diffusion controls the process. At the end of the second period there is a final increase of liquid flow. This is due to the existence of an over pressure (see Figure 4.16). The final increase of liquid flow increases to a

local maximum value when the gas pressure reaches the maximum value. When all vapour is removed all fluxes go down to zero. It is found that the diffusive molar air flux and the diffusive molar vapour flux are the same but in opposite direction ($\dot{N}_a^{diff} = -\dot{N}_v^{diff}$). This is because the (receding) front of evaporation is like a semi-permeable boundary for air flow, and in the presence of the diffusion process (due to concentration gradients) a convective (Stefan) flow occurs. Indeed, we found that net flux of air (total of convection and diffusion fluxes of air) is almost to zero. This means that air is almost immobile. A comparison between convection flux of air and convection flux of vapour shows that they are the same ($\dot{N}_a^{conv} = \dot{N}_v^{conv}$). This means that in terms of convection, air and vapour move together.
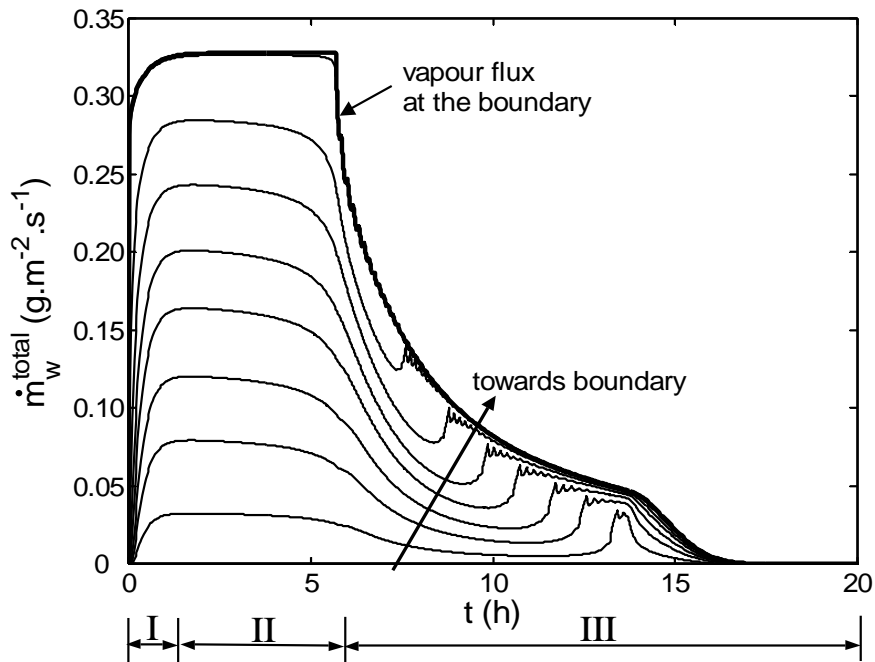
Figure 4.13 Drying of a plate: total water flux for approximately every 2.5 mm in distance and vapour flux at the boundary (fat curve) ($T_\infty = 80^oC$ and $\varphi = 0$).
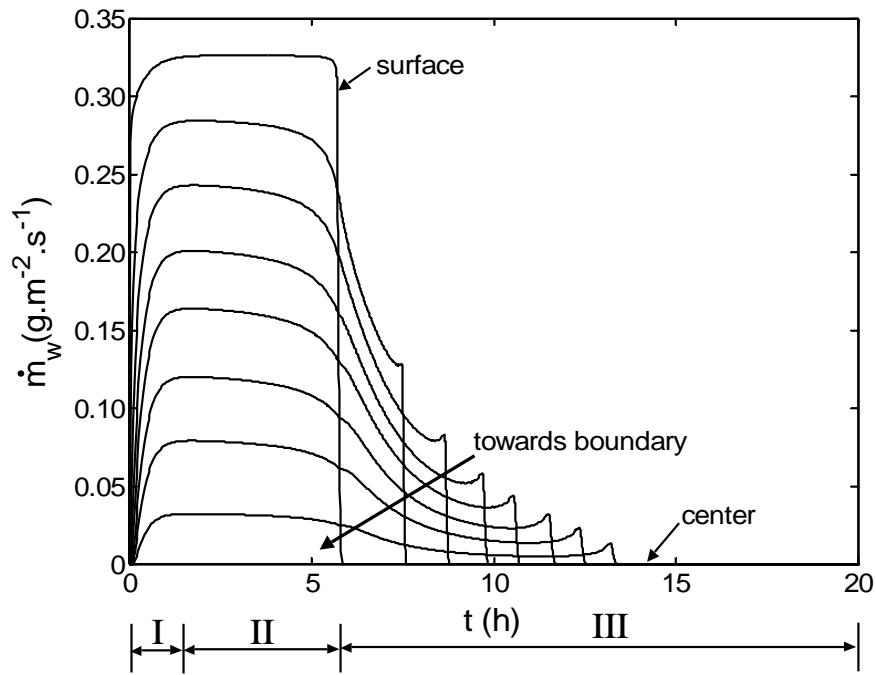
Figure 4.14 Drying of a plate: liquid water flux for approximately every 2.5 mm in distance ($T_\infty = 80^\circ$C and $\varphi = 0$).
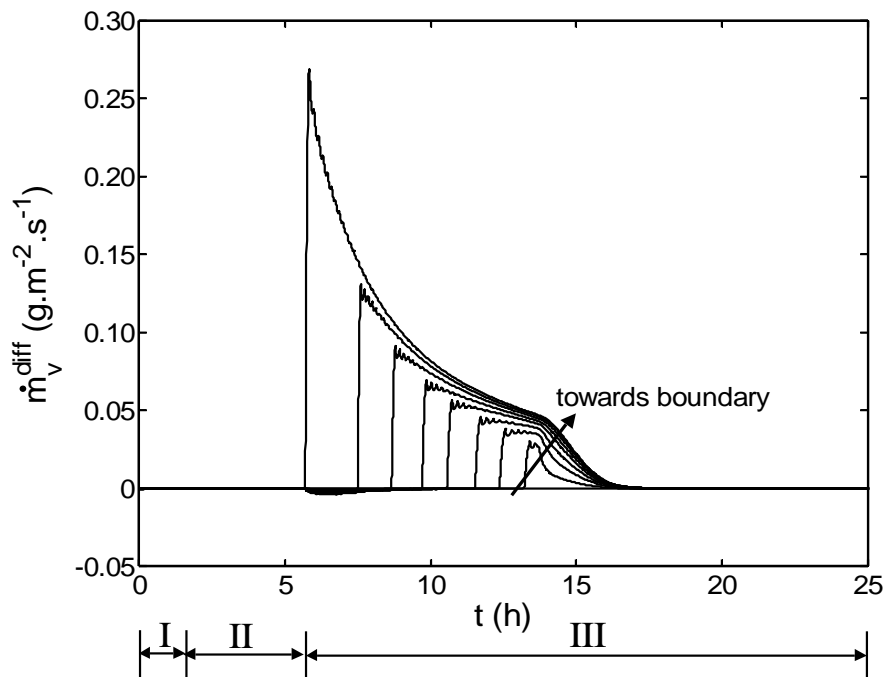
Figure 4.15 Drying of a plate: diffusion of vapour flux for approximately every 2.5 mm in distance ($T_\infty = 80^\circ$C and $\varphi = 0$).
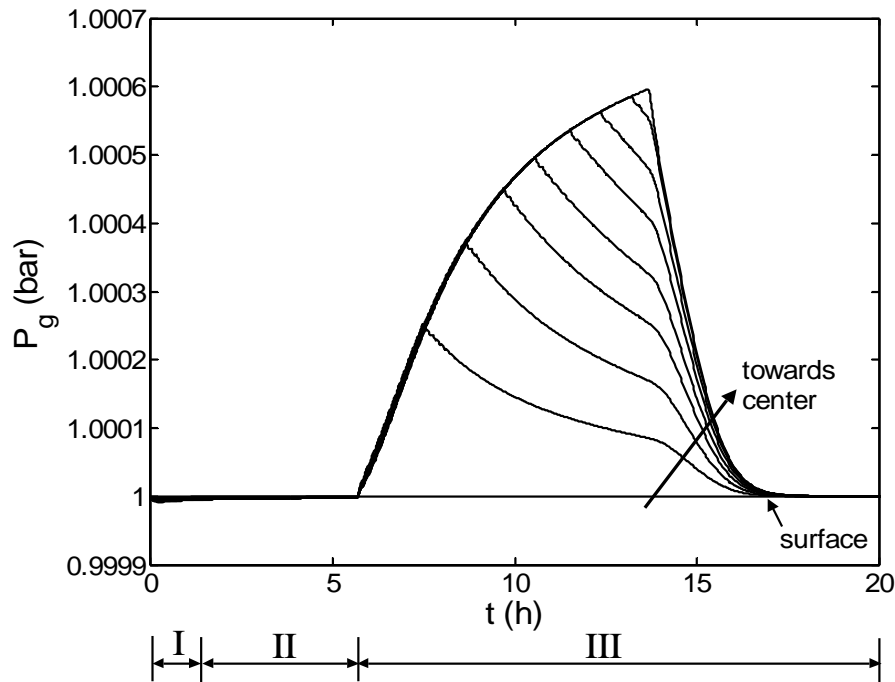
Figure 4.16 Drying of a plate: temporal evolution of pressure for approximately every 2.5 mm in distance ($T_\infty = 80^{\circ}$C and $\varphi = 0$).

4.4.7. *Influence of effective transport parameters – Parametric study*

The aim of this section is to study the sensitivity of the drying behaviour with respect to different model parameters such as effective diffusivity, effective thermal conductivity and absolute permeability, which are functions of moisture content (or saturation). The investigation is carried out by varying these parameters numerically and comparing the simulation results with the reference case analyzed in Section 4.4.4 above. The material, drying conditions, sample geometry and mesh are the same as in the analysis of Section 4.4.4.

4.4.7.1 *Influence of effective diffusivity*

Five different cases of effective diffusivity (the reference value of D_{eff} is scaled by factor 0.1, 0.5, 1, 2, and 3) are considered. The decrease of the effective diffusivity D_{eff} can be related to the increase of the tortuosity of the porous medium and on the contrary, the increase of D_{eff} can be linked to the decrease of tortuosity. The numerical results (drying rate curves) are plotted in Figure 4.17. The temporal evolutions of moisture profiles at the end of the simulation for the two extreme cases and the reference case (with effective diffusivity $0.1D_{eff}$, $3D_{eff}$ and D_{eff}) are presented in Figure 4.18.

The results indicate that the effective diffusivity has no effect during the first drying period (the curves coincide for $X_{av} \geq X_{cr} = 0.1774$) since in this period water migrates as liquid by capillary forces. But in the second drying period, the effective diffusivity controls directly the migration of water, now as vapour: the higher the value of D_{eff} the

78

higher the drying rate (Figure 4.17). By looking at the temporal evolution of moisture profiles (Figure 4.18), we can see that with a smaller D_{eff}, the moisture profiles are steeper since there is more resistance to the movement of vapour.
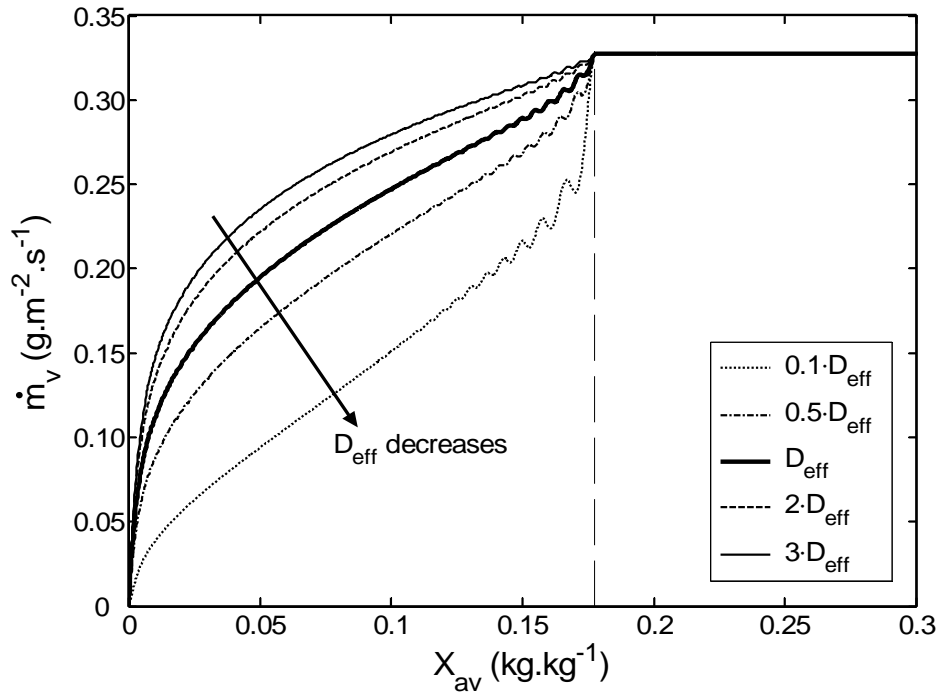

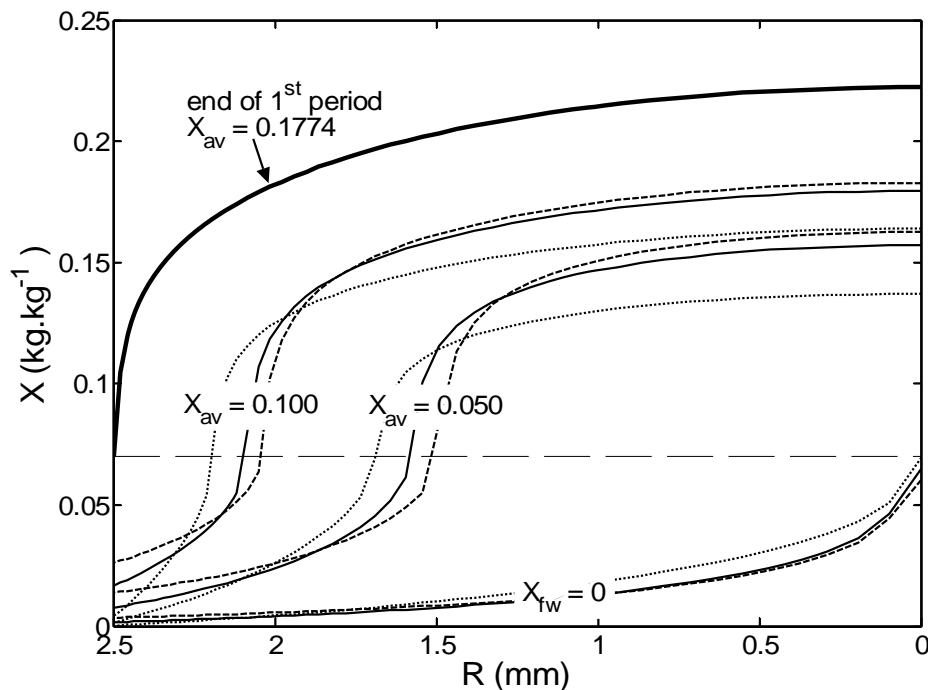**Figure 4.17** Influence of effective diffusivity: drying rate curves ($T_\infty = 80^{\circ}C$ and $\varphi = 0$).

Figure 4.18 Influence of effective diffusivity: moisture profiles for $0.1D_{eff}$ (dotted curves), D_{eff} (solid curves) and $3D_{eff}$ (dashed curves) ($T_\infty = 80^{\circ}C$ and $\varphi = 0$).

4.4.7.2 Influence of effective thermal conductivity

The effective thermal conductivity depends on the thermal conductivities of solid and water as well as on saturation. In this section, only the thermal conductivity of solid λ_s is varied since we keep the same liquid and we assume parallel heat conduction in both phases. In our analysis, for the reference case, the thermal conductivity of solid is $\lambda_s = 0.142$ W.m^{-1}.K^{-1} (Eq. (4-12)). The results from Figure 4.19 show that the effective thermal conductivity has little effect on the drying rate curve (the difference can only be seen when varying λ_s by a factor of 100; of course, $0.01\lambda_s$ is unrealistically small). In fact, λ_{eff} affects the warming-up period (higher values of λ_{eff} cause a slight speed up in the initial warming up period). This is not clearly visible in Figure 4.19 because of small sample size (2.5 mm in radius). In the second drying period, if λ_{eff} is decreased, the evaporation rate is decreased due to the decreased rate of heat supply to the place of evaporation by conduction.
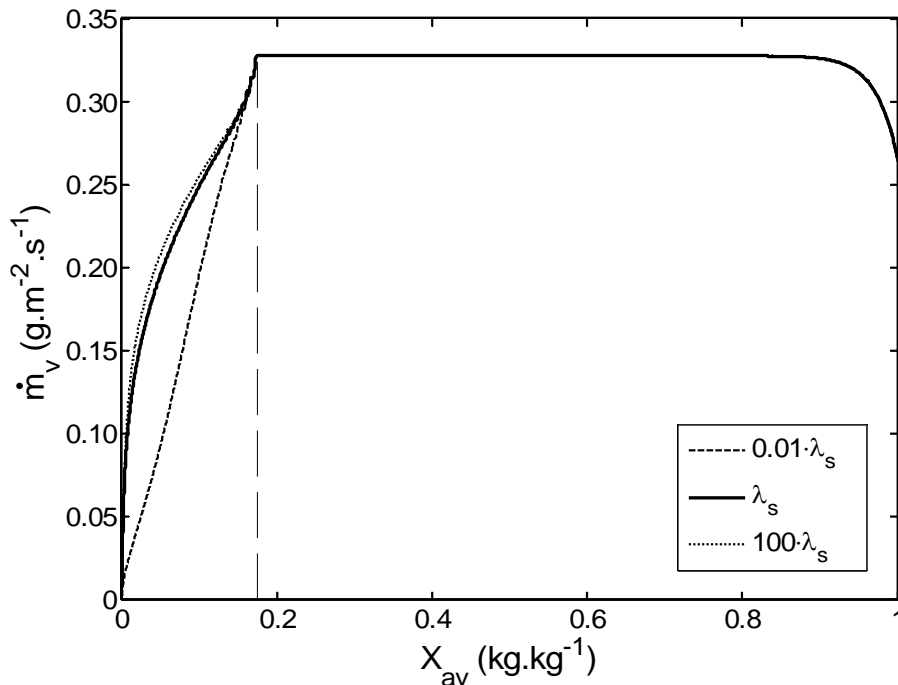
Figure 4.19 Influence of effective thermal conductivity: drying rate curves for different values of λ_s ($T_\infty = 80^{\circ}$C and $\varphi = 0$).

4.4.7.3 Influence of absolute permeability

The absolute permeability characterizes the ability of a single fluid phase to move through the porous medium. This parameter depends only on pore structure and is fluid independent. The influence of this parameter is mainly found on the first drying period. As it can be seen from Figure 4.20, the duration of the first drying period decreases when the absolute permeability decreases since it is more difficult for water to be pumped at the initial rate of evaporation over long distances. Therefore the external surface dries out at a higher average moisture content (the moisture content at the

surface reaches the irreducible value X_{irr} sooner). Different values of the absolute permeability and the corresponding critical moisture contents X_{cr} are given in Table 4.1

Table 4.1 Absolute permeability and critical moisture content.

K ($\cdot 10^{-13}$ m^2)	X_{cr}
0.2	0.2418
0.5	0.2030
1.0	0.1774
2.0	0.1575
5.0	0.1349

The temporal evolution of moisture profiles for the two extreme cases ($0.2K$ and $5K$) is presented in Figure 4.21. These results are plotted for average moisture content of 1, 0.8, 0.6, 0.4, 0.2 and 0.05. The fat curves represent the end of the first drying period. As we can see from this figure, the moisture profiles are flatter with larger value of the absolute permeability.
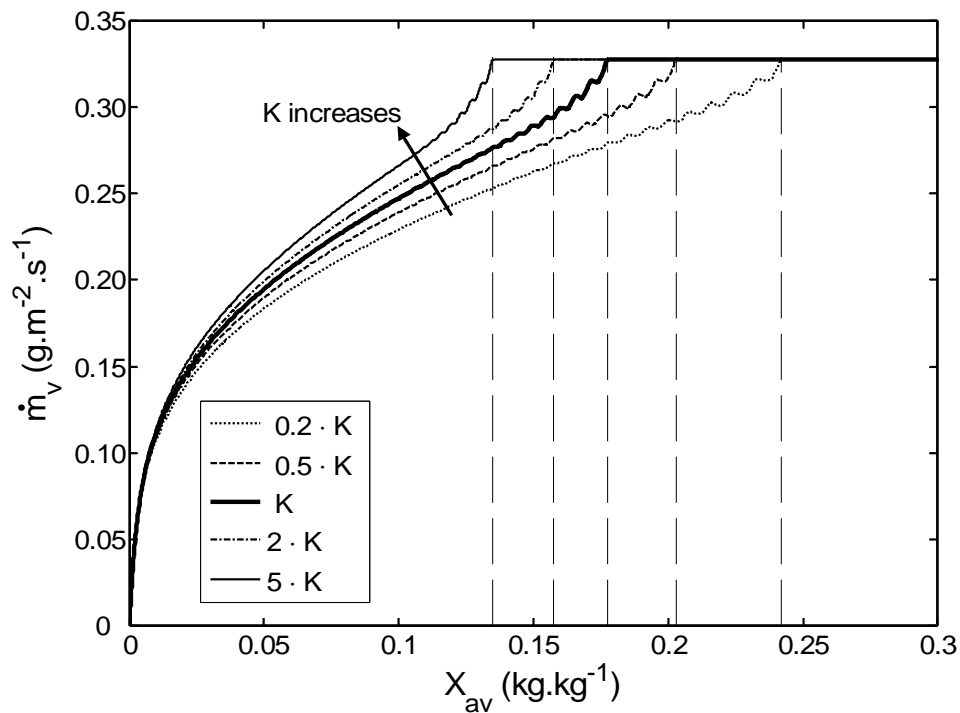
Figure 4.20 Influence of absolute permeability: drying rate curves for different values of K ($T_\infty = 80^{\circ}$C, $\varphi = 0$).
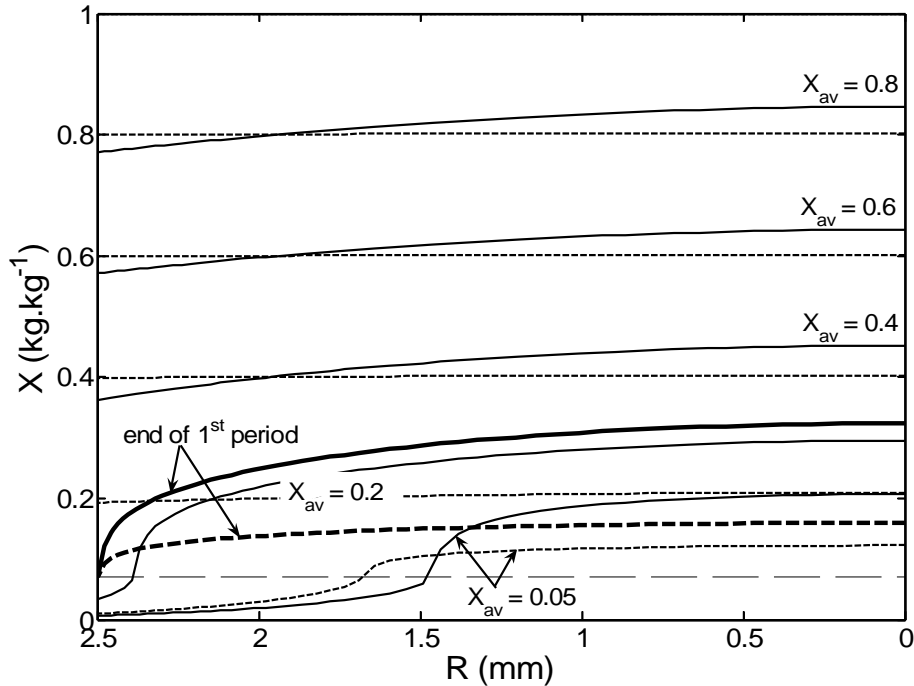
Figure 4.21 Influence of absolute permeability: moisture profiles for 0.2*K* (solid
curves) and 5*K* (dashed curves) ($T_\infty = 80^{\circ}$C and $\varphi = 0$).

Our parametric study leads to the conclusion that, among the different model
parameters, the drying behaviour is sensitive to the effective diffusivity and to the
absolute permeability. While the effective diffusivity only changes the drying kinetics
in the second drying period, the absolute permeability mainly influences the critical
moisture content. When these results are compared (in phenomena and characteristics of
the curves) with those obtained by the previous work of Nasrallah and Perré (1988 [58])
on brick, which is a similar kind of porous medium as light concrete, a good agreement
can be observed.

4.4.8. *Influence of the state of bulk air on drying behaviour*

The question arises, how the state of the bulk air (drying air) and the transfer
coefficients α and β affect the drying behaviour. In order to answer this question, the
relative humidity, the temperature and the mass transfer coefficient (or velocity) of the
drying air are varied numerically in the drying simulation of a sphere of light concrete.
The simulation results are then compared with the results obtained in the reference case
presented in Section 4.4.4. Except the mentioned parameters, the same material, drying
conditions, sample geometry and mesh are used.

4.4.8.1. *Influence of relative humidity*

In this section, the influence of the relative humidity of the drying air φ is investigated.
The values of the relative humidity φ, the corresponding values of partial vapour
pressure $P_{v,\infty}$, the wet bulb temperature T_{wb}, the equilibrium moisture content X_{eq}, the

critical moisture content X_{cr} and the evaporation rate of the first drying period $\dot{m}_{v,I}$ are reported in Table 4.2 (drying at $T_\infty = 80^o$C).

Table 4.2 Relative humidity and some corresponding relevant values

φ (%)	$P_{v,\infty}$ (bar)	T_{wb} (^{o}C)	X_{eq}	X_{cr}	$\dot{m}_{v,I}$ (g.m^{-2}.s^{-1})
0	0.0000	23.81	0.0000	0.1774	0.3285
5	0.0237	32.50	0.0018	0.1674	0.2790
10	0.0473	38.85	0.0036	0.1604	0.2433
20	0.0947	47.98	0.0074	0.1506	0.1909
40	0.1893	60.02	0.0158	0.1374	0.1206
60	0.2840	68.30	0.0257	0.1267	0.0712
80	0.3787	74.71	0.0386	0.1149	0.0324

The drying rate curves are plotted in Figure 4.22. It is observed that when the relative humidity is increased the evaporation rate of the first drying period $\dot{m}_{v,I}$ is decreased (because of the reduced driving force), the critical moisture content X_{cr} is lower (viscous forces that must be overcome by capillary forces are smaller) and the equilibrium moisture content X_{eq} is increased (according to sorption isotherm). The higher the relative humidity, the longer the drying process (28.5 min when $\varphi = 0$ as compared to 287.0 min when $\varphi = 80\%$). A comparison of the moisture profiles for two extreme cases ($\varphi = 0$ and $\varphi = 80\%$) is given in Figure 4.23. These results are plotted for average moisture content of 0.4, 0.2 and 0.1 as well as when the first drying period is finished (fat curves) and when all free water has been removed. The results indicate that with lower relative humidity ($\varphi = 0$) the moisture profiles are steeper due to higher drying rates.
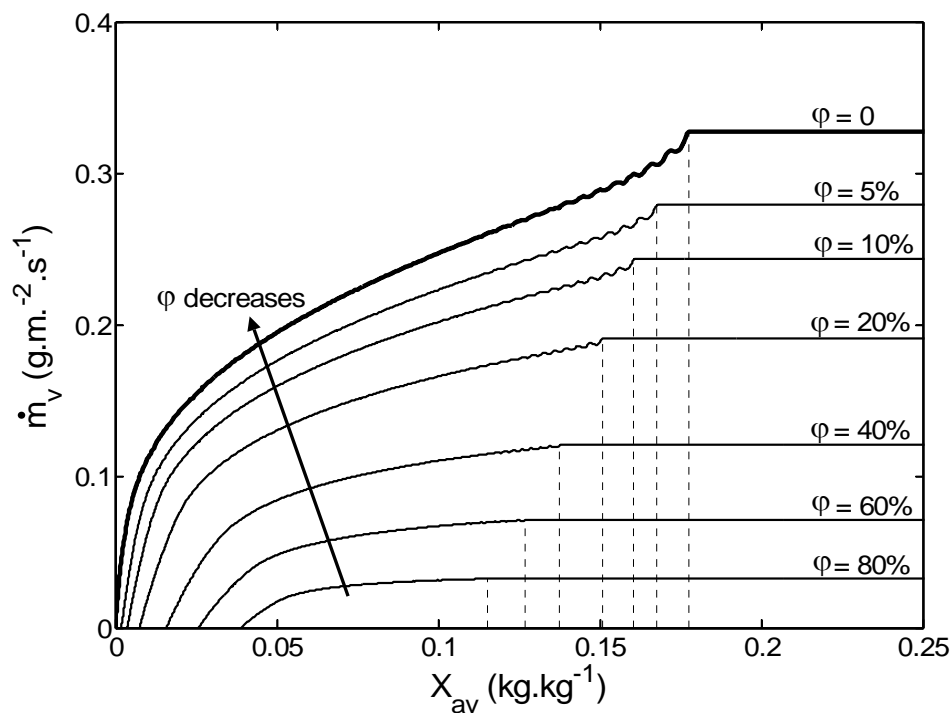

Figure 4.22 Influence of relative humidity of drying air: drying rate curves
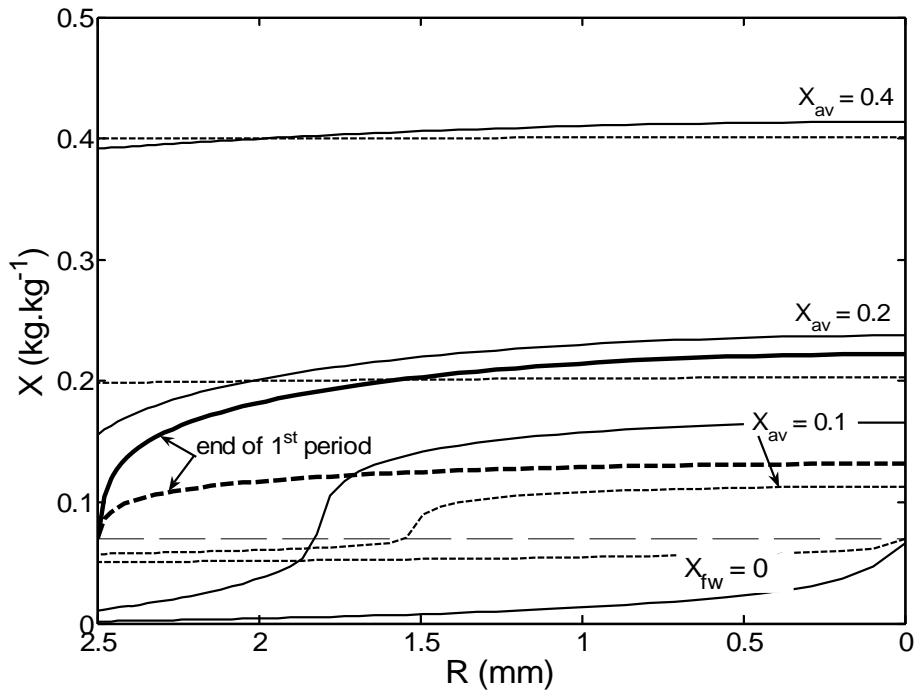(for $T_\infty = 80^o$C).

Figure 4.23 Influence of relative humidity of drying air: comparison of moisture
profiles at $\varphi = 0$ (solid curves) and $\varphi = 80\%$ (dashed curves) (for $T_\infty = 80^oC$).

4.4.8.2. *Influence of temperature of the drying air*

The influence of the temperature of the bulk air is examined by considering five
different temperature cases with zero relative humidity φ. The results are presented as
drying rate curves in Figure 4.24 and as normalized drying curves in Figure 4.25. It can
be observed that if the temperature of the bulk air is increased, the wet bulb temperature
is increased and therefore the saturation vapour pressure at the surface is higher
resulting in a higher initial drying rate $\dot{m}_{v,I}$ as we can see in Table 4.3. For higher
drying rates, the viscous forces are larger which leads to an increase in the critical
moisture content. The slowest process is at 20^oC (approximately 145.0 min of drying)
and the fastest is at 120^oC (approximately 26.0 min). If the wet bulb temperature T_{wb} of
the bulk air is smaller than the initial temperature of the sample T_0, a cooling process
will take place before the first drying period starts ($T_\infty = 20\,^oC$ and 60^oC in Figure 4.24).
On the contrary, if the wet bulb temperature is greater than the initial temperature of the
sample $T_{wb} > T_0$, a heating up period starts at the beginning of the process ($T_\infty = 80\,^oC$,
$100\,^oC$, and 120^oC – Figure 4.24).

It can be seen from the drying curves (especially Figure 4.25) that in the second drying
period the curves are not linear and become more and more convex when the
temperature is increased. This phenomenon is due to the heating up of the solid phase,
which is more important for larger temperature difference between the drying air and
the sample. A comparison for two extreme cases ($T_\infty = 20\,^oC$ and $T_\infty = 120^oC$) is given
in Figure 4.26 where moisture profiles are plotted for $X_{av} = 0.4$, 0.2 and 0.1 together
with the end of the first drying period (fat curves) and when $X_{fw} = 0$ holds everywhere in

the sample. These results show that the effect is similar for deceasing of φ and increasing of T_∞.

Table 4.3 Influence of temperature of drying air on drying behaviour $(P_{v,\infty} = 0)$.

$T_\infty(^oC)$	$T_{wb}(^oC)$	X_{cr}	$\dot{m}_{v,I}$ $(g.m^{-2}.s^{-1})$
20	3.68	0.1535	0.0933
60	18.56	0.1710	0.2404
80	23.81	0.1774	0.3285
100	28.19	0.1830	0.4203
120	31.94	0.1878	0.5172
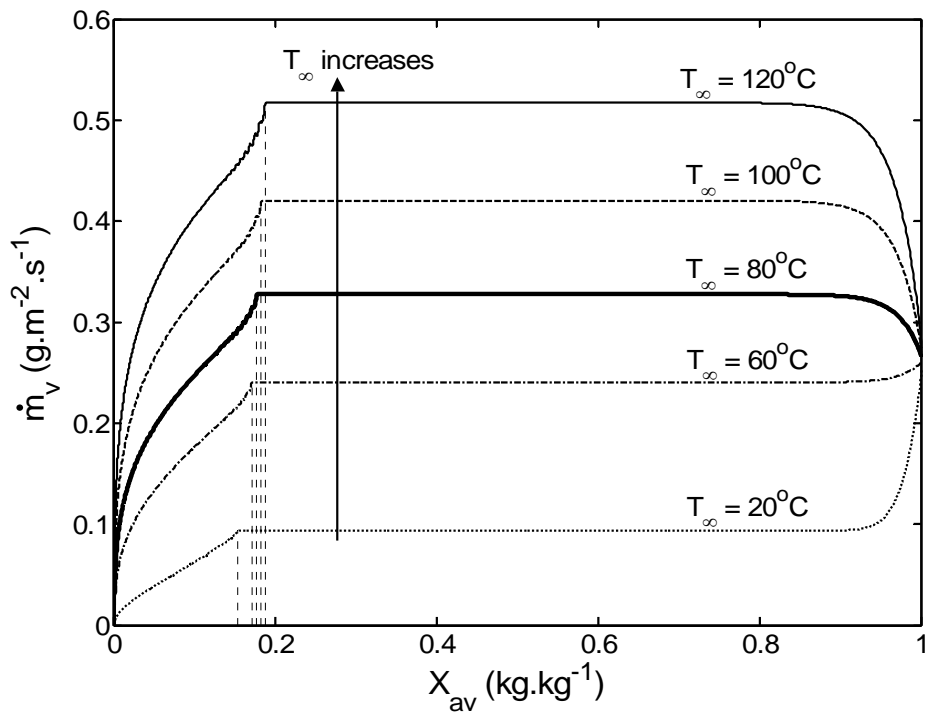
Figure 4.24 Influence of temperature of drying air: drying rate curves (for $\varphi = 0$).
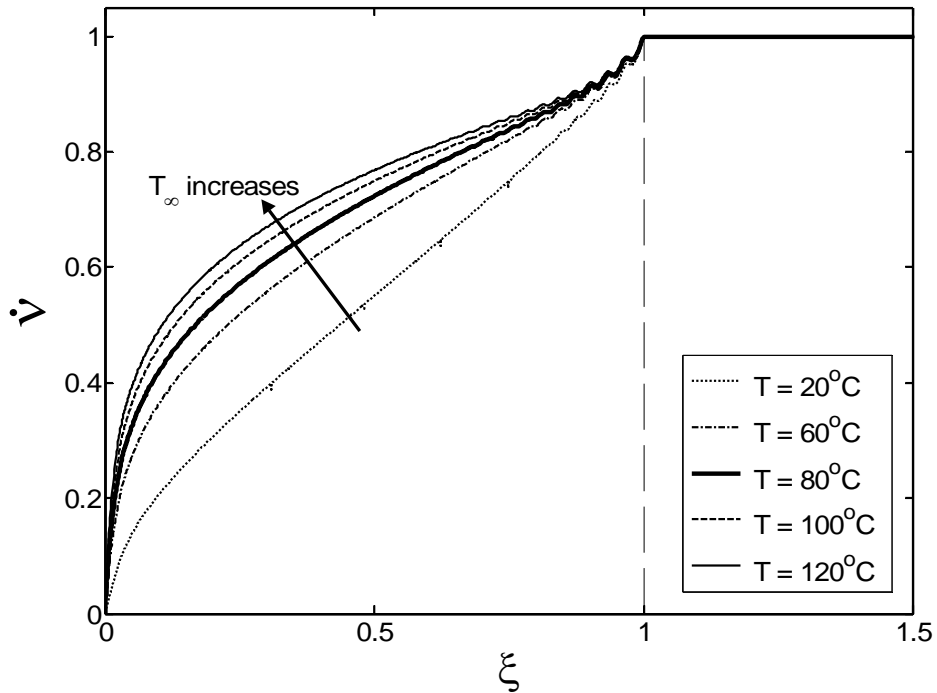
Figure 4.25 Influence of temperature of drying air: normalized drying curves ($\varphi = 0$).
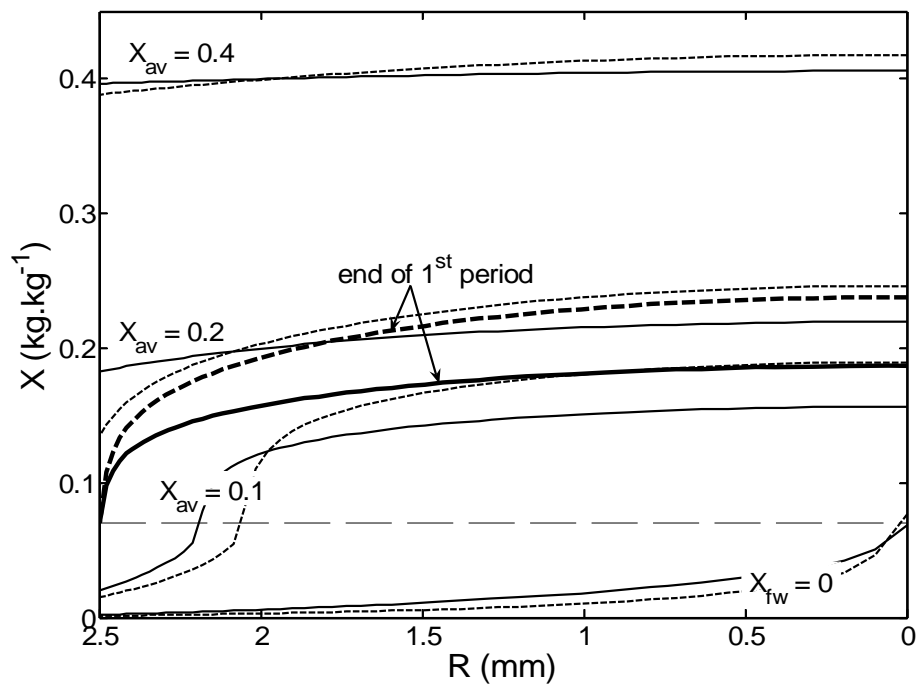
Figure 4.26 Influence of temperature of drying air: comparison of moisture profiles for $T_\infty = 20^\circ$C (solid curves) and $T_\infty = 120^\circ$C (dashed curves) (for $\varphi = 0$).

4.4.8.3. Influence of transfer coefficients

Figure 4.27 and Figure 4.28 present the influence of mass transfer coefficient β on the drying kinetics for five different cases of drying of a sphere of light concrete (by convectional air of zero relative humidity and temperature $T_\infty = 80^{\circ}$C). Note that the heat transfer coefficient α is changed together with the mass transfer coefficient β (the ratio α/β is 950). In our investigation, the assumption of symmetric boundary conditions is applied. The results show that if the mass transfer coefficient β (or in other words the velocity v of the drying air) is increased, the drying rate of the first drying period $\dot{m}_{v,I}$ is increased and the critical moisture content X_{cr} is increased as well. The values of β, $\dot{m}_{v,I}$, X_{cr}, v together with the Reynolds number Re are reported in Table 4.4. The velocity v can be computed by using the following relationship

$$\mathrm{Nu} = 2 + 0.664 \cdot \mathrm{Re}^{1/2} \cdot \mathrm{Pr}^{1/3}$$

$$\text{with} \quad \mathrm{Nu} = \frac{\alpha \cdot d}{\lambda}; \quad \alpha = \left(950 \cdot \beta\left[m.s^{-1}\right]\right) \ W.m^{-2}.K^{-1}; \quad \mathrm{Re} = \frac{v \cdot d \cdot \rho}{\eta} \qquad (4\text{-}17)$$

where Nu, Re and Pr are respectively the Nusselt, Reynolds and Prandtl number, d is the diameter of the particle, β the mass transfer coefficient, α the heat transfer coefficient, ρ the density and η the dynamic viscosity of drying air. These quantities are computed at the average temperature of drying air and the initial temperature of the sample.

Among the investigated cases, the fastest drying process happens when $\beta = 0.05$ m.s^{-1} (approximately 12.2 min) and the slowest happens when $\beta = 0.015$ m.s^{-1} (approximately 28.4 min).

Table 4.4 Influence of mass transfer coefficient on drying behaviour ($T_\infty = 80^{\circ}$C, $\varphi = 0$).

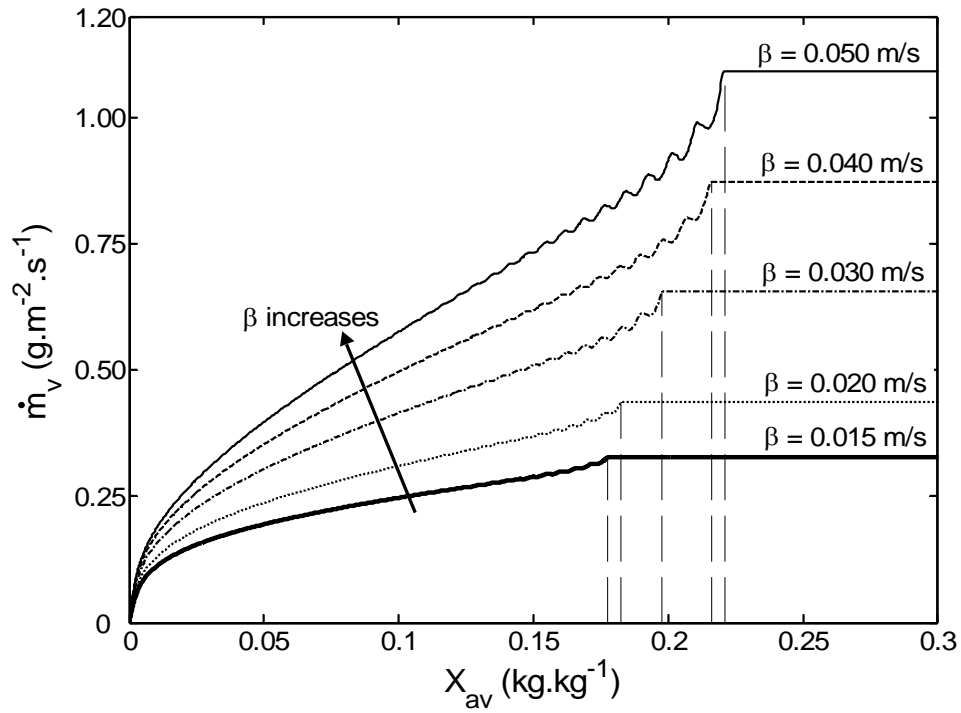| β (m.s^{-1})	Re	v (mm.s^{-1})	X_{cr}	$\dot{m}_{v,I}$ (g.m^{-1}.s)
0.015	0.879	3.210	0.1774	0.3275
0.020	5.640	20.602	0.1826	0.4366
0.030	27.557	100.665	0.1978	0.6550
0.040	66.002	241.104	0.2104	0.8734
0.050	120.974	441.918	0.2212	1.0917

Figure 4.27 Influence of transfer coefficients: drying rate curves
(for $T_\infty = 80^\circ$C and $\varphi = 0$).
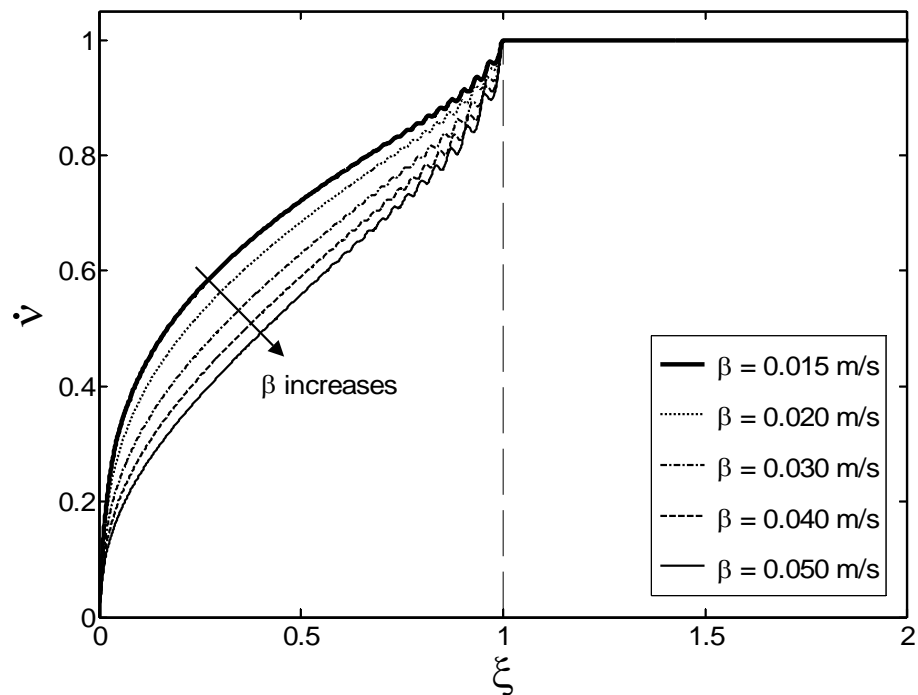

Figure 4.28 Influence of transfer coefficients: normalized drying curves
(for $T_\infty = 80^\circ$C and $\varphi = 0$).

4.4.9. *Influence of initial moisture content*

The influence of the initial moisture content of the sample is now considered. In principle, there are three types of initial moisture content corresponding to three different states of the porous medium: fully saturated medium (gas phase does not exist), unsaturated medium and completely dry medium (liquid phase does not exist). In this work, only unsaturated medium is treated directly. In the two other cases, difficulties appear in defining a set of rules to distinguish the three different states at each node of the mesh (Turner and Perré, 1996 [107]).

The influence of the initial moisture content on the drying behaviour is plotted in Figure 4.29 for initial moisture content $X_0 = 1$, 1.2, 1.4 and 1.58. Note that the sample is fully saturated at $X_{sat} = 1.6$. The results show that X_0 has effect only on the total drying time of the process. The evaporation rate and the critical moisture content are unchanged. The drying rate curves are identical in the second drying period. At a higher initial moisture content, more moisture has to be evaporated in the first drying period and the total drying process is therefore longer. The longest process is at $X_0 = 1.58$ (43.0 min) and the shortest at $X_0 = 1$ (28.4 min).
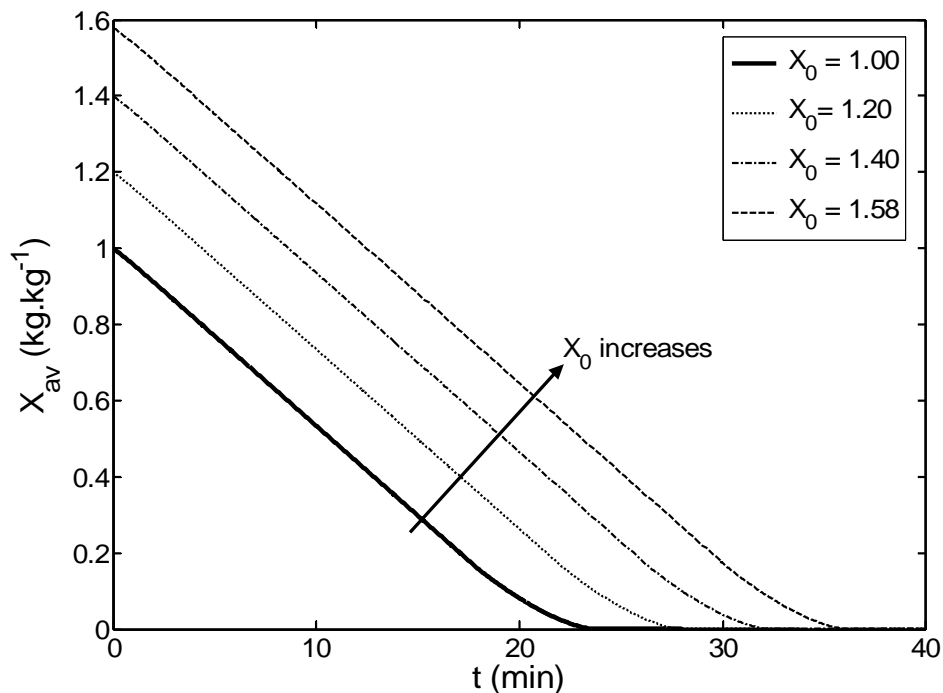

Figure 4.29 Influence of initial moisture content: evolution of average moisture content (for $T_\infty = 80^o$C, $\varphi = 0$).

4.4.10. *Isothermal and non-isothermal drying*

The isothermal drying and non-isothermal drying are compared in this section for the sphere sample mentioned above ($R = 2.5$ mm, $N = 51$ and $m_{ratio} = 0.2$). In this investigation, the drying air has temperature $T_\infty = 20^o$C and relative humidity $\varphi = 50\%$.

In order to model the isothermal case, we enhance heat transfer by setting $\alpha = 6000$ W/m^2/K and $\lambda_s = 6000$ W/m/K. For $T_\infty = 20°C$ in the isothermal case, the *imaginary* wet bulb temperature is 19.95°C while this quantity is 13.17°C in the non-isothermal case. In both cases, the variation of the gas pressure is almost identical (13.3 mbar) and the equilibrium moisture content is $X_{eq} = 0.0205$.

The numerical results are presented in Figure 4.30 to Figure 4.32. The evaporation rate in the first period and the critical moisture content for the isothermal case are $\dot{m}_{v,I} = 0.1310 \, \text{g.m}^{-2}.\text{s}^{-1}$ and $X_{cr} = 0.1538$. These values are 0.0394 g.m^{-2}.s^{-1} and 0.1320 for the non-isothermal case. In the isothermal case, the initial drying rate is higher compared to the non-isothermal case (Figure 4.30) since in the first drying period of the non-isothermal case, a cooling to the wet bulb temperature takes place (Figure 4.31) and the temperature rises back to the initial value ($T_0 = 20°C$) in the second drying period. For the isothermal case, the temperature of the sample stays almost constant (changing less than 0.06K during the whole drying process, see Figure 4.32). As a consequence, the total drying process is significantly longer in the non-isothermal case (290.9 minutes compared to 99.2 minutes). Clearly, heat transfer must be modelled to obtain realistic results.
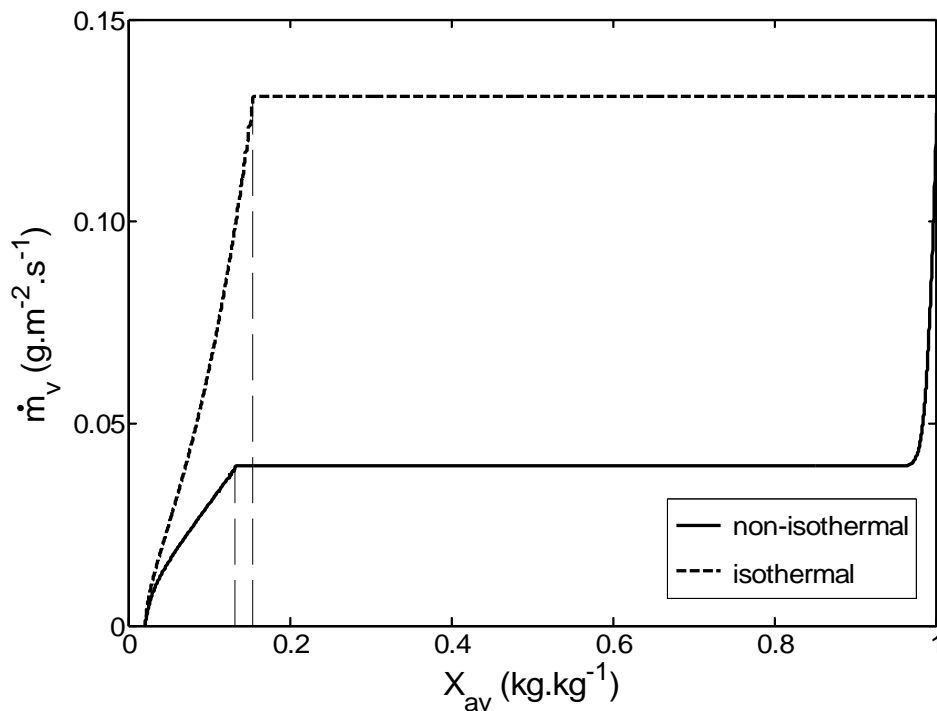

Figure 4.30 Isothermal and non-isothermal drying: drying rate curves
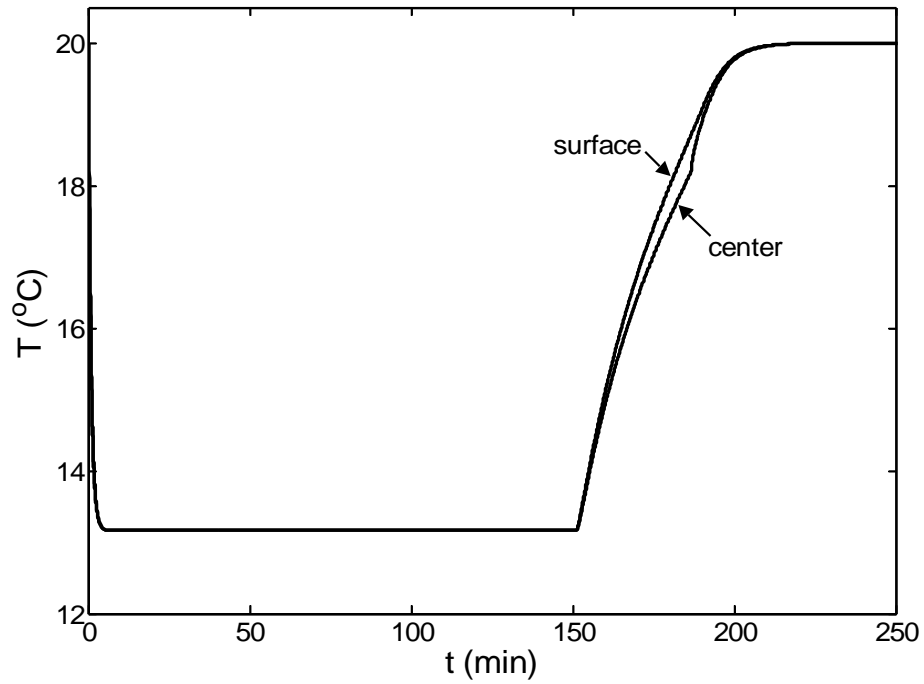(for $T_\infty = 20°C$ and $\varphi = 50$ %).

Figure 4.31 Non-isothermal drying: temporal evolution of temperature
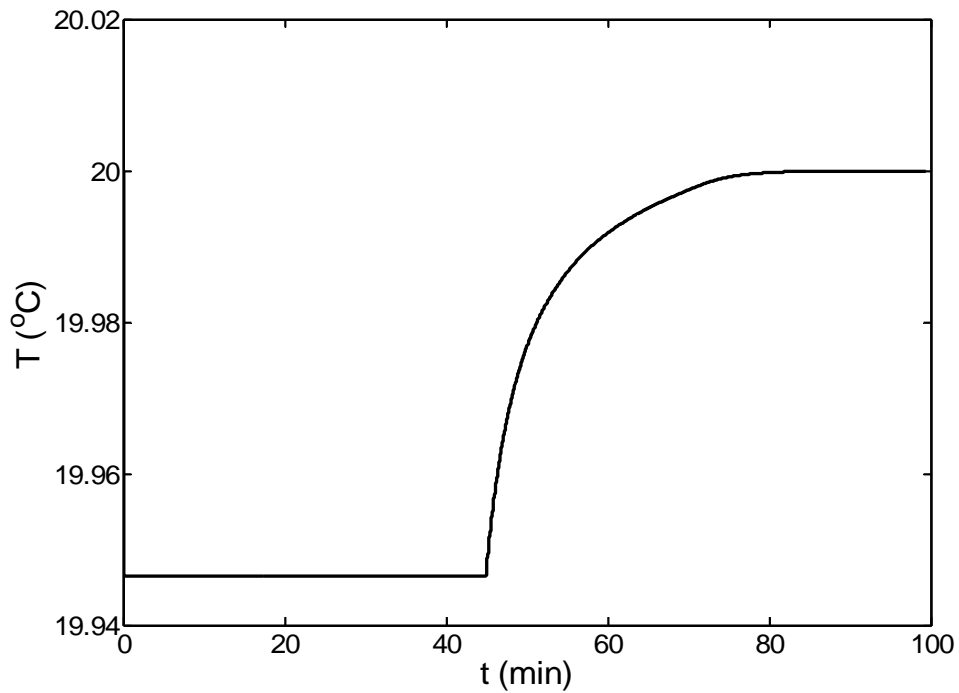(for $T_\infty = 20^{\circ}$C and $\varphi = 50$ %).

Figure 4.32 Isothermal drying: temporal evolution of temperature
(for $T_\infty = 20^{\circ}$C and $\varphi = 50$ %).

4.4.11. Influence of sample size on total drying time

4.4.11.1. Influence of sample size using continuous model

It is of course easy to understand that with the same drying conditions, it takes more time to dry a larger sample but the total drying time is not necessarily proportional to the size of the sample. An investigation about the influence of sample size on total drying time τ_{dry} is realized for the drying of a sphere and a plate of light concrete by varying the radius R or thickness $2L$, respectively. The drying air has temperature $T_\infty = 80^\circ$C and relative humidity $\varphi = 0$. The mesh ratio $m_{ratio} = 0.2$ is used. The number of nodes on the mesh is chosen corresponding to the sample size so that the numerical error is acceptable while the computational time is not too high. The total drying time τ_{dry} is defined as the time at which the average moisture content reaches the value $X_{end} = 10^{-3}$ or 10^{-5}.

The influence of sample size on drying time is presented in Table 4.5, Figure 4.33 and Figure 4.34. The drying rate curves are presented in Figure 4.35 for spheres and in Figure 4.36 for plates. It is observed that for a larger value of the sample size, the critical moisture content is higher (the constant rate period is shorter) and the drying rate in the falling rate period is lower. The drying times versus sample size for $X_{end} = 10^{-3}$ and $X_{end} = 10^{-5}$ are plotted in logarithmic scale in Figure 4.37. Obviously, the drying of a plate sample is longer than the drying of a sphere (of diameter equal to the thickness of the plate). From Figure 4.37, we can see that the slopes of the curves are different for $X_{end} = 10^{-3}$ and $X_{end} = 10^{-5}$ due to the difference of important mechanism (diffusion) at the end of drying. The results for both plate and sphere show that the drying time is not a linear function of the sample size: τ_{dry} increases more than linearly with R and L.

Table 4.5 Influence of sample size on drying of sphere and plate ($T_\infty = 80^\circ$C, $\varphi = 0$).

|	R or L (mm)	N	X_{cr}	τ_{dry} (min) ($X_{end} = 10^{-3}$)	τ_{dry} (min) ($X_{end} = 10^{-5}$)
sphere	1	31	0.1499	9.0	9.3
	1.5	41	0.1613	13.8	14.2
	2.5	51	0.1774	23.7	24.5
	5	101	0.2074	51.0	55.2
	7.5	151	0.2279	82.2	90.1
	10	151	0.2436	116.4	128.0
	12.5	151	0.2577	154.7	181.7
	15	151	0.2704	195.5	226.7
plate	1	31	0.1673	27.5	28.3
	1.5	41	0.1805	42.1	43.5
	2.5	51	0.2020	72.9	75.9
	5	101	0.2424	161.5	173.2
	7.5	151	0.2690	262.3	284.0
	10	151	0.2901	377.8	423.7
	12.5	151	0.3090	505.9	568.4
	15	151	0.3262	653.7	737.1
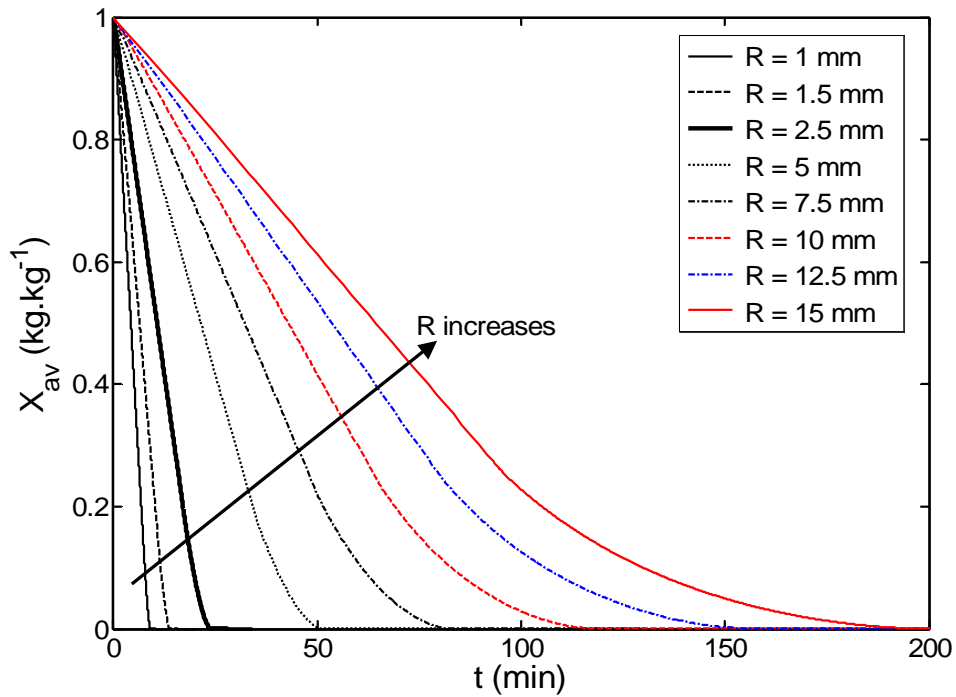
Figure 4.33 Influence of sample size on the drying of a sphere: evolution of average moisture content for different sample radii ($T_\infty = 80^\circ$C and $\varphi = 0$).
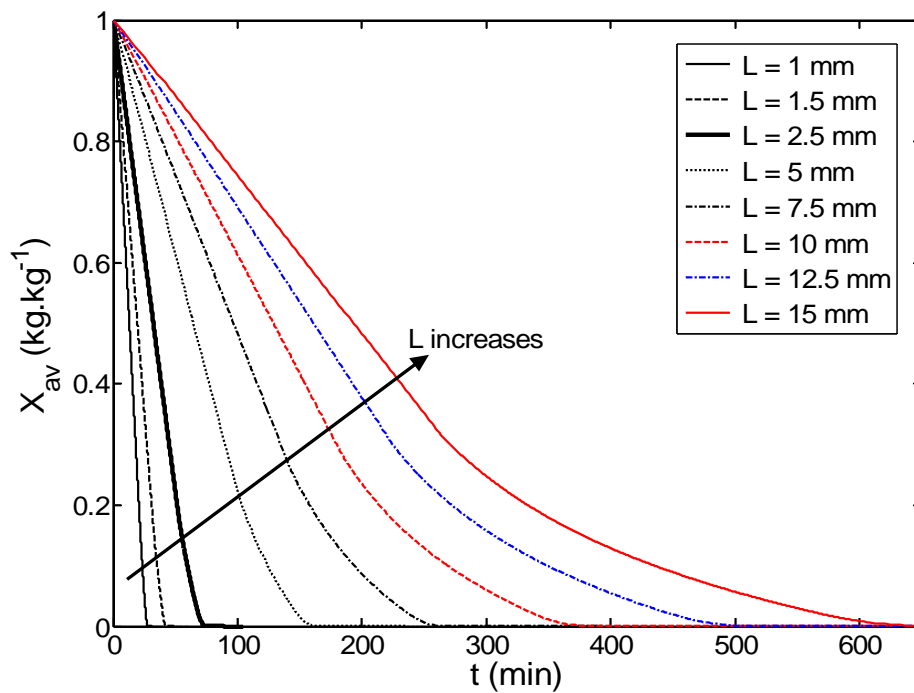

Figure 4.34 Influence of sample size on the drying of a plate: evolution of average moisture content for different L ($T_\infty = 80^\circ$C and $\varphi = 0$).
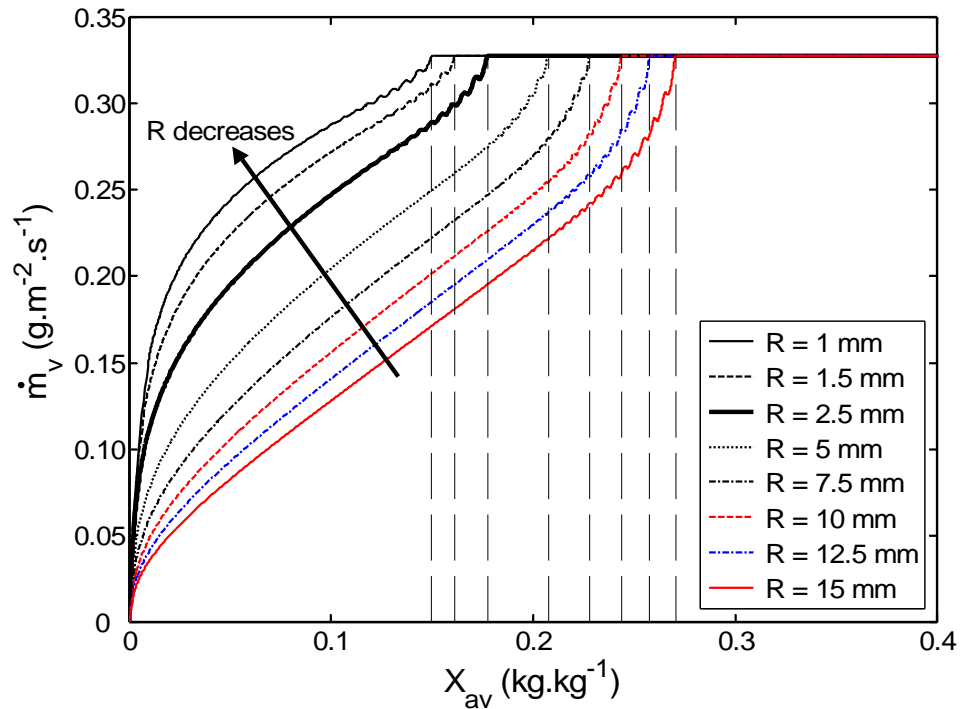
Figure 4.35 Influence of sample size on the drying of a sphere: drying rate curves for different sample radii ($T_\infty = 80^\circ$C and $\varphi = 0$).
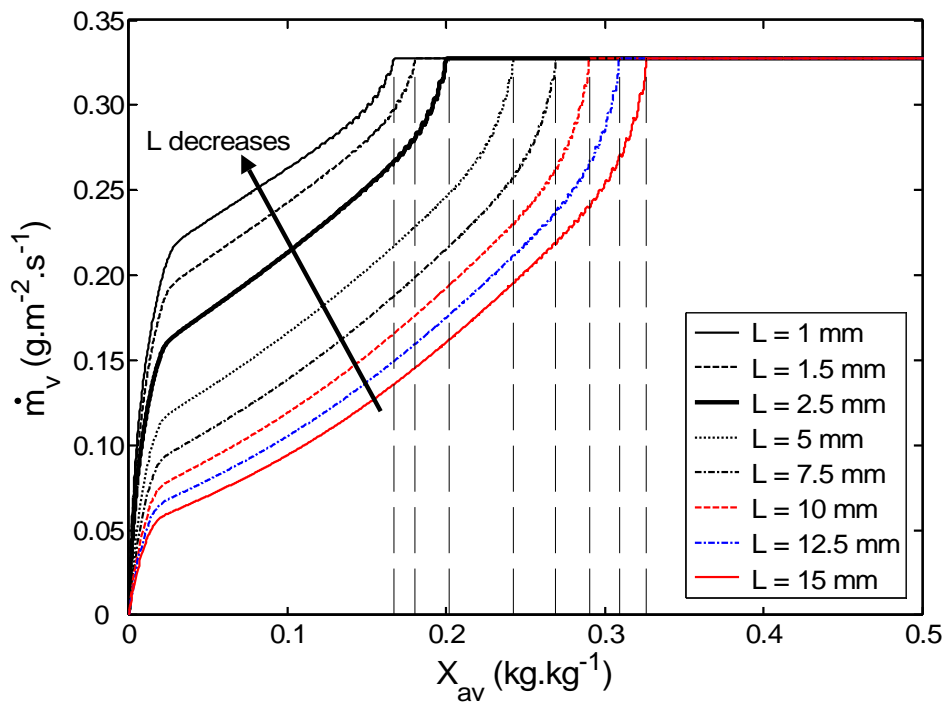

Figure 4.36 Influence of sample size on the drying of a plate: drying rate curves for different L ($T_\infty = 80^\circ$C and $\varphi = 0$).
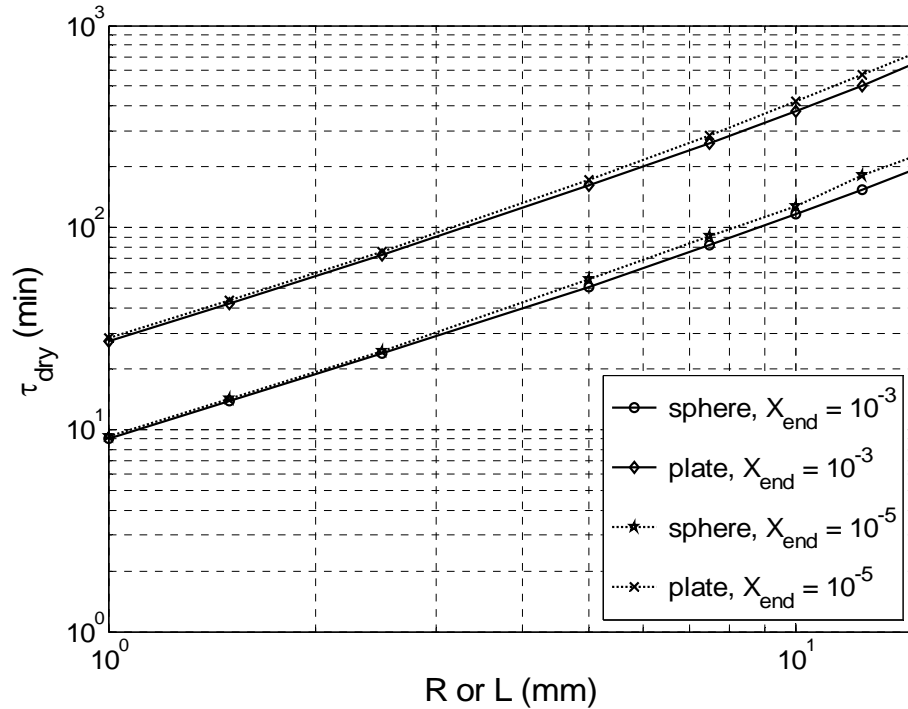
Figure 4.37 Drying time versus sample size for $X_{end} = 10^{-3}$ (solid curves) and $X_{end} = 10^{-5}$ (dotted curves) ($T_\infty = 80^o$C and $\varphi = 0$).

4.4.11.2. Influence of sample size using three different models for isothermal drying

The influence of sample size on drying time is now considered for isothermal drying of a spherical particle of light concrete by using three different models: the diffusion model, the continuous model and the receding front model. For all our considered cases below, the isothermal drying is set at $T_\infty = 20^o$C, drying air has zero moisture content, its pressure is set to 1 bar and the mass transfer coefficient is $\beta = 0.015$ m.s^{-1}. The initial moisture content is $X_0 = 1$ kg.kg^{-1}.

Diffusion model

We are using here a simple diffusion model for a sphere

$$\frac{\partial X(r,t)}{\partial t} = \frac{1}{r^2} \frac{\partial}{\partial r} \left(r^2 \delta^* \frac{\partial X}{\partial r} \right) \tag{4-18}$$

where r is the radial coordinate and the diffusion coefficient δ^* takes the constant value of $2.6 \cdot 10^{-5}$ m^2.s^{-1}.

The boundary conditions for a sphere of radius R are (Krischer, 1992 [40]):

$$\left(\frac{\partial X}{\partial r} \right)_{r=0} = 0 \tag{4-19}$$

and

95

$$\dot{m}_v = -\delta^* \rho_s \left(\frac{dX}{dr} \right)_{r=R} \tag{4-20}$$

where ρ_s is the density of the solid and $\dot{m}_v$ is the evaporation rate, which can be computed as

$$\dot{m}_v = -\beta \frac{P_g \tilde{M}_v}{\tilde{R}T} . \ln \left(\frac{P_g - P_{v,\infty}}{P_g - P_v} \right) \tag{4-21}$$

where the vapour pressure P_v is given by sorption isotherm (see Eq. (4-7)).

The system of equations (4-18)÷(4-21) is solved by using the PDE solver *pdepe* in MATLAB. Numerical results presented in Table 4.6 show the drying time as a function of the sample radius (N is the number of grid nodes used in simulation).

Table 4.6 Influence of particle size on drying time by diffusion model
(isothermal drying at $T_\infty = 20^{\circ}$C, $\varphi = 0$).

R (mm)	N	τ_{dry} (min) ($X_{end} = 10^{-3}$)	τ_{dry} (min) ($X_{end} = 10^{-5}$)
1.0	31	11.7	13.4
1.5	41	17.6	20.2
2.5	51	29.3	33.6
5.0	101	58.5	67.2
7.5	151	87.8	100.8
10.0	151	117.1	134.4
12.5	151	146.3	168.2
15.0	151	175.6	201.5

Receding front model

In this part, a simple receding front model is used. In this model, we assume that there is only vapour in the dry zone and in the wet zone only liquid exists (fully saturated pores, see Section 1.3.2). Adsorbed water is assumed to be negligible. Diffusion takes place in dry zone. For a plate, the relationship between the dry-wet front position and the momentary drying rate is

$$\dot{m}_v = -\left(\frac{1}{\beta} + \frac{s}{\delta^*} \right)^{-1} \frac{P_g \tilde{M}_v}{\tilde{R}T} . \ln \left(\frac{P_g - P_{v,\infty}}{P_g - P_v^*} \right) \tag{4-22}$$

where β is the mass transfer coefficient at the surface and s is the position of the font. The diffusion coefficient δ^* is computed as an effective diffusivity (Eq. (4-11)) with saturation $S = 0$. As we can see in this equation, the mass transfer resistance is obtained by addition: $1/\beta$ is the resistance in the boundary layer and s/δ^* is the resistance in the dry zone. For a spherical geometry, diffusion is through a shell with inner radius R-s and outer radius R, therefore the resistance in the dry zone can be computed as

$R \cdot s / [\delta^*(R - s)]$ and the time needed to evaporate the amount of water contained in a shell is

$$\Delta t = \frac{\rho_w \cdot \Delta V}{A \cdot \psi \cdot \dot{m}_v} \tag{4-23}$$

where A is the surface area of the sphere, ΔV the volume of the shell and ψ the porosity.

Based on Eqs. (4-22) and (4-23), for every value of s we have a set of the three values $(X, \Delta t, \dot{m}_v)$. From these values, the drying curves can be built. Numerical results presented in Table 4.7 show the drying time as a function of the sample radius (N is the number of grid nodes used in simulation).

Table 4.7 Influence of particle size on drying time by receding front model
(isothermal drying at $T_\infty = 20^o$C, $\varphi = 0$).

R (mm)	N	τ_{dry} (min) ($X_{end} = 10^{-3}$)	τ_{dry} (min) ($X_{end} = 10^{-5}$)
1.0	1000	64.0	65.0
1.5	1500	124.2	126.5
2.5	2500	301.0	307.4
5.0	5000	1072.0	1097.8
7.5	7500	2313.2	2371.1
10.0	10000	4024.2	4127.4
12.5	12500	6205.5	6366.7
15.0	15000	8857.1	9088.8

Continuous model

The continuous model is now applied for isothermal drying. Conditions for the isothermal drying "version" of the continuous model are given in Section 4.4.10. Numerical results presenting the drying time as a function of the sample radius are introduced in Table 4.8 (N is the number of grid nodes used in simulation).

Table 4.8 Influence of particle size on drying time by continuous model
(isothermal drying at $T_\infty = 20^o$C, $\varphi = 0$).

R (mm)	N	τ_{dry} (min) ($X_{end} = 10^{-3}$)	τ_{dry} (min) ($X_{end} = 10^{-5}$)
1.0	31	13.8	16.7
1.5	41	22.4	30.6
2.5	51	43.5	56.1
5.0	101	121.7	170.0
7.5	151	232.2	330.5
10.0	151	387.3	570.7
12.5	151	562.6	837.6
15.0	151	781.5	1156.5

<u>Comparison</u>

A comparison is presented in Figure 4.38 and Figure 4.39 for the case R = 2.5 mm. As we can see from Figure 4.39, all the three models capture the first value of evaporation rate $\dot{m}_{v,I} = 0.262\,\text{g.m}^{-2}.\text{s}^{-1}$ since for all three models the mass transfer is initially only controlled by the boundary layer. The receding front model has no first drying period. The first drying period of the diffusion model is longer ($X_{cr} = 0.0722$) than in the case of continuous model ($X_{cr} = 0.1687$).

It is clear that the drying times of three considered models cannot be compared in an absolute sense but only in a relative way when sample size is varied. Drying times versus sample size are plotted in logarithmic scale in Figure 4.40 (for $X_{end} = 10^{-3}$) and Figure 4.41 (for $X_{end} = 10^{-5}$). The results show that drying time is a linear function of the sample size for the case of diffusion model (see also Table 4.6) since in this considered case we have only outer resistance (due to small value of mass transfer coefficient, β). If outside resistance is negligible (mass transfer coefficient, β goes to infinite) we should obtain drying time as a quadratic function of the sample size. It is found that the drying time increases more than linearly with sample size in the case of continuous and receding front model. The behaviour of the curves does not change for diffusion and receding front models when X_{end} decreases (only small increase in period of inside resistance control, see Table 4.6, for example), but for the continuous model the curve and its slope change together with X_{end} because in this case inside resistance dominates (a big change in drying time, see Table 4.8).
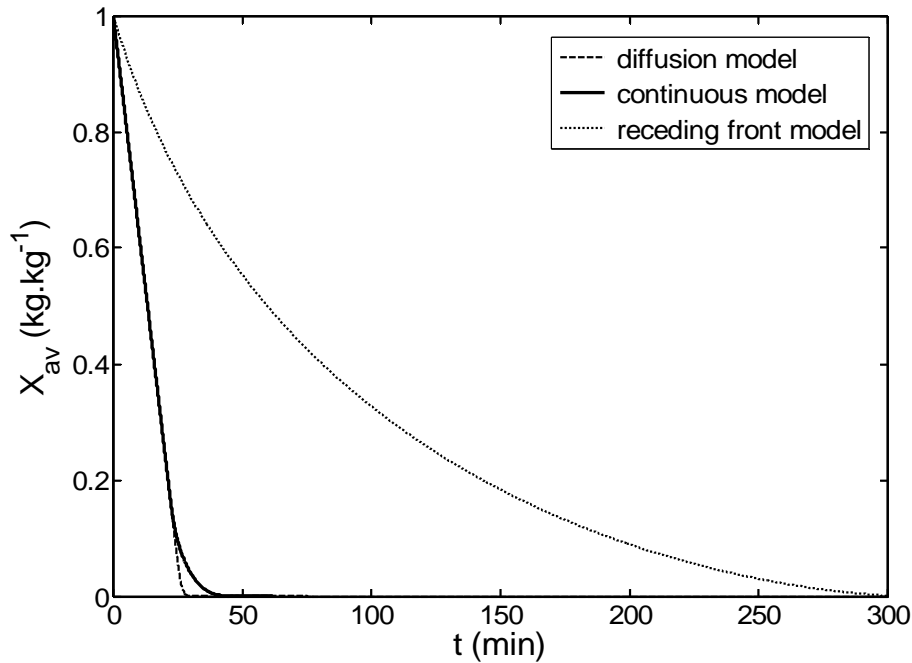

Figure 4.38 Evolution of average moisture content for isothermal drying of a spherical particle ($R = 2.5$ mm, $T_\infty = 20^\circ$C and $\varphi = 0$).

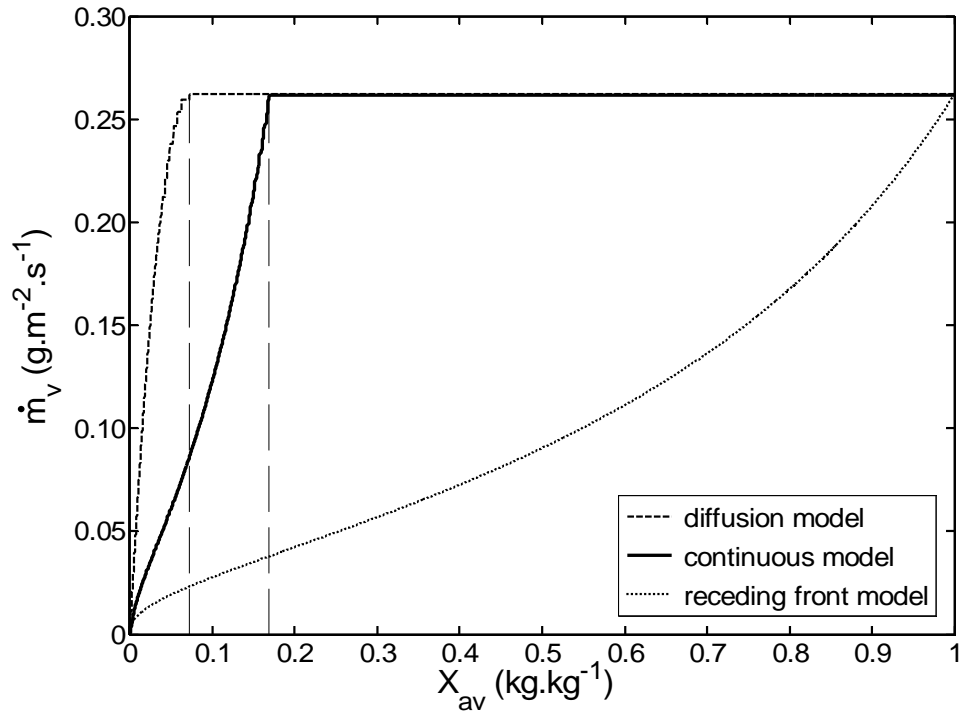***Figure 4.39*** Evaporation rates for isothermal drying of a spherical particle
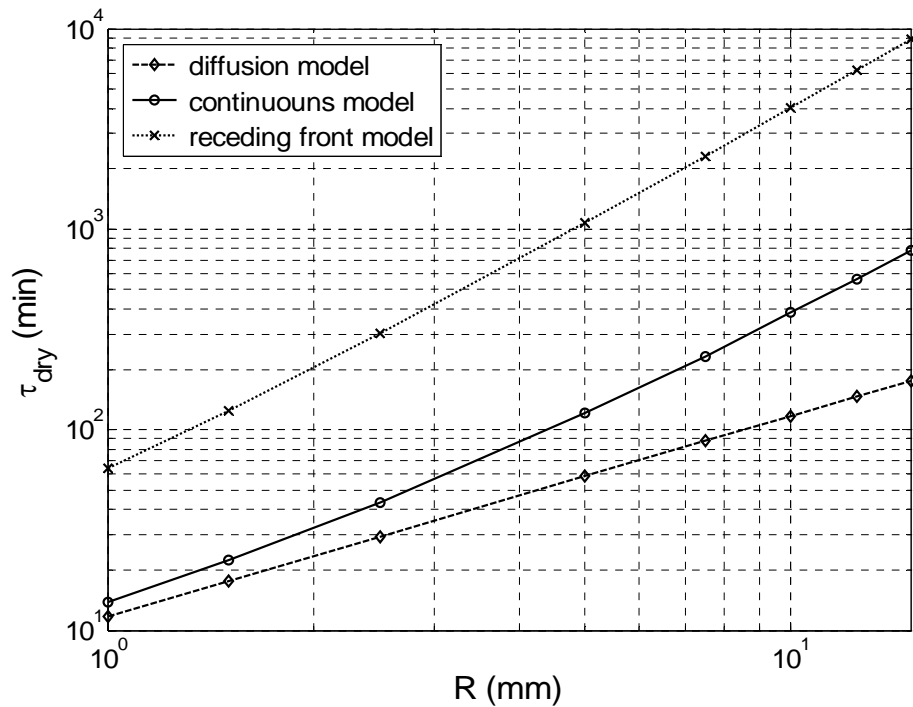($R = 2.5$ mm, $T_\infty = 20^\circ$C, $\varphi = 0$).

Figure 4.40 Influence of sample size: drying time versus sample size for $X_{end} = 10^{-3}$
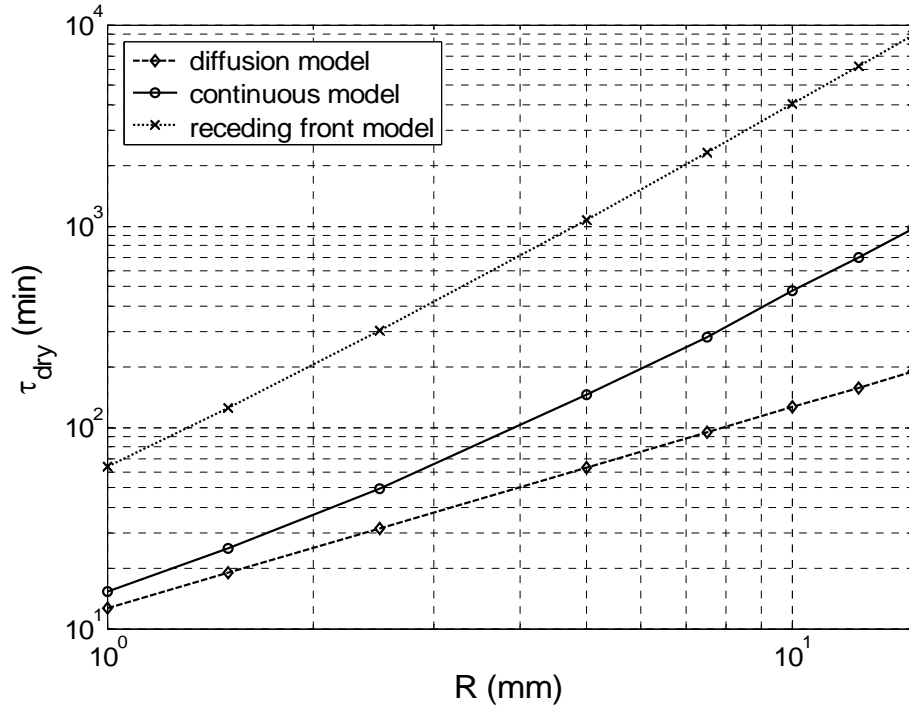(isothermal drying $T_\infty = 20^\circ$C, $\varphi = 0$).

Figure 4.41 Influence of sample size: drying time versus sample size for $X_{end} = 10^{-5}$
(isothermal drying $T_\infty = 80°C$, $\varphi = 0$).

4.5. Drying simulation for a bundle of capillaries and influence of pore size distribution on drying behaviour

In this section, the influence of pore size distribution on drying behaviour is considered by using a bundle of capillaries (with mono-modal and bimodal pore size distributions) to calculate the material properties (capillary pressure, absolute and relative permeabilities) as presented in Section 2.5. Comparisons between the continuous and discrete (using the capillary model of Metzger and Tsotsas [55] and the isothermal network model of Irawan *et al.* [30]) approaches are made for the drying of a plate. Instead of moisture content X, saturation S will be used in this section.

4.5.1. Material properties and drying conditions

For all investigated cases, the porosity of the material is $\psi = 0.5$, the heat capacity is $\overline{\rho C_p} = \varepsilon_s \rho_s \left(2000 + 4185X \right)$ J.kg^{-1}.K^{-1}. The solid has the density $\rho_s = 1000$ kg.m^{-3} and its thermal conductivity is $\lambda_s = 1$ W.m^{-1}.K^{-1}. The effective model parameters are computed from the bundle capillary model (see Section 2.5). The maximum amount of adsorbed water (linked to the irreducible moisture content X_{irr}) is chosen as $S_{sorb} = 15\%$ so that we can consider the material as hygroscopic. Initial saturation and temperature of the sample under consideration are $S_0 = 0.9$ and $T_0 = 20°C$. The pressure of the drying air is $P_\infty = 1$ bar, and, if not indicated otherwise, the drying air has zero moisture content and temperature $T_\infty = 80°C$.

4.5.2. *Drying simulation for a sphere*

The mono-modal pore size distribution is applied here in the drying simulation of a sphere with its radius $R = 2.5$ mm. The heat and mass transfer coefficients of the boundary layer are $\alpha = 14.25$ W.m^{-2}.K^{-1} and $\beta = 0.015$ m.s^{-1}, respectively. The mean capillary radius is $r_0 = 100$ nm and the standard deviation of radius is $\sigma_0 = 10$ nm. The mesh used in calculations is a geometric progression mesh with 51 grid nodes and mesh ratio $m_{ratio} = 0.2$.

The temporal evolution of saturation for approximately every 0.5 mm in distance (corresponding to nodes 1, 6, 13, 21, 33 and 51 from the centre to the surface) together with the evolution of average saturation (dashed fat curve) are shown in Figure 4.42. The profiles of saturation, temperature and pressure for different drying times are presented in Figure 4.43 to Figure 4.45. The saturation profiles are plotted at the times when the average saturation S_{av} has the values 0.8, 0.6, 0.4, 0.2, 0.1 (corresponding to drying time of 2.3, 6.8, 10.7, 15.0 and 17.3 min), at the end of the first drying period (where the critical saturation is $S_{cr}=0.1553$) and at the time when $S_{fw} = 0$. We can see that the saturation and temperature profiles are quite flat (Figure 4.43 and Figure 4.44) and there exists an over-pressure in the second period (Figure 4.45). It is found that the influence of pore size distribution on drying behaviour is not clearly visible due to the small size of the sample. Therefore in the following sections the drying of a plate with considerable thickness is examined.
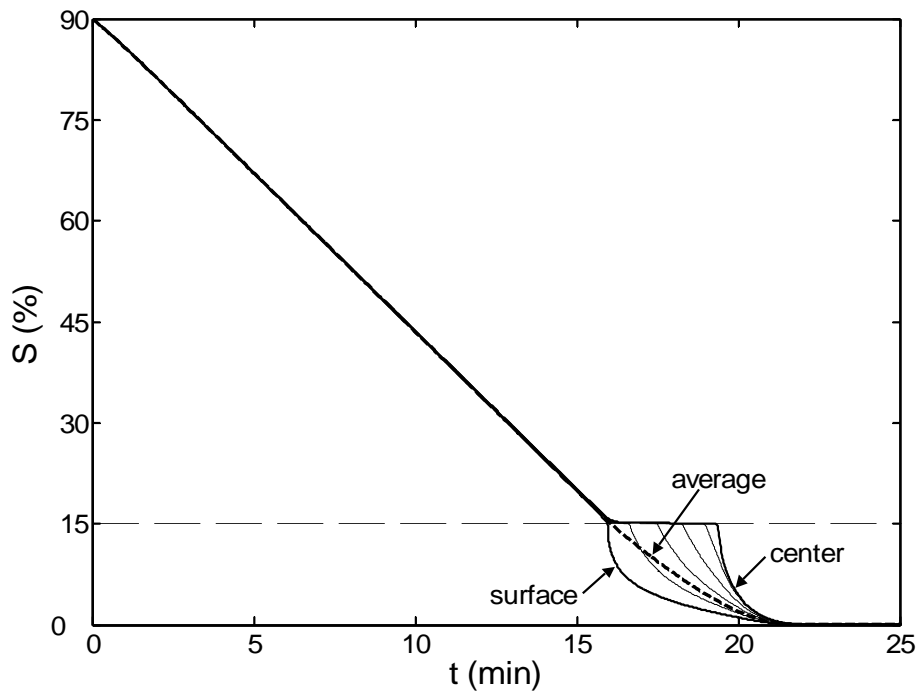

Figure 4.42 Drying of a sphere with bundle of capillaries pore geometry: temporal evolution of saturation (for $T_\infty = 80^{\circ}$C and $\varphi = 0$).
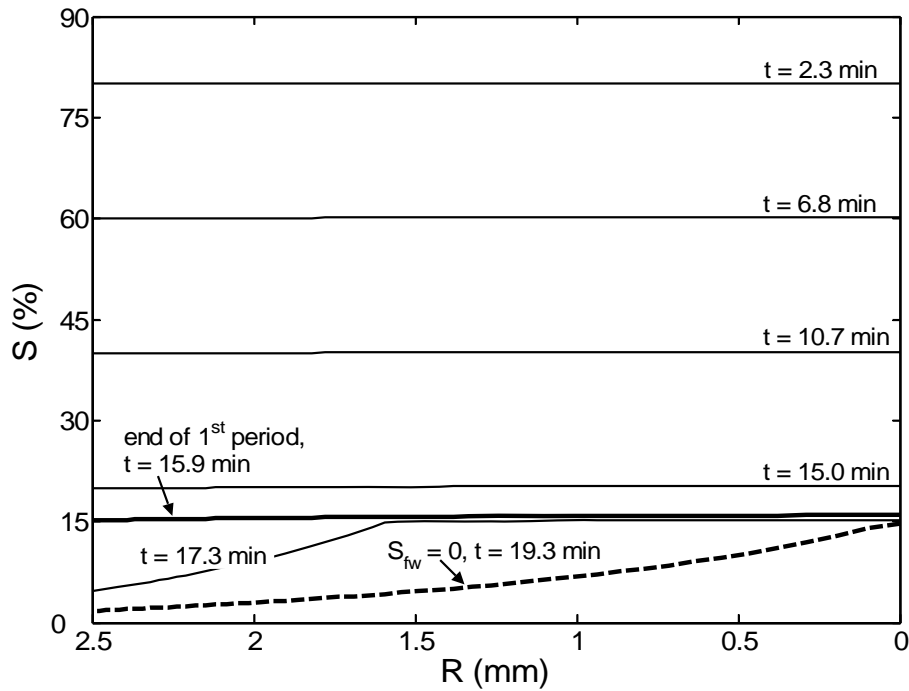
Figure 4.43 Drying of a sphere with bundle of capillaries pore geometry: saturation profiles (for $T_\infty = 80^\circ$C and $\varphi = 0$).
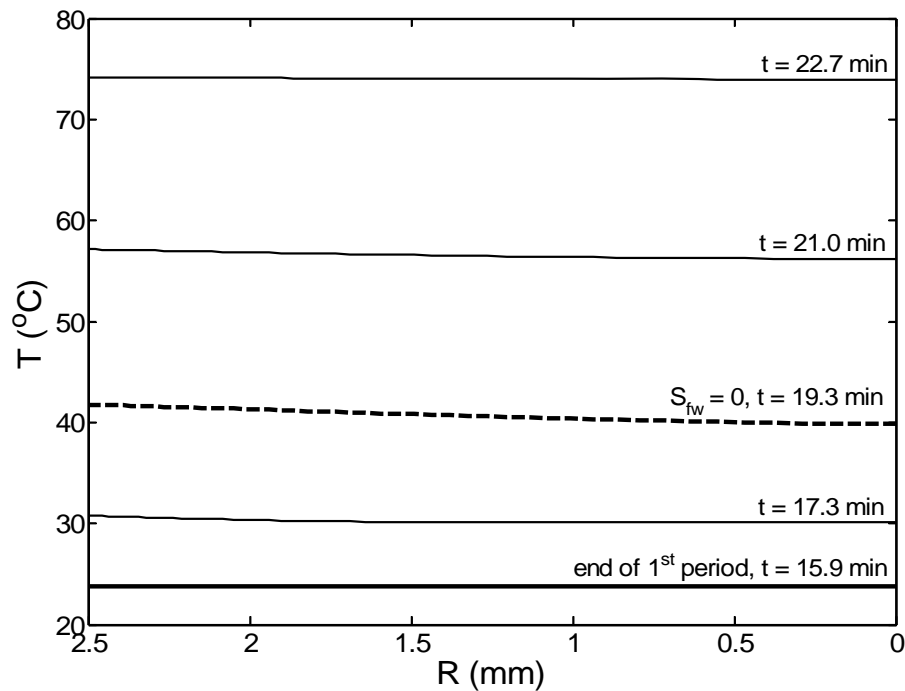
Figure 4.44 Drying of a sphere with bundle of capillaries pore geometry: temperature profiles (for $T_\infty = 80^\circ$C and $\varphi = 0$).
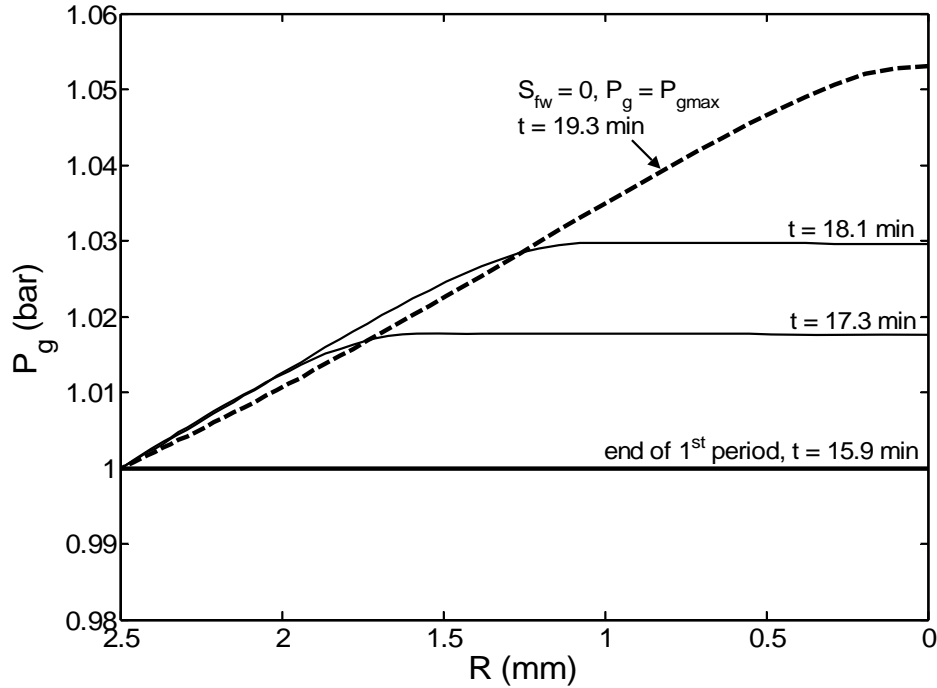
Figure 4.45 Drying of a sphere with bundle of capillaries pore geometry: pressure profiles (for $T_\infty = 80^oC$ and $\varphi = 0$).

4.5.3. Drying simulation for a plate

In this section, the drying of a plate with sample size of 100 mm (from the impermeable plane to the external surface) is considered. In all investigated cases, the heat and mass transfer coefficients are $\alpha = 95$ W.m^{-2}.K^{-1} and $\beta = 0.1$ m.s^{-1}, respectively. The mesh used in our calculations has 41 grid nodes with mesh ratio $m_{ratio} = 0.2$. Six cases with two types of pore size distribution (mono-modal and bimodal) with different mean pore radius r_0 and different standard deviation σ_0 are investigated. Information about the pore size distributions of these six cases and the corresponding absolute permeabilities is reported in Table 4.9. Additionally, some other cases of mono- and bi-modal pore size distributions are taken into account to investigate the influence of pore volume fractions of two modes and the influence of effective transport parameters. Details of these cases will be discussed later on. Two examples of the mono-modal (100 ± 5 nm) and bimodal (100 ± 10 nm; 200 ± 20 nm) pore size distributions with modification (see Appendix 3) are given in Figure 4.46 and Figure 4.47.

Table 4.9 Studied pore size distributions and corresponding absolute permeabilities.

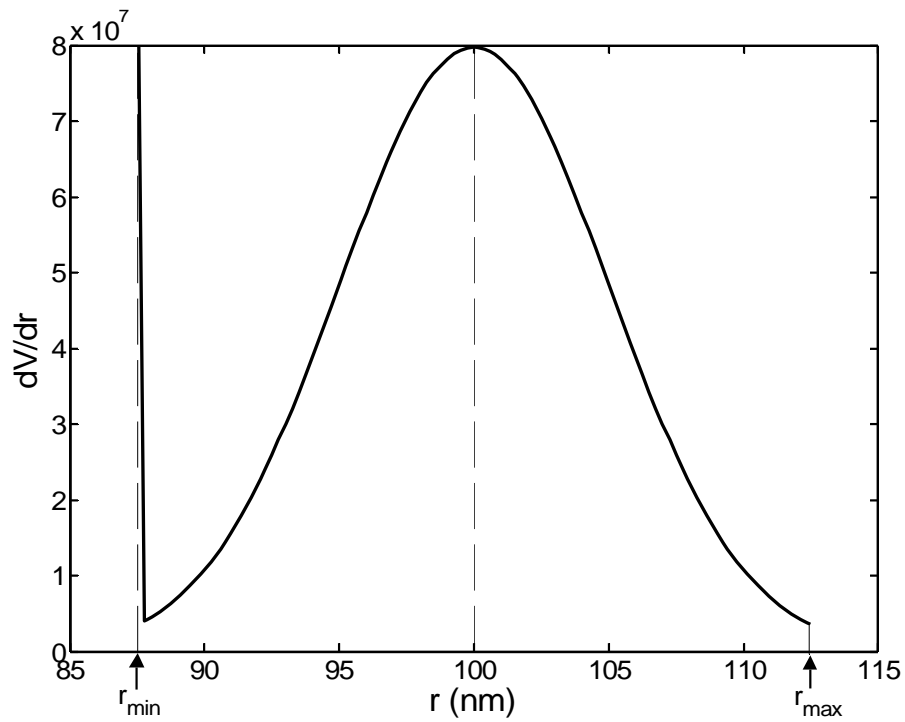|	$r_0 \pm \sigma_0$ (nm)	K ($\cdot 10^{-15}$ m^2)	
Case 1	100 ± 5	1.238	*Mono-modal*
Case 2	100 ± 20	1.280	
Case 3	200 ± 20	4.986	
Case 4	1000 ± 100	124.6	
Case 5	100 ± 10; 200 ± 20	3.119	*Bimodal*
Case 6	100 ± 10; 2000 ± 200	245.1	

Figure 4.46 Mono-modal pore size distribution (case 1: 100 ± 5 nm).
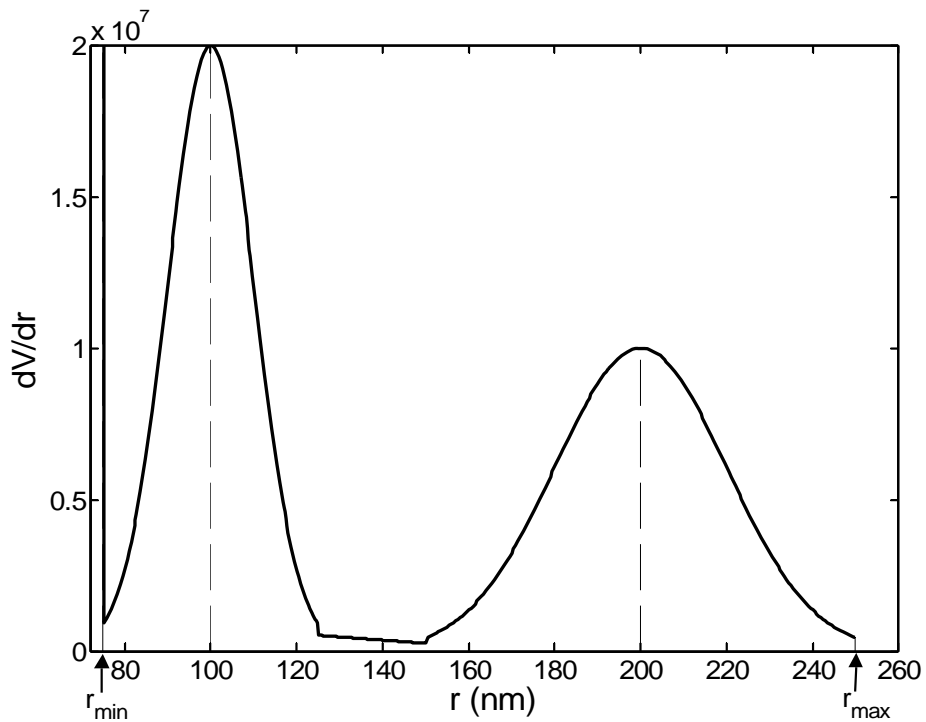

Figure 4.47 Bi-modal pore size distribution (case 5: 100 ± 10 nm; 200 ± 20 nm).

4.5.3.1. *Mono-modal pore size distributions*

The temporal evolution of saturation (together with average saturation – dashed fat curves), temperature and gas pressure for approximately every 20 mm in distance in the porous medium for case 1, 2, 3 and 4 are shown in Figure 4.48.a÷c. The corresponding saturation profiles with step equal to 10% of total saturation are presented in Figure 4.48.d, where z is the depth from the exchange surface. In these figures, the fat solid curves represent the end of the first drying period (S_{cr} = 0.670, 0.417, 0.395 and 0.230 corresponding to drying times of 1.5 h (case 1), 3.1 h (case 2), 3.3 h (case 3) and 4.3 h (case 4), respectively), the dashed fat curves represent the situations at which all free water has been moved from the sample (S_{fw} = 0, corresponding to drying times of 37.5 h (case 1), 28.5 h (case 2), 25.7 h (case 3) and 21.3 h (case 4), respectively). The drying rate curves are given in Figure 4.50.

For small pores with a narrow distribution (case 1), the first drying period is short (Figure 4.50), significant gas pressure gradients occur in the second period (Figure 4.48.c, case 1) and saturation gradients are relatively steep throughout the drying process (Figure 4.48.d, case 1). The large pore case with a broad distribution (case 4) has a long first drying period (Figure 4.50). Pressure and moisture gradients in this case are much smaller (Figure 4.48.c and Figure 4.48.d, case 4). It is observed that the standard deviation σ_0 has a strong effect on drying. For the same mean capillary radius r_0, the sample with small standard deviation (narrow mode, case 1) has steeper saturation gradients (Figure 4.48.d) and shorter first drying period (Figure 4.50) as compared to the sample with large standard deviation (broader mode, case 2). For the same value of σ_0, the variation of r_0 leads to changes in gas over pressure (Figure 4.48.c, case 2 and case 3), but has only a small effect on moisture profiles; and the first drying period is slightly shorter if r_0 is smaller (Figure 4.50). Considering the temperature evolution, it is found that the variation of the pore size distribution has little effect: only the wet bulb temperature prevails longer if the surface stays wet for longer (with larger pores) (Figure 4.48.b).
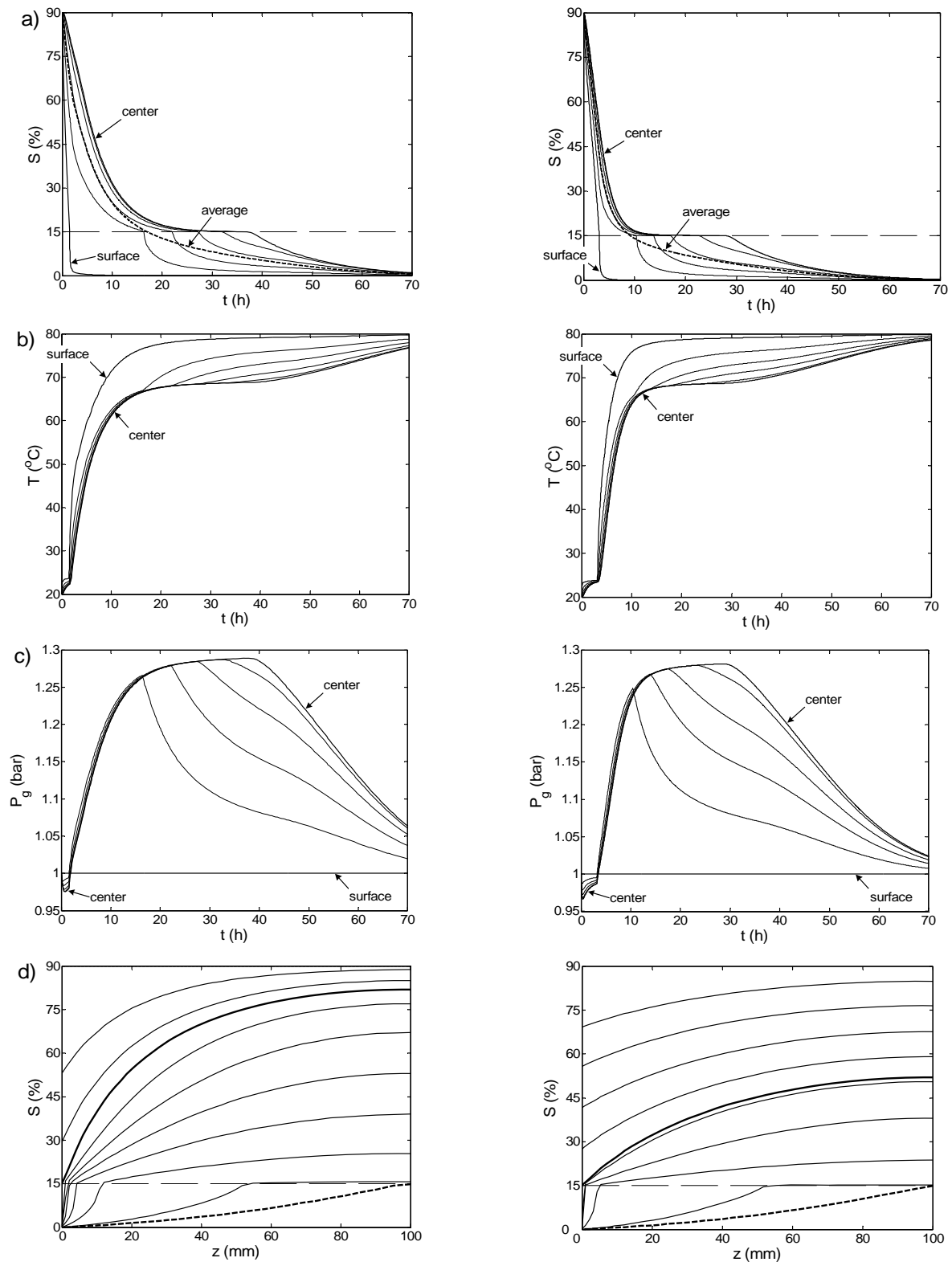
Figure 4.48 Drying a plate with bundle of capillaries pore geometry (mono-modal, $T_\infty = 80^{\circ}C$, $\varphi = 0$): a) temporal evolution of saturation; b) temporal evolution of temperature; c) temporal evolution of pressure; d) saturation profiles. First column: case 1 (100 ± 5 nm), second column: case 2 (100 ± 20 nm).
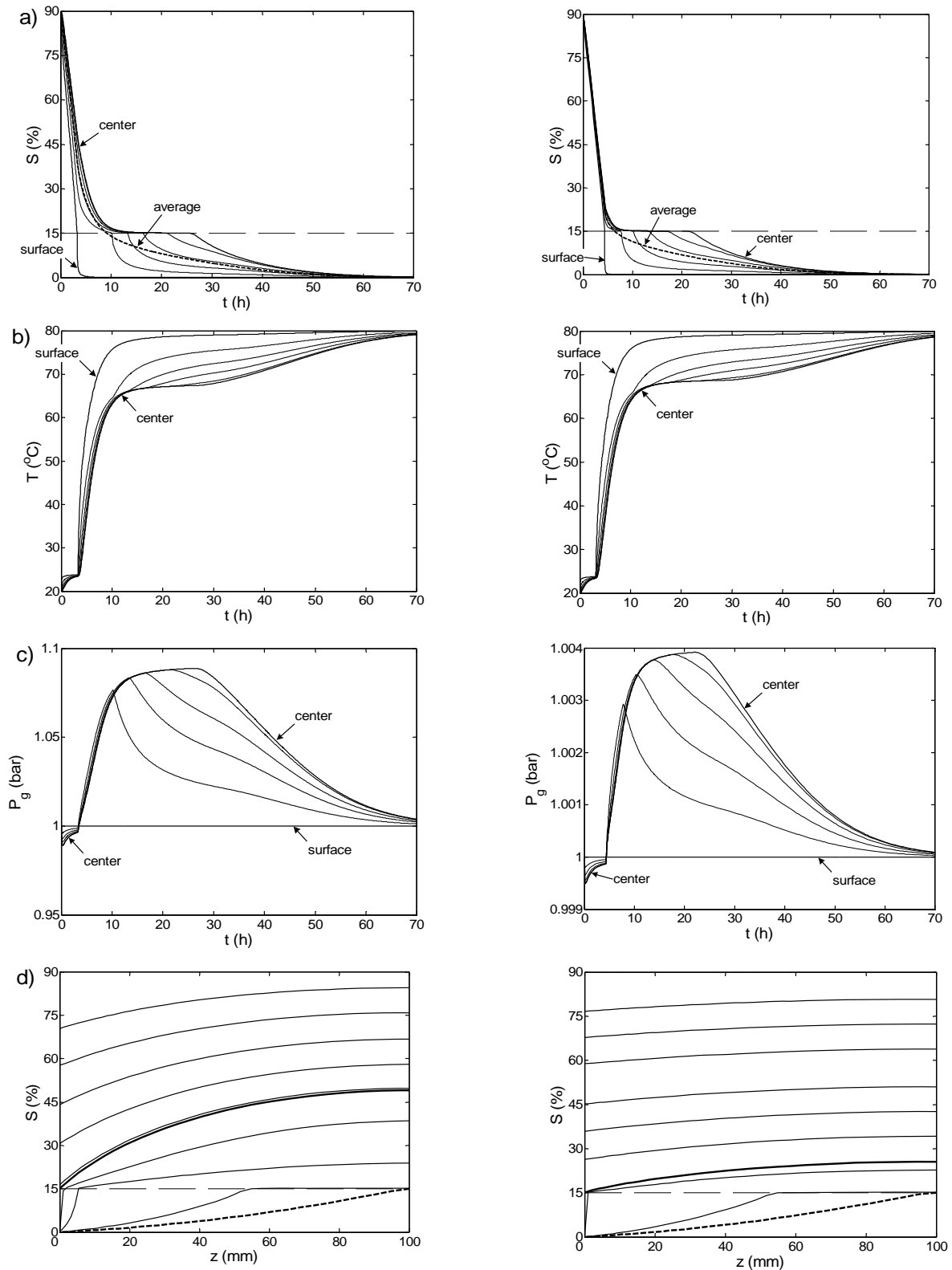
Figure 4.48 (Continued):
a) temporal evolution of saturation; b) temporal evolution of temperature;
c) temporal evolution of pressure; d) saturation profiles
First column: case 3 (200 ± 20 nm), second column: case 4 (1000 ± 100 nm).

4.5.3.2. *Bimodal pore size distributions*

Results for two cases of bimodal pore size distributions (case 5 and case 6) are given in Figure 4.49. In Figure 4.49.d the saturation profiles with step equal to 10% of total saturation are presented together with the saturation profile at the end of the first drying period (fat solid curve) and the saturation profile when all free water in the sample has been removed (dashed fat curve). The overall drying curve is shown in Figure 4.50. In our considered cases of bimodal pore size distributions, 4% of the total pore volume is assigned to the transition zones between the two modes (see Appendix 3). For convenience, in this section the concept of *micro* pore and *macro* pore will be used to present the small and large pores, respectively.

From the numerical results, it can be seen that the *macro* pores dry out completely at the high drying rate of the first period with small or even negligible saturation gradients (for case 5 or 6, respectively) because of small resistance. In the transition region, the saturation profile is flat in both cases (Figure 4.49.a). During the drying of the *micro* pores (narrow mode), steeper gradients develop and the second drying period starts (see Figure 4.49.d below fat curves). With a more important difference in size between the two modes and a broader large mode (case 6), the saturation profiles are even flatter during the drying of the *macro* pores (Figure 4.49.d above transition region), but the overall drying curve is unchanged (Figure 4.50).

Due to the fact that almost all *macro* pores are emptied in the first drying period, the distribution of *macro* pore usually plays no role, but the volume fraction of *macro/micro* pores (see Section 4.5.3.3 below) and the distribution of the *micro pores* are important since they define how much liquid can be removed in the first drying period. One may say that the *macro* pores in a bimodal distribution can significantly prolong the first drying period and we have better gas convection in larger *macro* pores. Therefore, the critical saturation $S_{cr} = 0.410$ is identical for both cases and is reached at the same time (after 3.2 hours of drying); the sample with smaller *macro* pore size (case 5) needs more time to remove all the free water (27.3 hours compared to 25.4 hours of case 6).

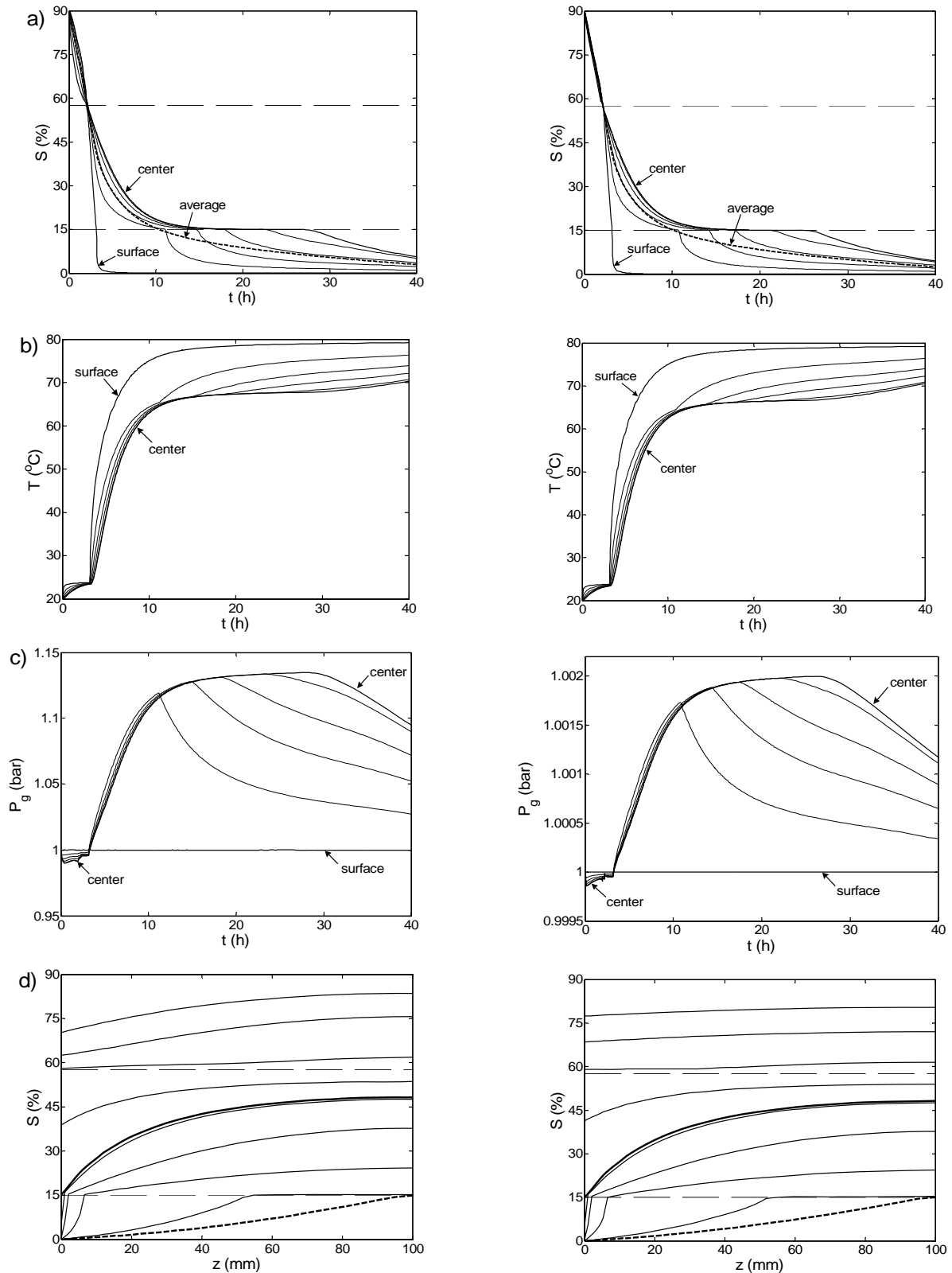**Figure 4.49** Drying of a plate with bundle of capillaries pore geometry (bimodal, $T_\infty =$ 80°C, $\varphi = 0$): a) temporal evolution of saturation. b) temporal evolution of temperature. c) temporal evolution of pressure. d) saturation profiles. First column: case 5 (100 ± 10 nm; 200 ± 20 nm); second column: case 6 (100 ± 10 nm; 2000 ± 200 nm).
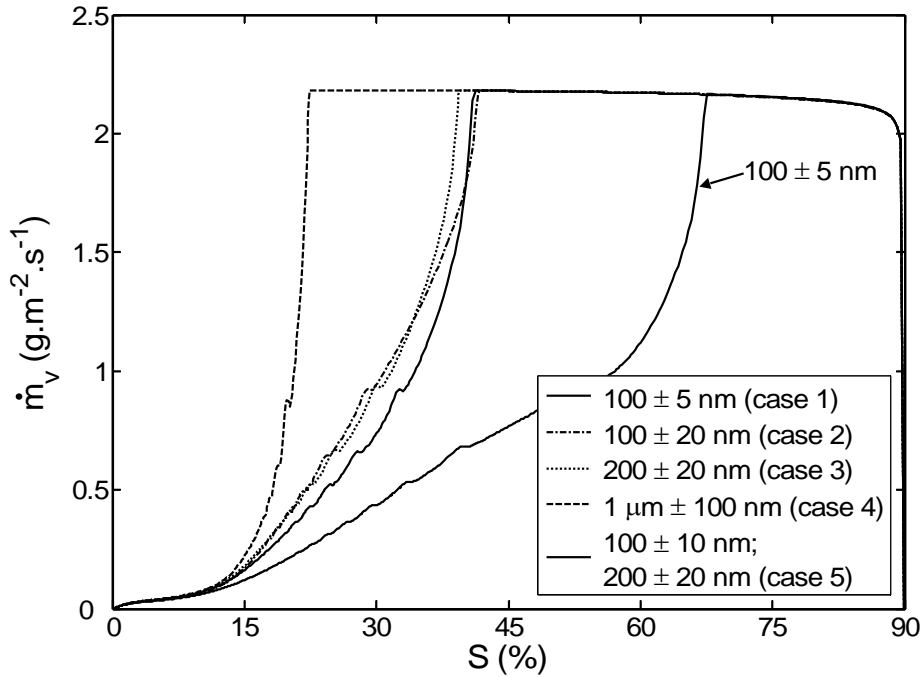
109

Figure 4.50 Drying curves for different pore size distributions (for $T_\infty = 80^\circ$C, $\varphi = 0$; case 6 with 100 ± 10 nm and 2000 ± 20 nm yields same curves as case 5).

4.5.3.3.   *Influence of pore volume fractions of two modes*

Like in the above section, the concept of *micro* and *macro* pores is also used here. In order to investigate the influence of the volume fraction of the *macro* and *micro* pores, we consider a bimodal distribution in which the *micro* capillaries have a radius of 100 nm with a standard deviation of either 5 nm or 25 nm; the *macro* pores have a radius of 500 nm with a standard deviation of 50 nm. Information about the different volume fractions used in our investigation and the corresponding critical saturation S_{cr} together with absolute permeability K is given in Table 4.10.

Table 4.10 Pore volume fraction and corresponding values.

	$r_0 \pm \sigma_0$ (nm)	V_{macro} (%)	V_{micro} (%)	V_{macro}/V_{micro}	S_{cr} (%)	K ($\cdot 10^{-15}$ m^2)
Case 1	100 ± 5; 500 ± 50	48	48	1.0	46.71	15.97
		81	15	5.4	26.93	26.03
		15	81	1.0/5.4	60.92	5.96
Case 2	100 ± 25; 500 ± 50	48	48	1.0	33.34	16.11
		81	15	5.4	24.61	26.17
		15	81	1.0/5.4	37.34	6.10

Note that in all cases, 4% of the total pore volume is assigned to the transition zones between the two modes. The obtained results are presented in Figure 4.51 and Figure 4.52. In these figures, the fat vertical curves indicate the moment where *micro* pores start to be emptied (*macro* pores and transition region are "inactive"). Clearly, for these

110

two cases, all macro pores have been dried in the first drying period. The results from these figures also give us the fractions of small pores, which are emptied in the first drying period. For case 1, they are 22.1%, 6.6%, and 34.2% for the case of $V_{macro} = V_{micro}$; $V_{macro} = 5.4 \cdot V_{micro}$ and $5.4 \cdot V_{macro} = V_{micro}$, respectively. For case 2, these values are 55.3%, 25.1% and 68.5%.

It is found that the length of the first drying period mainly depends on the volume fraction of the *macro* pore: the higher the amount of *macro* pores, the longer the first drying period since big pores are favourable for drying. Besides, the drying rate in the second period is higher for larger volume fraction of *macro* pores. However, the first drying period can also be influenced by the pore size distribution of the *micro* pores. For a sample with a broader distribution of the *micro* pores (case 2), the first drying period is longer and the drying rate in the second period is higher (Figure 4.52). Similar conclusions were found by Metzger and Tsotsas (2005 [55]).
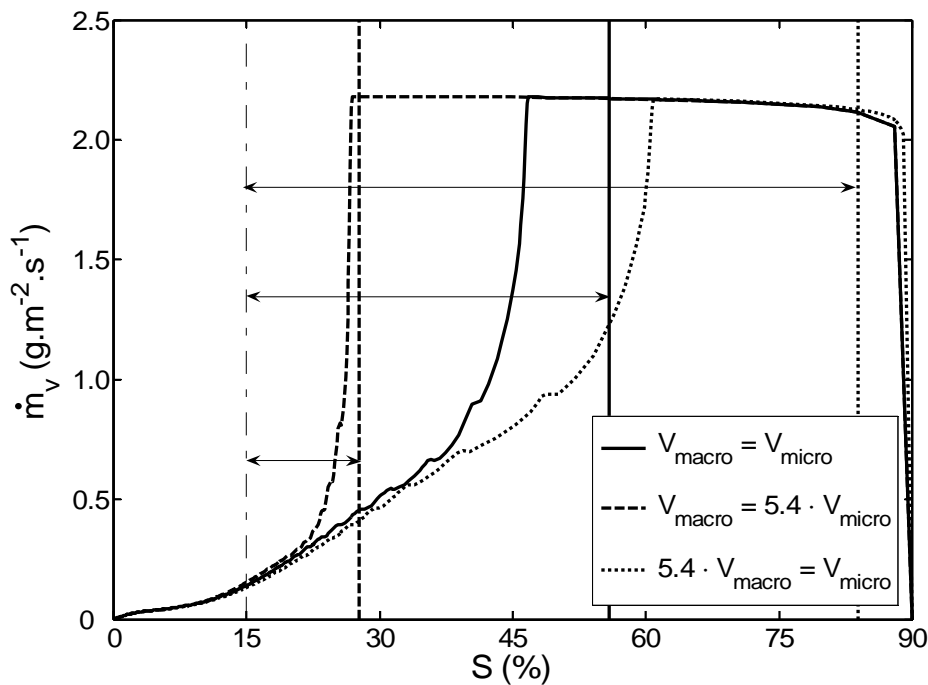

Figure 4.51 Drying of a plate with bundle of capillaries geometry at $T_\infty = 80^{\circ}C$ and $\varphi = 0$ (case 1: 100 ± 5 nm; 500 ± 50nm): drying curves for different volume ratio V_{macro}/V_{micro}.
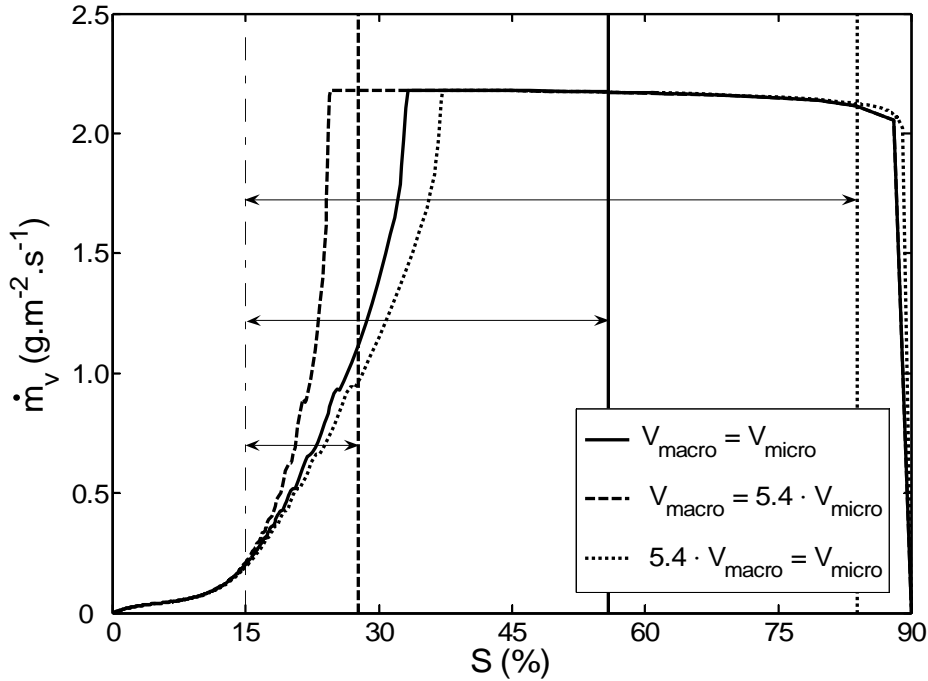
Figure 4.52 Drying of a plate with bundle of capillaries geometry at
$T_\infty = 80^\circ$C and $\varphi = 0$ (case 2: 100 ± 25 nm; 500 ± 50nm): drying curves for different
volume ratio V_{macro}/V_{micro}.

4.5.3.4. Influence of effective transport parameters with bundle of capillaries pore geometry – Parametric study (continued)

To see how the transport parameters influence the drying behaviour of a plate with bundle of capillaries pore geometry, we take the mono-modal pore size distribution (normal distribution with $r_0 = 100$ nm and $\sigma_0 = 10$ nm) as the reference case and vary the transport parameters (thermal conductivity of solid λ_s, absolute permeability K and effective diffusivity D_{eff}) one by one. The results are shown in Figure 4.53. It is observed that an increase of the solid thermal conductivity slightly slows down the initial warming up of the sample's surface and increases the drying rate in the second drying period since heat is better transferred to the place of evaporation. A reduction of the absolute permeability (by decrease of pore size) dramatically shortens the first drying period whereas a decrease in the effective diffusivity (by introducing tortuosity) only reduces the already low drying rates at the end of the second period when adsorbed water removal dominates the drying process. These results are very similar to those obtained for a sphere of concrete (see 4.4.7).
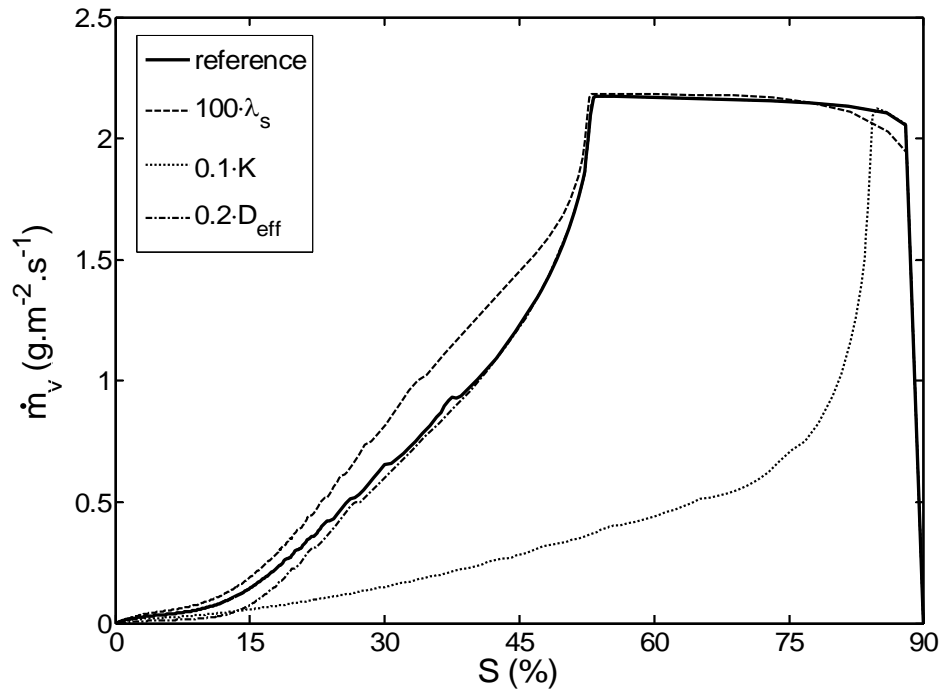
Figure 4.53 Drying of a plate with bundle of capillaries geometry at $T_\infty = 80°C$ and $\varphi = 0$ (mono-modal pore size distribution, 100 ± 10 nm): influence of effective parameters on drying behaviour.

4.5.3.5. Influence of drying air conditions (continued)

The influence of the drying conditions is now studied by keeping the above reference case ($r_0 \pm \sigma_0 = 100 \pm 10$ nm) and varying the temperature T_∞ and the relative humidity φ of drying air as well as the mass transfer coefficient β. The results are introduced in Figure 4.54. The well-known fact is confirmed that hotter and drier air with higher velocity (i.e. higher transfer coefficients) produces higher drying rates in the first period, but shortens its duration. It is noted that the results obtained here are very similar to those obtained for the drying of a sphere of light concrete (see Section 4.4.8).
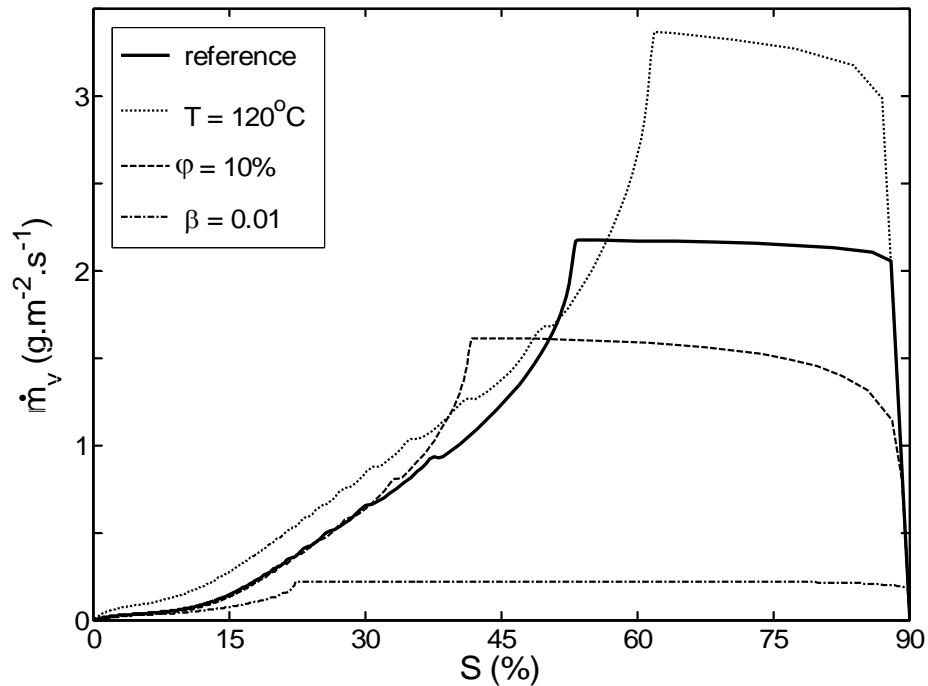
Figure 4.54 Drying of a plate with bundle of capillaries geometry at
$T_\infty = 80^{\circ}C$ and $\varphi = 0$ (mono-modal pore size distribution, 100 ± 10 nm): influence of drying conditions.

4.5.4. Comparison between continuous and discrete approaches using a bundle of capillaries
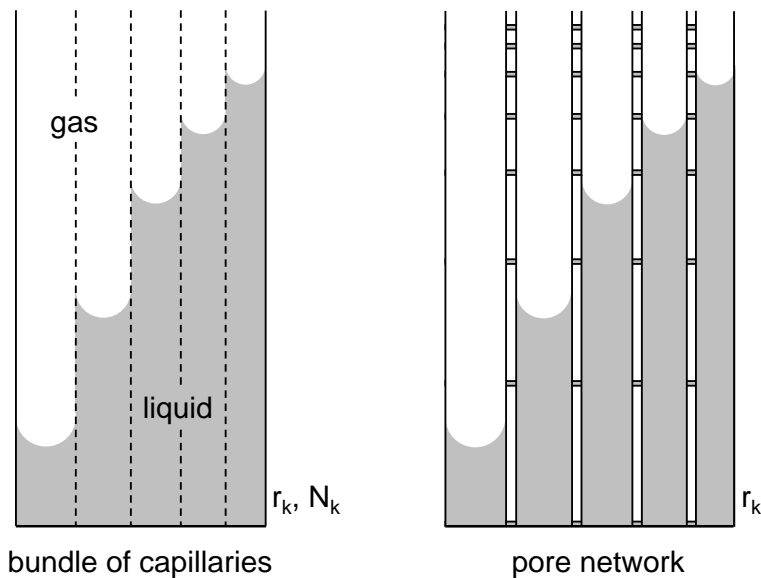
Figure 4.55 Two types of discrete model (Irawan *et al.*, 2006 [30]).

The continuous approach used in this work is now compared with the discrete approach represented here by two discrete models depicted in Figure 4.55. The first discrete

model is a one-dimensional (1D) isothermal capillary model presented by Metzger and Tsotsas (2005 [55]). In this model, the porous medium is represented by a bundle of capillaries with a radius distribution. The second is an isothermal pore network model introduced by Irawan *et al.* (2006 [30]). For the sake of clarity, the continuous model using a bundle of capillaries pore geometry (see Chapter 2) is called the continuous capillary model and the discrete 1D capillary model of Metzger and Tsotsas (2005 [55]) is called the discrete capillary model. In the two discrete models considered here, the transport mechanism of liquid is viscous capillary pumping and the transport mechanism of gas is vapour diffusion. Lateral resistances between the capillaries and in the boundary layer are entirely neglected in the 1D capillary model and made negligible in the network model. In the pore network model, the horizontal throats are short and have small radii, which assure that their volume can be neglected and that they empty last guaranteeing a continuous liquid phase for capillary pumping at all times (see Irawan *et al.*, 2006 [30]).

In order to compare with the discrete models, we consider the drying of a plate with sample size of 100 mm (from the impermeable plane to the external surface). A geometric progression mesh of 101 grid nodes with mesh ratio $m_{ratio} = 0.2$ is used. Convective drying by a flow of absolutely dry air at $T_\infty = 20°C$ and atmospheric pressure is applied. To set the isothermal condition, we enhance heat transfer by setting $\alpha = 6000$ W/m^2/K and $\lambda_s = 6000$ W/m/K. For $T_\infty = 20°C$, the *imaginary* wet bulb temperature is 19.3°C (to be used in isothermal model) and gas pressure varied only by 20 mbar as compared to being constant in the two discrete models. The amount of adsorbed water is set to $S_{irr} = 1\%$ to approach the case of no sorption in the discrete models.

4.5.4.1. *Comparison with discrete capillary model*

In this section, one case of mono-modal pore size distribution ($r_0 \pm \sigma_0 = 100 \pm 10$ nm) is used in the continuous capillary model. The numerical results (Figure 4.56 and Figure 4.57) show that the continuous model yields a slightly longer first drying period and flatter moisture profiles than the discrete one. The divergence of the two models may be explained by two differences in modelling. The first one concerns the discretization process: in the discrete capillary model, the pore size distribution is represented by discrete capillary classes with menisci continuously moving in space whereas in the continuous model only space is discretized. At the end of the first period, the last meniscus moves back from the surface and a small additional distance to vapour diffusion can immediately cause a dramatic drop in drying rate. In the discrete capillary model, the meniscus can move to any distance whereas in the continuous model the whole surface element (0.2 mm in size) must dry below S_{sorb} before the drying rate drops. The second difference is that the no-flux condition of the continuous model for the impervious boundary (which leads to locally vanishing moisture gradients) does not exist in the capillary model. Instead, menisci disappear one by one at the bottom, rather imposing a (capillary) pressure boundary condition (Vu, Metzger and Tsotsas, 2006 [112]).
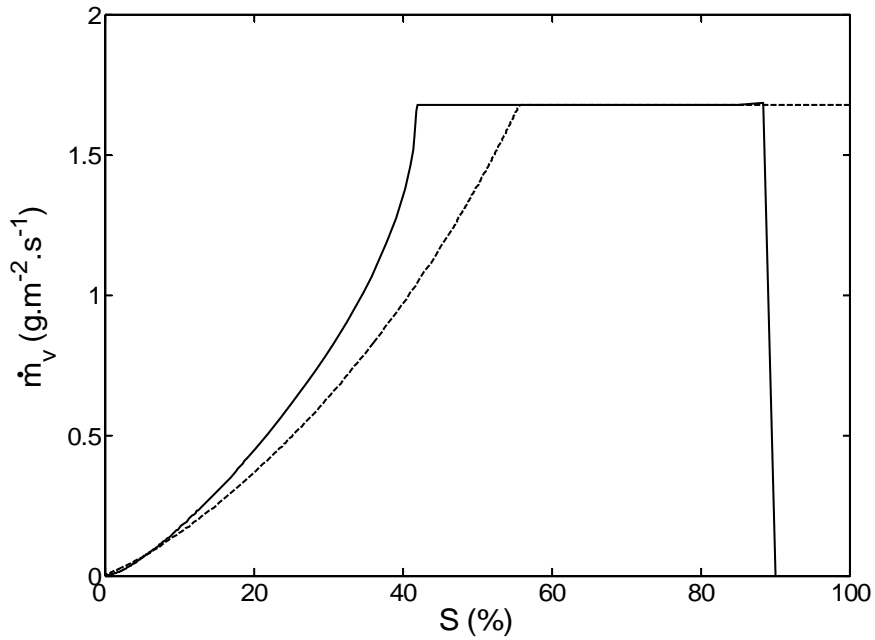
Figure 4.56 Drying of bundle of capillaries with $r_0 \pm \sigma_0 = 100 \pm 10$ nm:
drying rate curves for continuous (solid line) and discrete (dashed line) capillary model
($T_\infty = 19.3^{\circ}$C, $\varphi = 0$).

Figure 4.57 Drying of bundle of capillaries with $r_0 \pm \sigma_0 = 100 \pm 10$ nm:
saturation profiles in steps of 10% of total saturation for continuous (solid lines) and
discrete (dashed lines) capillary model ($T_\infty = 19.3^{\circ}$C, $\varphi = 0$).

4.5.4.2. Comparison with pore network model

The continuous model is compared with the pore network model for isothermal drying. Mono-modal pore size distributions are used. Information about the pore size distributions and the critical moisture content is given in Table 4.11.

Table 4.11 Critical moisture content of continuous and pore network model.

$r_0 \pm \sigma_0$ (nm)	S_{cr} (%)	
	Continuous model	Pore network model
$100 \pm\ \ 5$ nm	57.29	61.74
100 ± 10 nm	42.19	44.56
100 ± 25 nm	26.26	28.19

The numerical results are presented in Figure 4.58 by plotting the normalized drying rate versus saturation. Figure 4.59 depicts saturation profiles at the end of the first drying period and Figure 4.60 shows saturation profiles for the drying with 100 ± 10 nm pore size distribution. From the numerical results, it is observed that simulation using the continuous capillary model gives a slightly longer first drying period and slightly flatter moisture profiles than those obtained by the network model. This is similar to the observation obtained when comparing the continuous and discrete capillary models. However, the simulation results obtained by the continuous capillary model are much closer to the results obtained by the network model than to those obtained by the discrete capillary model. The non-smooth curves of the pore network model are due to assumption that partially filled throats have no resistance to vapour diffusion.
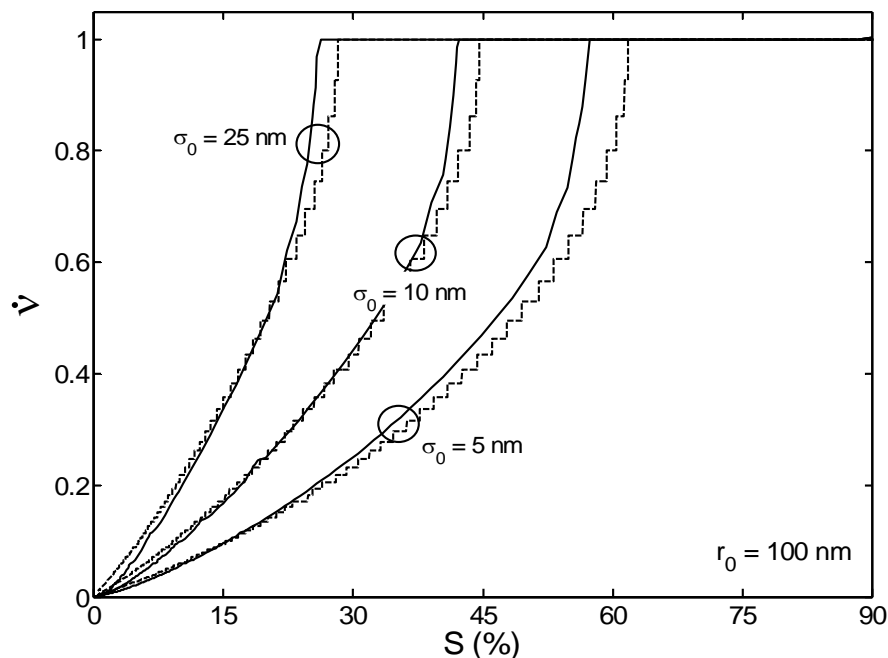
Figure 4.58 Drying of bundle of capillaries with $r_0 = 100$ nm and different standard deviations of capillary radius σ_0: evaporation rates for continuous (solid lines) and network (dashed lines) model (for $T_\infty = 19.3^\circ$C, $\varphi = 0$).
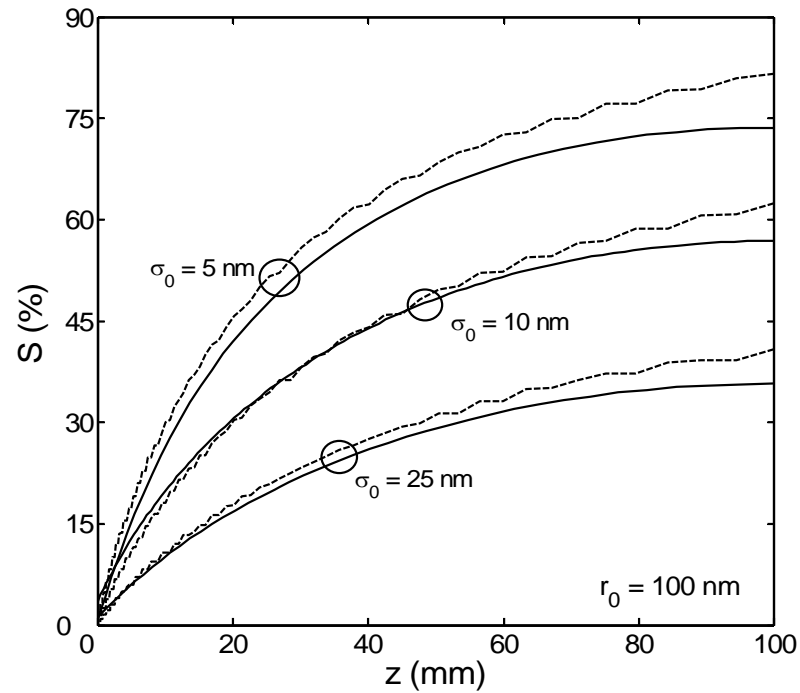
Figure 4.59 Drying of bundle of capillaries with $r_0 = 100$ nm and different standard deviations of capillary radius σ_0: saturation profiles at the end of first drying period for continuous (solid lines) and network (dashed lines) model ($T_\infty = 19.3^\circ$C, $\varphi = 0$).
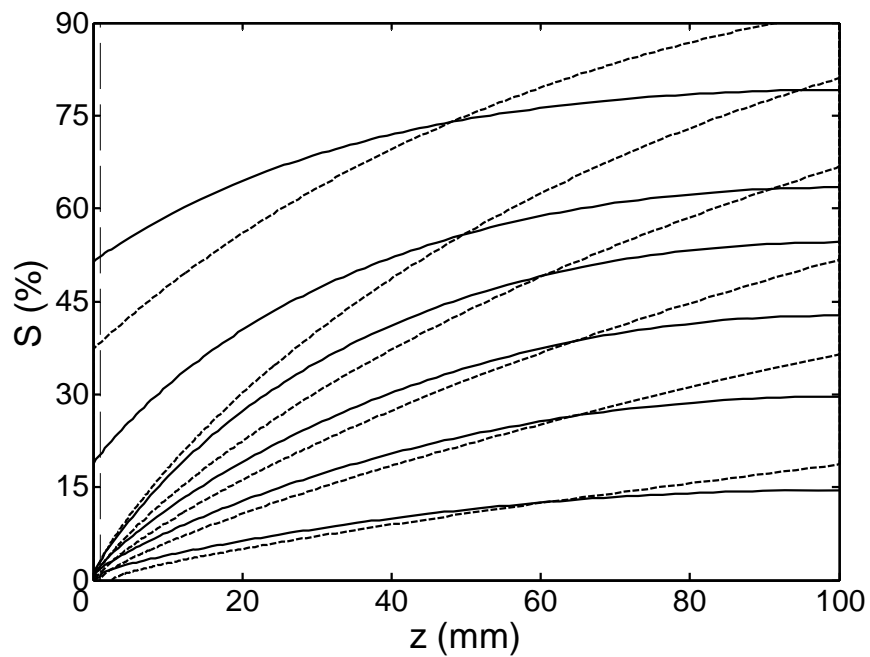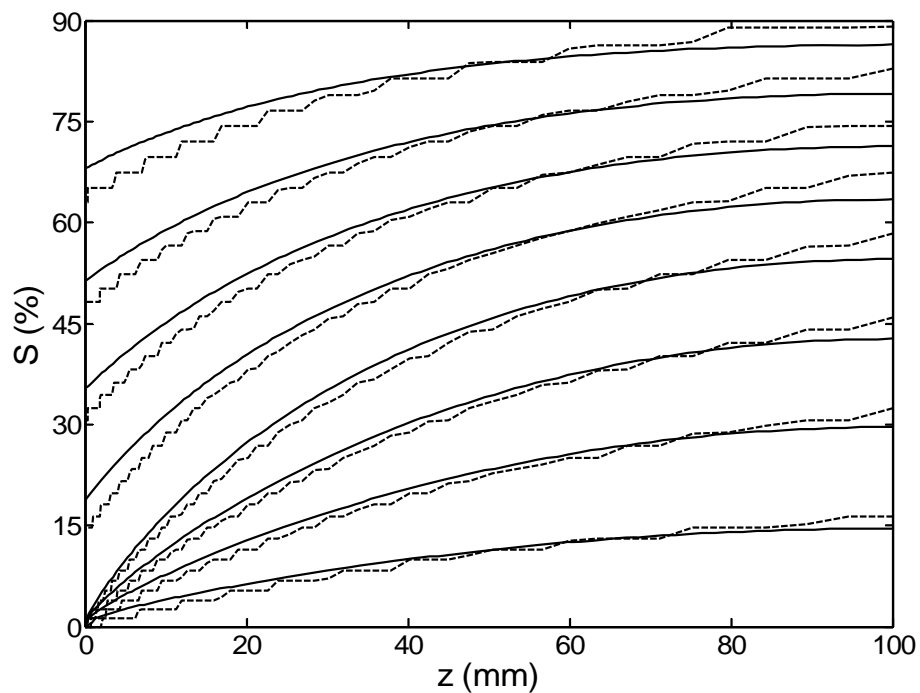

Figure 4.60 Drying of bundle of capillaries with $r_0 \pm \sigma_0 = 100 \pm 10$ nm: saturation profiles in steps of 10% of total saturation for continuous (solid lines) and network (dashed lines) model ($T_\infty = 19.3^\circ$C, $\varphi = 0$).

To summarize, in this chapter, numerical results of the drying simulation of porous media are presented. The accuracy of the numerical simulations is tested by considering the influence of the space discretization and by considering the overall conservation behaviour (of water and air). It is found that a good accuracy could be achieved. Numerical simulations of a sphere and a plate of light concrete show that the employed model is able to capture different drying characteristics of porous media such as the constant drying rate period, the falling rate period, the wet bulb temperature, etc. The influence of effective transport parameters, drying conditions (state of the drying air and transfer coefficients) as well as the initial condition of the sample (initial moisture content) on drying behaviour is investigated. Comparison with two other models (diffusion and receding front model) is made in analyzing the influence of sample size on the drying time. By applying the capillary model presented in Chapter 2, the influence of pore size distribution on the drying behaviour of porous materials is considered with mono and bimodal pore size distributions. A study is realized on the parameters of these distributions. The continuous model is compared with two discrete models for the case of isothermal drying. A good agreement is found. In the next chapter, the drying experiments of γ-Al_2O_3 particles will be presented.

Chapter 5

EXPERIMENTS WITH γ-Al$_2$O$_3$ PARTICLES

5.1. Introduction

Due to their highly hygroscopic property, γ-Al$_2$O$_3$ particles are used in many different industrial processes such as drying, acid removal, steam purification, hydrocarbon adsorption, etc. In drying, in order to have a reliable design, for example of industrial dryers, knowledge about the characteristics of the material to be dried is necessary. Additionally, knowledge about the interrelation between the structure of a product and its drying kinetics is helpful in predicting the drying behaviour of the product. In this work, drying experiments are carried out to determine the pore structure, the pore size distribution, the sorption isotherm, the dry mass and the drying kinetics of γ-Al$_2$O$_3$ particles. Modern and appropriate experimental methods are applied. Descriptions of the experimental methods and equipment are given in the next sections. Firstly, the pore structure of the particles is examined using environmental scanning electron microscopy (ESEM). Then, the pore size distribution, which is needed to calculate the capillary pressure curve, is studied using the Hg-porosimetry method. After that, the sorption isotherm measurement, which is used to determine the minimum moisture content of the samples for given drying conditions, is realized. The determination of the dry mass of the particles is carried out by using a magnetic suspension balance. By using this method, the material drying kinetics are also investigated.

5.2. Product data

The typical properties of the sample as given by *Almatis AC, Inc.* [3] are presented in Tables 5.1 and 5.2. Table 5.1 introduces the major components of the sample. Selected physical properties for a particle are presented in Table 5.2. Note that in this table, based on the original information, properties have been transformed into relevant volume specific quantities with an assumption of 40% bed porosity for a packing of monodispersed spheres.

Table 5.1 Chemical properties of γ-Al$_2$O$_3$ particle F-200

Components	Weight percentage, wt %
Al$_2$O$_3$	93.10
SiO$_2$	0.02
Fe$_2$O$_3$	0.02
Na$_2$O$_3$	0.03
Loss on ignition	6.83

Table 5.2 Selected physical properties of γ-Al$_2$O$_3$ particle F-200

Properties	Value
Diameter, mm	4.80
Volume specific surface area a_v, m^2.cm^{-3}	436
Porosity ψ, %	0.64
Density of particle ρ_0, kg.m^{-3}	1282.00

5.3. Investigation of pore structure by environmental scanning electron microscopy (ESEM)

5.3.1. Experimental instrument

Scanning electron microscopy (SEM) is widely used in microanalyses of materials. This method creates magnified images by using electrons instead of light waves and shows very detailed monochromatic images. The ESEM instrument used in our experiment is presented in Figure 5.1. The working principle of an SEM instrument is depicted in Figure 5.2. Firstly, the non-metallic samples should be made to conduct electricity (by coating with a very thin layer of gold in a so-called sputter coater) before the experiment takes place (this is because the SEM instrument illuminates the sample with electrons in the microscope's vacuum column and electrical charges must be removed). The sample is then glued firmly into a basket and put into the sample chamber. A beam of high-energy electrons is produced by an electron gun, which uses filament-heating supply, at the top of the microscope. This electron beam flows through the vacuum column of the microscope in the vertical direction. The use of vacuum is compulsory to avoid burn, ionization or low contrast and obscured details of the image. The electron beam is then condensed by a condenser lens and focused onto a very fine spot on the sample by the objective lens. A set of scanning coils near the bottom, which is energized by varying the voltage produced by the scan generator, creates a magnetic field that moves the focused beam back and forth across on the sample. As the electron beam hits the sample, *secondary electrons* (or backscattered electrons) are emitted from the sample surface. These electrons are then counted by a detector, converted to signals and amplified. The final image corresponding to the topography of the sample is built from these signals. More information on SEM can be found, for example, in the work of Chescoe and Goodhew (1990 [13]) or in the work of Chapman *et al.* (1986 [11]).
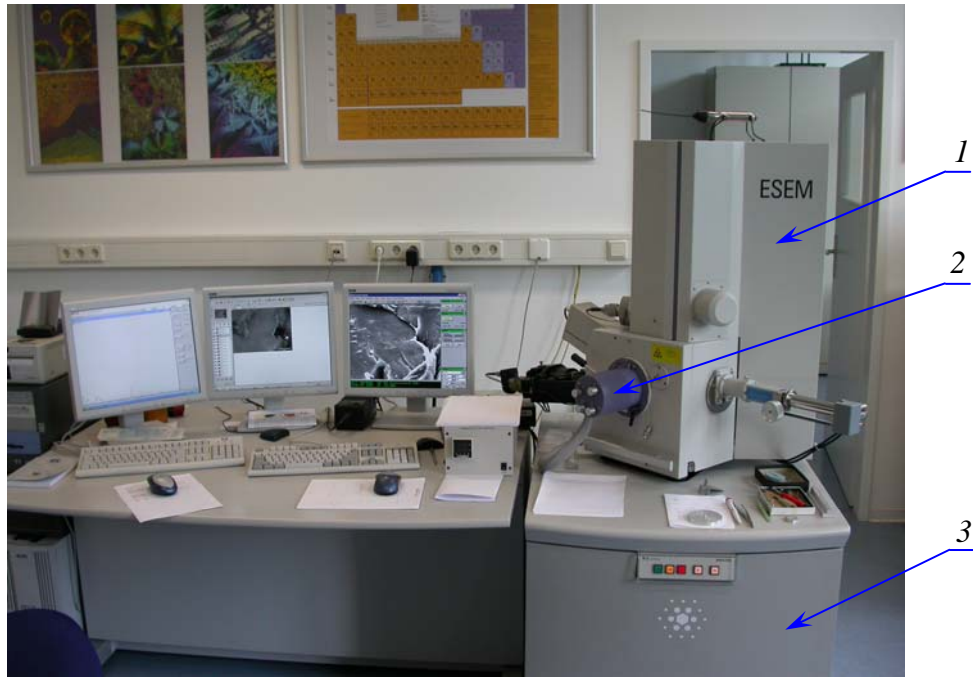
Figure 5.1 ESEM experimental system.
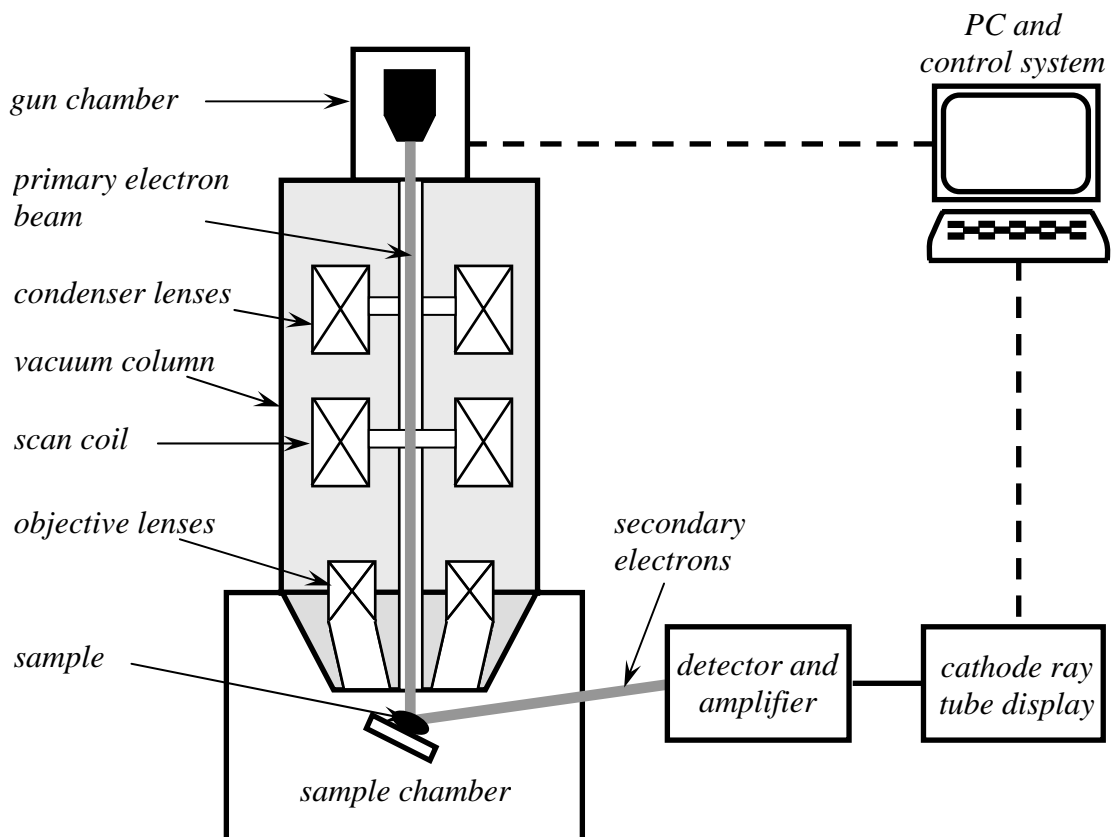*(1: Column; 2: Sample chamber; 3: Electronics).*

Figure 5.2 The major components of a SEM.

primary electron beam

detector electrode

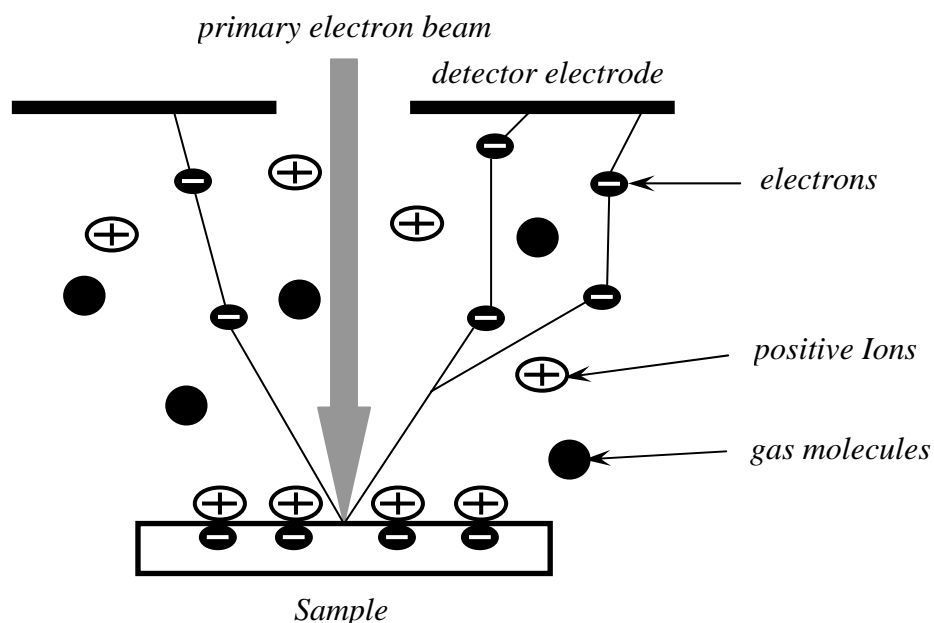*electrons*

positive Ions

gas molecules

Sample

Figure 5.3 Sample and detector electrode in an ESEM.

The environmental SEM (ESEM) is a modified version of SEM that allows the examination of a sample in a gaseous environment. This means that the ESEM can also be used to examine wet samples. When ESEM is used, it is not necessary to coat the sample surface with a thin layer of gold. In an ESEM instrument, the secondary electrons, which are emitted from the sample surface, are attracted to the positively charged detector electrode (Figure 5.3). Because the sample is put in a gaseous environment, collisions between electrons and gas molecules occur during the movement of the electrons. This causes the emission of more electrons and ionization of the gas molecules and leads to an increase in the amount of electrons, which effectively amplifies the original secondary electron signal. The positively charged gas ions are attracted to the negatively biased specimen and offset charging effects. The variation of the amplification effect depends on the number of secondary electrons. The larger the number of electrons emitted from a position on the sample the more intense the signal. The difference in signal intensity from different locations on the sample allows an image to be formed.

5.3.2. Experimental preparation and results

Two samples (particles) are analysed by ESEM in the Laboratory of *Institut für Werkstofftechnik und Werkstoffprüfung*, University Magdeburg. The *ESEM XL 30* by *FEI and Phillips* is used in this work. The first sample is a "*raw*" or original particle that is not subjected to any type of preparation (neither soaked with water nor dried). The second sample is a "*product*" particle, which has been used in determining the dry mass. The "*product*" particle is obtained by firstly saturating an original particle with water and then drying it at different temperatures. After being dried, the colour of the surface of the "*product*" particle is different from that of the original one (see Section 5.4). The two particles are then crushed so that the internal structure can be observed by ESEM.
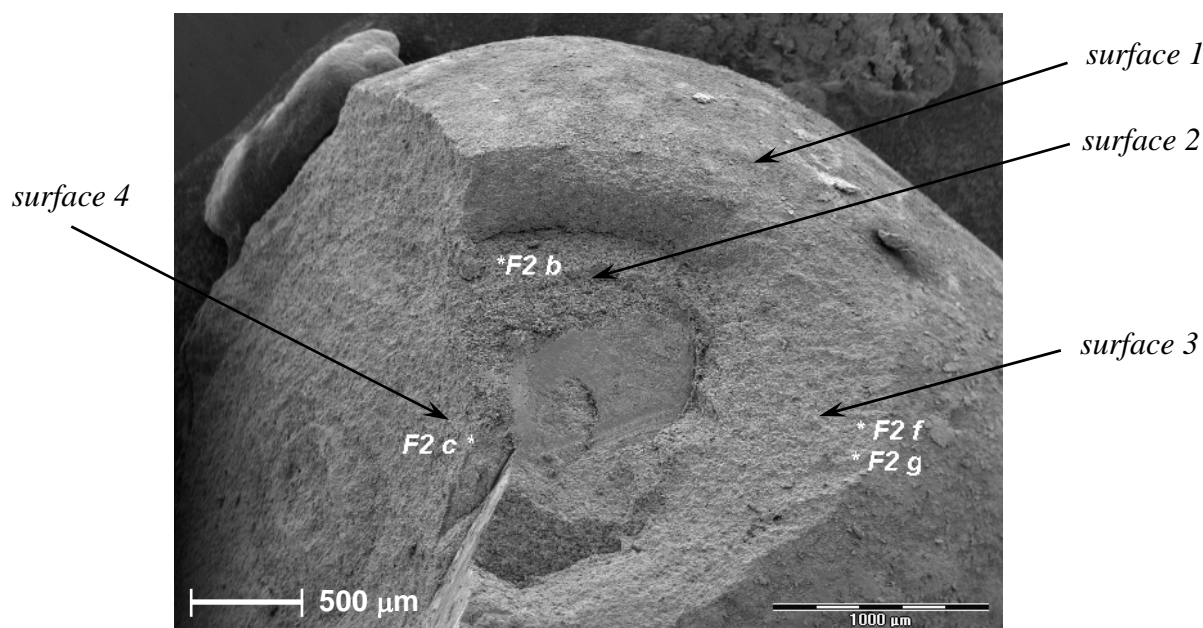
Figure 5.4 Microphotographs of a γ-Al$_2$O$_3$ particle surfaces: macroscopic scale.

The observation shows that the two particles contain several layers due to the production process. The colour inside the "*product*" particle is the same as the "*raw*" particle. At the macroscopic scale, the investigation of the structure concerns the particle surface (surface 1), the surface of inner shell (surface 2), the cross-section between two shells (surface 3) and the cross-section of the particle (surface 4). These surfaces are depicted in Figure 5.4. At the microscopic scale, some selected ESEM microphotographs are shown in Figure 5.5. Figure 5.5.a shows that γ-Al$_2$O$_3$ particles are assembled of bound primary granules and there is contribution of some crusts from the production process. The main component is the primary granules and these granules are connected by solid bridges. The pores between these granules are large pores (Figure 5.5.b). By looking into smaller details, it can be seen that a primary granule consists of crystal aggregates. The surface of a primary granule is introduced in Figure 5.5.c. Figure 5.5.d shows a primary granule which contains *smaller* particles and the internal pores inside granule (small pore). It is concluded that the two samples have a bimodal pore size distribution with large pores (approximate 1.5 µm) and small pores (approximate 15 nm). No difference in pore structure and surfaces could be observed between the two particles.

124
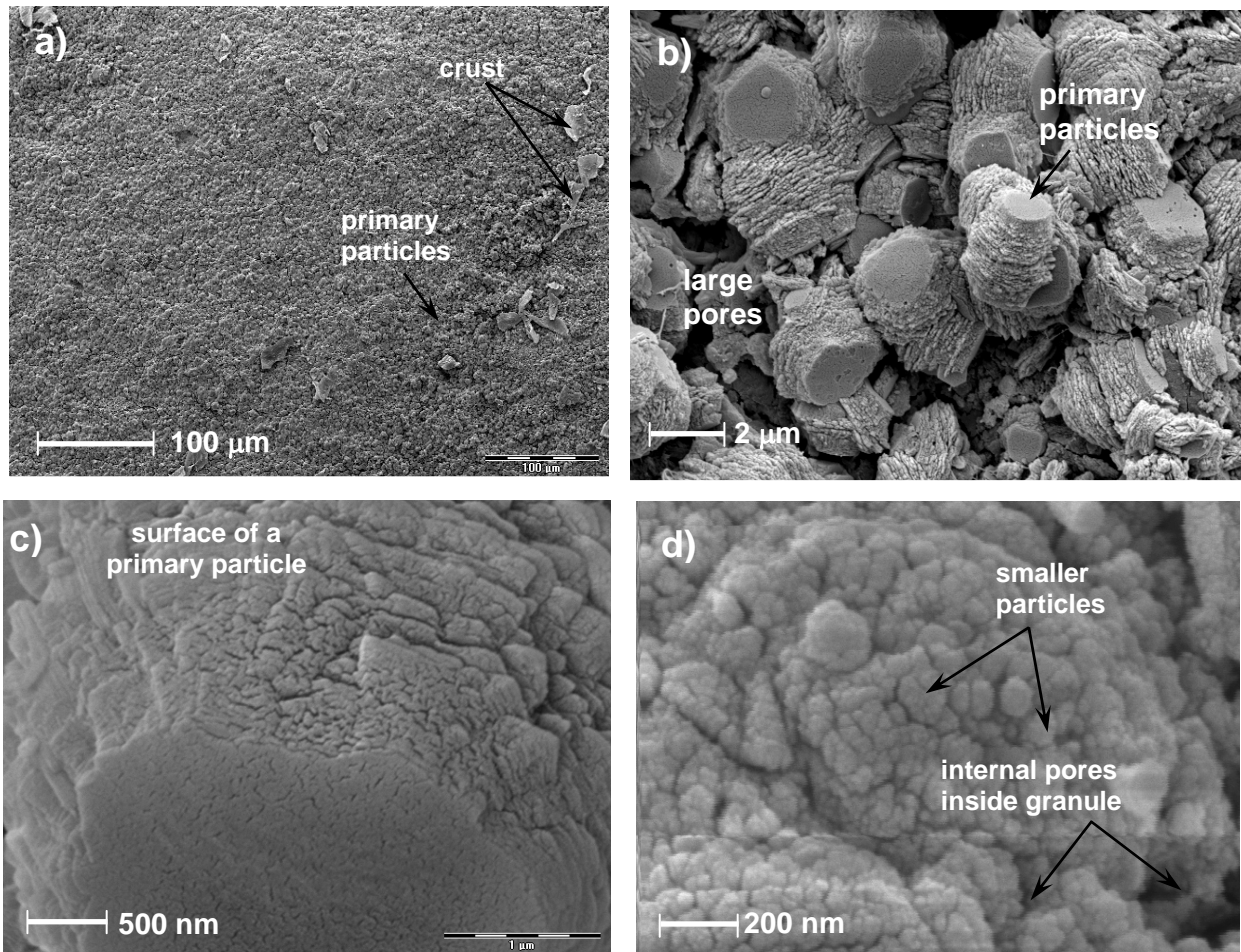
Figure 5.5 Microphotograph of surface of a γ-Al$_2$O$_3$ particle (corresponding to surface 1 in Figure 5.4): microscopic scale.

5.4. Measurement of pore size distribution by Hg porosimetry method

The experimental method of mercury porosimetry for the determination of the pore size distribution of porous material is well known. Mercury (Hg) is used because of its non-wetting property. For the measurement, it is assumed that when mercury is in contact with a porous medium the surface tension σ and contact angle θ of mercury are constant at a given condition. When a pressure P is applied to make mercury intrude into the pores of the porous medium, the higher the pressure P, the smaller the pores being invaded. The relationship between the pressure and the pore radius r is given by the Washburn equation

$$P = -(2\sigma\cos\theta)/r \tag{5-1}$$

By monitoring the pressure P and the intruded volume V, the pore size distribution of the sample can be determined. During one experiment, mercury is first intruded into the pores with increasing pressure and then extruded when the pressure is released. More

details on the Hg porosimetry method can be found, for example, in the work of Lowell and Shields (1991 [49]).

One experiment was carried out at the Laboratory of *Institut für Verfahrenstechnik*, University Magdeburg, with *Pore sizer 9320* by *Micromeritics*. In this experiment, 57 *"raw"* or original particles (not yet subjected to any type of preparation such as soaked with water or dried) are packed in a tube and vacuum is applied to assure that the pores are empty. Mercury is then applied to fill the volume between particles. This process continues until the pressure reaches the value of 5.17 bar corresponding to the mean pore radius of 1.360 μm. After that the pressure is increased up to the maximum pressure of 1720.32 bar in order to obtain the pore size distribution inside the particles. Physical parameters of mercury used in this experiment are shown in Table 5.3. With the assumption that all particles used in the experiment have average diameter of 5 mm, the experimental results is converted for one particle in Table 5.4.

Table 5.3 Physical properties of Hg.

Specifications	Value
Contact angle, degrees	130
Surface tension, N.m^{-1}	485.10^3

Table 5.4 Summary of experimental results by Hg-porosimetry.

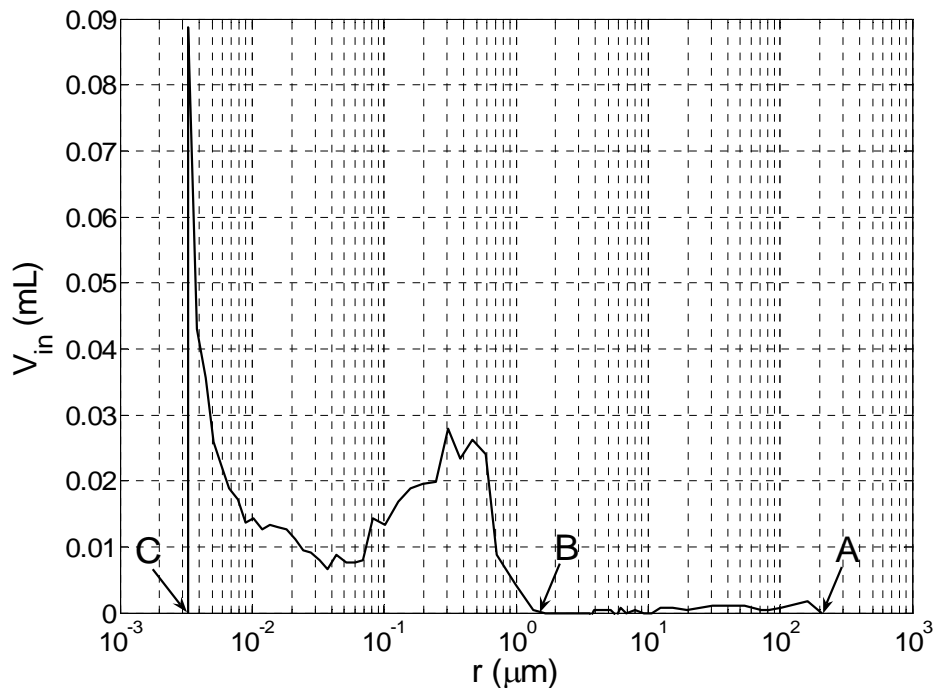| Specifications	Value
Total intrusion volume V_{in}, cm^3	0.0153
Volume specific pore area a_v, m^2.cm^{-3}	51.19
Density of particle ρ_0, kg.m^{-3}	1288.7
Porosity ψ, %	23.36

Figure 5.6 Pore volume distribution - mercury intrusion curve.

126

Figure 5.6 illustrates on a logarithmical scale the intrusion volume of mercury versus pore radius. By integrating this curve, the volume of pores within the particles can be obtained. We consider three areas under the curve corresponding to three ranges of pore radius. The first area is the area from point A to point B. In this area the mean pore radius is in the range of 1.360 to 207.174 μm. It is clear that this area represents the volume between particles with some small contribution from large pores of the particles. In calculation, this area is ignored because of its small value compared to the remaining areas. The second area (point B to point C) is the main area and this area is used in the calculation of the pore size distribution of the particles. In this area, the mean pore radius varies from 1.360 μm to 3.3 nm which corresponds to the maximum intrusion pressure of 1720.32 bar of the experimental device. Due to this limited maximum pressure of the device, it is physically impossible to detect pores of smaller size (or pores which are separated by "bottle necks" of this size from the outside). The missing part is confirmed by comparing the obtained results (Table 5.4) with the product data given by Table 4.2. Actually, only around 37% of the pore volume of the particles is measured, the other 63% are missing. One way to overcome this problem could be to vary the missing part of pore size distribution in order to get the best correspondence between experiments, drying data and drying model. Another possibility is the use of other techniques such as Helium adsorption.

5.5. Sorption isotherm measurement
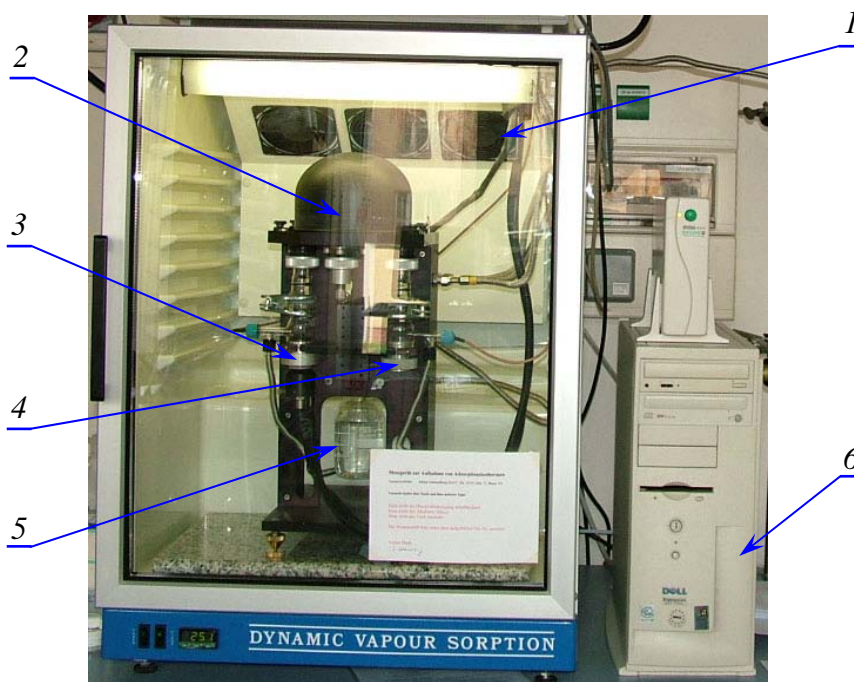
5.5.1. Experimental set-up

Figure 5.7 Experimental system for sorption measurement
(1: Temperature controlled chamber; 2: Microbalance; 3: Sample; 4: Reference;
5: Moistener; 6: Data acquisition).

127

The measurement of the sorption isotherm is carried out at the Laboratory of *Institut für Apparate- und Umwelttechnik*, University of Magdeburg, using a DVS (dynamic vapour sorption) device provided by *Surface Measurement Systems Limited*. The equipment is presented in Figure 5.7. The scheme of the experimental system is shown in Figure 5.8.
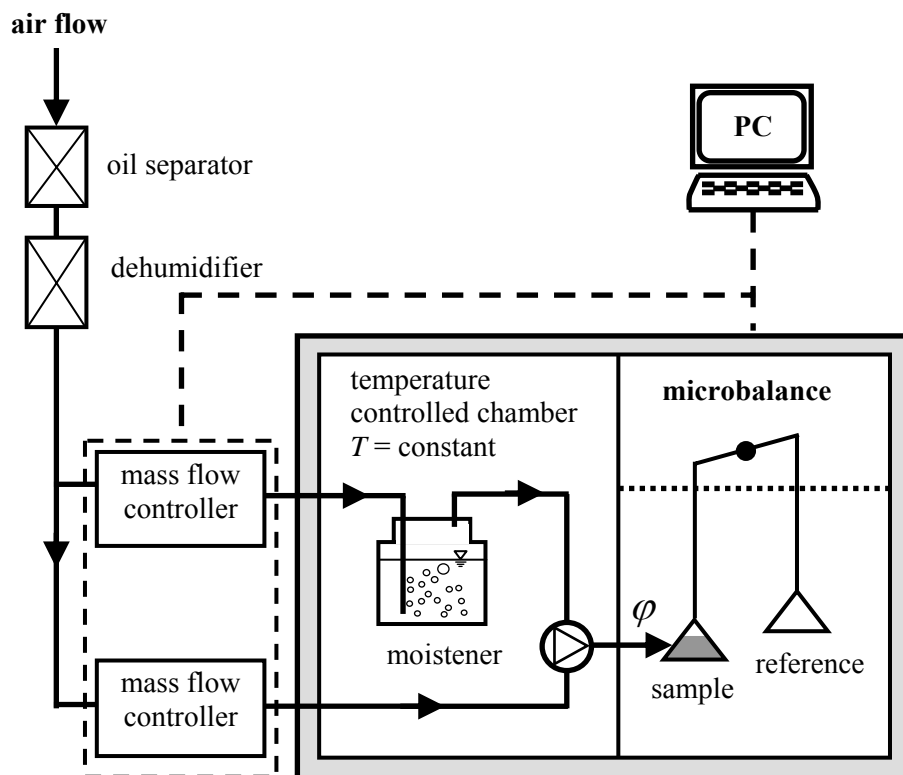
Figure 5.8 Experimental setup for sorption measurement.

In this system, two air flows are used. The sample (powder obtained by crushing γ-Al₂O₃ particles) is placed in a chamber of adjustable temperature T (in the range from 5 to 50°C). This temperature is kept constant with the help of a thermostat. Firstly, gas flows are cleaned and dried, by an oil separator and a dehumidifier. After that, one gas flow is humidified at the temperature of the measurement by a moistener: the gas flow is conducted through water at temperature T, and becomes saturated with vapour ($\varphi_1 = 1$) corresponding to vapour pressure $P_v^*(T)$. The second gas flow is kept dry ($\varphi_2 = 0$). The two flows are then mixed to get the desired relative humidity. This preconditioned gas then flows through the sample. By controlling the ratio of saturated and dry gas, different relative humidities φ in the range between 0 and 0.98 can be adjusted. The weight change of the sample is measured continuously by a microbalance with precision of 0.1 μg. The advantage in using this microbalance is that it allows very small samples (typically 1 to 30 mg) to be measured. This advantage helps to reduce the time needed to reach equilibrium. At the beginning, the experiment starts at $\varphi_1 \approx 0$ to determine the dry mass of the sample. Usually, the time for this period is 6 hours (set by the program). In our experiment, 15.493 mg powder is used in measuring one sorption isotherm at 24.8 ± 0.1°C. Twenty points of adsorption and twenty points of desorption isotherm are measured in one run. The time used to measure one sorption isotherm is 234 hours.

5.5.2. *Experimental results*

The sorption isotherm is shown in Figure 5.9. These curves are plotted by taking the lowest sample mass of the whole experiment as mass of dry solid (M_s = 15.15 mg) and calculating the moisture contents. This result shows a significant hysteresis (not the same values are measured in adsorption and desorption).
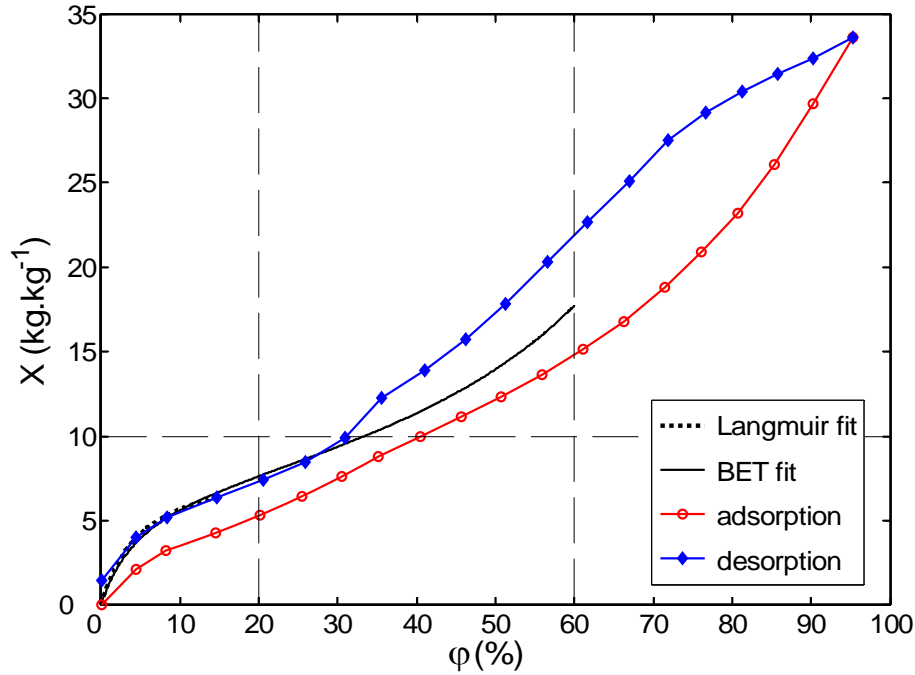
Figure 5.9 Sorption isotherm measurement: experimental data of γ-Al₂O₃ at 24.8°C and Langmuir / BET model fitting.

To prove equilibrium, the kinetics of the sorption measurement is considered. Three states: at the beginning of the process (Figure 5.10.a), at the end of adsorption (Figure 5.10.b) and at the end of the experiment (end of desorption, Figure 5.10.c), are shown as an example. Figure 5.10.a shows that in the short initial period (6 hours) of the experiment, equilibrium is not attained; therefore, a small error will occur when moisture contents are calculated by taking the lowest sample mass as dry mass.

The experimental result is compared with two theoretical equations. The first one comes from Langmuir's theory ($\varphi \leq 15\%$) of monomolecular adsorption. The second one comes from Brunauer, Emmett and Teller (BET theory, $\varphi \leq 30\%$) and describes multimolecular adsorption. Note that the ranges of relative humidity φ used in Langmuir's and BET theory are usual ranges of validity.
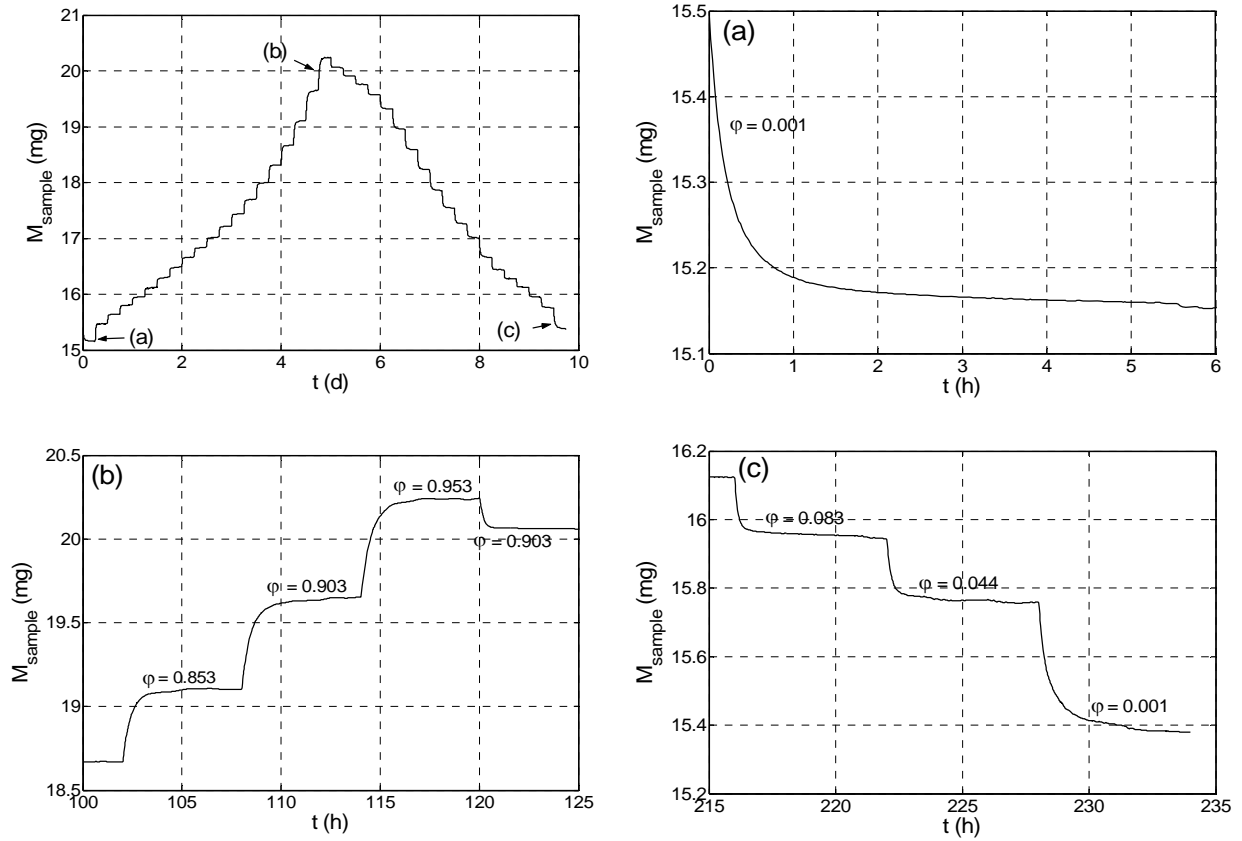
Figure 5.10 Kinetics of sorption measurement.

The Langmuir equation is written in the form

$$X = X_m \frac{c\varphi}{1+c\varphi}$$ (5-2)

and the BET equation is

$$X = X_m \frac{c\varphi}{(1-\varphi)(1-\varphi+c\varphi)}$$ (5-3)

In the above equations, X_m represents the moisture content that corresponds to a full monolayer, c is a constant and can be approximated by

$$c \approx \exp\left(\frac{\widetilde{M}_v}{\widetilde{R}T} \Delta h_s\right)$$ (5-4)

where Δh_s is the sorption enthalpy (needed to remove the molecules from the solid).

For estimation of X_m and c, Eq. (5-2) is rewritten in terms of φ/X and Eq. (5-3) in terms of $\varphi/[X(1-\varphi)]$, both of which depend linearly on φ and can be used in fitting the two models to the experimental data. For the Langmuir case, $X_m = 0.0865$ and $c = 19.0769$, is obtained. For the BET case, $X_m = 0.0733$ and $c = 19.9480$, can be

calculated. The results of the fitting are presented in Figure 5.9 together with the corresponding experimental data.

From Figure 5.9, it can be seen that for moisture contents under 10% (corresponding to relative humidity of 30%) the Langmuir and BET models fit quite well with the desorption experimental data. This indicates that for moisture contents under 10% the assumption of monomolecular adsorption (Langmuir) and the assumption of multimolecular adsorption (BET) provide a good approximation. But, it should be recalled that hysteresis occurs along the whole sorption isotherm.

In Figure 5.9, corresponding to 4% of the relative humidity φ the moisture content X is 3.8%. This value is to be compared with the final moisture content in the drying experiments at 25°C in the following section.

5.6. Determination of dry mass and drying kinetics by magnetic suspension balance method

5.6.1. Introduction

In order to measure the drying kinetics of a single porous particle, different experimental methods such as conventional microbalance, drying tunnel (Hirschmann and Tsotsas, 1998 [27]; Hirschmann *et al.*, 1998 [28]), acoustic levitator (Groenewold *et al.*, 2000 [23]) can be used. However, the major limitation of these methods is that at high temperature and realistic velocity, the mass of the sample cannot be accurately measured. To overcome this problem, a new technique, which involves the use of a magnetic suspension balance, is recommended (Kwapinski and Tsotsas, 2004 [41]).

In a magnetic suspension balance system, the sample can be weighed under nearly all kinds of environment. The major advantage of this method is that instead of hanging the sample directly at the balance (as in traditional methods), the probe chamber and balance are separated; therefore the mass measurement (balance) is not disturbed by extreme conditions of temperature and pressure ($T > 100^{o}C$ and vacuum, for instance). However, this method is suitable only for limited size and weight of the investigated samples.

The drying experiments with a magnetic suspension balance by *Rubotherm* were carried out at the Laboratory of *Lehrstuhl für Thermische Verfahrenstechnik*, University of Magdeburg. This device allows measurements at temperature up to 250°C and pressures up to 3 *bar*. The drying air velocity can be up to 1 m/s. The measuring weight (with hanger – a device to hang the sample) is up to 8 g with an accuracy of 1 μm (Rubotherm, [87]).

The equipment and its instruments used in our experiments are shown in Figures 5.11 to 5.13. In this system, the sample is linked to a suspension magnet, which contains a permanent magnet; a sensor core and a device for decoupling the measuring load (see Figure 5.14). The suspension magnet is linked to a balance via an electromagnet. This electromagnet maintains a freely suspended state of the suspension magnet via an electronic control unit. Thus, the measuring force is transmitted contactlessly from the measuring chamber to the microbalance, which is separated from the chamber.
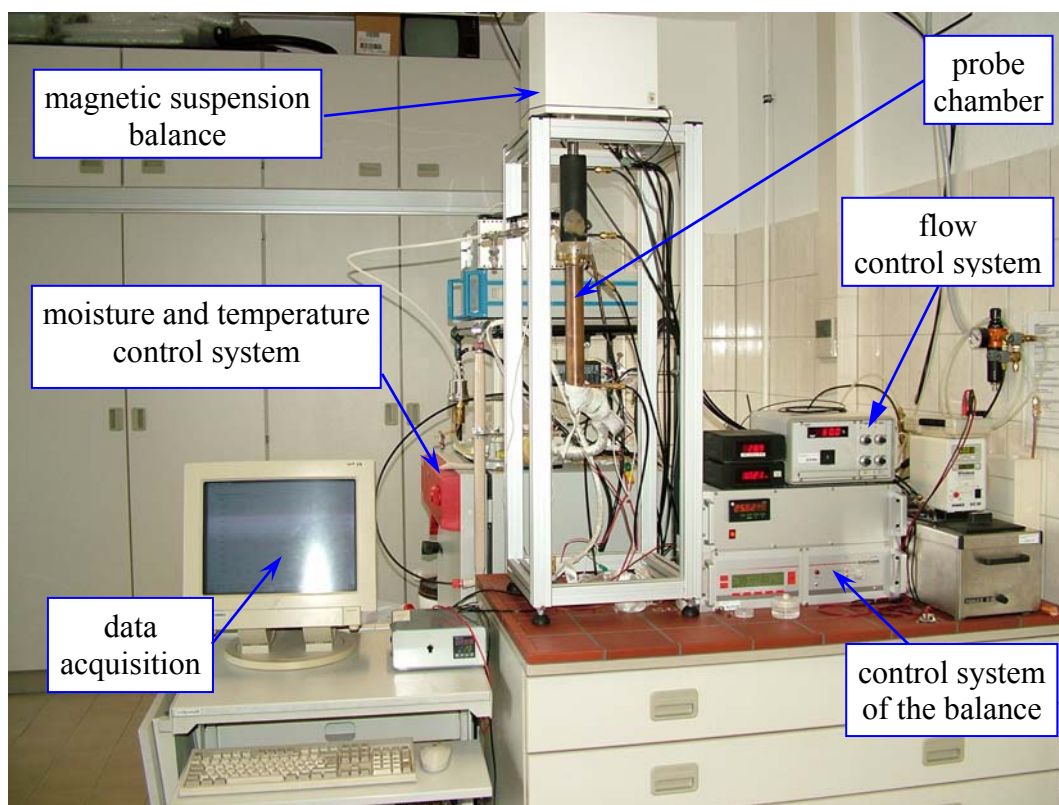
Figure 5.11 Experimental system of magnetic suspension balance.

Figure 5.12 Magnetic suspension balance (Rubotherm, [87]).

Figure 5.13 Sample and hanger.

5.6.2. Experimental set-up

The set-up of the experimental system is schematically shown in Figure 5.14. Like in the sorption isotherm experiment, two air flows are used. The first is humid air, which is humidified by a moistener. The second is dry. The desired humidity of drying air can be obtained by mixing these two air flows. The relative humidity is measured by a dew point mirror hygrometer provided by *Michell Instruments*. The temperature in the air condition cabinet is kept constant at temperature T. The drying air conditions are characterized by velocity, humidity and temperature. For the case of vacuum drying, a vacuum pump is used and the pressure P is controlled to be less than 1 mbar. In this case, only dry air flows through the sample by using a bypass valve. The temperature in the probe chamber is controlled by a thermostat at temperature T.

The particle is attached to a hanger in the probe chamber. In our experiments, this hanger is individually designed and made of three small metal fibres (0.25 mm in diameter - Figure 5.13). This hanger ensures that the evaporation surface of the particles will not be disturbed by the hanger. The weight of the hanger is 3.787 g.

Figure 5.14 Setup for drying experiments with magnetic suspension balance.

133

After conditioning, the drying air enters the probe chamber and flows around the sample. The mass of the particle is measured and recorded at defined *time intervals* (in our experiments 15 or 30 seconds). The zero point is set every 10 min by decoupling. Every 12 zero points (120 min) the calibration of the balance will take place using a reference of 5 grams inside the balance.
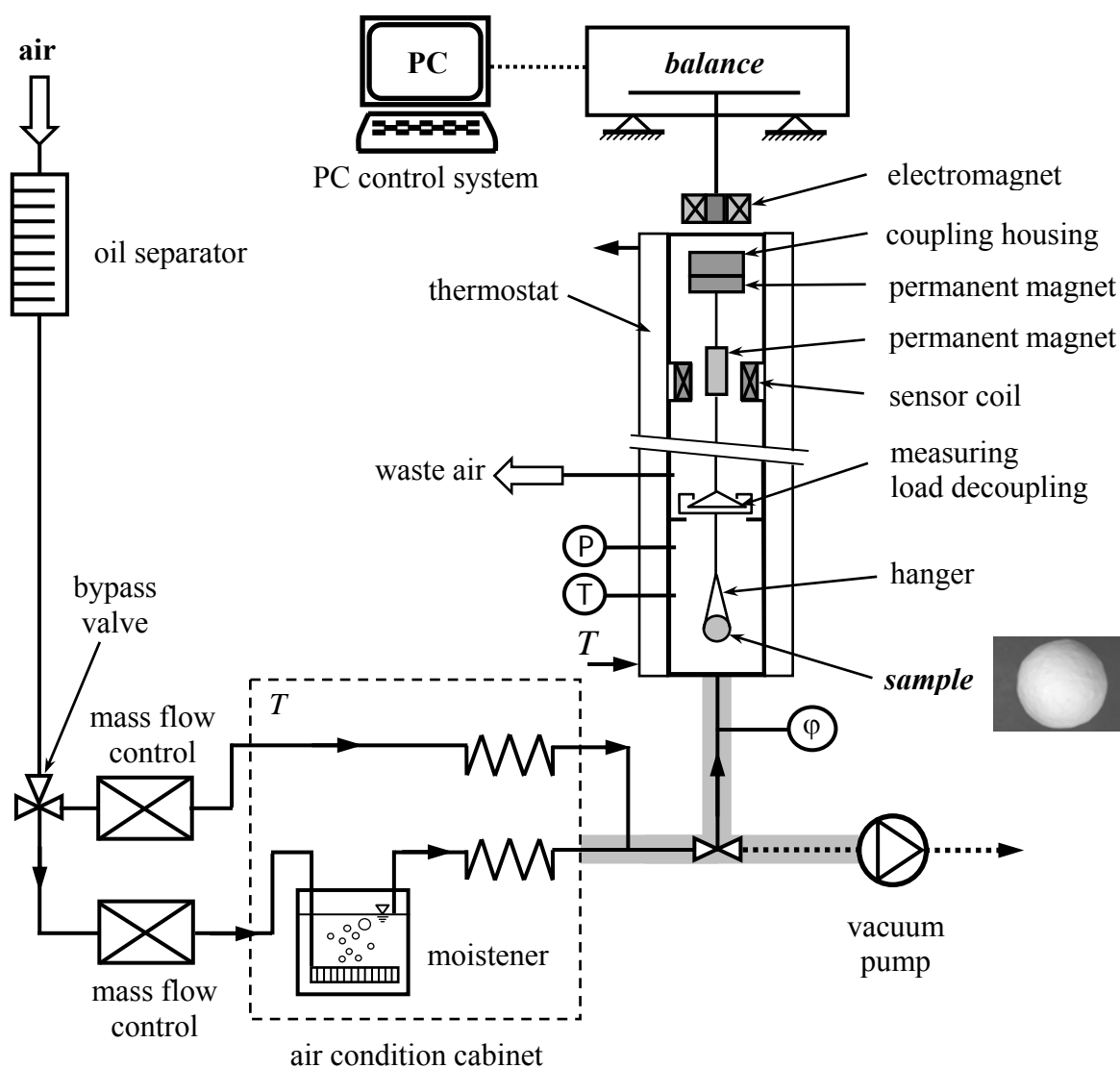
During drying at room conditions, the temperature of drying air is 25°C at atmospheric pressure and the dew point temperature is less than -18°C corresponding to a relative humidity $\varphi < 4\%$. In our experiments, the moistener was not used. The volumetric air flow rate is set to 0.2 l/min corresponding to a velocity of 7.37 mm/s in the sample chamber. This velocity assures that the drying process is slow and that symmetric conditions can be assumed. For the drying conditions mentioned here and for the particle diameter $d = 5.52$ mm, the Reynolds number is Re = 2.57. The buoyancy effect is neglected.

5.6.3. Experimental results

5.6.3.1. Determination of dry mass

One long experiment was carried out to determine the dry mass of one particle. The particle is first saturated with water by putting it into a water-filler placed in vacumm ($P \leq 1$ mbar) for 24 hours. The particle is then dried in the magnetic suspension balance at temperature 25°C and at atmospheric pressure. After that, the particle is set in the probe chamber and dried further at vacumm and temperature 110°C, 120°C, and 130°C, successively. The results (for drying in vacumm) are presented in Figure 5.15 by plotting the mass of the particle against time. Due to the limitations in data storing of the used software, the experiment has to be handled in several steps (indicated by the different colour of the curves).
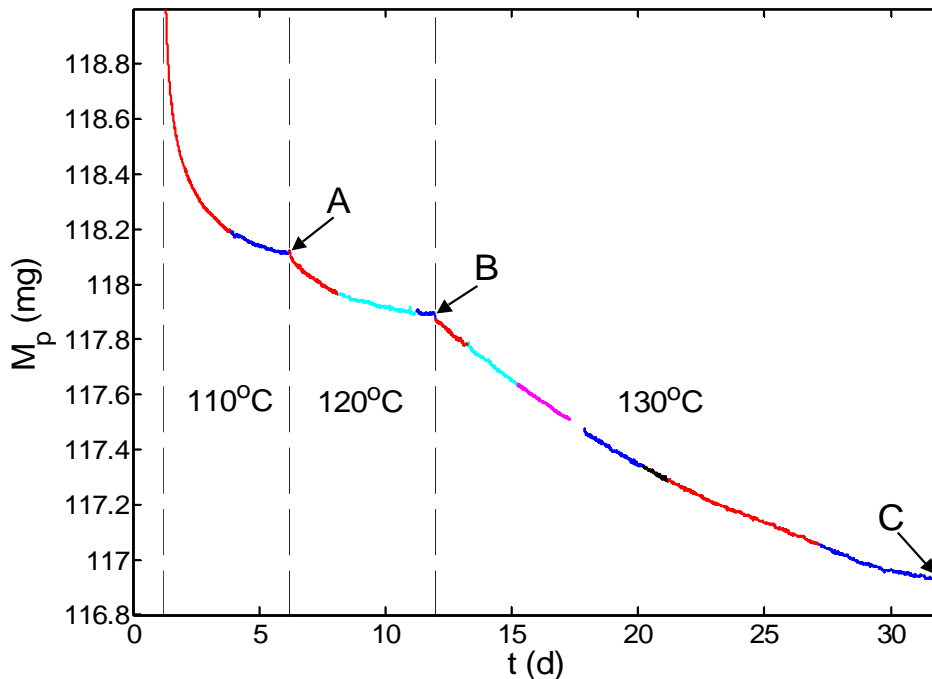

Figure 5.15 Protocol for determination of the dry mass.

Table 5.5 Dry mass of four selected particles

Sample no.	d (mm)	M_{dry} (mg)	ΔM (mg)
22	5.52	117.560	4.657
24	5.50	116.840	5.160
25	5.49	114.670	3.598
26	5.54	117.660	3.526

The initial mass of the particle is 169.16 mg (with d = 5.52 mm). The particle was dried at 25°C for 28 hours. After this period, the particle's weight reduced to 120.737 mg. During drying in vacuum, the mass of the particle slowly decreases. In the first step of this period, the temperature 110°C was applied. After 120 hours, the mass of the particle is 118.121 mg. (point A – Figure 5.15). By continuing the drying process at temperature 120°C, after 137 hours the particle's weight achieves the value of 117.874 mg (point B – Figure 5.15). In the last step of drying in vacuum, the particle is dried at temperature 130°C during 464 hours. At the end of the process, the remaining mass is 116.921 mg (point C – Figure 5.15).

The results in the Figure 5.15 show that at points A and B, equilibrium seems to be reached, but not at point C (for very long times of vacumm drying at 130°C). The reason may be that at a high temperature other components than water are still removed. One should note that after the experiment was finished the colour of the particle had changed from white to light yellow (this could be seen by naked eye). This particle is later crushed to investigate the internal structure by the ESEM (see Section 5.3). It is found that only the colour of the surface is changed, not the colour inside of the particle.

In practice, the value at point B can be used as dry mass of the sample. Indeed, from Figure 5.15 it is seen that the difference between the value at point B (accepted as dry mass) and the value at the end of the whole experiment after very long time (end of experiment at 130°C) is 0.953 mg. This value is small enough compared to the value of the saturated, or even dry particles. Therefore, the drying in vacuum at 120°C is chosen in order to determine the dry mass of the sample. By using the value of the density of the particle given by the producer (see Appendix 1), the dry mass of above particle is calculated as 112.903 mg. The difference between this value and the value at point B (117.874 mg) is 4.971 mg.

After the above experiment, the dry mass M_{dry} of four other particles is determined by drying in vacuum with $P \leq 1$ mbar at 120°C for 72 hours for each particle. The value of M_{dry} together with particle diameter d and the difference ΔM between M_{dry} obtained by our measurement and the dry mass calculated by using the value of the density of the particle given by the producer are given in Table 5.5. These particles were then used in the investigation of the drying kinetics at 25°C presented in the next section.

5.6.3.2. Drying experiments at 25°C

Drying experiments of four saturated particles were carried out at 25°C. The drying conditions are explained in Section 5.6.3.1. The initial moisture content, the moisture content at the end of the experiment together with the moisture content after several times of drying for these four selected particles are introduced in Table 5.6. The

moisture contents as functions of time are given in Figure 5.16. Figure 5.17 presents the evaporation rate for particle no. 25 as an example. By using the drying experiment results (of particle no. 25 – see Figure 5.17, for instance) together with the information of the sorption isotherm of γ-Al$_2$O$_3$ given in Section 5.5.2, the normalized drying rate curve can be obtained (Groenewold, 2004 [24]). The longest experiment is the drying of particle no. 22 (23.15 h of drying) and the shortest one is the drying of particle no. 24 (8.42 h of drying). As we can see from Table 5.6, after 8 h of drying the moisture content of the particles reduces only very slowly and tends to the equilibrium moisture content as determined in the sorption experiment, namely 3.8 % (see Section 5.5.2). Two particles (no. 22 and no. 25) are dried further until 22 h, but the moisture content of these particles stays almost constant (the last column of Table 5.6). Therefore, it could be concluded that for drying at room temperature with almost dry air, the value of moisture content after 8 h of drying can be used as the *equilibrium* moisture content in practical calculations.

Table 5.6 Moisture content after several time of drying at 25$^{\text{o}}$C
for four selected particles.

Sample no.	X_0	X after 6h	X after 8h	X after 11h	X after 18h	X at the end
22	0.504	0.045	0.042	0.041	0.041	0.041
24	0.465	0.043	0.042	-	-	0.042
25	0.505	0.045	0.043	0.042	0.042	0.041
26	0.507	0.046	0.044	0.043	0.043	0.043
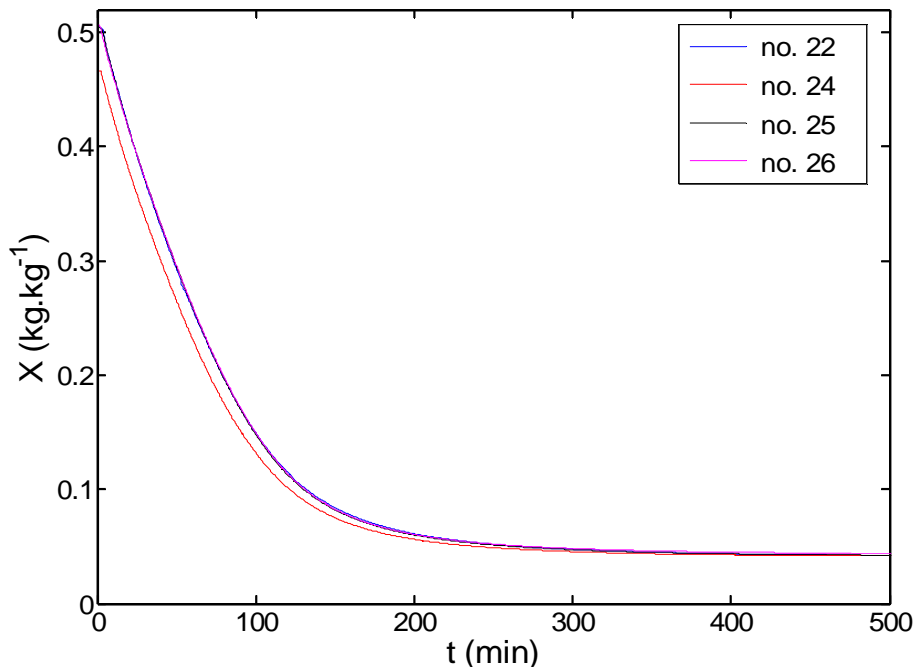
Figure 5.16 Moisture content as function of drying time
for four selected particles at 25$^{\text{o}}$C.
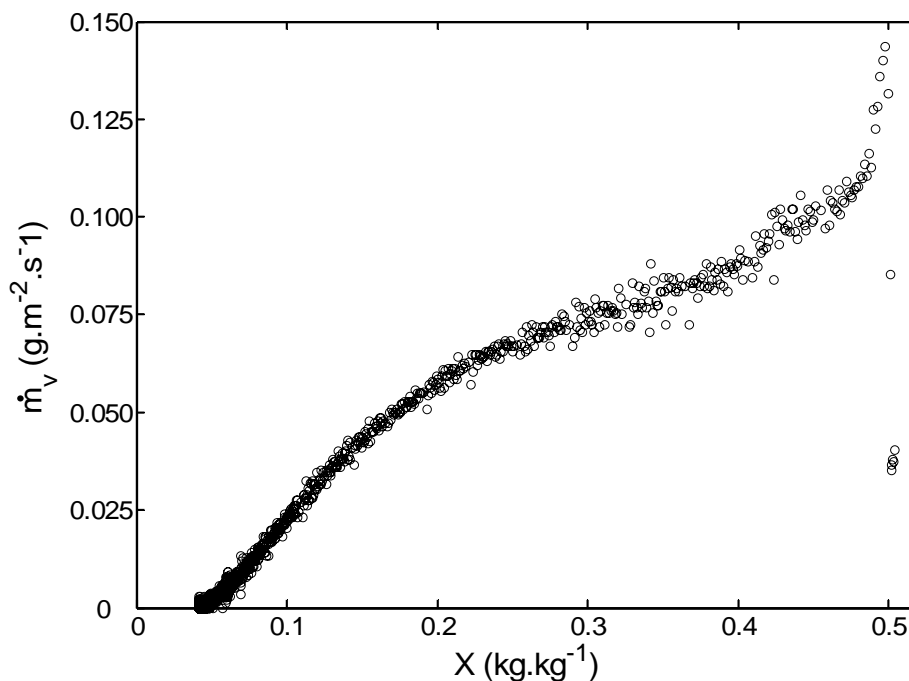
Figure 5.17 Drying rate curve of particle no. 25

To summarize, in this chapter, the drying experiments of γ-Al$_2$O$_3$ particles are presented. By using the environmental scanning electron microscopy (ESEM), it is observed that the samples have a bimodal pore size distribution with large pores (approximately 1.5 μm) and small pores (approximately 15 nm). The pore size distribution of the sample is studied using Hg-porosimetry. However, due to the limitations of the device not all small pores can be detected. To overcome this problem it is suggested to vary the missing part of pore size distribution or to use other techniques such as Helium adsorption. Sorption isotherm measurement was carried out by using a dynamic vapour sorption device. The results are compared with Langmuir and BET theoretical equations. For moisture contents under 10% a good agreement is found. By using a magnetic suspension balance, the dry mass of γ-Al$_2$O$_3$ particles is determined. In addition, drying experiments at 25°C for four selected particles were carried out to determine theirs drying kinetics. Experimental results obtained from this chapter could be used in future work.

CONCLUSION AND OUTLOOK

The drying of porous media is studied in this thesis by means of the continuous approach and the control volume method. Both transport phenomena inside the porous medium and overall drying kinetics are analyzed. In dealing with the numerical simulation of drying, the thesis presents a new method to investigate the influence of microscopic properties, namely the pore size distribution, of porous materials on their macroscopic drying behaviour.

Based on the drying models developed by Whitaker (1977 [115]; 1980 [116]) and by Perré and Turner (1999 [71]) a system of governing equations representing a continuous model used in drying simulation is established. The control volume element method is used to discretize and solve this governing system. Numerical studies with a reference material (light concrete) show that the drying simulations capture very well different drying characteristics of porous media such as the constant drying rate of the first drying period, the falling rate during the second period, the wet bulb temperature that is reached during drying, etc. The accuracy of the numerical simulations is tested by considering the influence of the space discretization and by considering the overall conservation behaviour of water and air. It is found that a good accuracy could be achieved. The influence of different factors such as drying conditions, sample shape and size, etc. on the drying kinetics is investigated numerically. Parametric studies are realized to examine the sensitivity of the drying behaviour with respect to different model parameters such as the effective diffusivity, the effective thermal conductivity and the absolute permeability. By comparing the results with those obtained by previous works, a good agreement is observed.

Investigations on the influence of sample size on the total drying time in the drying of plates and spheres show that the drying time increases more than linearly with the sample size. In order to compare the results obtained by the continuous model with others, the influence of sample size is also examined by employing the diffusion and the receding front models for isothermal drying of spherical particles. The results show that the drying time increases more than linearly with the sample size in the case of continuous and receding front models.

By using a bundle of capillaries with a radius distribution as a representation of the pore space, some of the most important parameters used in the continuous model (capillary pressure, absolute and relative permeabilites of liquid and gas phases) are computed as functions of material pore size distribution. These functions create a link between the

microstructure of porous materials and their macroscopic behaviour in drying. By using this micro-macro link, the influence of the material microstructure on the drying kinetics can be investigated. Numerical results show that by using the capillary model the drying characteristics of porous media can be captured (the constant and the falling rate periods, the wet bulb temperature). Investigations are realized to see how different pore size distributions affect the drying behaviour by using mono-modal and bimodal pore size distributions. The major results of these investigations are:

❑ For materials having mono-modal pore size distribution, with small pores and a narrow distribution, the first drying period is short, significant gas pressure gradients occur in the second period and saturation gradients are relatively steep throughout the drying process. With large pores and a broad distribution, a long first drying period is observed. Pressure and moisture gradients in this case are much smaller. It is observed that the standard deviation σ_0 also has a strong effect on drying. For the same mean capillary radius r_0, a sample with small standard deviation has steeper saturation gradients and shorter first drying period as compared to a sample with large standard deviation. It is found that the variation of the pore size distribution has little effect on the temperature evolution during drying: only the wet bulb temperature prevails longer with larger pores.

❑ For materials having bimodal pore size distribution, it is noted that the *macro* pores dry out completely at the high drying rate of the first drying period. Due to this fact, the distribution of the *macro* pores usually plays no role, but the volume fraction of *macro/micro* pores and the distribution of the *micro* pores are important. It is found that the length of the first drying period mainly depends on the volume fraction of the *macro* pores: the higher the amount of *macro* pores, the longer the first drying period since big pores are favourable for drying. Besides, the drying rate in the second period is higher for larger volume fraction of the *macro* pores. However, the first drying period can also be influenced by the pore size distribution of the *micro* pores: a broader distribution of the *micro* pores leads to a longer first drying period and the drying rate in the second period is higher.

When pore size distribution is taken into account, the influences of other factors such as drying conditions and other material properties are also studied. It is observed that these influences have the same characteristics as found in the drying of the reference material.

The numerical results obtained in this work are compared with those obtained by one-dimensional capillary model proposed by Metzger and Tsotsas (2005 [55]) and two-dimensional network model proposed by Irawan *et al.* (2006 [30]) in the case of isothermal drying. With the same geometry, the same pore size distribution and the same drying conditions, the comparison shows that for the simple geometry of a bundle of capillaries the results obtained by the continuous approach (with macroscopic governing equations and effective parameters) are very similar to those obtained by the discrete approach (drying is modelled at pore scale).

By using γ-Al_2O_3 particles, experiments are carried out to examine the microstructure and the drying behaviour of γ-Al_2O_3 material. Maximum and minimum sizes of the pores are determined by using environmental scanning electron microscopy. By using Hg porosimetry, the pore size distribution is studied and by using magnetic suspension

gravimetry, the drying kinetics are measured. Ideally, the information obtained from these experiments should be used in and compared with numerical simulations. However, the model in the present work is valid only for large pores (larger than the pore size of γ-Al$_2$O$_3$) and due to the lack of some material data, this task will have to be done in a future work.

Based on the current work, the next step in research should be to improve the model for smaller pores (by adding Knudsen effect) and extend the use of the control volume method in two and three-dimensional problems. Experiments should be carried out to determine the exact pore size distribution of a given material and experimental results on the drying kinetics should be compared with numerical simulations to see how the material properties can be properly modelled using the information about pore size distribution. More precisely, the modelling of material properties can be done in two steps. First, an advanced method such as the nuclear magnetic resonance imaging method should be used to obtain the drying kinetics of the considered material (for example moisture content X_{exp} as function of space and time). Second, the inverse problem should be solved by modifying progressively the material dependent transport parameters such as diffusivity and permeabilities until the simulated drying kinetics (X_{sim}) match the experimental ones (X_{exp}). The forward problem (drying simulation) can be solved by the control volume method and the inverse solution can be obtained with the help of the nonlinear least square method. The difficulty will be how to deal with the nonlinear least square method since the inverse problem in most cases belongs to the so called global optimization, which remains one of the most challenging problems yet to be overcome by engineers and mathematicians.

Besides the use of a bundle of capillaries, future work should also use pore network models (in two and three dimension), where not only the pore size distribution of a material is varied but really the pore structure, to obtain the effective parameters of the continuous model. In this context, it will be of interest to see how the liquid has to be distributed in the network for a given saturation: by filling up pores according to the rule "starting with the smallest radius" as it was reasonable in our one dimensional capillary model or according to phase distributions as obtained from network drying simulations. By applying gradients of liquid and gas pressure, vapour pressure and temperature, effective parameters may be computed and used in the continuous model. This will allow us to see to what extent the discrete and continuous approach are equivalent.

REFERENCES

[1]   Akpinar, E. K. and Dincer, I. (2005), Application of moisture transfer models to solids drying, *Proceedings of the Institution of Mechanical Engineers, Part A: Journal of Power and Energy* **219** (3), pp. 235÷244.

[2]   Akpinar, E. K. and Dincer, I. (2005), Moisture transfer models for slabs drying, *International Communications in Heat and Mass Transfer* **32** (1-2), pp. 80÷93.

[3]   Almatis AC, Inc. Adsorbents & Catalysts (2005): *Product data of Activated Aluminas F-200.*

[4]   Berger, D. and Pei, D. C. T. (1973), Drying of hygroscopic capillary porous solids – A theoretical approach, *International Journal of Heat and Mass Transfer,* Vol. **16** (2), pp. 293÷302.

[5]   Bird, R. B., Stewart, W. E. and Lightfoot, E. N. (2002), Transport phenomena, 2nd Edition, J. Wiley, New York.

[6]   Blackband, S. and Mansfield, P. (1986), Diffusion in liquid-solid systems by NMR imaging, *J. Phys. C: Solid State Phys*. **19**, L49÷L52.

[7]   Bories, S. (1989), Recent advances in modelisation of coupled heat and mass transfer in capillary – porous bodies, *Drying '89*, pp. 46÷62.

[8]   Boukadida, N. and Nasrallah, S. B. (1995), Two dimensional heat and mass transfer during convective drying of porous media, *Drying Technology* **13** (3), pp. 661÷694.

[9]   Boukadida, N., Nasrallah, S. B. and Perré, P. (2000), Mechanism of two-dimensional heat and mass transfer during convective drying of porous media under different drying conditions, *Drying Technology* **18** (7), pp. 1367÷1388.

[10]   Ceaglske N. H. and Hougen, O. A. (1937), Drying of granular solids, *Industrial and Engineering Chemistry*, Vol. **29**, No.7, pp. 805÷813.

[11]   Chapman, S. K., Booth, J. and Harrison, J. (1986), Working with a scanning electron microscope, Lodgemark Press, England.

[12]   Chen, P. and Schmidt, P. S. (1990), An integral model for convective drying of hygroscopic and non-hygroscopic materials, *Drying '89*, pp. 162÷168.

[13]   Chescoe, D. and Goodhew, P. J. (1990): The operation of transmission and scanning electron microscopes, Oxford Univ. Press.

[14]   Crapiste, G. H., Whitaker, S. and Rotstein, E. (1988), Drying of cellular material - I. A mass transfer theory, *Chemical Engineering Science*, Vol. **43** (11), pp. 2919÷2928.

[15]   Crapiste, G. H., Whitaker, S. and Rotstein, E. (1988), Drying of cellular material - II. Experimental and numerical results, *Chemical Engineering*

Science, Vol. **43** (11), pp. 2929÷2936.

[16]   De Vries, D. A. (1958), Simultaneous transfer of heat and moisture in porous media, *Transactions, American Geophysical Union*, Vol. **39**, pp. 909-916.

[17]   De Vries, D. A. (1987), Theory of heat and moisture transfer in porous media revisited, *International Journal of Heat Mass Transfer*, Vol. **30**, No. 7, pp. 1343÷1350.

[18]   Dullien, F. A. L. (1992), Porous media: Fluid transport and pore structure, 2nd Edition, Academic Press Inc., San Diego.

[19]   Efremov, G. I. (2002), Drying kinetics derived from diffusion equation with flux-type boundary conditions, *Drying Technology* **20** (1), pp. 55÷66.

[20]   Ferguson, W. J. (1995), A control volume finite element numerical simulation of the high temperature drying of spruce, *Drying Technology* **13** (3), pp. 607÷634.

[21]   Fortes, M. and Okos, M. R. (1980), Drying theories: their bases and limitations as applied to foods and grains. In: *Advances in Drying* **1**, Mujumdar, A. S. (Editor), Hemisphere Publ. Corp., Washington DC, pp. 119÷154.

[22]   Glück, B. (1986), Zustands- und Stoffwerte- Wasser, Dampf, Luft-Verbrennungsrechnung, VEB Verlag für Bauwesen, Berlin.

[23]   Groenewold, C., Möser, C., Groenewold, H., Tsotsas, E. (2000), Determination of single-particle drying kinetics in an acoustic levitator, *Proceedings of the 12th International Drying Symposium (IDS 2000)*, pp. 58÷61.

[24]   Groenewold, H. (2004), Wirbelschichttrocknung mit indirekter Beheizung, *PhD thesis*, Otto-von-Guericke-Universität Magdeburg.

[25]   Guillard, V., Broyart, B., Bonazzi, C, Guilbert, S. and Gontard, N. (2002), Water transfer in multi-component heterogeneous food: Moisture distribution measurement and prediction. In: *Drying'2002, Proceedings of the 13th International Drying Symposium (IDS'2002),* Vol. B, pp. 1155÷1160.

[26]   Hadley, G. R. (1985), Numerical modeling of the drying of porous materials. In: *Drying'85, Proceedings of the 4th International Symposium on Drying, Kyoto (1984)*, pp. 135÷142.

[27]   Hirschmann, C. and Tsotsas, E. (1998), Impact of the pore structure on particle-side drying kinetics, *Proceedings of the 11th International Drying Symposium (IDS '98)*, pp. 216÷223.

[28]   Hirschmann, C., Fyhr, C., Tsotsas, E. and Kemp, I.C. (1998), Comparison of two basic methods for measuring drying curves: Thin layer method and drying channel, *Proceedings of the 11th International Drying Symposium (IDS '98)*, pp. 224÷231.

[29] Hougen, O. A., Cauley, H. J. and Marshall, W. R. (1939), Limitations of diffusion equations in drying, *American Institute of Chemical Engineers*, pp. 183÷209.

[30] Irawan, A., Metzger, T. and Tsotsas, E. (2006), Isothermal drying of pore networks: influence of friction for different pore structures, *15th International Drying Symposium (IDS 2006)*, Budapest (accepted).

[31] Irudayaraj, J. and Wu, Y. (1996), Analysis and application of Luikov's heat, mass, and pressure transfer model to a capillary porous media, *Drying Technology* **14** (3-4), pp. 803÷824.

[32] Jaros, M., Cenkowski, S., Jayas, D.S. and Pabis, S. (1992), A method of determination of the diffusion coefficient based on kernel moisture content and its temperature, *Drying Technology*, **10** (1), pp. 213÷222.

[33] Jayantha, P. A. and Turner, I.W. (2003), A second order finite volume technique for simulating transport in anisotropic media, *International Journal of Numerical Methods for Heat and Fluid Flow* **13** (1), pp. 31÷56.

[34] Kast, W. (1988), Adsorption aus der Gasphase: Ingenieurwissenschaftliche Grundlagen und technische Verfahren, VCH Verlagsgesellschaft GmbH, Weinheim.

[35] Kaviany, M., Mittal, M. (1987), Funicular state in drying of a porous slab, *International Journal of Heat and Mass Transfer* **30** (7), pp.1407÷1418.

[36] Keey, R. B. (1980), Theoretical foundations of drying technology. In: *Advances in Drying* **1**, Mujumdar, A. S. (Ed.), Hemisphere Publ. Corp., Washington DC, pp. 1÷22.

[37] Ketelaars, A. A. J., Pel, L., Coumans, W. J. and Kerkhof, P. J. A. M. (1995), Drying kinetics: a comparison of diffusion coefficients from moisture concentration profiles and drying curves**,** *Chemical Engineering Science* **50** (7), pp. 1187÷1191.

[38] Koponen, H. (1987), Moisture diffusion coefficients of wood, *Drying '87*, pp. 225÷232.

[39] Koptyug, I. V., Kabanikhin, S. I., Iskakov, K. T., Fenelonov, V. B., Khitrina, L. Yu., Sagdeev, R. Z. and Parmon, V. N. (2000), A quantitative NMR imaging study of mass transport in porous solids during drying, *Chemical Engineering Science* **55**, pp. 1559÷1571.

[40] Krischer, O. and Kast, W. (1992), Die wissenschaftlichen Grundlagen der Trocknungstechnik, erster Band, dritte Auflage, Springer, Berlin.

[41] Kwapinski, W. and Tsotsas, E. (2004), Experimental determination of single-particle kinetics and equilibria for convective drying, desorption or adsorption by a magnetic suspension balance, *Drying 2004 - Proceedings of the 14th International Drying Symposium (IDS 2004)*, pp. 1419÷1426.

[42] Lartigue, C., Puiggali, J. R. and Quintard, M. (1990), A simplified study of moisture transport and shrinkage in wood, *Drying '89*, pp. 169÷179.

[43] Lasseux, D., Quintard, M. and Whitaker, S. (1996), Determination of permeability tensors for two-phase flows in homogeneous porous media: Theory, *Transport in Porous Media,* Vol. **24** (2), pp. 107÷137.

[44] Laurindo, J. B. and Prat, M. (1996), Numerical and experimental network study of evaporation in capillary porous media. Phase distributions, *Chemical Engineering Science*, Vol. **51**, No. 23, pp. 5171÷5185.

[45] Laurindo, J. B. and Prat, M. (1998), Modeling of drying in capillary–porous media: A discrete approach, *Drying Technology* **16** (9-10), pp. 1769÷1787.

[46] Lewis, R.W. and Ferguson, W. J. (1990), The effect of temperature and total gas pressure on the moisture content in a capillary porous body, *International Journal for Numerical Methods in Engineering* **29** (2), pp. 357÷369.

[47] Li, Z. and Kobayashi, N. (2005), Determination of moisture diffusivity by thermo-gravimetic analysis under non-isothermal condition, *Drying Technology* **23** (6), pp. 1331÷1342.

[48] Lim, L. C., Tasirin, S. M. and Daud, W. R. W. (2004), Derivation of new drying model from theoretical diffusion controlled drying period. In: *Drying 2004, Proceedings of the 14th International Drying Symposium (IDS 2004),* Vol. A, pp. 430÷435.

[49] Lowell, S. and Shields, J. E. (1991), Powder surface area and porosity, 3rd Edition, Chapman & Hall, London.

[50] Luikov, A. V. (1966), Application of irreversible thermodynamics methods to investigation of heat and mass transfer, *International Journal of Heat and Mass Transfer,* Vol. **9**, pp. 139÷152.

[51] Luikov, A. V. (1966), Heat and mass transfer in capillary-porous bodies, Translated by Harrison, Translation edited by Pun, W.M, Pergamon Press Ltd., Oxford.

[52] Luikov, A.V. (1975), Systems of differential equations of heat and mass transfer in capillary-porous bodies (review), *International Journal of Heat and Mass Transfer*, Vol. **18** (1), pp. 1 ÷ 14.

[53] McDonald, P. J., Pritchard, T. and Roberts, S. P. (1996), Diffusion of water at low saturation levels into sandstone rock plugs measured by broad line magnetic resonance profiling, *Journal of Colloid and Interface Science* **177** (2), pp. 439÷445.

[54] Metzger, T., Kwapinska, M., Peglow, M., Saage, G. and Tsotsas, E. (2006), Modern modeling methods in drying, *Transport in Porous Media (accepted).*

[55] Metzger, T., Tsotsas, E. (2005), Influence of pore size distribution on drying

kinetics: a simple capillary model, *Drying Technology 23*, pp.1797÷1809.

[56] Michel, D., Quintard, M. and Puiggali, J.-R. (1987), Experimental and numerical study of pine wood drying at low temperature, *Drying '87*, pp. 185÷193.

[57] Mourad, M., Hemati, M. and Laguerie, C. (1996), A new correlation for the estimation of moisture diffusivity in corn kernels from drying kinetics, *Drying Technology* **14** (3-4), pp. 873÷894.

[58] Nasrallah, S. B. and Perré, P. (1988), Detailed study of a model of heat and mass transfer during convective drying of porous media, *International Journal of Heat and Mass Transfer*, Vol. **31**, No. 5, pp. 957÷967.

[59] Nowicki, S. C., Davis, H. T. and Scriven, L. E. (1992), Microscopic determination of transport parameters in drying porous media, *Drying Technology* **10** (4), pp. 925÷946.

[60] Oliveira, A. C. and Fernandes, E. O. (1986), Simulation of the convective drying of capillary-porous materials. In: *Drying '86, Vol. 1, Proceedings of the 5th International Symposium on Drying,* pp. 65÷70.

[61] Ouelhazi, N., Arnaud, G. and Fohr, J.-P. (1991), The drying of a wood plank below boiling point. Influence of internal gaseous pressure in 1D and 2D, *Drying '91*, pp. 507÷517.

[62] Patankar, S. V. (1980), Numerical heat transfer and fluid flow, Hemisphere Publ. Co., New York.

[63] Pel, L. Broken, H. and Kopinga, K. (1996), Determination of moisture diffusivity in porous media using moisture concentration profiles, *International Journal of Heat and Mass Transfer* **39** (6) , pp. 1273÷1280.

[64] Pel, L., Ketelaars, A. A. J, Adan, O. C. G and Van Well, A. A. (1993), Determination of moisture diffusivity in porous media using scanning neutron radiography, *International Journal of Heat and Mass Transfer* **36** (5), pp. 1261÷1267.

[65] Perré P., Nasrallah, S. B. and Arnaud, G. (1986), A Theoretical study of drying: Numerical simulations applied to clay-brick and softwood. In: *Drying '86,* Vol. **1***, Proceedings of the 5th International Symposium on Drying,* pp. 382÷390.

[66] Perré, P. (1987), Le séchage convectif de bois résineux: choix, validation et utilisation d'un modèle, *PhD thesis*, University Pasis VII.

[67] Perré, P. (1997), Image analysis, homogenization, numerical simulation and experiment as complementary tools to enlighten the relationship between wood anatomy and drying behavior, *Drying Technology* **15** (9), pp. 2211÷2238.

[68] Perré, P. and Degiovanni, A. (1990), Simulation par volumes finis des transferts couplés en milieux poreux anisotropes : séchage du bois a basse et à haute

temperature, *International Journal of Heat and Mass Transfer* **33** (11), pp. 2463÷2478.

[69]   Perré, P. and Turner, I. W. (1996), The use of macroscopic equations to simulate heat and mass transfer in porous media: Some possibilities illustrated by a wide range of configurations that emphasise the role of internal pressure. In: Turner, I. and Mujumdar, A. S. (Eds.), *Mathematical modeling and numerical techniques in drying technology*, Marcel Dekker, New York.

[70]   Perré, P. and Turner, I. W. (1998), Transpore: A generic heat and mass transfer computational model for understanding and visualising the drying of porous media. In: *Drying'98, Proceedings of the 11*[th] *International Drying Symposium (IDS'98),* Vol. A, pp. 365÷374.

[71]   Perré, P. and Turner, I. W. (1999), A 3-D version of TransPore: a comprehensive heat and mass transfer computational model for simulating the drying of porous media, *International Journal of Heat and Mass Transfer* **42**, pp. 4501÷4521.

[72]   Perré, P. and Turner, I. W. (2000), An efficient two-dimensional CV-FE drying model developed for heterogeneous and anisotropic materials, *Proceedings of the 12*[th] *International Drying Symposium (IDS' 2000)*, Vol. A, pp. 262.

[73]   Perré, P. and Turner, I. W. (2001), Determination of the material property variations across the growth ring of softwood for use in a heterogeneous drying model. Part 1. Capillary pressure, tracheid model and absolute permeability, *Holzforschung*, Vol. **55** (3), pp. 318÷323.

[74]   Perré, P. and Turner, I. W. (2001), Determination of the material property variations across the growth ring of softwood for use in a heterogeneous drying model. Part 2. Use of homogenization to predict bound liquid diffusivity and thermal conductivity, *Holzforschung*, Vol. **55** (3), pp. 417÷425.

[75]   Perré, P. and Turner, I. W. (2002), A heterogeneous wood drying computational model that accounts for material property variation across growth rings, *Chemical Engineering Journal* **86** (1-2) , 117÷131.

[76]   Perré, P., Fohr, J. P. and Arnaud, G. (1989): A model of drying applied to softwoods: the effect of gaseous pressure below the boiling point. In: *Drying '89*, pp. 91÷98.

[77]   Perré, P., Moser, M. and Martin, M. (1993): Advances in transport phenomena during convective drying with superheated steam and moist air, *International Journal of Heat and Mass Transfer* **36** (11), pp. 2725÷2746.

[78]   Philip, J. R. and De Vries, D. A. (1957), Moisture movement in porous materials under temperature gradient, *Transactions, American Geophysical Union*, Vol. **38**, No. 2, pp. 222÷232.

[79]   Porto, P. S. S. and Lisbôa, A. C. L. (2004), Drying modelling of a parallelepipedic oil shale particle. In: *Drying 2004, Proceedings of the 14*[th]

International Drying Symposium (IDS 2004), Vol. A, pp. 542÷548.

[80] Prat, M. (1998), Discrete models of liquid-vapour phase change phenomena in porous media, Revue générale de thermique, Vol. **37** (11), pp. 954÷961.

[81] Prat, M. (2002), Recent advances in pore-scale models for drying of porous media, *Chemical Engineering Journal* **86** (1-2), pp. 153÷164.

[82] Press, W. H. (1992), Numerical recipes in C: the art of scientific computing, Cambridge Univ. Press.

[83] Puiggali, J. R., Quintard, M. and Whitaker, S. (1988), Drying granular porous media: Gravitational effects in the isenthalpic regime and the role of diffusion models, *Drying Technology* **6** (4), pp. 601÷629.

[84] Quintard, M. and Puiggali, J.-R. (1986), Numerical modelling of transport processes during the drying of a granular porous medium, *Heat and Technology* **4** (2), pp. 37 ÷ 57.

[85] Quintard, M. and Whitaker, S. (1988), Two-phase flow in heterogeneous porous media: The method of large-scale averaging, *Transport in Porous Media* **3** (4), pp. 357÷413.

[86] Ribeiro, J. A., Pereira, A. W., Oliveira, D. T. and Barrozo, M. A. S. (2002), Determination of drying kinetic parameters of *Bixa orellana* seeds in thin layer. In: *Drying'2002, Proceedings of the 13ᵗʰ International Drying Symposium (IDS'2002),* Vol. B, pp. 1293÷1300.

[87] Rubotherm Präzisionsmesstechnik GmbH: Magnetic suspension balances – Technical document.

[88] Saravacos, G. D. and Raouzeos, G. S. (1986), Diffusivity of moisture in air – drying of raisins. In: *Drying '86,* Vol. 2, *Proceedings of the 5ᵗʰ International Drying Symposium,* pp. 487÷491.

[89] Schluender, E.-U. and Tsotsas, E. (1988), Wärmeübertragung in Festbetten, durchmischten Schüttgütern und Wirbelschichten, Thieme Verlag, Stuttgart.

[90] Schrader, G. W. and Litchfield, J. B. (1992), Moisture profiles in a model food gel during drying: Measurement using magnetic resonance imaging and evaluation of the Fickian model, *Drying Technology* **10** (2), pp. 295÷332.

[91] Segura, L. A. and Toledo, P. G. (2005), Pore-level modeling of isothermal drying of pore networks: Effects of gravity and pore shape and size distributions on saturation and transport parameters, *Chemical Engineering Journal,* Vol. **111** (2-3), pp. 237÷252.

[92] Sherwood, T. K. (1929), The drying of solid – I, *Industrial and Engineering Chemistry*, Vol. **21**, no. 1, pp. 12÷16.

[93] Silva, M. A. (2000), A general model for moving boundary problems –

147

application to drying of porous media, *Drying Technology* **18** (3), pp. 601÷624.

[94] Spolek, G. A. and Plumb, O. A. (1980), A numerical model of heat and mass transport in wood during drying, *Drying'80,* Vol. 2: *Proceedings of the second International Symposium on Drying* (IDS '80), pp. 84÷92.

[95] Srikiatden, J. and Roberts, J. S. (2005), Measuring moisture diffusivity of potato and carrot (core and cortex) during convective hot air and isothermal drying, *Journal of Food Engineering,* Vol. **74** (1), pp. 143÷152.

[96] Strumillo, C. and Kudra, T. (1986), Drying : principles, applications and design, Gordon and Breach Science Publ., New York.

[97] Suzuki, M. and Maeda S. (1978), An approximation of transient change of moisture distribution within porous material being dried, *Proceedings of the first International Symposium on Drying* (IDS '78), pp. 42÷47.

[98] Thijssen, H. A. C. and Coumans, W. J. (1985), Short-cut calculation for non-isothermal drying of shrinking and non-shrinking particles and of hollow spheres containing an expanding central gas core. In: *Drying '85: Selection of papers from the 4th International Drying Symposium, Kyoto (1984)*, pp. 11÷20.

[99] Tien, H. C., Vafai, K. (1990), A synthesis of infiltration effects on an insulation matrix, *International Journal of Heat and Mass Transfer* **33** (6), pp. 1263÷1280.

[100] Truscott, S. (2004), A heterogenous three-dimensional computational model for wood drying, *PhD thesis*, University of Queensland.

[101] Truscott, S. L. and Turner, I. W. (2005), A heterogeneous three-dimensional computational model for wood drying, *Applied Mathematical Modelling* **29** (4), pp. 381÷410.

[102] Tsotsas, E. (1992), Measurement and modelling of intraparticle drying kinetics: A review. In: *Drying'92, Proceedings of the 8th International Drying Symposium,* Part A, pp. 17÷41.

[103] Turner, I. W. (1991), The modelling of combined microwave and convective drying of a wet porous material, *PhD Thesis*, University of Queensland.

[104] Turner, I. W. and Ferguson, W. J. (1995), An unstructured mesh cell-centered control volume method for simulating heat and mass transfer in porous media: Application to softwood drying, Part I: The isotropic model, *Applied Mathematical Modelling*, Vol. **19** (11), pp. 654÷667.

[105] Turner, I. W. and Ferguson, W. J. (1995), An unstructured mesh cell-centered control volume method for simulating heat and mass transfer in porous media: Application to softwood drying, Part II: The anisotropic model, *Applied Mathematical Modelling*, Vol. **19** (11), pp. 668÷674.

[106] Turner, I. W. and Perré, P. (1995), A comparison of the drying simulation codes

TRANSPORE and WOOD2D which are used for the modelling of two-dimensional wood drying processes, *Drying Technology* **13** (3), pp. 695÷735.

[107] Turner, I. W. and Perré, P. (1996), A synopsis of the strategies and efficient resolution techniques used for modelling and numerically simulating the drying process. In: Turner, I. and Mujumdar, A. S. (Eds.), *Mathematical modeling and numerical techniques in drying technology*, Marcel Dekker, New York.

[108] Turner, I. W. and Perré, P. (2001), The use of implicit flux limiting schemes in the simulation of the drying process: A new maximum flow sensor applied to phase mobilities, *Applied Mathematical Modelling* **25** (6), pp. 513÷540**.**

[109] Van der Kooi, J. (1971), Moisture transport in cellular concrete roofs, *PhD Thesis*, Uitgeverij Waltman – Delft.

[110] Vargaftik, N. B., Vinogradov, J. K. and Yargin, V. S. (1996), Handbook of physical properties of liquids and gases : pure substances and mixtures, 3rd Edition, Begell House, NewYork.

[111] VDI-Wärmeatlas (2002), Berechnungsblätter für den Wärmeübergang, VDI-Gesellschaft Verfahrenstechnik und Chemieingenieurwesen (GVC), **9**. Auflage, Springer, Berlin.

[112] Vu, T. H., Metzger, T. and Tsotsas, E. (2006), Influence of pore size distribution via effective parameters in a continuous drying model, 15th *International Drying Symposium (IDS 2006)*, Budapest *(accepted)*.

[113] Wei, C. K., Davis, H. T., Davis, E. A. and Gordon, J. (1985), Heat and mass transfer in water-laden sandstone: Convective heating, *AIChE Journal* **31** (8), pp. 1338÷1348.

[114] Wei, C. K, Davis, H. T., Davis, E. A. and Gordon, J. (1985), Heat and mass transfer in water-laden sandstone: Microwave heating, *AIChE Journal* **31** (5), pp. 842÷848.

[115] Whitaker, S. (1977), Simultaneous heat, mass, and momentum transfer in porous media: A theory of drying, *Advances in Heat Transfer* **13**, pp.119÷203.

[116] Whitaker, S. (1980), Heat and mass transfer in granular porous media. In: *Advances in Drying* **1**, Mujumdar, A. S. (Ed.), Hemisphere Publ. Corp., Washington DC, pp. 23÷61.

[117] Whitaker, S. (1998), Coupled transport in multiphase systems: A theory of drying, *Advances in Heat Transfer* **31**, pp.1÷104.

[118] Whitaker, S. (1999), The Method of Volume Averaging, Kluwer Academic Publishers, The Netherlands.

[119] Whitaker, S. and Chou, W. T.-H. (1983): Drying granular porous media – Theory and experiment, *Drying Technology* **1** (1), pp. 3÷33.

Appendix 1

MATERIAL CONSTANTS

A.1. Liquid water ([22]; [110]; [111])

Density:

$$\rho_w = 1000 \ \text{kg·m}^{-3} \tag{A1-1}$$

Specific heat capacity:

$$c_{pw} = 4185 \ \text{J·kg}^{-1}\text{·K}^{-1} \tag{A1-2}$$

Dynamic viscosity:

$$\eta_w = -1.27 \cdot 10^{-9} \left(T[^oC]\right)^3 + 3.42 \cdot 10^{-7} \left(T[^oC]\right)^2$$
$$- 3.43 \cdot 10^{-5} \left(T[^oC]\right) + 1.56 \cdot 10^{-3} \qquad \text{Pas} \tag{A1-3}$$

Surface tension:

$$\sigma(T) = -1.3 \cdot 10^{-7} \cdot T[^oC]^2 - 1.58 \cdot 10^{-4} \cdot T[^oC] + 0.07606 \ \text{N.m}^{-1} \tag{A1-4}$$

Thermal conductivity:

$$\lambda_w(T) = \left(-2.9 \cdot 10^{-8} \cdot T[^oC]^4 + 4.1 \cdot 10^{-5} \cdot T[^oC]^3\right.$$
$$\left. - 0.016 \cdot T[^oC]^2 + 2.5 \cdot T[^oC] + 550\right) \cdot 10^{-3} \qquad \text{Wm}^{-1}\text{K}^{-1} \tag{A1-5}$$

A.2. Water vapour ([22]; [110]; [111])

Specific heat capacity:

$$c_{pv} = 1874 \ \text{J·kg}^{-1}\text{·K}^{-1} \tag{A1-6}$$

Molecular weight:

$$\tilde{M}_v = 0.018015 \ \text{kg·mol}^{-1} \tag{A1-7}$$

Dynamic viscosity:

$$\eta_v = 8.86 \cdot 10^{-6} \ \text{Pas} \tag{A1-8}$$

Saturation vapour pressure:

$$P_v^* = 133.32 \cdot e^{\left(18.584 - \frac{3984.2}{233.426 + T[^oC]}\right)} \tag{A1-9}$$

A.3. Air ([22]; [110]; [111])

Specific heat capacity:
$$c_{pa} = 1011 \ \text{J·kg}^{-1}\text{·K}^{-1} \tag{A1-10}$$

Molecular weight:
$$\tilde{M}_a = 0.02965 \ \text{kg·mol}^{-1} \tag{A1-11}$$

Dynamic viscosity:
$$\eta_a = 21.88 \cdot 10^{-6} \ \text{Pas} \tag{A1-12}$$

A.4. Others

Binary diffusion coefficient of vapour in air:

The binary diffusion coefficient of vapour in air is calculated from equation given by Schirmer (see Krischer, 1992 [40]):

$$\delta_{va}(T,P) = 2.26 \cdot 10^{-5} \cdot \left(\frac{T}{T_R}\right)^{1.81} \frac{P_R}{P_g} \ \text{m}^2.\text{s}^{-1} \tag{A1-13}$$

where T_R and P_R are reference temperature and pressure, respectively.

Dynamic viscosity of vapour-air mixture (Bird *et al.*, 1960 [5]):
$$\eta_g = \frac{\eta_v}{1+\Phi_1} + \frac{\eta_a}{1+\Phi_2} \ \text{Pas} \tag{A1-14}$$
where

$$\Phi_1 = \frac{1}{\sqrt{8}}\left(1+\frac{\tilde{M}_v}{\tilde{M}_a}\right)^{-\frac{1}{2}}\left[1+\left(\frac{\eta_v}{\eta_a}\right)^{\frac{1}{2}}\left(\frac{\tilde{M}_a}{\tilde{M}_v}\right)^{\frac{1}{4}}\right]^2 \tag{A1-15}$$

$$\Phi_2 = \frac{1}{\sqrt{8}}\left(1+\frac{\tilde{M}_a}{\tilde{M}_v}\right)^{-\frac{1}{2}}\left[1+\left(\frac{\eta_a}{\eta_v}\right)^{\frac{1}{2}}\left(\frac{\tilde{M}_v}{\tilde{M}_a}\right)^{\frac{1}{4}}\right]^2 \tag{A1-16}$$

Evaporation enthalpy (at 273.15 K):
$$\Delta h_{v0} = 2.5 \cdot 10^6 \ \text{J·kg}^{-1}\text{·K}^{-1} \tag{A1-17}$$

Gas constant:
$$\tilde{R} = 8.314 \ \text{J·kg}^{-1}\text{·K}^{-1} \tag{A1-18}$$

Reference gas pressure:
$$P_R = 101325 \ \text{Pa} \tag{A1-19}$$

Reference temperature:
$$T_R = 273.15 \ \text{K} \tag{A1-20}$$

Density of γ-Al$_2$O$_3$ particle (company's data)
$$\rho_0 = 1282 \ \text{kg.m}^{-3} \tag{A1-21}$$

Appendix 2

ACCURACIES OF WATER AND AIR FLOWS

Accuracy of water flow:

$$\varepsilon_w^{err} = \frac{\left|(\Delta M_w)_1 - (\Delta M_w)_2\right|}{(\Delta M_w)_1} \cdot 100\% \tag{A2-1}$$

Accuracy of air flow:

$$\varepsilon_a^{err} = \frac{\left|(\Delta M_a)_1 - (\Delta M_a)_2\right|}{(\Delta M_a)_1} \cdot 100\% \tag{A2-2}$$

The computation of ΔM_w and ΔM_a is explained in Section 4.4.2.

R (mm)	N	m_{ratio}	φ (%)	β (m/s)	T_∞ (^{o}C)	X_0 (kg.kg^{-1})	ε_w^{err} (%)	ε_a^{err} (%)
2.5	51	0.2	0	0.015	80	1	0.0189	0.0899
			0*				0.0235	0.5948
			5				0.0170	0.0744
			10				0.0165	0.0645
			20				0.0174	0.0463
			40				0.0226	0.0049
			60				0.0298	0.0493
			80				0.0382	0.1883
			50		20		0.1739	0.1286
			50		20 isothermal		0.0022	0.2302
					60		0.0107	0.0878
					100		0.0260	0.0708
					120		0.0357	0.0314
			0	0.020	80		0.0281	0.0297
				0.030			0.0502	0.0173
				0.040			0.0734	0.0064
				0.050			0.0969	0.0095
						1.2	0.2556	0.5946
						1.4	0.0523	1.0880
						1.58*	0.0531	3.8089
		0.05		0.015		1	0.0140	0.9945
		0.1					0.0175	0.0901
		1					0.0170	0.1082
1*	31	0.2		0.015	80	1	0.0437	0.2312
1.5*	41						0.0318	0.1483
5*	101						1.8350	2.9856
7.5*	151						1.1732	1.5261
10*							0.8962	1.0581
12.5*							3.8227	5.5309
15*							3.2123	4.5675
2.5*(plate)	51						0.0014	4.9550

* $tol = 10^{-8}$, all other cases $tol = 10^{-11}$.

Appendix 3

MODIFICATION OF PORE SIZE DISTRIBUTION

A.1. Capillary pressure curve

The first modification aims to get smooth capillary pressure curve near the transition point between free and adsorbed water (point A in Figure 2.4, Chapter 2). In the region between the first point (corresponds to radius of r_{min}) and the second point (corresponds to radius of r_2) of the pore radius grid, an asymptotic function (see Figure A3.1) is applied:

$$F_1 = r^2 \left(f_2 \sqrt{\frac{r_2 - r_{min}}{r - r_{min}}} \right)$$

(A3-1)

where f_2 is the value of the norm pore size distribution at r_2.

The modified pore size distribution to get smooth capillary curve is applied for both mono-modal and bi-modal cases.
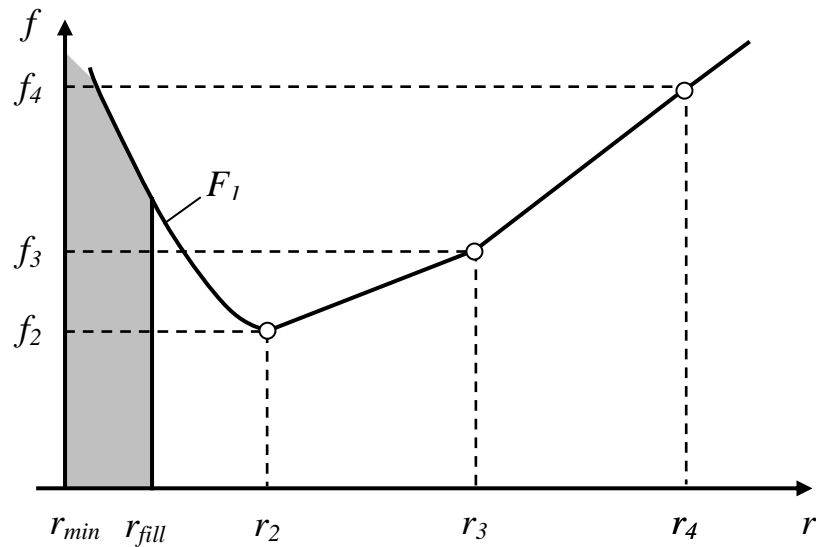

Figure A3.1 Modified pore size distribution to get smooth capillary curve.

A.2. Transition region

For bimodal distributions, the transition region (Figure A3.2) is treated as a trapezium responsible for A_t % of free saturation. The value of A_t is adjustable (normally less than 4%). It is assumed that the grid of *small* pore has n_1 elements and the grid of *large* pore has n_2 elements. Two sides of this trapezium are computed by the relationship

$$\frac{h_1}{(f_1)_{n_1-1}} = \frac{h_2}{(f_2)_2} \tag{A3-2}$$

In this equation, h_1 and h_2 are two sides of the trapezium, $(f_1)_{n_1-1}$ is the function value at $(r_1)_{n_1-1}$ of the *small* pore and $(f_2)_2$ is the function value at $(r_2)_2$ of the *large* pore. Here r_1 and r_2 denote the capillary radius of small and large pores.
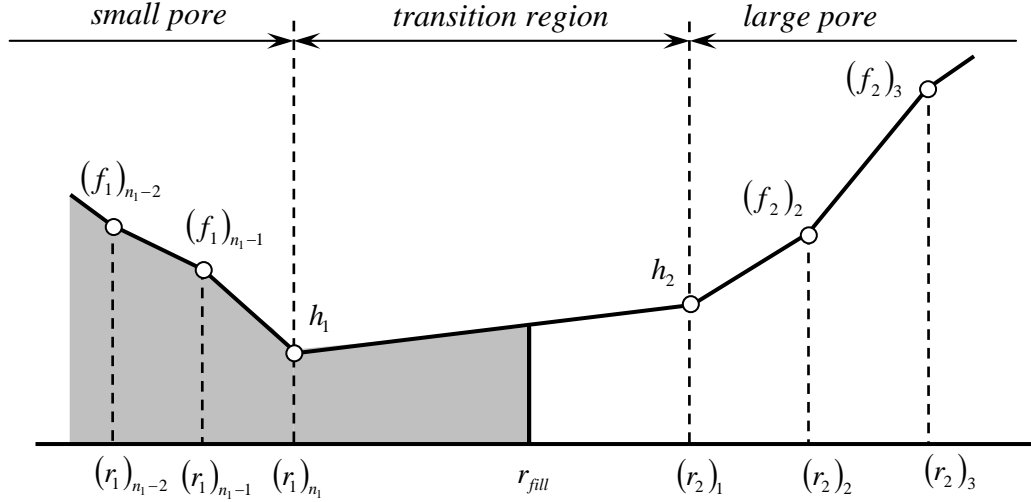

Figure A3.2 Transition region of bi-modal pore size distributions.

A.3. Relative permeability curves

In order to get smooth curves of relative permeabilities k_w and k_g, we use the values of modified pore size distribution as starting point and directly smoothen the relative permeability curves. These modifications are realized in the sample region as for the case of capillary curve. In this region, a cubic function is used

$$F_k = f_a \cdot x^3 + f_b \cdot x^2 + f_c \cdot x + f_d \tag{A3-3}$$

The factors f_a, f_b, f_c, f_d are computed by imposing

$$(F_k)_{min} = f_{min}; \quad (F_k)_2 = f_2; \quad \left(\frac{dF_k}{dr}\right)_{min} = \left(\frac{df}{dr}\right)_{min}; \quad \left(\frac{dF_k}{dr}\right)_2 = \left(\frac{df}{dr}\right)_2 \tag{A3-4}$$

where f_{min}, f_2 and $(F_k)_{min}, (F_k)_2$ are the values of relative permeabilities and function F_k at r_{min} and r_2, respectively. Note that below r_{min}, we set $k_w = 0$ and $k_g = 1$. Like capillary curve, the modification of relative permeability curves is applied for both mono-modal and bi-modal cases.

One example of the modification for the bi-modal case with $r_1 = 100 \pm 10$ nm; $r_2 = 200 \pm 20$ nm is presented in Figure A3.3 and Figure A3.4.
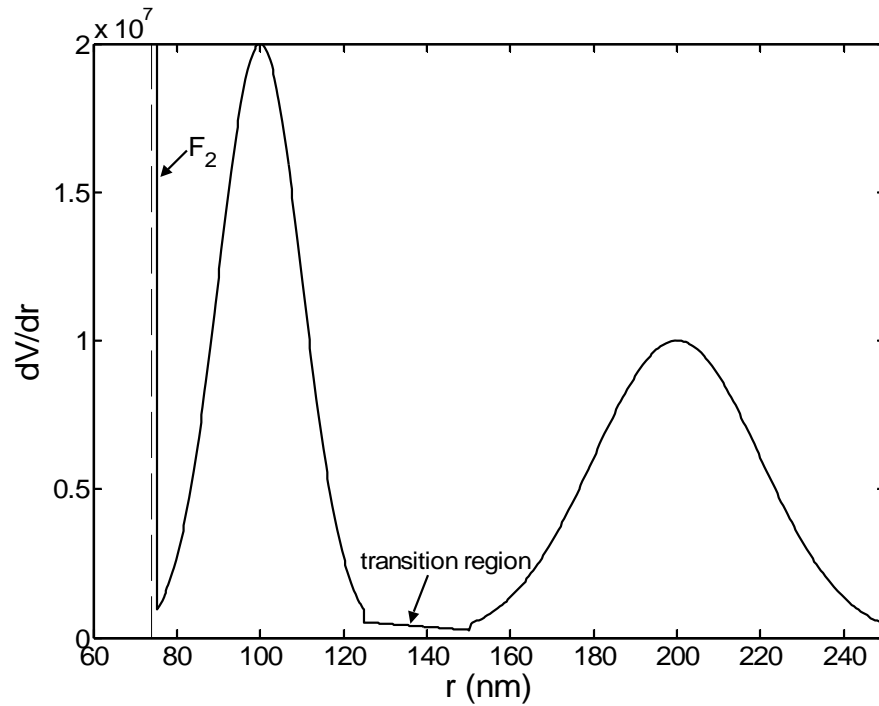
Figure A3.3 Modified bi-modal pore size distribution (100 ± 10 nm; 200 ± 20 nm).

a)   b)
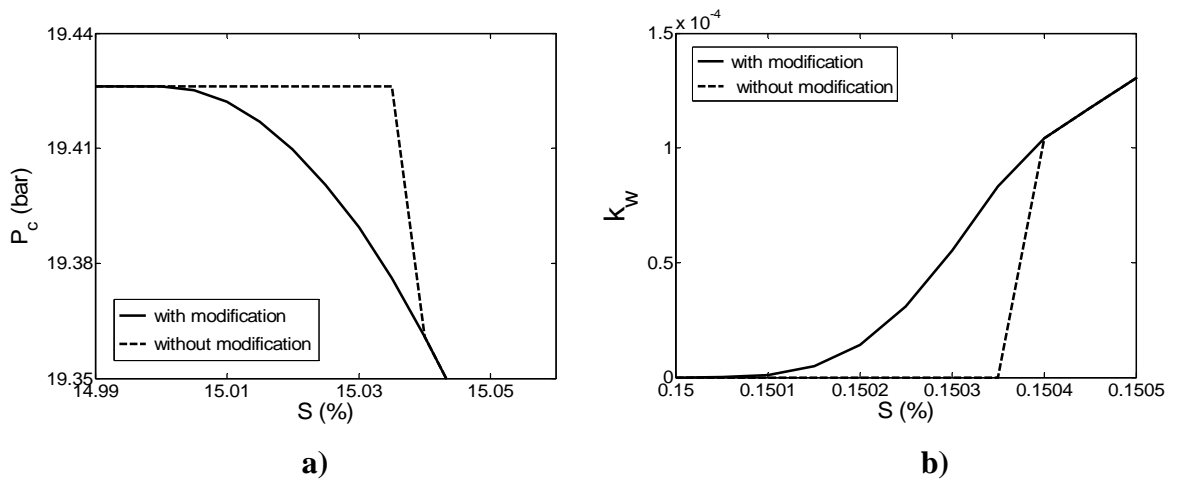
Figure A3.4

a) Effect of modification of bi-modal pore size distribution (100 ± 10 nm; 200 ± 20 nm)
on capillary curve.

b) Additional smoothing of relative permeability curve (for liquid) by cubic function.

LEBENSLAUF

Thai Hong Vu
Lehrstuhl für Chemische Apparatetechnik, Fakultät für Chemische Technik,
Technische Universität Hanoi
Raum 310 C$_{3-4}$, No. 1 - Dai Co Viet - Hanoi - Vietnam
Tel. (0084-4) 8 692510, Fax. (0084-4) 8 680070
geboren am 16. Juli 1974 in YenBai, Vietnam
ledig, vietnamesische Staatsangehörigkeit.

10/1991 – 5/1996	Diplom in Chemischer Apparatetechnik, Technische Universität Hanoi, Vietnam.
1994 – 1998	Diplom in Informatik, Technische Universität Hanoi, Vietnam.
10/1996 – 2/1999	Master of Engineering in Chemischer Apparatetechnik, Technische Universität Hanoi, Vietnam.
10/1999 – 1/2003	Dozent am Lehrstuhl für Chemische Apparatetechnik, Fakultät für Chemische Technik, Technische Universität Hanoi, Vietnam.
1/2003 – 12/2005	DFG – Promotionstipendium im Graduiertenkolleg 828 "Micro-Macro-Interactions in Structured Media and Particle Systems" am Lehrstuhl für Thermische Verfahrenstechnik an der Fakultät für Verfahrens- und Systemtechnik der Otto-von-Guericke-Universität Magdeburg.
seit 1/2006	wissenschaftlicher Mitarbeiter am Lehrstuhl für Thermische Verfahrenstechnik an der Fakultät für Verfahrens- und Systemtechnik der Otto-von-Guericke-Universität Magdeburg.

CURRICULUM VITAE

Thai Hong Vu

Department of Chemical Engineering Equipment and Machinery, Faculty of Chemical Technology, Hanoi University of Technology

Room 310 C_{3-4}, No. 1 - Dai Co Viet - Hanoi - Vietnam

Tel. (0084-4) 8 692510, Fax. (0084-4) 8 680070

born 16th July 1974 in YenBai, Vietnam

single, Vietnamese nationality.

10/1991 – 5/1996	Diploma in Chemical Engineering Equipment and Machinery, Hanoi University of Technology, Vietnam.
1994 – 1998	Diploma in Informatics, Hanoi University of Technology, Vietnam.
10/1996 – 2/1999	Master of Engineering in Chemical Engineering Equipment and Machinery, Hanoi University of Technology, Vietnam.
10/1999 – 1/2003	Lecturer at Department of Chemical Engineering Equipment and Machinery, Faculty of Chemical Technology, Hanoi University of Technology, Vietnam.
1/2003 – 12/2005	PhD scholarship of German Research Foundation (DFG) in the frame of Graduate School 828 "Micro-Macro-Interactions in Structured Media and Particle Systems" at Chair of Thermal Process Engineering, Faculty for Process and Systems Engineering, Otto-von-Guericke University Magdeburg, Germany.
since 1/2006	Research assistant at Chair of Thermal Process Engineering, Faculty for Process and Systems Engineering, Otto-von-Guericke University Magdeburg, Germany.